

On Lipid Migration from Particle-based Compacted Consumer Foods into Paper Packaging

by

Luc Dewulf 

Registration Number: 210116834

1st Supervisor: Professor Agba D. Salman

2nd Supervisor: Professor Joan L. Cordiner 

3rd Supervisor: Professor James D. Litster

Submitted to the School of Chemical, Biological, and Materials Engineering
in fulfilment of the requirements for the degree of
Doctor of Philosophy (PhD) in Engineering
at the
University of Sheffield

February 12, 2026



Abstract

Many particle-based consumer foods are in compacted or tableted form and contain lipids such as fats, oils and greases for nutritional, organoleptic, and technical functionalities. Driven by sustainability goals, consumer goods manufacturers aim to implement flexible paper-based packaging which however is more susceptible to lipid absorption due to its porous structure. Seasoning tablets or bouillon cubes are popular culinary condiments composed of compacted powders and lipids, wrapped individually in increasingly paper-based wrappers and often produce undesired lipid stains on the packaging. Research in lipid migration from foods has so far focused on chocolate. For the first time, a holistic approach is now taken to understand, characterise, and mitigate oil and fat migration from seasoning tablets into paper packaging. A literature review revisits fundamental mass transfer phenomena of lipid migration in particle-based food systems focusing on measurement, modelling and control approaches. The method of Raman chemical imaging and magnetic resonance imaging are further developed and applied for the first time to effectively quantify lipid mobility in seasoning food structures. As a migration mitigation strategy, interstitial pore size restructuration was performed by particle size variation of the salt fraction in the seasoning formulations. Capillary flow and diffusion modelling and experimental validation were performed. It was found that lipid migration out of the seasoning tablet into paper packaging was reduced in tablets with smaller pore microstructures, achieved with finer salt fractions. Lipid migration behaviour was explained by thermodynamic driving force being the relative difference of capillary suction between the food and paper matrices, and by kinetic resistance due to flow channel size in the food and paper porous media. This work for the first time investigated lipid migration from seasoning tablets into paper packaging, reviewing literature, developing advanced characterisation methodologies, and fundamentally describing and applying innovative migration mitigation strategies based on food microstructuration.

(300 words)

Ferar unus et idem
— Lord Collingwood

Acknowledgements

This work would not have been possible without the support of many people, that I cannot possibly all mention here. This list is not exhaustive and by no means is there any intention of ranking.

I am forever grateful for the support of my academic and industrial supervisors, Prof. Agba Salman and Prof. Joan Cordiner from the University of Sheffield, and Prof. Gerhard Niederreiter, Dr. Michael Hausmann, Dr. Annabel Bozon, and Prof. Stefan Palzer from Nestlé, who motivated, guided, and taught me many things about science and people during my PhD. I am very thankful for constant exchanges and insights with Dr. Riyadh Al-Asady, Dr. Christine Darnond, Dr. Richard Hodgkinson, Dr. Eleni Routoula, Prof. Siddharth Patwardhan, Dr. Vincent Meunier, Dr. Nicola Galaffu, Jean-Yves Chuat, Jean-Claude Delasoie, Dr. Jordan MacInnes, Dr. Steven Reynolds, Dr. Johannes Zimmer, Dr. Uli Bobe, Dr. Christoph Bolten, and Dr. Christoph Hartmann. Special thanks go to the many research assistants and workshop staff at the University and Nestlé R&D for training and assisting me: Abby Shipley, Andy Patrick, Adrian Lumby, Mario Dorna, Richard Stockley, Usman Younis, Oz McFarlane, Vinnie Walsh and Dave Miller.

I will be forever indebted to many friends and fellow students – from the iForge makerspace to our research group and Nestlé – for sticking together, motivating moments and making it through the rollercoaster journey of the PhD: Dr. Georgette Alejandra Fernandez Laris, Alexia Ioana Cazan, Dr. Sophie Groult, Dr. Yashodh Karanunayake, Shengda Hou, Yongang (Abdullah) Ma, Shen Fanglin, Mohamed Budri, Francesca Pinna, Eleni Georgiou, Jeanina Bungau, Alamir Katerji, Dr. Sarah Mohamed, Dr. Zheng (Harry) Wang, Dr. Xuquian (Owen) Li, Yifan Sun, Chenye (Tomáš) Liu, Daiyao (Ahri) Wu, Shijie (Leo) Liu, Dr. Suruthi Gnanenthiran, Dr. Jack Ledingham, and Dr. Alex Newman and Dr. Robyn Sutter. Particles may have strong cohesion, but the bonding in our PPG research group was unbreakable!

Last but not least, I would like to thank my family for their moral support and presence during the ups and downs of the PhD, especially my uncle Rutger Clemens, my aunt Isabelle Dewulf, my grandparents Marguerite and Jacques, and the wider Family.

My greatest thanks go to my parents, who have been role models for me, my mum with her independence, and my dad with his professional success and PhD. Unknowingly, they have educated me in the doctrine of Esther Wojcicki: «The only thing I can take credit for is teaching them to be independent». Thank you very much Muriel and Sigurd!

Contents

1	Introduction	10
2	Literature Review	16
3	Methodology	37
4	Mitigation Strategy	54
5	Modelling	66
6	Application	81
7	Summarising discussion	108
8	Conclusion	111
A	Additional data of application chapter	113
B	List and links of publications	116
C	Evidencing Development Summary	118

Chapter 1

Introduction

Many particle-based consumer foods are in compacted or tableted form and contain lipids such as fats, oils and greases for nutritional, organoleptic, and technical functionalities. Driven by sustainability goals, fast moving consumer goods manufacturers aim to implement flexible paper-based packaging which however is more susceptible to lipid absorption due to its porous structure. The ultimate aim in lipid migration research and the concerning industries has been to mitigate this undesired phenomenon. This necessitates understanding of the fundamental mass transfer mechanisms, which are still debated in literature, and knowledge of the food microstructure, formulation and lipid type, as well as of the packaging structure. As lipid stains manifest on packaging but originate from the food, characterisation techniques are required to locate and quantify lipid migration within the food matrix as well as in the packaging. Finally, predicting the performance of mitigation strategies requires appropriate modelling techniques.

Seasoning tablets, bouillon cubes or compacts (used interchangeably) are staple culinary condiments in many markets and contain majoritarily salt, sugar, starch, herbs and spices, and vegetable or animal lipids, in liquid and/solid form. During manufacturing, the food powders and lipids are mixed and compressed in tablet presses at up to 20 kPa pressure. The tablets are then wrapped in individual wrappers, increasingly of paper-based fibrous material. As commonly available seasoning tablets contain from 3 to 20 w/w% fat or oil depending on the market and recipe, lipid migration into paper packaging is of critical concern. Figure 1.1 shows a typical seasoning tablet in contact with paper and the resulting lipid stain after storage at 20 °C, 40 % relative humidity for 12 h. However, literature on lipid migration in seasoning tablets and into paper packaging is limited, as are industrially applicable solutions towards this undesired phenomenon. Hence, the present work aims to advance knowledge by first reviewing and proposing mitigation strategies based on microstructuration of the tablet particle and pore structure. Further by also developing high-end characterisation techniques applied for the first time to this food particle system, while first-principle modelling is applied in an attempt to predict lipid migration behaviour.

This thesis is structured as a *Publication format thesis* according to the University of Sheffield guidelines, which states that chapters either need to be published, in the process of publishing, or with the intention and quality to be published <https://www.sheffield.ac.uk/rpi/pgp/examination/formats>

The thesis follows a clear storyline in order to advance knowledge in the field of oil migration from particle-based compacted foods into paper packaging.

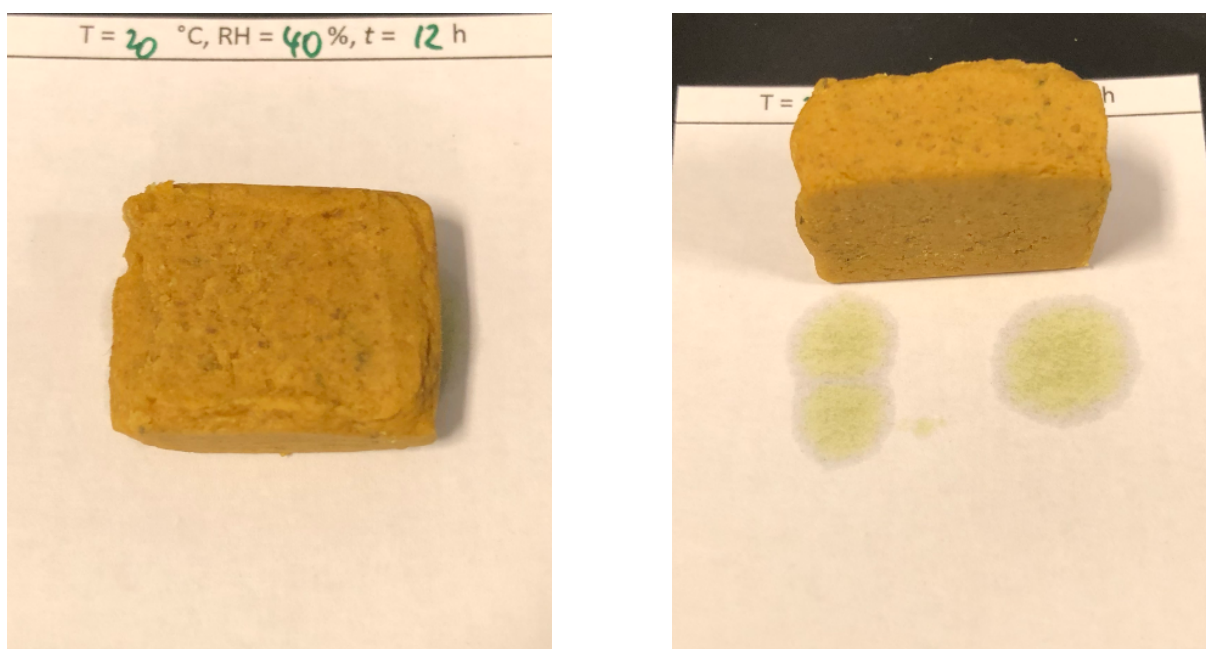


Figure 1.1: Lipid stain developing from a typical seasoning tablet on paper during storage at 20 °C, 40 % relative humidity for 12 h. Left hand photograph shows seasoning tablet resting on paper. Right hand photograph shows resulting fat lipid stains after lifting the tablet.

An extensive published literature review revisits prior public literature of lipid migration in particulate foods, focusing on current understanding of mass transfer mechanisms, reported characterisation techniques and their applicability to various lipid-particle food systems, first-principle and empiric modelling approaches, and physical strategies for lipid stabilisation and hence migration mitigation. (ii) Next, a pre-print published methods paper explains in detail Raman chemical imaging, the major characterisation technique employed in this work. The hardware and software setup to acquire and reconstruct images of the lipid profile on seasoning tablets is described. (iii) Further, a published article describes for the first time the mitigation approach of reducing particle size and thereby generating a microstructure that physically stabilises sunflower oil in a model salt and oil seasoning compact. Raman chemical imaging is used for the first time to accurately depict surface oil concentration as a function of particle size and temperature in a shelf-life test. (iv) To advance understanding of the fundamental physical mass transfer mechanism, an published manuscript attempts modelling of the liquid fat migration flow in a salt and fat compact. It is hypothesised that both the seasoning compact and paper packaging are porous bodies in contact with each other, and thus fat migration depends on the relative capillary pressure and permeability differences between the two media. A mechanistic capillary flow model is built and validated with a physical shelf-life experiment replicating the model and using Raman chemical imaging and optical imaging for quantification. (v) While the type of lipid was changed from sunflower oil to palm fat to show universality of this research, the particle matrix remained unchanged as salt. To further show applicability of this work to real seasoning tablets, the last chapter uses a more complex 7-component formulation. In this unpublished manuscript, sunflower oil migration in more realistic formulations is assessed on the surface via Raman chemical imaging and inside the tablet by employing magnetic resonance imaging for the first time to seasoning tablets, given that the tablets are opaque to Raman

surface techniques. As the microstructure is similarly more complex, diffusion modelling was applied to relate diffusivity with particle size changes of the formulation.

As such, this thesis in publication format follows a coherent storyline building scientific understanding from prior art, advanced experimental techniques and theoretical models, starting with model salt-oil systems and finishing with applied formulations.

Literature review

The thesis begins with an extensive published literature review titled *Particle-based food systems subject to lipid migration – A review of measurement, modelling, and mitigation approaches*. It is revisiting prior public literature of lipid migration in entirely particle-based foods or soft-matter systems containing particles. The focus is on current understanding of mass transfer mechanisms, reported characterisation techniques and their applicability to various lipid-particle food systems, first-principle and empiric modelling approaches, and physical strategies for lipid stabilisation and hence migration mitigation.

For this purpose, the literature review is formed of four main sections: (i) A fundamental section discussing the origins of lipid migration being thermodynamic instability but some kinetic deceleration effects, resulting in metastability. The two main mass transfer phenomena diffusion and capillary flow are described. (ii) A full review section is dedicated to characterisation techniques for lipid migration described in literature. From this section is it learned that most techniques have been developed for surface characterisation in 2D, mostly with gravimetric or optical techniques, with limited used of spectroscopic techniques. In addition, 3D characterisation of lipid migration is limited due to the need for tomographic equipment. (iii) As the aim of characterisation is to explain and predict, the third section is entirely dedicated to modelling approaches for lipid migration described in literature. Systems such as chocolate with complex microstructure and ingredient formulation are preferably modelled with a diffusion approach, as little structural and compositional information is required. Only few systems are modelled with a more fundamental capillary approach. (iv) As another objective is to find practical solutions to prevent lipid migration, literature-sourced physical approaches to lipid stabilisation are classified into their technologies and described. An outcome of the review here is that many lipid structuring approaches exist for emulsified systems but only few for mostly solid systems, especially for tablets. The literature review was thus used to find gaps in the literature and direct the following research.

Methodology

Following from the literature review, the methodology is described in a methods manuscript titled *A Method for Raman Chemical Imaging from Point Probes: Hyperspectral Characterisation of Food Powder Structures*. The literature review identified Raman spectroscopy as a powerful technique for 2D surface characterisation, yet it has not been used for lipid migration studies or compacted consumer foods.

This chapter describes the two approaches employing hyperspectral characterisation: distribution Raman chemical imaging, aiming to visualise the location of individual ingredients, and global intensity imaging, aiming to assess the spatial concentration of a single component over a surface. Raman spectroscopes for imaging are often prohibitively expensive and thus

a hardware and software setup were developed by the author and are described herein making them open-source. The relationship between particle size and resolution is described to obtain optimal results and the Matlab code for Raman signal processing is shared. Due to the novelty of this method and application, Raman imaging was used as the main characterisation technique in this thesis, and therefore this chapter solely concerns this application. Method details on the tablet composition and other experimental techniques as well as modelling are described in separate chapters, as is the nature of a thesis by publication.

Mitigation strategy

One conclusion of the literature review was the novelty of Raman imaging for lipid migration characterisation. In terms of mitigation strategies for lipid migration, a literature gap was identified for lipid stabilisation in particle compacts such as tablets. In particle beds the Young-Laplace equation predicts increasing capillary pressure for smaller interstitial pore sizes, effected by smaller particles. This theory was used to propose a tablet structure from smaller particles as a strategy to reduce lipid migration from the food tablets into paper packaging.

This chapter on the mitigation strategy is a published article titled *Food vs packaging: Dynamics of oil migration from particle systems into fibrous material* and presents the first work on mitigating sunflower oil migration from pure salt tablets of varying particle sizes. Raman imaging described in the methodology chapter is applied to trace the oil leaking on the tablet surface, while automated oil stain measurement on the packaging paper is used to quantify the resultant stain. It was shown that oil migration was reduced to almost 0 cm² on paper with little detectable changes of oil concentration on the tablet surface, when particle size was reduced from 500 to 50 μm. This reinforces the applicability of Raman imaging and stain imaging on paper as complementary methods to characterise the migration behaviour in both the food and packaging bodies. Further, this proof of concept was successful in suggesting that pore microstructuration is an effective method to reduce lipid mobility while enabling powder compaction into tablets.

Modeling

The methodology and mitigation strategy chapters showed suitable characterisation techniques and a successful mitigation strategy for lipid migration. The literature review further showed that capillary modelling is underutilized for lipid migration modelling due to frequent microstructural and compositional complexity of food bodies. To explain and predict mathematically the mass transfer behaviour observed in the prior mitigation chapter, a dedicated modelling chapter follows. Pursuing the thesis format in publication style, the chapter is titled *Fat migration from a particulate food system into fibrous material via capillary flow – first-principle modelling and experimental validation* and is a published article.

This chapter thus builds a theoretical mathematical model based on capillary flow for the same lipid-salt model system as the previous *Mitigation strategy* chapter to allow a one-to-one translation. Palm fat was used here instead of oil to use a lipid that is solid at preparation temperature but liquid at experimental conditions. Material characteristics (density, viscosity, surface tension), the thermodynamic system properties (capillary pressure), and the system kinetic properties (permeability) were evaluated in auxiliary measurements and fed into the

model. Those supporting experiments were washburn sorption type tests for fat-free salt tablets to assess fat sorption properties, and x-ray tomography to measure pore size. As microstructure was modulated by particle size, fat-salt tablets with particle size of $d_{50} = 5 \mu\text{m}$, $d_{50} = 250 \mu\text{m}$, and $d_{50} = 500 \mu\text{m}$ were evaluated systematically. An underlying ternary design of experiments was constructed by varying the quantity of the three size fractions into single, dual and ternary blends. The model predicted fat migration in the tablet assuming a 1D flow, and in the packaging paper assuming a 1D radial axisymmetric flow. For thorough experimental comparison, the model was validated in an exact physical replicate. Fat migration in the cube was measured as in prior chapters via Raman chemical imaging, and fat migration in the packaging paper as previously with automated image quantification. Model and experiments compared well for large particle sizes in which model parameters were easily measured, but failed for the prediction in the tablet for very fine fractions. It was hypothesised that the 1D assumption does not hold as fat rapidly migrated into the tablet core away from the surface.

Application

The prior chapters built a coherent storyline from literature review over methodology and strategy, to modelling. As a start, prior chapters discussed simple lipid-salt systems; sunflower oil and palm fat based with different salt size fractions. The preceding modelling chapter partly predicted the effect of microstructure on lipid migration from lipid-salt tablets into paper packaging. Yet, it was hypothesised that the lipid disappearance of surface fat from the tablet surface was due to capillary flow into the tablet core. While a novel and powerful technique, Raman imaging is a surface characterisation method, and does not enable tomographic imaging of the tablet core. In order to visualise tablet core and assess lipid migration in a more complex real system as opposed to lipid-salt only, the last chapter covers the application. Following from prior chapters, this is a manuscript currently submitted and unpublished titled *Surface and core effects in oil migration from particulate seasoning tablets into paper packaging via Raman and Magnetic Resonance Imaging*.

Instead of two-component lipid-salt tablets, genuine 7-component seasoning tablets were prepared from salt, sunflower oil, sugar, starch, maltodextrin, and monosodium glutamate. In addition to Raman chemical imaging for tablet surface characterisation, nuclear magnetic resonance (NMR) tomography was used for lipid visualisation in the tablet core. As previously, lipid characterisation of the tablet was complemented with automated fat stain quantification. It was shown that migration profiles of surface (Raman) and core (NMR) are congruent for the 7-component tablets which would justify a 1D vertical flow. However, the 2-component fat-salt tablet and 7-component seasoning tablet showed different migration profiles, suggesting that formulation differences between the two tablets result in different mass transfer behaviours. As the 7-component system's microstructure is complex to evaluate, a 1D diffusion model was established. It is novel as it omits simplifications described so far in oil migration literature and instead uses a numerical solution to Fick's second law.

This thesis builds a wholistic storyline from a prior art review, develops application-specific characterisation techniques, innovates with a modern physical mitigation strategy, and applies fundamental mass transfer modelling techniques alongside experimental results. This work

therefore advances knowledge in understanding, mitigating, measuring and modelling lipid migration in compacted particle-based food structures.

Chapter 2

Literature Review



Contents lists available at ScienceDirect

Powder Technology

journal homepage: www.journals.elsevier.com/powder-technology

Particle-based food systems subject to lipid migration – A review of measurement, modelling, and mitigation approaches

Luc Dewulf^{a,*}, Michael K. Hausmann^b, Annabel Bozon^c, Gerhard Niederreiter^b, Stefan Palzer^b, Agba D. Salman^a

^a Department of Chemical and Biological Engineering, University of Sheffield, Mappin Street, Sheffield S1 3JD, United Kingdom

^b Nestlé Research, Route du Jorat 57, 1000 Lausanne, Switzerland

^c Nestlé Product Technology Centre, Lange Straße 21, 78221 Singen, Germany

HIGHLIGHTS

- Two thirds of consumer foods are sold in particle-based forms and contain lipids.
- Oil, fat and grease are subject to migration within and out of the particle system.
- Lipid leaking results in quality defects on the food surface and the packaging.
- Modern migration measurement techniques, diffusion and capillary models are reviewed.
- Innovative oil stabilisation strategies for particulate foods types are discussed.

GRAPHICAL ABSTRACT



ARTICLE INFO

Keywords:

Oil migration
De-oiling
Particulate food

ABSTRACT

Many consumer food products such as confectionary or culinary seasonings are particle-based systems containing varying amounts of lipids such as oils, fats, and greases. Lipid migration is the result of inherent metastability of multiphase particulate food systems. Lipid instability is further aggravated by climatic conditions, interaction with packaging, porosity, material transitions, and even gravity. Resulting lipid mobility can lead to various

Abbreviations: C, Carbon; CLSM, Confocal laser scanning microscope; CMC, Carboxy methyl cellulose; CPMG, Carr, Purcell, Meiboom and Gill sequence for NMR relaxometry; DAG, Diacylglycerides; EDX, Electron-dispersive x-ray spectroscopy; FID, Free induction decay; FMCG, Fast moving consumer goods; FOGs, Fats oils greases; FRAP, Fluorescence recovery after photobleaching; HOSO, High oleic sunflower oil; LSE, Least squares error; MAG, Monoacylglycerides; MRI, Magnetic resonance imaging; N, Nitrogen; NCT, Neutron computed tomography; NIR, Near infrared spectroscopy; NMR, Nuclear magnetic resonance; O, Oxygen; o/w, Oil-in-water; PFG-STE, Pulsed field gradient stimulated echo experiments for NMR diffusivity; PLM, Polarised light microscopy; RF, Radio frequency; RH, Relative humidity; SCE, Specular component excluded; SCI, Specular component included; SD, Standard deviation; SEM, Scanning electron microscopy; SFC, Solid fat content; SG, Surface gloss (-); SSE, Error sum of squares; T₂, NMR spin-spin relaxation time (s); TAG, Triacylglycerides; w/o, Water-in-oil; WI, Whiteness index (-); XCT, X-ray computed tomography.

* Corresponding author.

E-mail address: ldewulf1@sheffield.ac.uk (L. Dewulf).

<https://doi.org/10.1016/j.powtec.2024.120097>

Received 25 May 2024; Received in revised form 11 July 2024; Accepted 16 July 2024

Available online 19 July 2024

0032-5910/© 2024 Published by Elsevier B.V.

Food powders
Chocolate

quality defects such as fat bloom on chocolate or oil stains on fibrous paper-based wrappers. This review revisits the factors influencing lipid migration and the generally accepted transport mechanisms diffusion and capillary flow. The most common measurement methods and modelling approaches described in the literature are discussed and assessed. Modern mitigation strategies to control lipid mobility are reviewed, with discussion on applicability to different particle-based food types and structures. Current trends towards healthier diets, clean-label recipes and sustainable packaging challenge traditional methods to stabilise lipids in food. As such a fundamental understanding, and measurement, modelling and mitigation strategies of lipid migration are highly relevant for a wide range of lipid-containing particulate foods.

Nomenclature			
A	Migration cross sectional area (m^2)	m	Mass concentration (kg m^{-3})
A_{stain}	Oil stain area (m^2)	M	Oil mass (kg)
a^*	Colour space a-axis	M_{∞}	Equilibrium oil mass (kg)
b	Exponent (–)	M_t	Oil mass at time t (kg)
b^*	Colour space b-axis	n	Number of terms (–)
Bo	Bond number (–)	P_{gas}	Gas-side pressure (Pa)
C	Mass fraction (kg kg^{-1})	P_{liq}	Liquid-side pressure (Pa)
C_{∞}	Equilibrium mass fraction (kg kg^{-1})	R^2	Correlation coefficient (–)
Ca	Capillary number (–)	r_{cap}	Capillary radius (m)
D	Diffusivity ($\text{m}^2 \text{s}^{-1}$)	r_{eff}	Effective radius (m)
D_{eff}	Effective diffusivity ($\text{m}^2 \text{s}^{-1}$)	r_m	Molecular radius (m)
D_{50}	Median particle size (m)	r_{men}	Meniscus radius (m)
d	Times (s)	T	Temperature (K)
d_p	Particle diameter (m)	t	Time (s)
E_{bind}	Electron binding energy (J)	t_0	Midpoint time (s)
E_{kin}	Electron kinetic energy (J)	$t_{1/2}$	Recovery half-time (s)
G	Magnetic field gradient amplitude (T m^{-1})	v	Flow velocity (m s^{-1})
g	Acceleration due to gravity (m s^{-2})	w	Bleached area radius (m)
h	Jurin's height (m)	x	Migration distance (m)
h_p	Planck's constant (J s)	β	Avrami index (–)
I	Intensity (au)	γ	Gyromagnetic ratio (–)
I_0	Intensity at 0 T m^{-1} magnetic field gradient (au)	Δ	Diffusion time (s)
I_{int}	Integral spectral intensity (au)	ΔP	Pressure difference (Pa)
i_{ω}	Intensity (au) at each Raman shift ω	δ	Pulse duration (s)
J	Mass flux ($\text{kg m}^2 \text{s}^{-1}$)	ϵ	Voidage (–)
k	Rate constant (s^{-1})	θ	Contact angle ($^{\circ}$)
k_b	Boltzmann's constant (J K^{-1})	μ	Viscosity (Pa s)
k_c	Crystallisation rate constant (s^{-1})	σ	Surface tension (N m^{-1})
k_m	Oil migration rate constant ($\text{kg s}^{-0.5}$)	ρ	Oil density (kg m^{-3})
k_s	Dissolution rate constant (s^{-1})	τ	Tortuosity (–)
L	Capillary length (m)	ν	Frequency (Hz)
l	Food body length (m)	ω	Raman shift (cm^{-1})
L^*	Lightness (–)	ω_0	Lower spectral limits (cm^{-1})
		ω_n	Upper spectral limits (cm^{-1})

1. Introduction

An estimated 70% of all dry fast moving consumer goods (FMCG) for humans and pets are sold in particulate form, either as powders, granules, tablets, or particle-based dispersions [1]. A significant proportion of FMCG contain oils, greases, or fats added for food texturing, mouth-feel, flavour enhancement, health benefits from addition of essential oils, for purposely increasing calorific energy content, or for technical reasons such as dust control during manufacturing [2].

Generally, fats, oils, and greases (FOGs), amongst other components like lecithins, are classified as lipids. Oils are usually considered liquid at room temperature, whereas fats are solid, although many exceptions exist and thus a distinction based on their structure is more helpful. Fatty acids are aliphatic carboxylic acids and can contain from 4 to 24 carbon atoms in foodstuffs. Melting points for fully saturated fatty acids

range from about 0 to 90 °C, whereas their unsaturated homologues do not tend to exceed 70 °C in melting temperature, owing to the alkene group. The absence of double bonds in saturated fatty acids generally results in a crystalline packing arrangement upon solidification, whereas in unsaturated structures the packing is less efficient due to the non-linearity induced by the double-bond, especially in the *cis* configuration [2].

When fatty acids are esterified with glycerol, mono-, di-, or triacyl glycerides (MAG, DAG, TAG) are formed, that solidify at room temperature. A given TAG molecule can crystallise in different polymorphs which bear different stabilities and thus melting points [2].

Greases are generally considered a biphasic mixture of liquid oil dispersed in a stabilising gelator matrix such as fats or waxes [3]. In particulate food systems, the lipid phase is essentially dispersed and in direct contact between particles, which for food products generally consist of crystalline or amorphous material. Crystalline particles are

generally inert to oil and humidity below their critical relative humidity (RH) due to their rigid crystal structure, but undergo deliquescence at higher atmospheric water content (75 %RH for table salt, 85 %RH for sucrose) [4]. Amorphous materials do not have a characteristic point beyond which they absorb water. Instead they gradually take up water and undergo sintering at rising environmental humidity due to an increase in free volume as small molecules such as water mobilise clusters of molecules [5]. Accordingly, various physicochemical phenomena in the lipid, crystalline, and amorphous phase can induce mobility of the lipid phase within, and out of the particulate food structure to its surrounding packaging. This metastability often referred to as fat, oil, or grease migration, release, or leaking [6], has serious implications for consumers and manufacturers alike, such as in fat bloom in chocolate confectionary [7–10] or in grease proofness of food packaging [11,12].

One of many consequences, oil leaking out of its protective food matrix is exposed to the oxygen containing environment and more prone to oxidation, responsible for the rancid off-flavour influencing taste perception of consumers [13]. For example, fat oxidation in dried dairy powder beverages is the main reason for rancid taste [14] and increase of surface fat is known to enhance powder caking and impede conveying, dispensing, and dissolution in manufacturing and vending settings [15].

Chocolate is also considered a particulate system majoritarily consisting of sugar and cocoa powder dispersed in a continuous cocoa butter or other fat matrix. Notorious fat bloom on chocolate implies a reduced quality in consumer preference [16,17] and it has been shown that visual opinionation influences taste perception of confectionary products [18]. Beyond organoleptic and hedonistic effects, hardness of chocolate has been shown to reduce as a result of oil migration due to lack of oil acting as a plasticizer, rendering the chocolate more brittle [19].

With the rising trend in food packaging paperisation, further technical implications on barrier properties are increasingly gaining importance. Paper and other fibrous packaging are porous media and thus generally have high affinity towards oils and greases compared to conventional packaging such as plastic, metal, or glass [20–22]. Fibrous packaging is thus more prone to lipid imbibition producing undesired visible stains on the exterior side of packaging. Visual packaging defects are a major reason for consumers rejecting food products, associating packaging damage with qualitatively inferior food [23]. Additionally, it has been shown that oils migrating into printed paper or cardboard can dissolve petrochemical-based inks and other oleosoluble coatings and contaminants, potentially entering into contact with food [24,25].

Other challenges within oil migration stem from current consumer trends in FMCG such as healthy diets, sustainable packaging, and shelf-life extension to reduce food waste. Classical approaches to prevent oil migration have been based on chemical transformations such as hydrogenation or interesterification that lead to higher fat viscosity at ambient temperature or fat crystallisation, thus rendering the lipid phase immobile. Substitution of fully saturated hard fats with unmodified (poly)unsaturated oils for health benefits results in a less viscous lipid phase, thus being more mobile to conditions driving oil migration [26,27]. Similarly, incorporating less processed but more whole foods into food structures means less structural modifications of the food microstructure for oil stabilisation can be undertaken [28,29]. Lastly, manufacturers' clean-label policies and legislative frameworks restrict certain additives in oil retention strategies [30]. For example, a clean-label approach would avoid artificial amphiphilic emulsifiers such as polysorbates and instead favour natural lecithin-based ones, that can however be less effective in lipid stabilisation [31] and allergenic due to residues from the plant they were derived from. In terms of packaging, comparisons of surveys show consumers rate paper as the most sustainable packaging type over plastic, metal, and glass [32–34], for which oil imbibition into its fibrous structure remains a challenge for oil migration control due to paper's strong capillary driven imbibition.

It is clear that lipid migration in particulate foods is a major quality concern in human and petfood alike. A fundamental understanding, and

measurement, modelling and mitigation strategies are thus timely and relevant in the face of challenging consumer preferences on food and packaging. After having set out the motivation for oil migration control in particulate foods, this review revisits the current understanding of oil migration in particulate food systems (section 2), before describing recent measurement techniques (section 3) and modelling approaches (section 4) and discussing modern advances in mitigation strategies (section 5).

2. Oil migration in particulate food systems

As most multiphase materials derived from nature that consist of more than a single pure compound, food containing particles and lipids is inherently thermodynamically metastable. The instability arises from concentration gradients due to localised concentration of material (e.g. liquid oil dispersed a fat matrix), due to pressure gradients (e.g. air in capillaries), or due to surface energy differences (e.g. small particles with large surface area) [35]. Kinetic constraints prevent the food from destabilisation immediately after preparation and in fact thermodynamic equilibrium is rarely reached [36]. Yet, microstructural and external phenomena such climatic conditions, interaction with packaging, porosity changes, material transitions, and even gravity can accelerate the destabilisation kinetics and result in enhanced mobility of the lipid phase. Lipid migration has generally been accepted to occur via three main routes: diffusion, capillary flow, or advection (convective mass transfer), whereby multiple processes are possible in the same system due to the typical complex structure of particulate food systems [8]. Lipid migration then manifests itself in various forms such as white fat bloom on chocolate, glossy greasy surface as in seasoning cubes, or oil stains on pet food paper packaging, besides secondary organoleptic effects as rancidity and reverse migration of packaging components into food [8,24,25,37,38].

2.1. Metastability

Metastability in particulate lipidous foods arises because the thermodynamic drive towards equilibrium and phase separation is slowed via kinetic effects [36]. Yet, mobile lipid fractions are subject to migration, of which several mass transport mechanisms are possible, either acting individually or combined.

Oils and fats are influenced by temperature and heat transfer between the environmental temperature and the food product, as for many fats used in foods the melting point is in the range of the ambient temperature on the planet and of the human mouth. With increasing temperature, oils become less viscous and more mobile, thus flow easier through a particle system and may be subjected to diffusion, capillary flow or advective flow [8]. Fats are generally composed of a mixture of multiple triacylglycerides and melt gradually from entirely solid to entirely liquid upon heating, with the range characterised by the solid fat content (SFC). Thus, increasing temperature increases the liquid fraction of the fat and its mobility for fat migration. Many fats exist in multiple polymorphic forms that can be achieved via controlled cooling or tempering from an initial molten state, and enhanced by seeding of the liquid fat with solid fat particles [39]. For cocoa butter triacylglycerides in chocolate for instance, six forms have been identified with different physical characteristics. Forms I to IV have the looser double chain packing, whereas forms V and VI have a denser triple chain packing, which also have a higher SFC at a given temperature, compared to looser less stable polymorphs [8,9]. Eutectic fat mixtures are mixtures of two or more fats that show incompatibilities between different fat phases and de-mix or segregate. This phase separation can cause fat migration by freeing the mobile fraction from a binding interaction with the less mobile fraction [40]. Multiple studies directly correlate viscosity, SFC and polymorph structures of cocoa butter and other fats with migration phenomena in chocolate [8,9].

Filled confectionary systems differ from the above single fat phase

systems by containing a core rich in liquid oils, such as cream, ganache, wafers or nuts, enrobed with a chocolate shell, that in itself contains a continuous fat phase. While there is evidence of fat migration leading to surface bloom in single triacylglyceride fat phase chocolate [41], most research focusses on oil-induced fat bloom. The suggested mechanisms inducing metastability are a dissolution of triacylglycerides in oil at the filling-chocolate interface, and diffusive transport of oil and triacylglycerides to the chocolate surface, driven by the concentration gradient between the oil-poor chocolate surface and oil-rich filling. Recrystallisation of triacylglycerides then occurs at the surface completing the migration pathway [42].

Many particulate food systems also occur as emulsions, either water-in-oil (w/o) or the reverse (o/w), or oil entrapped in fat. Metastability here is mostly induced by surface energy effects and insufficient interfacial stability between segregated phases. In emulsions, Ostwald ripening causes larger droplets or particles to grow at the expense of smaller ones [43], which in extreme cases leads to phase separation and thus frees any previously emulsified and stabilised phase to migrate, possibly via diffusion or capillary migrative flow. Similarly, in solid-liquid food systems such as chocolate, solid crystalline and amorphous particles can aggregate either due to moisture forming solid bridges between crystalline particles upon dissolution-recrystallisation, or due to sinter bridges between amorphous particles upon sintering [5]. While entrapment of oil into porous cocoa agglomerates seems plausible, hypotheses of pressure gradients for example induced by particle aggregation and oil displacement, leading to advective oil migration have also been proposed [10].

2.2. Diffusivity

Diffusion is defined as the transport of molecules of a mobile primary phase through a continuous stationary secondary phase, macroscopically driven by a concentration gradient, and microscopically by Brownian motion [44]. It was formalised into Fick's law by first assuming a constant concentration gradient between the rich diffusant and the depleted stationary phase [45,46]. At any instant in time dt , the mass flux J ($\text{kg m}^{-2} \text{s}^{-1}$) in and out of the interfacial area A is proportional to $m(x-l)l$ and $m(x+l)l$ respectively, where m is the diffusant concentration (kg m^{-3}), x is the diffusion distance, and l is the length of the food body through which diffusion occurs (m). (Fig. 1). The net flux is the difference of the two

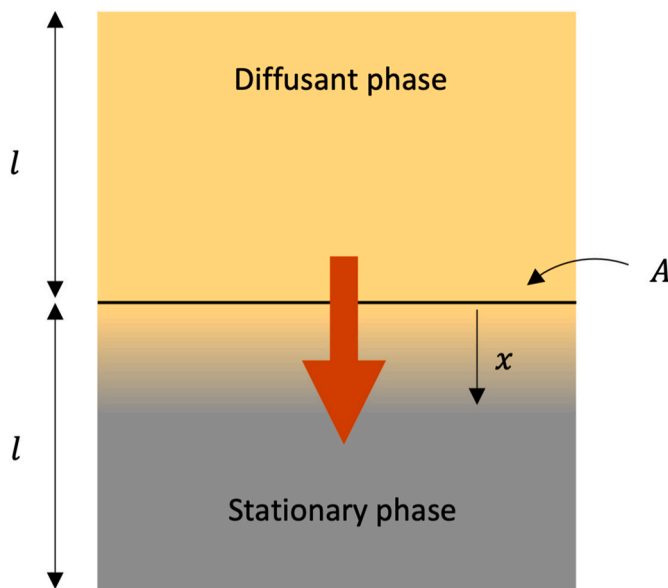


Fig. 1. Schematic of mass transport via diffusion.

$$J = m(x-l)l - m(x+l)l = m.x - ml^2 - m.x - ml^2 = -2ml^2 \quad (1)$$

However, m changes with location along the diffusing path, that is, there is a concentration gradient $m = \frac{dm}{dx}$. Hence,

$$J = -2l^2 \frac{dm}{dx} = -D \frac{dm}{dx} \quad (2)$$

which is Fick's first law in 1 dimension for constant concentration gradient $\frac{dm}{dx}$ across the cross sectional area A . The diffusivity D absorbs $2l^2$ in a proportionality constant.

Diffusive migration of oil in most food products can be regarded as a batch process. This is because the amount of diffusant oil phase l and the size of the stationary phase l are limited, without constant influx or outflux. As a result, the concentration changes with distance x , yielding Fick's 2nd law

$$\frac{dm}{dt} = -D \frac{d^2m}{dx^2} \quad (3)$$

From the above derivation it follows, that the stationary phase needs to be permeable to the mobile phase. In particulate food products such as chocolate, the diffusion approach has been especially used to explain migration of oil through the fat phase, such as from an oil-rich filling or nuts through a chocolate coating to its surface, developing fat bloom. Explanations of fat permeability to oil have been proposed as a dissolution-recrystallisation or swelling process. In the dissolution-recrystallisation pathway, oil dissolves the fat upon its contact, allowing migration followed by recrystallisation and precipitation of the fat on the chocolate surface [42]. In the swelling mechanism, oil-induced imbibition of fat crystals and consecutive expansion increase the free volume in the fat matrix, allowing diffusive passage of oil, akin to moisture diffusion in polymer networks [47]. The free volume approach is supported for the chocolate system by the ability to reduce oil migration through the cocoa butter phase in chocolate by polymorph selection. Cocoa butter crystals of form I to IV are less dense owing to their double-chain structure compared to the denser triple-chain V and VI forms, resulting in less oil induced fat bloom. Additionally, D is affected by temperature as the thermal energy increases according to Einstein's relation $D = kT/6\pi\mu r_m$ where kT is the thermal energy (J), μ is the viscosity (Pa s) and r_m is the molecular radius (m) [48]. Generally, diffusion is considered a slow process compared to bulk flow of liquids via capillary action or advection [49].

2.3. Capillarity

While diffusion explains well transport in continuous biphasic systems, it does not fundamentally explain transport in triphasic solid-liquid-gas systems. Especially particulate food systems can contain porous voids either as interparticle or intraparticle space. For example, roasted cocoa particles contain up to 25 v/v% void space [50], while mercury porosimetry studies revealed a pore volume of up to 4 v/v% for chocolate overall [51]. An energy-dispersive x-ray spectroscopic study on fat migration in chocolate showed rapid oil transport that could not be explained by the slower diffusion time scales, but rather by taking into account the microstructural capillarity [52].

A liquid column held in a tube or particle system of sufficiently small diameter develops a meniscus and pressure gradient across the liquid/air interface, with high pressure on the air side and low pressure on the liquid side, given by the Young-Laplace equation [53,54].

$$P_{\text{gas}} - P_{\text{liq}} = \frac{2\sigma}{r_{\text{men}}} = \frac{2\sigma \cos\theta}{r_{\text{cap}}} \quad (4)$$

where σ is the surface tension, r_{men} is the radius of the meniscus-tube curvature, and r_{cap} is the radius of a perfectly spherical capillary tube. In a monodispersely distributed spherical particle system (Fig. 2), an

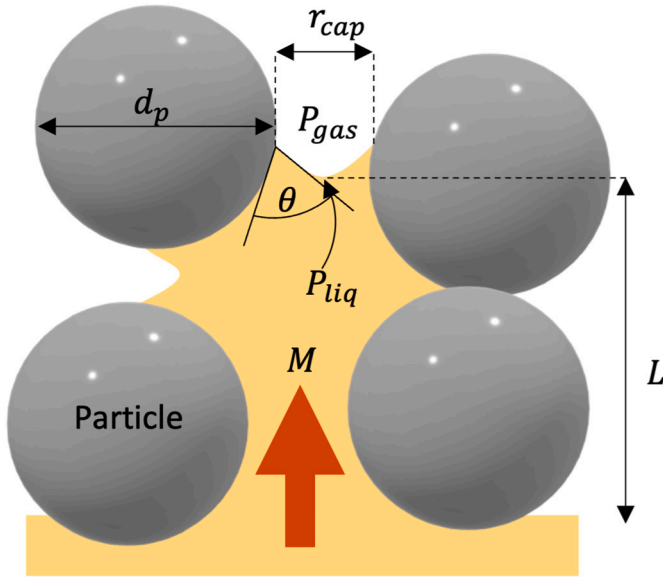


Fig. 2. Schematic of mass transport via capillary flow.

effective capillary radius r_{eff} (m) can be approximated by the voidage ϵ (–) and particle diameter d_p (m) [55,56].

$$r_{eff} = \frac{\epsilon d_p}{3(1 - \epsilon)} \quad (5)$$

ϵ denotes the volume of space between particles that might for example, be filled by lipids or air. In real particulate food systems, measuring r_{eff} is challenging and requires advanced techniques such as gas adsorption or microtomography. In chocolate, pore diameters were estimated via atomic force microscopy to be 2 to 8 μm in diameter [57]. In a different study on chocolate employing synchrotron x-ray tomography, pore diameters of between 7 and 125 μm and several millimetre length were measured [58].

The pressure difference across the meniscus makes the liquid travel through the porous medium, in a vertical geometry until gravity balances the capillary suction, and in a horizontal or downwards flow until viscous forces balance. The maximum capillary rise h is given by Jurin's law [59,60].

$$h = \frac{2\sigma\cos\theta}{\rho g r_{cap}} \quad (6)$$

where ρ is the liquid density, in the present case for example oil. Given that capillary rise is affected by gravity and viscosity, the question arises which force dominates. The transition from a capillary dominated to gravity controlled flow is suggested at a Bond number of $Bo = (2\rho g r_{cap})/\sigma = 1$; and similarly the switch from capillary controlled to viscous effects dominated flow is given as in the capillary number $Ca = \mu v/\sigma = 10^{-5}$, where v is the oil flow velocity [61,62]. In order to model the dynamics of liquid flow driven by the Laplace pressure, the flow regime is safely assumed to be laminar in the case of oil migration through food structures given the relatively long timescales required, and hence the Hagen-Poiseuille equation is applicable [63,64].

$$v = \frac{r_{cap}^2 \Delta P}{8 \mu L} \quad (7)$$

Neglecting inertial and gravity forces, the pressure gradient is then replaced with the Laplace pressure, yielding the Washburn equation, linking the fluid flow distance with time, or mass transported with time [65].

$$L = \sqrt{\frac{t\sigma r_{cap}\cos\theta}{2\mu}}, \text{ or } M = \rho\epsilon A \sqrt{\frac{t\sigma r_{cap}\cos\theta}{2\mu}} \quad (8)$$

Because of the heterogeneous nature of many porous media with different pore sizes, a combined mechanism for cellulose foams for example has been suggested to consist of fast initial capillary suction to reach Jurin's height, followed by slow diffusion. In such a system of parallel diffusion and capillary flow, the relative favour of capillary controlled flow over diffusion is generally given if the Péclet number $Pe = vL/D$ is larger than 1.0 [62].

3. Oil migration measurement in particulate food systems

The need to understand, predict, and mitigate oil migration and its adverse effects in particulate food systems has led to the development of multiple experimental monitoring techniques, illustrated in Fig. 3. They are direct measurements of oil migration such as the amount of oil released, the oil stain area on a contacting absorbing paper, or the amount of whiteness on a chocolate surface as a result of fat recrystallisation. In addition, the increased need to not only measure oil migration directly, but to also understand fundamental material properties, has led to additional measurement techniques that help understand microstructural metastability. While these techniques are indirect measurements of oil mobility, direct links between oil migration and for example differential thermograms, rheology, magnetic resonance, and x-ray scattering and diffraction patterns have been established. In the following sections, only key references are discussed to illustrate the different techniques but further examples of each measurement technique have been comprehensively tabulated in Table 1 in the same consecutive order.

3.1. Gravimetry

One of the most popular direct measurements of oil migration is the gravimetric weight determination of oil released (Fig. 3a). In order to measure the oil fraction migrated, the leaked oil needs to be separated from the food structure either in a filter paper or as the supernatant by centrifugation, and as such this technique is especially applicable to particulate food systems with high mobile oil fraction and permeable structures that leak oil fast, with rather capillary-controlled oil transport as opposed to diffusion. For example, multiple studies investigated formulation composition, amount of emulsifier, and the effect of edible fibre addition on oil release via gravimetry in the popular confectionary called halva [69]. As halva is made from sesame paste containing high amounts of liquid sesame oil in between sesame seed particles, oil migration into paper wrappers is of considerable concern in warm climate. To accelerate the gravimetric measurement, samples were centrifuged at up to 2000 g, allowing faster measurements. Centrifugation followed by gravimetry has also been used for ready-to-eat therapeutic food with high mobile oil fraction [72]. The disadvantage of centrifugation is that comparison with typical shelf-life conditions and packaging interactions is not possible, as normal gravity is only 1 g. Further examples are listed in Table 1.

3.2. Solvent extraction

Fats that are solid at room temperature don't readily flow into absorbing paper or phase-separate from the particle structure during centrifugation, and hence measuring oil migration is difficult, yet important. The fat migrating to the exterior surface in chocolate results in fat bloom, and fat migration into interparticle space of milk or cocoa powder causes caking, lumping, and poor reconstitution by rehydration and dissolution in water due to a hydrophobic fat layer. The fat contained in such particulate foods can be extracted by placing the sample into a bath of aliphatic or halogenated straight or cyclic hydrocarbons or

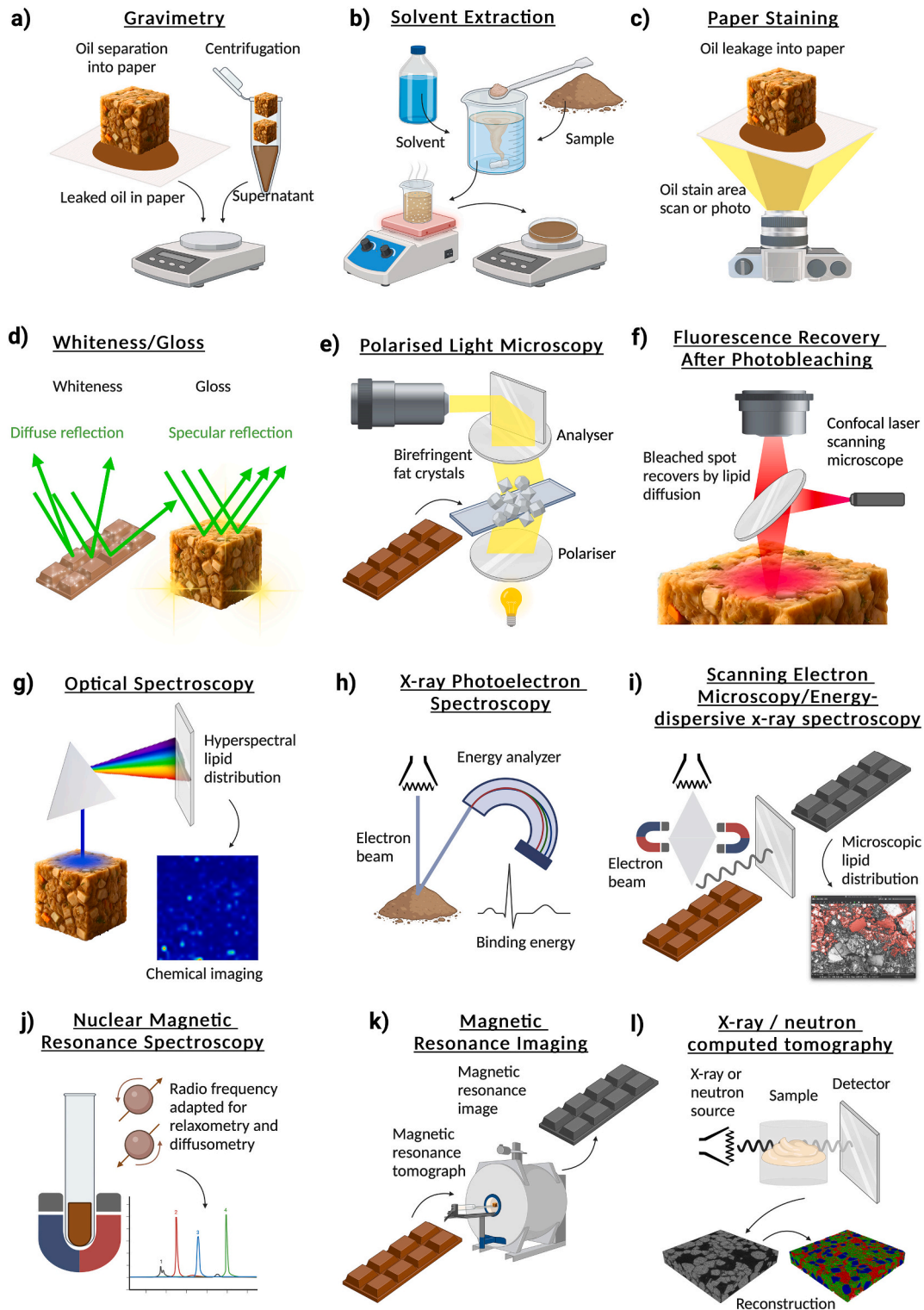


Fig. 3. Methods for measuring oil migration: a) gravimetry, b) solvent extraction, c) paper staining, d) whiteness and gloss, e) polarised light microscopy, f) fluorescence recovery after photobleaching, g) optical spectroscopy, h) x-ray photoelectron spectroscopy, i) scanning electron microscopy and energy-dispersive x-ray spectroscopy, j) nuclear magnetic resonance spectroscopy, k) magnetic resonance imaging, l) x-ray and neutron computed tomography.

alcohols (Fig. 3b). Gentle and short stirring at ambient temperature generally only dissolves surface free-fat, whereas the total fat content (surface and encapsulated) can be extracted by vigorous longer stirring at elevated temperatures [75]. The dissolved fat is then recovered gravimetrically after solvent evaporation. A clear separation of surface and encapsulated fats becomes difficult however with samples

containing high porosity or prone to disintegration, and thus the protocol needs adjusting for different food materials. Jacquot et al. [73] and Petit et al. [74] used solvent extraction into petroleum ether for surface free and total fat quantification to evaluate fat migration in cocoa powder. Over 60 days at 20 and 40 °C, the surface free fat content increased from 6 to 9 w/w% of total cocoa powder mass, but still

Table 1
Common measurement techniques of oil migration in particulate food systems.

Measurement	Food material	Investigation	Ref
Gravimetric	Phytosterol-sunflower oil oleogel	Effect of phytosteryl/HOSO ratio on oil migration into paper substrate	[66]
	Fat blend (Saturated/unsaturated soybean oil)	Effect of fat/oil ration and emulsifier type on oil migration into paper substrate	[67]
	Halva (sesame paste, sugar, corn fibres)	Effect of emulsifiers and corn fibres on oil migration into filter paper by centrifugation	[68]
	Halva (sesame paste, sugar, sesame testae (sesame hull waste), date fibres)	Effect of emulsifiers, sesame testae and date fibres on oil migration into filter paper by centrifugation	[69]
	Halva (sesame paste, sugar, palm oil, citric acid, glycerol, CMC, gelatine etc)	Effect of additives on oil migration into paper substrate	[70]
	Halva (sesame paste, sugar)	Effect of type of emulsifier on oil migration into paper substrate	[71]
	Ready-to-use therapeutic food (ground peanuts, palm oil, soybean oil, sugar, milk, micronutrients, emulsifiers)	Effect of emulsifier type and quantity on oil release upon centrifugation	[72]
	Cocoa powder	Effect of storage temperature on fat migration to surface	[73]
Solvent extraction	Cocoa powder	Effect of cocoa type and storage temperature on fat migration into interparticle voids	[74]
	Skimmed, whole and cream milk powder	Effect of storage time on fat migration to particle surface	[75]
	Model pet food (Silica gel and greases)	Grease release from pet food via oil stain extent on paper	[38]
	Palm kernel fat	Effect of high-intensity ultrasound on oil migration into paper	[76]
Optical oil stain area on paper	Oleogel (rapeseed oil, Myverol, sunflower oil, candelilla wax)	Oil migration from oleogel via growth of grease stain extent on paper	[77]
	Model stock cube (salt, sunflower oil)	Effect of crystalline phase particle size on oil migration via extent of oil stains on paper	[37]
	Fat blend (cocoa butter, tricaprillin, flaxseed oil, safflower oil, peanut oil)	Effect of oil viscosity on oil migration through fat matrix	[78]
Whiteness index and surface gloss	Dark chocolate (cocoa butter, cocoa, sucrose, lecithin, cocoa butter seeds)	Effect of tempering and seeding on fat migration to chocolate surface	[79]
	Chocolate-enrobed cream-filled wafer cookies	Effect of packaging wrapper on oil migration from cream filling to chocolate coating surface	[80]
	Dark chocolate (cocoa butter, cocoa, sucrose, lecithin)	Effect of sucrose particle size on fat migration to chocolate surface	[81]

Table 1 (continued)

Measurement	Food material	Investigation	Ref
Polarised light microscopy	Dark chocolate (cocoa butter, cocoa, sucrose, lecithin)	Effect of phospholipid emulsifiers on fat migration to chocolate surface	[82]
	Chocolate (cocoa mass, cocoa butter seeds)	Effect of temperature cycling on fat migration to chocolate surface	[41]
	Dark chocolate (cocoa butter, palm fat, mango kernel fat)	Effect of physical blends and interesterification on surface fat crystallisation	[83]
	Model chocolate (cocoa butter, sand)	Effect of sand particle size on oil migration to chocolate surface	[84]
	Dark chocolate (cocoa butter, cocoa, sucrose, stearates)	Effect of stearate and storage conditions on oil migration to chocolate surface	[85]
	Chocolate filled with white chocolate ganache cream	Effect of storage pressure and temperature on oil migration from filling and into chocolate	[86]
	Chocolate (cocoa butter, cocoa nib, lecithin, sucrose, maltitol, tagatose)	Effect of sweetener on fat migration to surface	[87]
	Fat blend (soft palm mid fraction, high oleic sunflower oil)	Effect of liquid oil fraction on surface fat crystallisation	[88]
	Palm kernel fat	Effect of high-intensity ultrasound on surface fat crystallisation	[76]
	Chocolate (cocoa mass, cocoa butter seeds)	Effect of temperature cycling on surface fat crystallisation	[41]
Fluorescence recovery after photobleaching	Dark chocolate (cocoa butter, palm fat, mango kernel fat)	Effect of physical blends and interesterification on surface fat crystallisation	[83]
	Fat blend (palm/peanut oil layer on cocoa butter layer)	Effect of TAG composition on surface fat crystallisation	[89]
	Palm kernel fat/soybean fat blend with triolein	Effect of TAG/fat ratio on surface oil crystallisation	[90]
	Phytosterol-sunflower oil oleogel	Effect of phytosterol/HOSO ratio on surface oil crystallisation	[66]
Optical spectroscopy	Cream filling (peanut oil, interesterified hydrogenated palm oil, lecithin, sugar), cocoa butter	Effect of cream filling composition (lecithin, sugar) and shear rate of shear-crystallised cocoa butter on surface fat crystallisation	[91]
	Chocolate (sugar, cocoa butter, cocoa)	Effect of pre-crystallisation and particle addition on oil diffusion	[92]
	Fat blend (saturated/unsaturated canola oil)	Effect of SFC on oil diffusion through fat	[93]
Optical spectroscopy	Fat blend (palm kernel fat, soybean fat, triolein)	Effect of TAG/fat ratio oil diffusion through fat	[90]
	White chocolate	Surface composition and pore morphology of white chocolate linked to fat bloom	[94]
Optical spectroscopy	Model stock cube (salt, sunflower oil)	Effect of crystalline phase particle size on oil migration via surface oil concentration chemical imaging	[37]

(continued on next page)

Table 1 (continued)

Measurement	Food material	Investigation	Ref
Scanning electron microscopy	Chocolate-enrobed cream-filled wafer cookies	Effect of packaging wrapper on oil migration from cream filling to chocolate coating surface	[80]
	Dark chocolate (cocoa butter, cocoa, sucrose, lecithin)	Effect of sucrose particle size on surface fat crystallisation	[81]
	Dark chocolate (cocoa butter, cocoa, sucrose, lecithin)	Effect of phospholipid emulsifiers on surface fat crystallisation	[82]
	Chocolate (cocoa mass, cocoa butter seeds)	Effect of temperature cycling on surface fat crystallisation	[41]
	Chocolate (cocoa butter, cocoa nib, lecithin, sucrose, maltitol, tagatose)	Effect of sweetener on fat migration to surface	[87]
	Silicone oil/canola oil impregnated cotton pad on chocolate	Effect of type of oil migration through chocolate to opposite side via EDX	[52]
	Chocolate (cocoa, cocoa butter, milk powder, sucrose)	Effect of tempering and storage conditions on fat migration to surface	[95]
X-ray photoelectron spectroscopy	Cocoa powder	Effect of storage temperature on fat migration to surface	[73]
	Cocoa powder	Effect of cocoa type and storage temperature on fat migration into interparticle voids	[74]
Nuclear magnetic resonance	Fat blend (soft palm mid fraction, high oleic sunflower oil)	Effect of liquid oil fraction on diffusion through fat matrix	[88]
	Oleogel (sunflower wax, hazelnut oil, MAG, DAG)	Effect of wax and emulsifiers on oil diffusion through oleogel	[96]
	Fat blend (tricastin and tristearin)	Effect of oil-gelator ratio and SFC on oil migration through fat blend	[97]
	Fat blend (palm oil, peanut oil layer on cocoa butter)	Effect of TAG composition on oil migration through fat matrix	[89]
Magnetic resonance imaging	Chocolate layer (cocoa liquor, cocoa butter, icing sugar, stevia, sucralose, maltodextrin) in contact with hazelnut paste	Effect of sugar and sweeteners combination on oil migration through chocolate layer	[98]
	Cream filling layer (hazelnut oil, interesterified hydrogenated palm oil, lecithin, sugar) on cocoa butter layer	Effect of cream filling composition (lecithin, sugar) and shear rate of shear-crystallised cocoa butter on oil migration through cocoa butter matrix	[91]
	Almond cream filling layer on dark chocolate layer	Effect of different almond filler formulations on diffusion through chocolate	[99,100]
X-ray and neutron computed tomography	Oleofom from high oleic sunflower oil and cocoa butter	Effect of oleofom formulation composition, whipping time, and storage time on bubble morphology via x-ray tomography	[101]
	Couscous grains exposed to high humidity environment	Effect of storage time and humid air flow rate on grain morphology	[102]

Table 1 (continued)

Measurement	Food material	Investigation	Ref
		via combined x-ray and neutron ray tomography	
	Starch and spirulina extrudate	Effect of formulation composition on mechanical and morphological properties via neutron computed tomography	[103]

remaining below the total fat content of 10.5%, thus suggesting that 1.5 w/w% of fat remained encapsulated within the cocoa powder. Fat migration was more pronounced at elevated temperatures and resulted in increased unwanted powder caking, which is highly undesirable for beverages containing cocoa powder such as hot chocolate. Kim et al. [75] investigated fat migration in skimmed, whole, and cream milk powders with 1, 27, and 72 w/w% fat contents over 6 months. Surface free-fat was extracted with a brief hexane wash over filter paper, whereas total fat extraction was carried out with 50 °C water and hexane/isopropanol mixture for 30 min. It was found that surface free-fats almost doubled in percentage over the shelf-life period, highlighting that even fats solid at ambient temperature undergo significant migration dynamism. The works discussed are summarised in Table 1.

3.3. Paper staining

In the case of oil migration from particles structures into paper substrate, it was shown for model seasoning cubes that gravimetric measurements are equivalent to evaluation of oil stain area. This equivalence is given as long as the fibrous structure is isotropic and of constant thickness, as the volume of oil in the oil stain on paper is linearly related its mass by the oil density [37]. Due to this, monitoring oil migration into fibrous substrates by measuring oil stain area is an attractive technique to evaluate oil stability in contact with food packaging, especially with the increasing trend of packaging paperisation often resulting in porous fibrous materials in direct contact with foods (Fig. 3c). Notably oil migration measurements for greasy foods such as pet nutrition [38], stock cubes [37], or foods based on oil gels (oleogel) emulsions [3,77] have been reported by oil stain migration. Simple manual area estimation as well as sophisticated automated imaging via photography or scanning were employed. Because of refractive index matching of paper fibres and oil, light transmission of oil-imbibed paper is augmented in contrast to oil-free paper with more scattering, and thus resulting in different grey values [37]. By calibrating the ratio of pixel to actual distance on paper, the number of darker pixels can be thresholded and quantified in area units via an image analysis software such as imagej/fiji [104]. The observed elliptical elongation of oil stains on rolled paper is due to the fibre orientation along the machine direction during manufacturing, which can be circumvented by using pressed paper or blotting paper. Table 1 summarises the studies using paper staining measurements.

3.4. Whiteness and gloss

In particulate food systems with dense structures and little to no porosity, oil migration is slower and rather diffusion controlled and may involve other phenomena such as dissolution/recrystallisation, and hence gravimetric and paper substrate methods may not be useful. A prominent technique for such types of particulate foods like chocolate is measurement of the amount of white colour formed due to surface fat recrystallisation as a result of oil entrained migration (Fig. 3d). Compared to the smooth glossy surface of fresh chocolate, fat crystals deposits are coarse and rough, causing incident light diffraction into the

full spectrum leaving a white appearance on the chocolate surface. Spectrophotometry or colorimetry of chocolate samples is able to measure L^* , a^* , b^* as either specular reflectance included (SCI) and specular reflectance excluded (SCE), where L^* is the lightness, and a^* and b^* are the axes in the CIELAB colour space [105]. The white appearance on chocolate can then be expressed using the colour parameters as whiteness index, WI [106]

$$WI = 100 - \sqrt{(100 - L_{SCE}^*)^2 + (a_{SCE}^*)^2 + (b_{SCE}^*)^2} \quad (9)$$

Closely related to WI is the surface gloss, SG , defined as [107].

$$SG = \sqrt{(L_{SCE}^* - L_{SCI}^*)^2 + (a_{SCE}^* - a_{SCI}^*)^2 + (b_{SCE}^* - b_{SCI}^*)^2} \quad (10)$$

It is less prominent than WI but has been used alongside it to measure the decrease in surface glossiness as migrated fat crystals increasingly diffract light, hence SG showing an inverse trend to WI [79]. Further literature of particle systems, especially chocolate, employing whiteness measurements are summarised in Table 1.

3.5. Polarised light microscopy

Another measurement technique to assess fat crystallisation as a result of oil migration is polarised light microscopy (PLM) (Fig. 3e). It has been applied mostly qualitatively for crystallised cocoa fat blends [88] and chocolate containing crystalline sugar particles [91]. In this contrast enhancing technique, light is passed through a linearly polarising filter and then through the sample, which rotates the incident light depending on the extent of crystallisation. The light is recombined by a second polarising filter, creating an image where the birefringent nature of crystalline material allows passage of light as opposed to non-birefringent material, blocking the light leaving a black contrast. When analysing fat blends, crystalline sugar particles interfering with the fat crystals can be washed out with deionised water [83]. PLM is thus similar to WI as it allows measurement of surface fat crystallisation induced by oil migration, with the disadvantage of PLM to require thin samples to avoid visible light opacity. Also, during PLM the sample is sandwiched between two glass slides, which in most cases is different to the native state of the product. Further works employing PLM are listed in Table 1.

3.6. Fluorescence recovery after photobleaching

While the above optical methods allow to quantify surface effects of oil migration, it is also beneficial to measure mass transport properties to explain and model oil migration. An optical technique developed for this purpose is Fluorescence Recovery After Photobleaching (FRAP), within a Confocal Laser Scanning Microscope (CLSM) [108] (Fig. 3f). A dye that exhibits fluorescence when exposed to the laser wavelength of the CLSM is used as a tracing agent within the sample. A localised spot of the fluorophore on the sample surface is destroyed or bleached by a strong laser pulse, and the optical density during closure of the spot monitored. Closure of the patch depends on the mobility of the dye, which can be expressed by the formula developed for a Gaussian distribution of the bleaching laser beam, to account for diminished laser intensity towards the edges of the spot [108].

$$D = \frac{0.88w^2}{t_{1/2}} \quad (11)$$

where w is the bleached area radius, and $t_{1/2}$ the recovery half-time. FRAP has been used to measure diffusivity of oil during migration processes in particulate food samples. As listed in Table 1 for example, Svanberg et al. [92] used the fluorescent fatty acid BODYPY FL C₁₆ as oil in model chocolate containing cocoa butter as the fat phase, cocoa and sugar particles. Diffusivities between 1×10^{-13} to 7×10^{-12} m² s⁻¹ were reported. Green and Rousseau [93] and Chai et al. [90] used lipophilic

fluorochromes fluorofol yellow 088 and Nile Red mixed with the liquid fraction (canola oil, or triolein), in fat blends with saturated canola oil or saturated palm fat respectively as gelators, assuming that the dye migrates at the same rate as the oils, which is a reasonable assumption if molecule shape and molecular weight are similar. Measured diffusivities ranged from 1×10^{-13} to 1.5×10^{-11} m² s⁻¹. As all surface techniques, also CLSM and FRAP capture only surface phenomena, which may be different to the behaviour within a particulate system.

3.7. Optical spectroscopy

Besides photographic or spectrophotometric techniques, also optical spectroscopic methods for oil migration measurement have been reported, such as Raman and Near Infrared spectroscopy (Fig. 3g). Raman spectroscopy is a technique in which a monochromatic light, e.g., from a laser source, is shone on a specimen and the inelastic backscattering (stokes scattering) is quantified by counting the number of photons excited or absorbed in a charge-coupled device camera, expressed as intensity for a certain wavelength, customarily expressed as wave-number (cm⁻¹). For a sample to exhibit a Raman effect, the molecules must be polarisable, which is generally the case in covalently bonded samples such as organics, but not in purely ionic species without shared electrons. It is thus possible to differentiate between organic and inorganic substances, as well as between multiple organic materials as different functional groups exhibit different Raman signatures. Near infrared techniques are similar to Raman with the difference that NIR cameras capture the infrared absorption, but similarly exhibit fingerprint regions with peaks characteristic of certain molecules. For analysis or imaging scenarios, it is generally aimed to identify non-overlapping spectral peaks for each material, which essentially depends on the resolution of the acquisition equipment. If peak separation is possible, integral intensity can be calculated as the area under the characteristic peak, approximated as [37].

$$I_{int} = \int_{\omega_0}^{\omega_n} i_{\omega} = \sum_{\omega_0}^{\omega_n} i_{\omega} \quad (12)$$

where I is the integral intensity (au), ω_0 and ω_n are the lower and upper spectral limits respectively (cm⁻¹), and i_{ω} is the intensity (au) at each Raman shift ω . When acquiring spectra not only at single point but in a 2D array, resolving the integral intensity in the x-y map can provide a visual representation of the sample's chemical nature as a chemical image, which is otherwise invisible to optical or photometric techniques. Both Raman and NIR spectroscopy have been applied for measurements of oil migration. In cream-filled wafer chocolate, Fourier transform NIR (FT-NIR) was used to obtain spectra of the chocolate surface under different packaging materials, enabling to link fat migration and bloom with packaging type and storage time [80]. Spatial Raman measurements were performed on white chocolate generating chemical images of the surface composition and fat distribution [94]. In a study on model stock cubes in contact with paper packaging, spatiotemporal Raman chemical imaging was performed rendering quantitative images of sunflower oil concentration at 1 day time intervals. Augmentation of chemical imaging by a time dimension allowed to visualise the oil dynamism on the food surface, which was not achieved previously [37].

3.8. X-ray photoelectron spectroscopy

Instead of using visible or infrared light, also x-rays can be used for spectroscopy. X-ray photoelectron spectroscopy (XPS) or electron spectroscopy for chemical analysis (ESCA) makes use of the photoelectric effect in which electrons are emitted from a sample due to incident x-rays of a fixed energy, for example 1486.7 eV for an Al K α source [109] (Fig. 3h). If the binding energy E_{bind} holding the electrons with atoms is less than the incident energy $h\nu$ (where h is Planck's constant and ν the frequency), then the kinetic energy of the E_{kin} of the released electron

follows Einstein's photoelectric relation [110].

$$E_{kin} = h\nu - E_{bind} \quad (13)$$

By measuring E_{kin} for example via a hemispherical energy analyser, E_{bind} can be found and plotted against its detection intensity, yielding an XPS spectrum. E_{bind} is dependent on the atom itself and on neighbouring atoms that share valence electrons across covalent bonds. Thus, each atomic element and group of two to three bonded atoms has a characteristic E_{bind} , giving rise to fingerprint XPS spectra that can be used to determine surface composition, and thus also lipids. Due to x-rays finite energy the sampling depth is usually limited to 5–10 nm below the sample surface, and ultra-high vacuum is required to avoid interaction of x-rays with matter excluding the sample.

James and Smith [95] investigated fat bloom on chocolate surfaces as a result of fat migration and recrystallisation over 30 days for chocolate prepared under different tempering conditions. XPS profiles were generated for pure material based on the prominent covalent bonds in the material (e.g. O-C-O in sucrose, O=C-OH in cocoa butter), allowing to monitor the development of surface composition over time. This technique is however laborious for complex formulations as detailed preliminary information on the ingredients chemical structures is required. For particulate foods containing less complex compositions, simple aggregation of atoms is sufficient. For example, lipids have a relatively higher carbon © content than carbohydrates, which tend to contain more oxygen (O), whereas proteins are characterised by the presence of nitrogen (N). As such, the C/O ratio and percentage of N were used to characterise fat migration in different types of cocoa powder stored under temperatures of 20 to 40 °C [73,74]. Fat migration into interparticle spaces in cocoa, such as in powdered beverages, are major reasons for caking, visual quality defects, and difficult reconstitution. Over time, especially at higher storage temperatures, the XPS showed an increasing C/O ratio, whereas the surface N percentage decreased, as a result of fat gradually covering carbohydrate and protein areas on the cocoa particles. Increased powder caking was attributed to formation of interparticle fat bridges as a result of fat migration.

3.9. Scanning electron microscopy

Another classical surface characterisation technique applicable to oil migration measurements in particulate foods is scanning electron microscopy (SEM), in which an electron beam accelerated by a certain voltage and guided by an electromagnetic field is targeted at the surface of a bulk sample and the backscattered or secondary electrons detected (Fig. 3i). SEM can also be used to spatially map materials of different chemical natures by employment of energy-dispersive x-ray spectroscopy (EDX), in which photons of individual chemical elements are emitted at specific acceleration voltages, a process termed *Bremsstrahlung*. The characteristic peaks on an x-ray emission spectrum can thus be used to identify different materials based on key chemical elements contained within them, akin to chemical imaging with other spectroscopic methods. SEM has been employed to monitor surface fat crystallisation in chocolate as a result of oil migration, while EDX was used to identify the surface composition over time of a silicon enriched oil-filled chocolate sample during oil migration events [52]. While oil migration is usually considered a relatively slow diffusion driven process, spots of oil from the filling on the chocolate surface were identified surprisingly fast after preparation of the chocolate, which the authors attributed to capillary flow through or adjacent to porous cocoa particles. Table 1 lists further works employing SEM.

3.10. Nuclear magnetic resonance

While the adverse effects of oil migration such as fat bloom or grease-imbibed packaging are affecting the food surface, there is an increasing interest to measure and understand oil migration phenomena within particulate food structures. Thus, methods that not only probe the food

surface but similarly the interior structure are necessary. Nuclear magnetic resonance has been used as a non-destructive technique in various experimental configurations to monitor various aspects of oil migration (Fig. 3j). Magnetic nuclei in molecules enter into resonance when subjected to strong electromagnetic fields, which's oscillation frequency can be measured to obtain spectra. In the simplest free induction decay (FID) setup, ¹H NMR spectra for different materials give rise to peaks at different chemical shifts, characteristic of the proton(s) in the analyte's functional groups, giving rise to a molecular fingerprint [88,96,97]. NMR relaxometry moves beyond mere analytical characterisation and enables estimation of molecular mobility based on the relaxation process to equilibrium. This transverse relaxation is commonly induced by sequencing the pulses of radio frequency (RF) in a multi echo sequence according to Carr, Purcell, Meiboom and Gill (CPMG) [111]. The measured spin-spin relaxation time, T_2 , is linked to the molecular motion: large T_2 corresponds to fast molecular motion and short T_2 corresponds to slow molecular motion. NMR diffusometry allows quantitative evaluation of the mobility by expression as diffusivity, D , from pulsed field gradient stimulated echo experiments (PFG-STE). D is obtained from the Stejskal and Tanner equation [112].

$$\frac{I}{I_0} = \exp\left(-\gamma^2 G^2 \delta^2 \left(\Delta - \frac{\delta}{3}\right) D\right) \quad (14)$$

where the signal intensity I at the magnetic field gradient amplitude $G = 0 \text{ T m}^{-1}$ is given by I_0 , γ is the gyromagnetic ratio, δ the pulse duration, and Δ is the diffusion time. All three NMR techniques were used to measure liquid oil migration in solid fat matrices in fat blends or oleogels. Trapp et al. [96] analysed hazelnut oil-based oleogels with sunflower seed wax or mono- and diglycerides, the latter found in chocolate confectionary. First, FID was used to obtain NMR spectra for each raw component of the oleogel formulations, followed by relaxometry (CPMG) and diffusometry (PFG-STE). Adam-Berret et al. [97] and Nelis et al. [88] also applied the latter two techniques to tricapratin and tristearin blends, and sunflower oil-palm fat mixtures respectively. Representations of I/I_0 against $-\gamma^2 G^2 \delta^2 (\Delta - \delta/3)$ in the Stejskal and Tanner equation yield steep negative exponential curves for the mobile phase such as oil, and flatter negative exponential curves for the gelator phase, such as wax or glycerides, while oleogels or fat blends lie inbetween. NMR diffusometry measurements gave diffusivity values in the range 1×10^{-11} to $1 \times 10^{-10} \text{ m}^2 \text{ s}^{-1}$ across all three studies.

3.11. Magnetic resonance imaging

While NMR gives measurements as spectra and discrete data, the application and detection of RF frequency in multiple axes enables magnetic resonance imaging (MRI) or tomography (Fig. 3k). Just as in ¹H NMR, MRI relies on relative proton densities and spin-spin (T_2) relaxation times to generate contrasts between components in mixtures. In particulate food formulations such as chocolate, dry components have low proton densities due to lack of water and can thus be differentiated from organic phases rich in hydrogen-containing hydrocarbons. In the lipid phase, liquid oil can be discerned from solid fat given that the larger triacylglyceride molecules generally have T_2 relaxations of 9–17 ms, while the shorter fatty acids have timescales around 6 ms [10]. MRI was used in several particulate food systems to evaluate oil migration such as palm and peanut oil migration through cocoa butter [89], hazelnut oil filling in contact with chocolate [98], or almond cream layers in contact with dark chocolate [99,100]. While NMR was primarily used on soft matter samples, MRI is suitable for particulate matter inclusions due to the ability to visually discern phases. In contrast, diffusivity is not evaluated directly from detected intensities, but rather from image analysis of reconstructed MRI images. MRI diffusivity values of the mobile oil phase were found to be similar to NMR values across different food systems, between 1×10^{-13} to $8 \times 10^{-10} \text{ m}^2 \text{ s}^{-1}$. A disadvantage of MRI techniques are the generally the low spatial

resolutions of tens of microns and long acquisition times due the low RF intensity, such that rapid migration phenomena cannot be captured [113].

3.12. X-ray and neutron tomography

Two other prominent tomographic techniques are x-ray computed tomography (XCT) and neutron computed tomography (NCT). While lipid migration techniques employing XCT and NCT are absent, it can provide valuable information on the food microstructure, which in turn aids understanding and model development. Both XCT and NCT are similar in their operation principles (Fig. 3). X-rays or neutrons are emitted from x-ray or spallation sources aimed at the sample. While x-rays interact with an atom's electrons, neutrons interact with the nucleus. XCT is therefore useful to image hard particulate matter from heavier atoms. Conversely neutrons are more sensitive to atoms with less electrons, such as hydrogen, which makes it more useful for soft fluidic food samples rich in oils and water [113]. To achieve similar imaging contrasts with XCT, contrast agents can be added such as water-soluble potassium iodide for watery phases, or oil-soluble 1,4-diodobenzene for lipid phases. The recorded attenuation of the x-rays or neutron rays are reconstructed in 2D slices that can be rendered in 3D volumes for visual representation of the microstructure. Frequently, further quantification for parameters such as porosity, density, particle size, shape, and surface area is undertaken. Depending on the sample field of view (usually between 0.5 and 5 cm), voxel resolution is in the range of a few 100 nm to a few microns.

XCT has been employed in various food microstructure studies. Reinke et al. [58] simulated stress distributions in chocolate after different tempering conditions by feeding tomogram images to a finite element analysis. Haedelt et al. [114] used XCT to image chocolate with bubble inclusions produced by different foaming gases, leveraging tomographic analysis to correlate bubble size and number with sensory properties. Application and advanced analysis of XCT for edible oil foams (oleofoams) has been extensively covered by Metilli et al. [101]. Neutron tomography on the other hand has been less reported in the literature. Vego et al. [102] harnessed the strength of both XCT and NCT by simultaneous tomographic measurements on a physical two component mixture: couscous particles exposed to humid air. XCT was used to image the solid particulate phase, while NCT was better suited to monitor the hydrogen-rich vapour phase and absorbed water in the food. Spatial and temporal water uptake by the hygroscopic food was thus enabled. The sensitivity of NCT towards water makes it also suitable to analyse drying phenomena. Defraye et al. [115] employed 2D NCT studying the effect of natural and forced convective and radiative drying of apple slices, in presence and absence of the apple peel. Beyond water transport, NCT characterisation of semi-solid starch and spirulina extrudates [103] has been reported. The relatively long exposure times necessary of up to several hours for a single scan make x-ray and neutron ray tomography rather useful for imaging static samples, and less so for dynamic transport phenomena like lipid migration. Synchrotron facilities offer higher performance XCT and NCT infrastructure and may enable future work on more dynamic food systems.

Table 2
Mathematical modelling approaches for oil migration in particulate food systems.

Food system	Model	Fit	Ref
Diffusion			
Cream filling (peanut oil, interesterified hydrogenated palm oil, lecithin, sugar), cocoa butter	$\frac{M_t}{M_\infty} = 4 \left(\frac{Dt}{\pi l^2} \right)^{\frac{1}{2}}$	LSE 0 to 0.02	[91]
Fat blend (cocoa butter, tricaprylin, flaxseed oil, safflower oil, peanut oil)	$\frac{M_t}{M_\infty} = \frac{\sqrt{Dt}}{l}$	R ² 0.71 to 0.96	[78]
Fat blend (fully hydrogenated soybean oil, soybean oil, emulsifiers)	$\frac{M_t}{M_\infty} = \frac{\sqrt{D_{eff}t}}{l}$	R ² 0.5 to 0.97	[67]
Fat blend (palm oil+peanut oil layer on cocoa butter with different TAGs)	$\frac{M_t}{M_\infty} = 1 - \sum_{n=0}^{\infty} \frac{8}{(2q+1)^2 \pi^2} e^{-\left(\frac{D_{eff}(2q+1)^2 \pi^2}{l^2} \right) t}$	R ² 0.5 to 0.99	[89]
Fat blend of palm kernel fat and soybean fat with triolein, prefer to use diffusion	$D_{eff} = \frac{0.88w^2}{4t_{1/2}}$	SD 0 to 10%	[90]
Chocolate layer (cocoa liquor, cocoa butter, icing sugar, stevia, sucralose, maltodextrin) in contact with hazelnut paste	$\frac{C(x,t)}{C_\infty} = 1 - e^{kt} \frac{\cos x \left(\frac{k}{D} \right)^{\frac{1}{2}}}{\cos l \left(\frac{k}{D} \right)^{\frac{1}{2}}}$	R ² 0.81 to 0.91	[98]
Chocolate layer (cocoa liquor, cocoa butter, icing sugar, stevia, sucralose, maltodextrin) in contact with hazelnut paste	$\frac{16kt^2}{\pi} \sum_{n=0}^{\infty} \frac{(-1)^n e^{-\left(\frac{D(2n+1)^2 \pi^2 t}{4l^2} \right)}}{(2n+1) \left(4kl^2 - D\pi^2(2n+1)^2 \right)} \cos \frac{(2n+1)\pi x}{2l}$	R ² 0.91 to 0.99	[98]
Cocoa butter from different geographical locations, tempered vs non-tempered, solubilisation, recrystallisation, diffusion	$\frac{\partial C}{\partial t} = D \frac{\partial^2 C}{\partial x^2}$ IC : $C(l,t) = \frac{C_\infty}{1 + e^{-k(t-t_0)}}$ BC : $\frac{\partial C}{\partial x} \Big _{(x=0)} = 0$ BC : $C(l,t) = C_\infty 1 - e^{-kt} $	R ² 0.33 to 0.96	[42]
Capillary			
Sunflower oil penetration with emulsifiers into chocolate crumb beds	$L^2 = t \left(\frac{r_{eff} \sigma \cos \theta + \Delta P}{2\tau^2 \mu} \right)$	R ² 0.99	[116]
Empirical			
Oleogel (rapeseed oil, Myverol, sunflower oil, candelilla wax) migrating into contacting paper substrate	$A_{stain} = kt^b$	R ² = 0.99	[77]
Cream filling (peanut oil, interesterified hydrogenated palm oil, lecithin, sugar), cocoa butter; Fat blend (palm oil+peanut oil layer on cocoa butter with different TAGs)	$\frac{M_t}{M_\infty} = (1 - e^{-kt})$	R ² = 0.98 to 0.99; SSE = 0.06 to 0.39	[89,91]

4. Modelling of oil migration in particulate food systems

There have been many attempts to model and predict lipid migration in particulate foods as a result of lipid metastability. Depending on the adverse result intended to monitor, such as fat bloom, oil staining on packaging, or the fundamental mass transfer phenomena, different models have been employed. As Tabulated in Table 2, literature can generally be divided into first-principle diffusion and capillary methods, and additional empirical methods that do not emerge from fundamental physical laws.

4.1. Diffusion models

By far the most extensively used models are based on Fick's second law of diffusion. This is mostly due to the mathematical simplicity of basic equations yielding acceptably accurate correlations with experimental results, but also due to the few required input data, compared to capillary models. Diffusion-based models are applicable to fundamental molecular diffusion problems, such as oil migration through a fat matrix, but also allow macroscopic modelling of transport phenomena when the food microstructure is too complex. Particulate systems are complicated and the microscopic flow between multiphase formulations is generally not purely diffusional transport, especially not in the presence of capillaries. Yet, lumping the effect of different physical phenomena together into a single term and measuring overall properties, an effective diffusivity D_{eff} can be evaluated to feed into diffusion models. Exact D_{eff} measurements depend on the definition of the modeller and the subject microstructure, but for particulate food formulations is generally expressed as

$$D_{eff} = D \frac{\epsilon}{\tau} \quad (15)$$

where ϵ is the void fraction of the structure and τ the tortuosity of the diffusion path. τ is subject to various definitions but is generally the length of the tortuous flow path divided by the straight line connecting its ends [117]. Thus, for a straight path $\tau = 1$, for a semi-circular flow path $\tau = \pi/2$, and for a circle $\tau = \infty$.

Ziegler [118–120] was the first to comprehensively report the use of Fick's law to model oil migration in chocolate, on which many works have been based to this date, listed in Table 2. Using the simplest form $M_t/M_\infty = (D_{eff} t)^{0.5}/l$ the only parameters required to evaluate the diffusivity are thus a measure of oil concentration after a few intervals of time t , for example the concentration, spectral intensity, or mass M_t , the mass or equivalent measure of oil after equilibrium or saturation has been reached M_∞ , and the superficial path length l of diffusive transport. It should be noted that here D_{eff} is used and the superficial path length or height of food item – the real diffusivity might be well lower and much more difficult to evaluate, while the real path length might be longer if accounting for void fractions and tortuosity. The attractiveness of diffusion models to bulk food system was used to model peanut oil and palm oil migration through cocoa butter with different lecithin emulsifier ratios and sugar powder by magnetic resonance imaging [91]. The diffusion equation proposed by Peppas and Brannon-Peppas [121] was used, with least squares errors between 0 and 0.02, and yielding diffusivities between 2×10^{-14} to $4 \times 10^{-13} \text{ m}^2 \text{ s}^{-1}$.

Ziegler's model was similarly used to model coloured soybean, flaxseed, safflower and peanut oil diffusion through cocoa butter fat blends measured by tracing the coloured oil front with a flatbed scanner [78] and to model soybean oil migration out of a fat matrix into filter paper [67]. The models fitted with correlation coefficients R^2 of 0.5 to 0.96, generally showing the applicability of the diffusion equation in this mostly oil-fat biphasic scenario, yielding diffusivities from 1×10^{-14} to $4.5 \times 10^{-11} \text{ m}^2 \text{ s}^{-1}$. A more elaborate model to Ziegler's was used to evaluate diffusivities of palm and peanut oil through cocoa butter with different TAG blends via magnetic resonance imaging, also

listed in Table 2 [89]. R^2 statistics of 0.5 to 0.99 were reported with diffusivities of 5×10^{-14} to $6 \times 10^{-13} \text{ m}^2 \text{ s}^{-1}$, similar to previous work for oil/fat systems, showing again the applicability of Fick's law. In a different work, a diffusion model adapted to the output of the analytical technique was used to evaluate the diffusivities from FRAP measurements [90]. While no fitting statistics of the model were reported, diffusivities of the range 2×10^{-13} to $4 \times 10^{-12} \text{ m}^2 \text{ s}^{-1}$ were found, similar to findings employing different acquisition techniques. Cikrikci and Oztop [98] used an advanced analytical solution to Fick's second law derived by Crank [122] to model oil migration from hazelnut paste in contact with chocolate via MRI. Diffusivities of 7×10^{-11} to $2 \times 10^{-10} \text{ m}^2 \text{ s}^{-1}$ and R^2 of up to 0.9 were reported.

A commonality of most previous diffusion models was the discrepancy between model and experimental data especially at early time-scales, resulting in poor fits of around $R^2 = 0.5$. Cikrikci and Oztop [98] addressed this issue by using an empirically found logistics model as boundary condition in the diffusion model. The numerically solved solution fitted each experimental data set well with $R^2 > 0.95$ in all cases over the entire timescale.

Besides Fickian diffusion, other models were developed. For example, a solubilisation-recrystallisation-diffusion model was proposed by Marangoni for the migration of the liquid fraction of fats through the solid fat matrix, finding a rate constant for both the solubilisation and recrystallisation. While no formal diffusivity was used, a migration rate constant k_m was incorporated ranging from 0.2 to 1.2 $\text{kg s}^{-0.5}$, resulting in R^2 goodness-of-fit values between 0.33 and 0.96.

4.2. Capillary models

By the higher amount of published work it is apparent that diffusion models are popular for modelling oil flow through the fat phase in particulate systems, yet frequently fail to capture fast liquid transport characteristic of capillary flow. While diffusion seems suitable for capturing the rather slow migration processes in chocolate systems, multiple works suggest that oil migration may also involve capillary flow [8]. This has been supported by fast migration measurements in early timescales via EDX that defies the typically longer time scales of diffusion [52]. A recent review highlighted the fallacy of simplifying food transport models to diffusion, showing evidence that many food manufacturing processes such as deep fat frying are more fundamentally explained by capillary action [123]. Many works on liquid imbibition flowing into particulate food structures, as in reconstitution, use capillary models [124]. However in lipid migration studies in which liquid is leaking out of particle structures, capillary models are underrepresented.

Within the area of oil migration under storage conditions, as listed in Table 2, Carbonell [116] used the classical Washburn eq. 8 to model sunflower oil penetration into D_{50} 14–20 μm chocolate crumbs, varying surface tension and viscosity of the penetrating oil. Despite angular nonspherical crumbs it was found that White's equation for effective pore radius r_{eff} yielded predicted void space, while ϵ of the bed was found by nitrogen gas adsorption. R^2 values of 0.99 showed applicability of Washburn's theory to this scenario.

Clearly, research on lipid migration investigating capillary flow is underrepresented. Powerful measurement techniques described earlier such as x-ray tomography now offer means to use more microstructural data and encourages a more granular analysis of lipid migration phenomena.

4.3. Empirical models

The complexity of oil migration processes in particulate foods has also led to the employment of empirical equations not based on fundamental physical understanding but statistical data regression. For rapeseed oil migrating out of a wax oleogel into paper, an exponential-

th order equation was fitted that modelled the area of expanding oil stain on the packaging substrate, matching with an R^2 of 0.99 [77]. Interestingly, similar to the diffusion and capillary flow models that have an exponent of $\frac{1}{2}$, the exponent here was 0.5 ± 0.001 . This suggests oil flow through the oleogel matrix could be modelled as diffusive flow in analogy to the fat cases earlier [67,78,91], while the expanding oil stain on paper could be modelled as capillary flow through a porous medium. Indeed, many authors describe imbibition of liquid into paper via capillary flow approaches, as summarised in this review [22]. Two further works concerned with peanut and palm kernel oil migration through a system of cocoa butter and sugar particles employ an exponential model with goodness-of-fit of $R^2 > 0.98$ [89,91]. While empirical models for oil migration are useful for complex systems that can not readily be analysed with first principle methods, findings are less transferable between food systems and offer less understanding on migration processes and possible mitigation strategies.

Overall, it is evident that diffusion models have attracted the most attention in modelling oil migration, yielding for chocolate systems generally similar diffusivity results across different studies. Capillary models are seldom employed, which is attribute to the additional microstructural data required [123].

5. Mitigation of oil migration in particulate food systems

The adverse sensorial, textural, and technical effects of oil migration have led to an increasing interest in strategies to control and prevent it. Mitigation of oil migration has been approached from multiple directions, such as stabilisation of the oil within the food, such as via oleogelation, pickering emulsification, particle size reduction and capillary suspensions, or encapsulation; enclosing the entire food in an edible coating; or by protecting fibrous packaging to avoid oil staining, illustrated in Fig. 4 and comprehensively summarised in Table 3. Each strategy bears its own advantages and disadvantages, and depending on the approach and final goal, different measurement (and modelling) methods were applied, revealing different success rates in controlling oil migration. With increasing consumers seeking healthy natural diets and moving away from saturated fat intake [28], conventional chemical approaches to oil stabilisation such as esterification and hydrogenation have been omitted, discussing only modern techniques of physical oil stabilisation without chemical modifications.

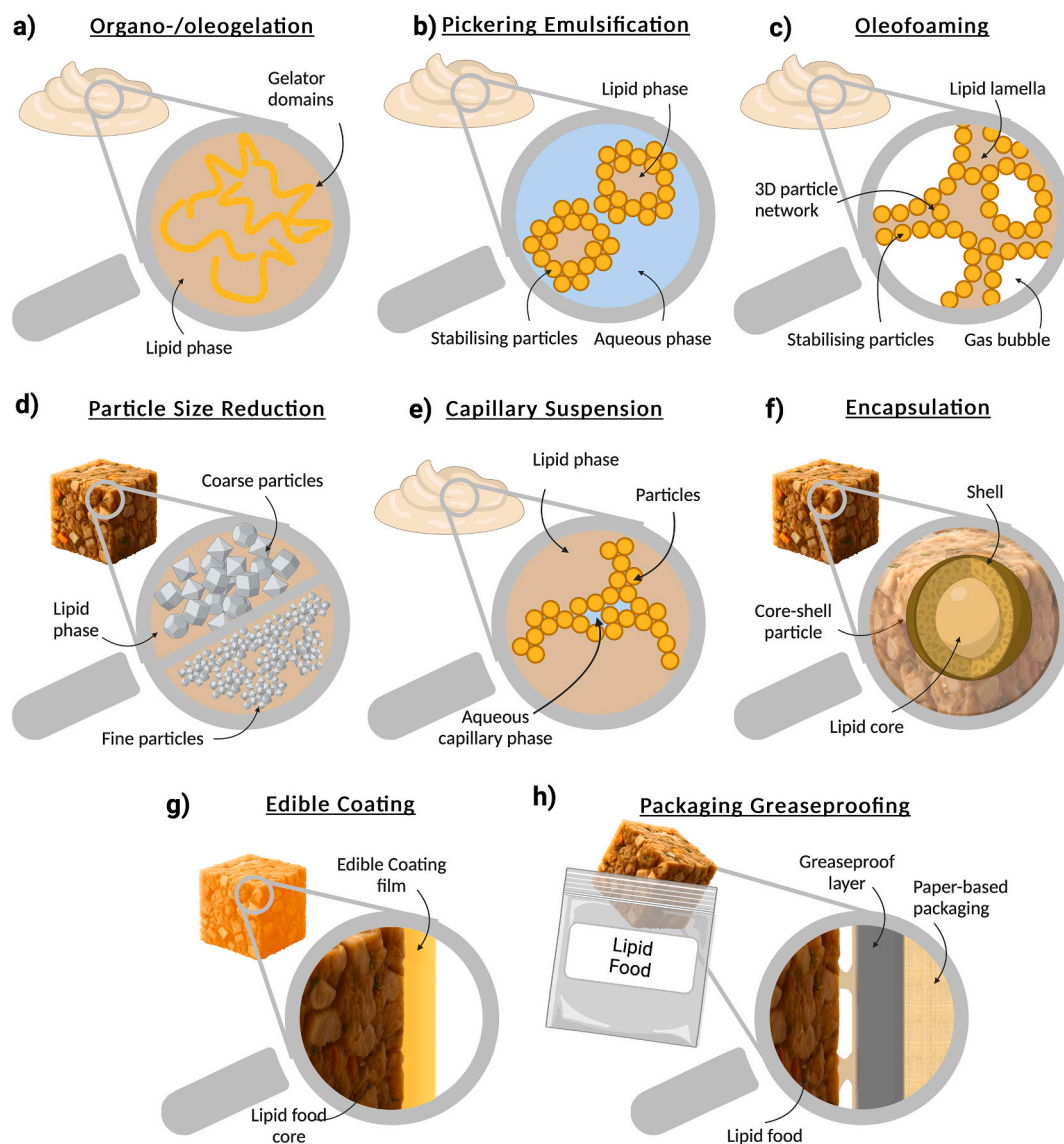


Fig. 4. Strategies for mitigation of oil migration: a) organogelation or oleogelation, b) oleofoaming, c) pickering emulsification, d) particle size reduction, e) capillary suspension, f) encapsulation, g) edible coating, h) packaging grease proofness.

Table 3
Modern oil migration mitigation strategies.

Method	Description	Amount of oil leakage	Advantages (+), disadvantages (-)	Ref
Organo-/oleogelation	Wax-oleogelation of tahini halva with sunflower wax, beeswax, shellac between 1 and 5 w/w%	< 7% gravimetrically via absorption onto filter paper	(+) Applicable in melted, molded, extruded and pressed products as preparation is a melting-colling process, crystallisation can be influenced by tempering and shearing; (-) subject to labelling, regulatory landscape unclear for bulk products beyond confectionary coating	[125]
	Chocolate with hybrid hydro-oleogel bigel from grape seed oil, beeswax, sodium alginate dispersion	No reduction in WI compared to control sample		[126]
	Chocolate with <i>Lycium barbarum</i> seed oil gelated with beeswax, rice bran wax and lacquer wax	< 1.2% gravimetrically after centrifugation		[127]
Pickering emulsion	High internal phase Pickering oil/water emulsion of corn oil stabilised by proteins	< 6% gravimetrically after centrifugation		[128]
	Chocolate ganache emulsion from chocolate and whipped cream, with cocoa powder particles	< 15% gravimetrically after centrifugation	(+) Particles for pickering stabilisation can be native to recipe; (-) only applicable to emulsified products, melting and pressing damages pickering structure	[129]
	Pickering oil/water emulsion from camellia oil, water, and silica particles	50–90% by ethanol extraction		[130]
Oleofoaming	Oleofoam from soybean and high oleic sunflower oil with diacylglycerides	0–100% by visual inspection		[131]
	Oleofoam from sunflower oil and fatty alcohols and fatty acids	2–8% gravimetrically after centrifugation	(+) Health benefits from replacement of lipids with air, particles for foam stabilisation can be native to recipe; (-) foam cannot be mixed or compacted into other products after formation due to bubble collapse	[132]
	Oleofoam from soybean oil, glycerol monostearate, soy protein isolate, and κ-carrageenan	0–100% volumetrically in measuring cylinder		[133]
Particle size reduction	Chocolate with various sucrose particle sizes	~ 10% lower migration rate via WI and SG	(+) No foreign particle introduction required, high oil retention possible, applicable for molten and pressed products; (-) particle size reduction requires energy intensive milling, particle size reduction can influence bulk physical properties	[81]
	Chocolate with various sucrose particle sizes	~ 10% lower migration rate via WI and SG		[134]
	Model seasoning cube from salt particle and sunflower oil	0–50% via gravimetry, optical scanning, and Raman spectroscopy		[37]
Capillary gels/suspensions	Oleogel from zein particles dispersed in soybean oil with water capillary bridges	0% by visual inspection of inverted tests		[135]
	Oleogel from wheat middlings dispersed in sunflower oil, with water capillary bridges	9% based on maximum maximum oil holding capacity of pure wheat middlings, gravimetry	(+) No foreign ingredients necessary, only water by capillary bridges required; (-) water migration can impact amorphous and crystalline material	[136]
	Oleogel from zein, whey, and soy protein dispersed in corn oil, with sinapine aqueous solution bridges	40–10% by centrifugation and gravimetry		[137]
Encapsulation	Cinnamon and paprika oleoresins encapsulated in hard palm fat via spray chilling and from saturated gas solutions	2–30% by dispesing in ethanol and spectrophotometry		[138]
	<i>R. officinalis</i> , <i>L. angustifolia</i> , and <i>C. aurantium</i> volatile oil encapsulated in β-cyclodextrin	10–45% by dispersing in ethanol followed by hexane extraction	(+) Potential for controlled release of essential oils; (-) energy-intensive spray drying or other encapsulation processes	[139]
	Chia seed oil with vitamin D3 encapsulated in soy protein isolate, maltodextrin, inulin via spray drying	0–15% by cold hexane extraction		[140]
Edible coating	Olive oil in pouches from chitosan, gelatin, and allic acid films	0% by visual inspection of pouches		[141]
	Pectin and starch films with eggshell waste particles, in contact with oil (no type specified)	Poor, only qualitative data available	(+) Potential for additional moisture and oxygen barrier included in edible coating; (-) frequently introduces foreign ingredient as coating agent; influences visual appearance	[142]
	Film from sunflower oil cake, sodium alginate and glycerol in contact with sunflower oil	18–34 mg mm m ⁻² d ⁻¹		[143]
Packaging strategies	Sodium carboxymethyl cellulose and cellulose nanofibrils coated molded pulp trays for fruits packaging	Kit test 12		[144]
	Alkyl ketene dimer modified sodium alginate coated 60 gsm paper	Kit test 6	(+) Food product unaffected; (-) often difficulties of label printing and appealing visual appearance on shelf with porous material	[145]
	Chitosan and sodium carboxymethyl cellulose coated pizza cardboard box and molded pulp tray	Kit test 12		[146]

5.1. Organo-/oleogelation

Organogelation or oleogelation is an attractive strategy to stabilise the lipid phase in particulate food products, combining high volume fractions of up to >90 w/w% liquid oil with small volume fractions down to <10 w/w% of a gelator via melting and cooling, trapping the oil domain in the gelator matrix [147] (Fig. 4a). Rheological studies have shown that even at small gelator loads, the oleogel adapts viscosities higher than the pure oil, thus creating hindrance to oil diffusion. The

crystal structure of the gelator can also be influenced by the cooling rate, applied shear during cooling, and ultrasound, influencing the crystal packing density [148,149]. Due to the melting and cooling process in oleogel preparation, this strategy is attractive for molten, molded, tableted or extruded foods, compared to emulsion techniques, offering great potential for oil migration control and saturated fat reduction. Yet, many gelator materials such as waxes require declaration on the ingredient list and as such are scrutinised from a regulatory perspective, hampering wide-spread commercial adoption [30]. In its latest research

applications to chocolate, oleogels prepared from grape seed oil and lyceum barbarum oil, gelled with beeswax, rice bran wax, and lacquer wax, achieved oil retention of up to 98.8 w/w% (i.e. 1.2 w/w% oil released from oleogel). Despite reduced oil migration, a decrease in the whiteness index due to fat bloom on chocolate was not measured, suggesting yet more effective oil retention is required [126,127]. In Tahini halva, sunflower oil was oleogelated with beeswax and shellac, reducing oil release to a maximum 7 w/w% [125].

5.2. Pickering emulsification

Oil stabilisation from melts is not suitable for heat sensitive foods, for which other strategies are necessary. Pickering emulsification involves small solid particles in dosages as low as 1 w/w% to stabilise the oil-water interface, creating a particle shell around oil or water droplets at the interface [150,151] (Fig. 4b). While elevated temperature or pressure damage the interfacial microstructure, the added particles can be ingredients native to the recipe, or alternatively foreign particles like fat powder [152], amphiphilic particles such as proteins [153], or even janus particles tailored to the lipid and aqueous phases [154] or enhanced interfacial stability. Recently, high internal phase corn oil in water was emulsified by albumin protein, and an oil leakage of <6 w/w% was reported [128]. For chocolate, water-containing whipped cream was stabilised with cocoa particles, resulting in oil leakage of maximum 15 w/w%, exemplifying use of a native material for Pickering stability to reduce oil migration [129]. Involving foreign added particles, camellia oil was stabilised with silica particles, yet oil leakage was higher than in previous works with 50–90 w/w% oil leakage [130].

5.3. Oleofoaming

When the aqueous phase in pickering emulsion is inverted and replaced with air, an oil foam or oleofoam is formed (Fig. 4c). Generally, oleofoams are prepared from oleogels by whipping or sparging with gas. Bubble entrapment then occurs by cooling and solidification in the case of solid fats, by addition of surfactants in the case of liquid oils, or by particle inclusion. Particles can be prepared ex-situ and added to the oleogel, such as proteins or polysaccharides [133], or crystallise from the oleogel in-situ upon cooling, such as for diacylglycerides [131] (Table 3). Stabilisation of the gas-oil interface then occurs by particle adsorption at the interface, reducing the surface energy of the bare particles and bubbles by clustering. Partial oil and gas wettability is thus important to prevent immersion of the particles in either pure phase. Further, interparticle van der Waals and intermolecular hydrogen bonds form a 3D network, stabilising the entrapped bubbles. Destruction of the foam occurs either due to liquid oil drainage out of the lamella, due to dissolution of the gas in the liquid, or due to bubble Oswald ripening [155]. Measurement of this instability is usually quantified as the amount of oil drained by storage under gravity or centrifugation. For microstructural bubble analysis, tomographic techniques have proven useful [101]. Oleofoams have gained importance as a means to partially replace lipids with air, yet adoption outside of niche confectionary or dairy products is limited. The risk of foam collapse makes it less suitable for mixed or compacted products. A study by Ribourg-Birault also found that lipids in oleofoams tend to oxidise faster than in oleogels due to more exposure to oxygen in the bubbles [156]. This issue could be circumvented by air replacement with inert gases such as N₂, CO₂, or N₂O. Oil retention within oleofoams has been reported ranging from 0 to 100% depending on formulation and environmental conditions [155].

5.4. Particle size reduction

Another particle-based strategy in oil migration control is particle size reduction (Fig. 4d). By lowering the particle size but retaining the same mass, surface area of the particles increases while reducing the interparticle distance, thus creating narrower flow channels for the oil

and thereby increasing the pressure drop of the oil flow [157–160]. If not advective flow but mass transport via diffusion is expected, particle size reduction creates a more tortuous path, increasing the tortuosity parameter in eq. 15 [161], leading to a reduction in diffusivity. In addition to the dynamic effects of reduced oil flow velocity (advective migration) or diffusion (diffusive migration), the thermodynamic effect of capillarity can be affected. As the inter particle pore size is reduced with smaller particles, capillary radii reduce, increasing the capillary pressure according to the Young-Laplace Eq. 4, suggesting more oil is retained within the food structure. On the other hand, a net increase of surface area results in an increase in particle surface energy, attracting particles towards each other to reduce surface area, which may destabilise the system if particles are sufficiently mobile [35]. Again, this technique is attractive for manufacturing routes involving melting or tableting, as a delicate food structure prone to thermal or mechanical degradation is absent. Moreover, a rigid final structure is desired over a fluid state, to prevent phase separation into solids and liquids induced by the high surface energy particles. Equal to pickering emulsions, the smaller particles can simply be native to the original recipe and do not need to be foreign. Hence particle size reduction of sugar in chocolate systems was tested and oil migration monitored via the whiteness index and surface gloss. As expected, whiteness index formation rate and surface gloss reduction rate was slower for smaller particles, and faster for large particles, thus suggesting a rate decrease for smaller particles. Interestingly, *WI* and *SG* reached plateau values that were the same across all particle sizes after 7 days, suggesting that no oil was statically retained but that the rate reduction was rather dynamic. Mechanistically, this rather suggests a decrease in diffusivity by creation of a more tortuous path caused by the smaller particles, as opposed to an increase in capillary suction pressure that would have retained more oil as the particle size was reduced. Particle size of salt in model sunflower oil-stock tablets was reduced down to 5 μm, achieving 0 w/w% oil release, measured gravimetrically, by scanning, and Raman spectroscopy. Due to the liquid nature of sunflower oil and the absence of a fat phase, as was the case in chocolate, oil retention was attributed to capillary action and liquid holdup rather than diffusion [37].

5.5. Capillary suspension

A similar particle-technological approach harnessing capillary action but in a suspended form is termed capillary gels or capillary suspensions involving one solid and three liquid phases. The solid particles are dispersed with tightly controlled ratios of a preferentially wetting liquid and a non-preferentially wetting liquid [162] (Fig. 4e). Depending on the relative ratios of the three phases, ternary mixtures ranging from the pendular state with majoritarily non-preferentially wetting liquid, to the capillary state with majoritarily preferentially wetting liquid are produced. In the latter case, food particles could be native to the recipe avoiding addition of non clean-label components, and the major liquid phase could be oil, while minor amounts of water, < 0.5%, have been reported sufficient to induce capillary stability. Being a soft matter strategy, this technique is less suitable for products undergoing thermal manufacturing due to microstructure collapse. Moreover, the effect of water migration into neighbouring crystalline and amorphous particles needs assessing with regard to crystalline bridge formation or amorphous sintering. Previous reports employed zein or wheat middling particles, suspended in soybean, sunflower, or corn oil stabilised by water or other aqueous solutions. Oil migration measured gravimetrically or by centrifugation ranged from poor 40 to excellent 0 w/w% percent [135–137].

5.6. Encapsulation

A complete enclosure of the lipid phase and thus oil migration mitigation is attempted by encapsulation, consisting of the lipid core and a wall substance (Fig. 4f). Various wall materials from CaCl₂-crosslinked

sodium alginate to solid fats, sugars, and proteins have been reported [163]. While wall properties can be tuned for controlled release of essential oils for instance, generally the produced capsules are unsuitable for compaction or extensive further processing due to the risk of breakage of the shell. Thus, encapsulated lipids are rather suitable in free-flowing bulk particulate form. Report of cinnamon and paprika oleoresin encapsulated in solid fat via spray drying and saturated gas solution achieved 2–30 w/w/% of oil leakage [138]. For essential oils *R. officinalis*, *L. angustifolia*, and *C. aurantium* encapsulated in β -cyclodextrin, oil migration was reported between 10 and 45 w/w%, while for chia seed oil enclosed in soy protein, maltodextrin, or inulin, oil migration was measured as 0–15 w/w%, using ethanol and hexane extraction methods [139,140].

5.7. Edible coating

A further development of encapsulation as oil mitigation strategy is to not only coat on a microscopic particle or granule level, but to wrap the entire macroscopic food item in an edible wall material, often biopolymers based on proteins or polysaccharides (Fig. 4g). Edible packaging or wrapping has been the subject of many research works, with the potential for additional moisture and oxygen barriers. In fact, for edible packaging moisture and oxygen barrier properties are more frequently investigated than oil barrier performance [164]. The aqueous solutions are usually applied as a spray, curtain, or dip coating, with the disadvantage of large moisture ingress into the hygroscopic food, damaging the microstructure. Additionally, application of a layer usually results in significant visual changes of the food appearance, potentially affecting consumer acceptance. Recent work on edible coatings and packaging specifically to mitigate oil migration reports the use of chitosan, gelatine, and gallic acid mixes to create oilproof pouches, achieving 0% oil leaking [141]. Other works on packaging for human consumption report pectin and starch films with eggshell waste as oil barrier packaging [142], or sunflower oil cake and alginate to package sunflower oil [143]. Yet generally, very little data is reported of the oil barrier properties of the edible coatings.

5.8. Packaging grease proofing

Mitigation of oil migration by stabilising the oil within the food is beneficial to avoid the adverse textural changes within the food due to oil loss (e.g. hardening), sensorial effects on the food (e.g. fat bloom) or to avoid food packaging interactions such as oil staining or ink dissolution into oil (Fig. 4h). Yet, in some instances the packaging wrapper might be the last barrier of defence to oil migration. Pressured by consumers and stricter legislation, more sustainable alternatives to conventional plastic, metallised plastic or paper, or *per*- and polyfluoroalkyl treated paper are required [11]. Most modern particle-technological alternative techniques for use in disposable packaging apply fine cellulose-derived fibres or particles in a dry coating process or biopolymer dispersion in a wet coating process in order to create oil-repulsive barriers on the paper surface [165]. Advantages of packaging modifications are of course that the food product remains unchanged, which is beneficial for consumer fidelity, while paper, board or card bear their own challenges such as reduced water and oxygen barrier properties, printability and marketability, and oftentimes higher cost [11]. Applying particle technology, in a recent work, molded pulp trays for fruit packaging was dry coated with sodium carboxymethyl cellulose and cellulose nanofibrils, achieving the highest kit test barrier value of 12 [144]. The same oil barrier performance was achieved when dry coating pizza cardboard boxes with chitosan and sodium carboxymethyl cellulose [146]. For 60 gsm paper, kit test values of 6 were achieved when wet coating with alkyl keteer dimer-modified alginate [145], demonstrating that an oil migration barrier is also achievable on the paper side of particulate food-packaging systems.

6. Final remarks

Particle-based consumer foods comprise the majority of fast moving consumer foods, of which many contain lipids in the form of oils, fats, and greases. Multiple factors influence lipid metastability, resulting in lipid migration within, or out of the food structure. This review revisited the factors inducing lipid migration and the most common transport mechanisms diffusion and capillary flow. The ease of application of diffusion models make it the predominant mechanism investigated. Many works on liquid imbibition flowing into particulate food structures, as in reconstitution, use capillary models. However in lipid migration studies in which liquid is leaking out of particle structures, capillary models are underrepresented. Compared to Fickian diffusion models, Washburn-type capillary flow models necessitate more data on the food microstructure, making them challenging to implement. The most common oil migration monitoring methods were revisited, showing the trend towards advanced spectroscopic and tomographic methods. Many macroscopic techniques such as oil stain analysis on paper are performed manually, leaving scope for more objective and efficient measurements using automated imaging tools. Modern mitigation strategies for oil migration control were discussed, with a focus on physical stabilisation approaches as opposed to unpreferred chemical stabilisation. The use of different strategies for different food types and structures is discussed, emphasising the relevance of oil migration issues beyond chocolate, but also for other confectionary and culinary food products consisting of particle-based systems.

CRedit authorship contribution statement

Luc Dewulf: Writing – review & editing, Writing – original draft, Visualization, Methodology, Investigation, Formal analysis, Conceptualization. **Michael K. Hausmann:** Writing – review & editing, Supervision. **Annabel Bozon:** Writing – review & editing, Supervision. **Gerhard Niederreiter:** Writing – review & editing, Supervision, Funding acquisition. **Stefan Palzer:** Writing – review & editing, Funding acquisition. **Agba D. Salman:** Writing – review & editing, Supervision, Project administration, Funding acquisition.

Declaration of competing interest

The authors declare the following financial interests/personal relationships which may be considered as potential competing interests:

Luc Dewulf reports financial support was provided by Engineering and Physical Sciences Research Council. Luc Dewulf reports financial support was provided by Nestle Research & Development. If there are other authors, they declare that they have no known competing financial interests or personal relationships that could have appeared to influence the work reported in this paper.

Data availability

No data was used for the research described in the article.

Acknowledgements

The author thanks EPSRC (grant 2602203) and Nestlé for funding this research, and Yongang (Abdullah) Ma for drawing a 3D stock cube used in the graphics.

References

- [1] J. Litster, *Design and Processing of Particulate Products*, Cambridge University Press, Cambridge, 2016.
- [2] E.W.C. Vickie, A. Vaclavik, Tad Campbell, *Essentials of Food Science*, Springer, Berlin, 2020.

- [3] Q. Zhang, F. Mugele, P.M. Lugt, D. Van Den Ende, Characterizing the fluid–matrix affinity in an organogel from the growth dynamics of oil stains on blotting paper, *Soft Matter* 16 (2020) 4200–4209.
- [4] L.J. Mauer, Deliquescence of crystalline materials: mechanism and implications for foods, *Curr. Opin. Food Sci.* 46 (2022) 100865.
- [5] S. Palzer, Chapter 13 agglomeration of dehydrated consumer foods, in: A. D. Salman, M.J. Hounslow, J.P.K. Seville (Eds.), *Handbook of Powder Technology*, Elsevier, Amsterdam, 2007.
- [6] L. Manzocco, S. Calligaris, M. Camerin, L. Pizzale, M.C. Nicoli, Prediction of firmness and physical stability of low-fat chocolate spreads, *J. Food Eng.* 126 (2014) 120–125.
- [7] V. Ghosh, G.R. Ziegler, R.C. Anantheswaran, Fat, moisture, and ethanol migration through chocolates and confectionary coatings, *Crit. Rev. Food Sci. Nutr.* 42 (2002) 583–626.
- [8] J.M. Aguilera, M. Michel, G. Mayor, Fat migration in chocolate: diffusion or capillary flow in a particulate solid?—a hypothesis paper, *J. Food Sci.* 69 (2004) 167–174.
- [9] C. Delbaere, D. Van de Walle, F. Depypere, X. Gellynck, K. Dewettinck, Relationship between chocolate microstructure, oil migration, and fat bloom in filled chocolates, *Eur. J. Lipid Sci. Technol.* 118 (2016) 1800–1826.
- [10] S. Cikrikci, M.H. Oztop, Mathematical modeling and use of magnetic resonance imaging (MRI) for oil migration in chocolate confectionery systems, *Food Eng. Rev.* 9 (2017) 50–70.
- [11] B.L. Tardy, J.J. Richardson, L.G. Greca, J. Guo, J. Bras, O.J. Rojas, Advancing bio-based materials for sustainable solutions to food packaging, *Nat. Sustain.* 6 (2023) 360–367.
- [12] M. Mujtaba, J. Lipponen, M. Ojanen, S. Puttonen, H. Vaitinen, Trends and challenges in the development of bio-based barrier coating materials for paper/cardboard food packaging - a review, *Sci. Total Environ.* 851 (2022).
- [13] W. Chaiyasit, R.J. Elias, D.J. McClements, E.A. Decker, Role of physical structures in bulk oils on lipid oxidation, *Crit. Rev. Food Sci. Nutr.* 47 (2007) 299–317.
- [14] C.W. Park, M.A. Drake, The distribution of fat in dried dairy particles determines flavor release and flavor stability, *J. Food Sci.* 79 (2014) R452–R459.
- [15] D. Angelopoulou, V. Meunier, L. Fornoy, G. Niederreiter, S. Palzer, A.D. Salman, Particle surface design for enhanced reconstitution of fat-based food powders, *Powder Technol.* 393 (2021) 397–404.
- [16] S. De Pelsmaecker, X. Gellynck, C. Delbaere, N. Declercq, K. Dewettinck, Consumer-driven product development and improvement combined with sensory analysis: a case-study for European filled chocolates, *Food Qual. Prefer.* 41 (2015) 20–29.
- [17] N. Biswas, Y.L. Cheow, C.P. Tan, L.F. Siow, Physical, rheological and sensorial properties, and bloom formation of dark chocolate made with cocoa butter substitute (CBS), *LWT Food Sci. Technol.* 82 (2017) 420–428.
- [18] Y. Cao, L. Miao, Consumer responses to suboptimal food products, *Appetite* 163 (2021) 105205.
- [19] L. Svanberg, L. Ahrné, N. Lorén, E. Windhab, A method to assess changes in mechanical properties of chocolate confectionery systems subjected to moisture and fat migration during storage, *J. Texture Stud.* 43 (2012) 106–114.
- [20] M. Dubé, M. Rost, M. Alava, Conserved dynamics and interface roughening in spontaneous imbibition: a critical overview, *Eur. Phys. J. B* 15 (2000) 691–699.
- [21] Q. Meng, H. Liu, J. Wang, A critical review on fundamental mechanisms of spontaneous imbibition and the impact of boundary condition, fluid viscosity and wettability, *Adv. Geo-Energy Res.* 1 (2017) 1–17.
- [22] M. Alava, M. Dubé, M. Rost, Imbibition in disordered media, *Adv. Phys.* 53 (2004) 83–175.
- [23] K. White, L. Lin, D.W. Dahl, R.J.B. Ritchie, When do consumers avoid imperfections? Superficial packaging damage as a contamination cue, *J. Mark. Res.* 53 (2016) 110–123.
- [24] S. Desobry, Packaging/fatty food interactions, *OCL-Oleagineux Corps Gras Lipides* 7 (2000) 427–430.
- [25] G.K. Deshwal, N.R. Panjagari, T. Alam, An overview of paper and paper based food packaging materials: health safety and environmental concerns, *J. Food Sci. Technol.* 56 (2019) 4391–4403.
- [26] A.G. Marangoni, Challenges and opportunities of fats and oils, *J. Agric. Food Chem.* 66 (2018) 3257–3259.
- [27] D.J. McClements, *Future Foods: How Modern Science Is Transforming the Way We Eat*, Springer, Cham, 2019.
- [28] A. Tarabella, *Food Products Evolution: Innovation Drivers and Market Trends*, Springer, CH, 2019.
- [29] V. Raikos, V. Ranawana, Reformulating foods for health-concepts, trends and considerations, in: V. Raikos, V. Ranawana (Eds.), *Reformulation as a Strategy for Developing Healthier Food Products: Challenges, Recent Developments and Future Prospects*, Springer, Cham, 2019.
- [30] R. Fernandes Almeida, L. Aguiar Borges, T. Torres da Silva, N. Serafim Timóteo dos Santos, F. Gianasi, E. Augusto Caldas Batista, P. Efraim, Chocolates, compounds and spreads: a review on the use of oleogels, hydrogels and hybrid gels to reduce saturated fat content, *Food Res. Int.* 178 (2024) 113986.
- [31] C. Arancibia, N. Riquelme, R. Zúñiga, S. Matiacevich, Comparing the effectiveness of natural and synthetic emulsifiers on oxidative and physical stability of avocado oil-based nanoemulsions, *Innovative Food Sci. Emerg. Technol.* 44 (2017) 159–166.
- [32] H. Lindh, A. Olsson, H. Williams, Consumer perceptions of food packaging: contributing to or counteracting environmentally sustainable development? *Packag. Technol. Sci.* 29 (2016) 3–23.
- [33] N.D. Steenis, E. van Herpen, I.A. van der Lans, T.N. Ligthart, H.C.M. van Trijp, Consumer response to packaging design: the role of packaging materials and graphics in sustainability perceptions and product evaluations, *J. Clean. Prod.* 162 (2017) 286–298.
- [34] S. Otto, M. Strenger, A. Maier-Nöth, M. Schmid, Food packaging and sustainability – consumer perception vs. correlated scientific facts: a review, *J. Clean. Prod.* 298 (2021) 126733.
- [35] J.N. Israelachvili, *Intermolecular and Surface Forces*, Academic Press, New York, 2011.
- [36] J.M. Aguilera, Food microstructures for health, well-being, and pleasure, in: R.S. José Miguel Aguilera, Jorge Welti-Chanes, Daniela Bermudez-Aguirre, Gustavo Barbosa-Canovas (Eds.), *Food Engineering Interfaces*, Springer, New York, 2011.
- [37] L. Dewulf, M.K. Hausmann, A. Bozon, G. Niederreiter, S. Palzer, A.D. Salman, Food vs packaging: dynamics of oil migration from particle systems into fibrous material, *Powder Technol.* 439 (2024) 119721.
- [38] J. Lange, C. Pelletier, Y. Wyser, Novel method for testing the grease -resistance of pet food packaging, *Packag. Technol. Sci.* 15 (2002) 65–74.
- [39] L. Svanberg, L. Ahrné, N. Lorén, E. Windhab, Effect of sugar, cocoa particles and lecithin on cocoa butter crystallisation in seeded and non-seeded chocolate model systems, *J. Food Eng.* 104 (2011) 70–80.
- [40] K.W. Smith, K. Bhaggan, G. Talbot, Phase behavior of symmetrical monounsaturated triacylglycerols, *Eur. J. Lipid Sci. Technol.* 115 (2013) 838–846.
- [41] H. Zhao, B.J. James, Fat bloom formation on model chocolate stored under steady and cycling temperatures, *J. Food Eng.* 249 (2019) 9–14.
- [42] A.G. Marangoni, *Kinetic Analysis of Food Systems*, Springer, Cham, 2017.
- [43] W. Ostwald, Studien über die bildung und umwandlung fester körper, 1. abhandlung: übersättigung und überkaltung, *Z. Phys. Chem.* 22U (1897) 289–330.
- [44] R. Brown, A brief account of microscopical observations made in the months of June, July and August 1827, on the particles contained in the pollen of plants; and on the general existence of active molecules in organic and inorganic bodies, *Phil. Mag.* 4 (1828) 161–173.
- [45] A. Fick, Über diffusion, *Ann. Phys.* 170 (1855) 59–86.
- [46] A. Fick, On liquid diffusion, the London, Edinburgh, and Dublin philosophical magazine and journal of, *Science* 10 (1855) 30–39.
- [47] L. Svanberg, N. Lorén, L. Ahrné, Chocolate swelling during storage caused by fat or moisture migration, *J. Food Sci.* 77 (2012) E328–E334.
- [48] A. Einstein, Über die von der molekularkinetischen theorie der wärme geforderte bewegung von in ruhenden flüssigkeiten suspendierten teilchen, *Ann. Phys.* 322 (1905) 549–560.
- [49] M. Mirzajanzadeh, V.S. Deshpande, N.A. Fleck, Water rise in a cellulose foam: by capillary or diffusional flow? *J. Mech. Phys. Solids* 124 (2019) 206–219.
- [50] R.F. Peña-Correa, B.A. Mogol, V. Fogliano, Fluidized bed roasting modifying the microstructure of cocoa nibs and improving cocoa butter quality, *J. Am. Oil Chem. Soc.* 100 (2023) 815–827.
- [51] C. Loisel, G. Lecq, G. Ponchel, G. Keller, M. Ollivon, Fat bloom and chocolate structure studied by mercury porosimetry, *J. Food Sci.* 62 (1997) 781–788.
- [52] H. Hondoh, K. Yamasaki, M. Ikutake, S. Ueno, Visualization of oil migration in chocolate using scanning electron microscopy—energy dispersive X-ray spectroscopy, *Food Struct.* 8 (2016) 8–15.
- [53] T. Young, An essay on the cohesion of fluids, *Philos. Trans. R. Soc. Lond.* 95 (1805) 65–87.
- [54] P.-S. Laplace, *Traite de Mechanique Celeste*, Courcier, Paris, 1805.
- [55] L.R. White, Capillary rise in powders, *J. Colloid Interface Sci.* 90 (1982) 536–538.
- [56] K. Washino, E.L. Chan, T. Kaji, Y. Matsuno, T. Tanaka, On large scale CFD–DEM simulation for gas–liquid–solid three-phase flows, *Particuology* 59 (2021) 2–15.
- [57] P.R. Smith, A. Dahlman, The use of atomic force microscopy to measure the formation and development of chocolate bloom in pralines, *J. Am. Oil Chem. Soc.* 82 (2005) 165–168.
- [58] S.K. Reinke, F. Wilde, S. Kozhar, F. Beckmann, J. Vieira, S. Heinrich, S. Palzer, Synchrotron X-Ray microtomography reveals interior microstructure of multicomponent food materials such as chocolate, *J. Food Eng.* 174 (2016) 37–46.
- [59] J. Jurin, An account of some experiments shown before the Royal Society; with an enquiry into the cause of the ascent and suspension of water in capillary tubes, *Philos. Trans. R. Soc. Lond.* 30 (1997) 739–747.
- [60] J. Jurin, An account of some new experiments, relating to the action of glass tubes upon water and quicksilver, *Philos. Trans. R. Soc. Lond.* 30 (1997) 1083–1096.
- [61] M.F. El-Amin, A. Salama, S. Sun, Numerical and dimensional investigation of two-phase countercurrent imbibition in porous media, *J. Comput. Appl. Math.* 242 (2013) 285–296.
- [62] D.R. Woods, *Rules of Thumb in Engineering Practice*, Wiley-VCH, Heidelberg, 2007.
- [63] G. Hagen, Ueber die Bewegung des Wassers in engen cylindrischen Röhren, *Ann. Phys.* 122 (1839) 423–442.
- [64] J.L.M. Poiseuille, Recherches sur les causes du mouvement du sang dans les veines, *J. Physiol. Exp. Pathol.* 10 (1830) 277–295.
- [65] E.W. Washburn, The dynamics of capillary flow, *Phys. Rev.* 17 (1921) 273–283.
- [66] A.J. Martins, M.A. Cerqueira, L.M. Pastrana, R.L. Cunha, A.A. Vicente, Sterol-based oleogels' characterization envisioning food applications, *J. Sci. Food Agric.* 99 (2019) 3318–3325.
- [67] N.C. Acevedo, B. MacMillan, B. Newling, A.G. Marangoni, Shear effects on the diffusive movement of oil in triacylglycerol networks, *RSC Adv.* 7 (2017) 1634–1642.

- [68] F. Aloui, B. Maazoun, Y. Gargouri, N. Miled, Optimization of oil retention in sesame based halva using emulsifiers and fibers: an industrial assay, *J. Food Sci. Technol. Mysore* 53 (2016) 1540–1550.
- [69] M. Elleuch, D. Bedigian, B. Maazoun, S. Besbes, C. Blecker, H. Attia, Improving halva quality with dietary fibres of sesame seed coats and date pulp, enriched with emulsifier, *Food Chem.* 145 (2014) 765–771.
- [70] K.I. Ereifej, T.M. Rababah, M.A. Al-Rababah, Quality attributes of halva by utilization of proteins, non-hydrogenated palm oil, emulsifiers, gum arabic, sucrose, and calcium chloride, *Int. J. Food Prop.* 8 (2005) 415–422.
- [71] O. Guner, M. Zorba, Effect of emulsifiers on oil separation problem and quality characteristics of tahin helva during storage, *J. Food Sci. Technol.* 51 (2014) 1085–1093.
- [72] M.I. Ordiz, K.N. Ryan, E.D. Cimo, M.E. Stoner, M.E. Loehnig, M.J. Manary, Effect of emulsifier and viscosity on oil separation in ready-to-use therapeutic food, *Int. J. Food Sci. Nutr.* 66 (2015) 642–648.
- [73] C. Jacquot, J. Petit, F. Michaux, E. Chávez Montes, J. Dupas, V. Girard, A. Gianfrancesco, J. Scher, C. Gaiani, Cocoa powder surface composition during aging: A focus on fat, *Powder Technol.* 292 (2016) 195–202.
- [74] J. Petit, F. Michaux, C. Jacquot, E. Chávez Montes, J. Dupas, V. Girard, A. Gianfrancesco, J. Scher, C. Gaiani, Storage-induced caking of cocoa powder, *J. Food Eng.* 199 (2017) 42–53.
- [75] E.H.J. Kim, X.D. Chen, D. Pearce, Surface composition of industrial spray-dried milk powders. 3. Changes in the surface composition during long-term storage, *J. Food Eng.* 94 (2009) 182–191.
- [76] T.L.T. da Silva, M. Marsh, V. Gibson, S. Martini, Sonocrystallization as a tool to reduce oil migration by changing physical properties of a palm kernel fat, *J. Food Sci.* 85 (2020) 964–971.
- [77] F. Valoppi, P. Lassila, A. Salmi, E. Haeggström, Automated image analysis method for oil-release test of lipid-based materials, *MethodsX* 8 (2021) 101447.
- [78] P.R. Ramel, A.G. Marangoni, Effect of oil viscosity on oil migration in a two-phase model system (cream-filled chocolate), *LWT* 84 (2017) 740–745.
- [79] N.J. Hendrik, I.A. Penagos, F. De Witte, D. Van de Walle, F.H. Marchesini, K. Dewettinck, Monitoring solidification and storage stability of well-tempered chocolates obtained through various pre-crystallization techniques, *Food and Bioprocess Technology* (2023).
- [80] C. Cevoli, A. Evangelisti, P. Gradari, A. Fabbri, Storage of wafer cookies: assessment by destructive techniques, and non-destructive spectral detection methods, *J. Food Eng.* 336 (2023).
- [81] L. Shen, J. Jin, X. Ye, Y. Li, C. Zhang, L. Jiang, L. Zhao, Effects of sucrose particle size on the microstructure and bloom behavior of chocolate model systems, *Food Struct.* 36 (2023) 100323.
- [82] X. Ye, J. Jin, C. Liang, J. Wang, L. Jiang, L. Zhao, Effects of individual phospholipids on chocolate model systems: particulate interaction, crystallization behavior, and fat bloom during storage, *J. Food Eng.* 357 (2023) 111618.
- [83] J. Jin, Q. Jin, X. Wang, C.C. Akoh, Improving heat and fat bloom stabilities of “dark chocolates” by addition of mango kernel fat-based chocolate fats, *J. Food Eng.* 246 (2019) 33–41.
- [84] H.H. Zhao, G. Bingol, B.J. James, Influence of non-fat particulate network on fat bloom development in a model chocolate, *J. Food Eng.* 225 (2018) 12–17.
- [85] M.H.M. Buscato, L.M. Hara, É.C. Bonomi, G.D.A. Calligaris, L.P. Cardoso, R. Grimaldi, T.G. Kieckbusch, Delaying fat bloom formation in dark chocolate by adding sorbitan monostearate or cocoa butter stearin, *Food Chem.* 256 (2018) 390–396.
- [86] J. Dias, P. Coelho, N.B. Alvarenga, R.V. Duarte, J.A. Saraiva, Evaluation of the impact of high pressure on the storage of filled traditional chocolates, *Innovative Food Sci. Emerg. Technol.* 45 (2018) 36–41.
- [87] Y.-J. Son, S.-Y. Choi, K.-M. Yoo, K.-W. Lee, S.-M. Lee, L.-K. Hwang, S. Kim, Anti-blooming effect of maltitol and tagatose as sugar substitutes for chocolate making, *LWT* 88 (2018) 87–94.
- [88] V. Nelis, L. De Neve, S. Danthine, K. Dewettinck, J.C. Martins, P. Van der Meeren, Oil diffusion in fat crystal matrices: characterization by nmr relaxometry and diffusometry, *Eur. J. Lipid Sci. Technol.* 123 (2021) 2000237.
- [89] H. Wang, F. Maleky, Effects of cocoa butter triacylglycerides and minor compounds on oil migration, *Food Res. Int.* 106 (2018) 213–224.
- [90] X.H. Chai, Z. Meng, P.R. Cao, J. Jiang, Y.F. Liu, Comparative analysis of small-molecule diffusivity in different fat crystal network, *J. Agric. Food Chem.* 66 (2018) 1015–1022.
- [91] H. Wang, X. Shi, S. Paluri, F. Maleky, Effects of processing and added ingredients on oil diffusion through cocoa butter using magnetic resonance imaging, *RSC Adv.* 6 (2016) 88498–88507.
- [92] L. Svanberg, L. Ahrné, N. Lorén, E. Windhab, Effect of pre-crystallization process and solid particle addition on cocoa butter crystallization and resulting microstructure in chocolate model systems, in: 11th International Congress on Engineering and Food (ICEF11), 2011, pp. 1910–1917.
- [93] N.L. Green, D. Rousseau, Oil diffusivity through fat crystal networks, *Soft Matter* 11 (2015) 5523–5530.
- [94] H. Dahlenborg, A. Millqvist-Fureby, B.D. Brandner, B. Bergenstahl, Study of the porous structure of white chocolate by confocal Raman microscopy, *Eur. J. Lipid Sci. Technol.* 114 (2012) 919–926.
- [95] B.J. James, B.G. Smith, Surface structure and composition of fresh and bloomed chocolate analysed using X-ray photoelectron spectroscopy, cryo-scanning electron microscopy and environmental scanning electron microscopy, *LWT Food Sci. Technol.* 42 (2009) 929–937.
- [96] L. Trapp, H. Schacht, L. Eymann, H. Nirschl, G. Guthausen, Oil mobility in hazelnut oil-based oleogels investigated by NMR, *Appl. Magn. Reson.* 54 (2023) 1445–1462.
- [97] M. Adam-Berret, M. Boulard, A. Riaublanc, F. Mariette, Evolution of fat crystal network microstructure followed by NMR, *J. Agric. Food Chem.* 59 (2011) 1767–1773.
- [98] S. Cikrikci, M.H. Oztop, Oil migration in hazelnut paste/chocolate systems using magnetic resonance imaging, *J. Food Meas. Charact.* 12 (2018) 1460–1472.
- [99] T.R. Rumsey, K.L. McCarthy, Modeling oil migration in two-layer chocolate–almond confectionery products, *J. Food Eng.* 111 (2012) 149–155.
- [100] A. Altan, D.M. Lavenson, M.J. McCarthy, K.L. McCarthy, Oil migration in chocolate and almond product confectionery systems, *J. Food Sci.* 76 (2011) E489–E494.
- [101] L. Metilli, M. Storm, S. Marathe, A. Lazidis, S. Marty-Terrade, E. Simone, Application of X-ray microcomputed tomography for the static and dynamic characterization of the microstructure of Oleofoams, *Langmuir* 38 (2022) 1638–1650.
- [102] I. Vego, A. Tengattini, N. Lenoir, G. Viggiani, The influence of water sorption on the microstructure of a hydro-sensitive granular material (couscous) deduced from simultaneous neutron and X-ray tomography, *Granul. Matter* 25 (2023) 65.
- [103] M. Martínez-Sanz, E. Larsson, K.B. Filli, C. Loupiac, A. Assifaoui, A. López-Rubio, P. Lopez-Sanchez, Nano-/microstructure of extruded Spirulina/starch foams in relation to their textural properties, *Food Hydrocoll.* 103 (2020) 105697.
- [104] C.A. Schneider, W.S. Rasband, K.W. Eliceiri, NIH image to ImageJ: 25 years of image analysis, *Nat. Methods* 9 (2012) 671–675.
- [105] ISO, ISO/CIE 11664-4:2019, Colorimetry. Part 4: CIE 1976 L*a*b* Colour Space, ISO, Geneva, 2019.
- [106] J. Bricknell, R.W. Hartel, Relation of fat bloom in chocolate to polymorphic transition of cocoa butter, *J. Am. Oil Chem. Soc.* 75 (1998) 1609–1615.
- [107] D.B. MacDougall, Principles of colour measurement for food, in: E. Kress-Rogers, C.J.B. Brimelow (Eds.), Instrumentation and Sensors for the Food Industry, Woodhead, Sawston, 2001, pp. 63–84.
- [108] D. Axelrod, D.E. Koppel, J. Schlessinger, E. Elson, W.W. Webb, Mobility measurement by analysis of fluorescence photobleaching recovery kinetics, *Biophys. J.* 16 (1976) 1055–1069.
- [109] K.M.G. Siegbahn, W.C. Price, D.W. Turner, A discussion on photoelectron spectroscopy - Electron spectroscopy for chemical analysis (e.s.c.a.), *Phil. Trans. Roy. Soc. Lond. Ser. A* 268 (1997) 33–57.
- [110] A. Einstein, Über einen die Erzeugung und Verwandlung des Lichtes betreffenden heuristischen Gesichtspunkt, *Ann. Phys.* 322 (1905) 132–148.
- [111] S. Meiboom, D. Gill, Modified spin-echo method for measuring nuclear relaxation times, *Rev. Sci. Instrum.* 29 (1958) 688–691.
- [112] E.O. Stejskal, J.E. Tanner, Spin diffusion measurements: spin echoes in the presence of a time-dependent field gradient, *J. Chem. Phys.* 42 (1965) 288–292.
- [113] L. Metilli, M. Francis, M. Povey, A. Lazidis, S. Marty-Terrade, J. Ray, E. Simone, Latest advances in imaging techniques for characterizing soft, multiphase food materials, *Adv. Colloid Interf. Sci.* 279 (2020) 102154.
- [114] J. Haedelt, S.T. Beckett, K. Niranjan, Bubble-included chocolate: relating structure with sensory response, *J. Food Sci.* 72 (2007) E138–E142.
- [115] T. Defraeye, B. Nicolai, D. Mannes, W. Aregawi, P. Verboven, D. Derome, Probing inside fruit slices during convective drying by quantitative neutron imaging, *J. Food Eng.* 178 (2016) 198–202.
- [116] S. Carbonell, M.J. Hey, J.R. Mitchell, C.J. Roberts, J. Hipkiss, J. Vercauteren, Capillary flow and rheology measurements on chocolate crumb/sunflower oil mixtures, *J. Food Sci.* 69 (2004) E465–E470.
- [117] M.T.Q.S. da Silva, M. do Rocio Cardoso, C.M.P. Veronese, W. Mazer, Tortuosity: a brief review, *Mater. Today Proc.* 58 (2022) 1344–1349.
- [118] G. Ziegler, C. Moser, J. GeierGreguska, Kinetics of fat migration within chocolate products. 1. Principles and analytics, *Fett-Lipid* 98 (1996) 196–199.
- [119] G. Ziegler, C. Moser, J. GeierGreguska, Kinetics of fat migration within chocolate products. 2. Influence of storage temperature, diffusion coefficient, solid fat content, *Fett-Lipid* 98 (1996) 253–256.
- [120] G. Ziegler, I. Schwingshandl, Kinetics of fat migration within chocolate products. Part III: fat bloom, *Fett-Lipid* 100 (1998) 411–415.
- [121] N.A. Peppas, L. Brannon-Peppas, Water diffusion and sorption in amorphous macromolecular systems and foods, in: P. Fito, A. Mulet, B. McKenna (Eds.), *Water in Foods*, Pergamon, Amsterdam, 1994, pp. 189–210.
- [122] J. Crank, *The Mathematics of Diffusion*, Clarendon Press, Oxford, 1975.
- [123] Y. Shah, P.S. Takhar, Capillary pressure in unsaturated food systems: its importance and accounting for it in mathematical models, *Food Eng. Rev.* 15 (2023) 393–419.
- [124] J. Kammerhofer, L. Fries, J. Dupas, L. Forn, S. Heinrich, S. Palzer, Dynamic wetting of multicomponent particle systems, *Powder Technol.* 357 (2019) 74–82.
- [125] M. Ögütçü, N. Arifoglu, E. Yılmaz, Restriction of oil migration in tahini halva via organogelation, *Eur. J. Lipid Sci. Technol.* 119 (2017) 1600189.
- [126] Z.B. Ghorghi, S. Yeganehzad, M.A. Hesarinejad, A. Faezian, V. Kutsenkova, Z. Gao, K. Nishinari, N. Nepovinnikh, Fabrication of novel hybrid gel based on beeswax oleogel: application in the compound chocolate formulation, *Food Hydrocoll.* 140 (2023) 108599.
- [127] Q. Zhu, W.-W. Zhang, Z.-J. Ni, K. Thakur, J.-G. Zhang, F. Hu, Z.-J. Wei, Development and characterization of novel Lycium barbarum seed oil-based oleogels and their application in functional chocolate, *Food Biosci.* 56 (2023) 103155.
- [128] L. Wang, X. Cheng, H. Lan, L. Jiang, X. Liu, J. Pei, M. Zhang, Q. Zhong, W. Chen, W. Chen, H. Chen, Development and characterization of novel ultra-stable high internal phase Pickering emulsions gel: Interface structure, stabilization mechanism, and applications, *Food Hydrocoll.* 151 (2024) 109817.

- [129] S.M. Kim, J.H. Woo, H.W. Kim, H.J. Park, Formulation and evaluation of cold-extruded chocolate ganache for three-dimensional food printing, *J. Food Eng.* 314 (2022) 110785.
- [130] Z. Li, X.X. Jiang, H.N. Liu, Z.H. Yao, A. Liu, L.S. Ming, Evaluation of hydrophilic and hydrophobic silica particles on the release kinetics of essential oil pickering emulsions, *ACS Omega* 7 (2022) 8651–8664.
- [131] Z. Li, Y. Ying Lee, Y. Wang, C. Qiu, Interfacial behavior, gelation and foaming properties of diacylglycerols with different acyl chain lengths and isomer ratios, *Food Chem.* 427 (2023) 136696.
- [132] M. Callau, K. Sow-Kébé, N. Jenkins, A.-L. Fameau, Effect of the ratio between fatty alcohol and fatty acid on foaming properties of whipped oleogels, *Food Chem.* 333 (2020) 127403.
- [133] B. Tirgarian, J. Farmani, A novel approach for the development of edible oleofoams using double network oleogelation systems, *Food Chem.* 426 (2023) 136634.
- [134] E.O. Afoakwa, A. Paterson, M. Fowler, J. Vieira, Fat bloom development and structure-appearance relationships during storage of under-tempered dark chocolates, *J. Food Eng.* 91 (2009) 571–581.
- [135] G.S. Wang, H.Y. Chen, L.J. Wang, Y. Zou, Z.L. Wan, X.Q. Yang, Formation of protein oleogels via capillary attraction of engineered protein particles, *Food Hydrocoll.* 133 (2022).
- [136] A. Pirozzi, A. Posocco, F. Donsì, Oil structuring through capillary suspensions prepared with wheat middlings micronized directly in oil by high-pressure homogenization, *Food Hydrocoll.* 145 (2023).
- [137] Y.D. Li, M.X. Duan, G.Y. Liu, L. Liang, X.F. Liu, J.X. Zhang, C.T. Wen, X. Xu, Effects of sinapine on structure, rheology, stability, and antioxidant properties of protein-based capillary bridging oleogels, *Food Biosci.* 58 (2024).
- [138] F.R. Procopio, S. Klettenhammer, G. Ferrentino, M. Scampicchio, P.J. Sobral, M. D. Hubinger, Comparative study of cinnamon and paprika oleoresins encapsulated by spray chilling and particles from gas saturated solutions techniques: evaluation of physical characteristics and oleoresins release in food simulated media, *Food Bioprocess Technol.* 16 (2023) 2147–2158.
- [139] S. El Kharraf, A. Farah, S. El-Guendouz, J.P. Lourenço, A.M.R. Costa, E. El Hadrami, A.M. Machado, C.S. Tavares, A.C. Figueiredo, M.G. Miguel, β -Cyclodextrin inclusion complexes of combined Moroccan *Rosmarinus officinalis*, *Lavandula angustifolia* and *Citrus aurantium volatile oil*: production optimization and release kinetics in food models, *J. Essent. Oil Res.* 35 (2023) 247–261.
- [140] B.M. Razavizadeh, M. Shahidi Noghabi, M. Molaveisi, A ternary blending of soy protein isolate/maltodextrin/inulin for encapsulation bioactive oils: optimization of wall material and release studies, *J. Food Process. Preserv.* 46 (2022) e16734.
- [141] M. Kurek, E. Descours, P. Poldan, A. Julou, A. Pitois, D. Klepac, N. Vallet, K. Galić, Possibility of storing olive oil in antioxidant biobased pouches made of chitosan and gelatin, *Food Hydrocoll.* 151 (2024) 109835.
- [142] M.N.D.L. Moreira, F.K.V. Moreira, A.S. Prata, Effect of adding micronized eggshell waste particles on the properties of biodegradable pectin/starch films, *J. Clean. Prod.* 434 (2024) 140229.
- [143] A. Petraru, S. Amariei, Sunflower oilcake as a potential source for the development of edible membranes, *Membranes* 12 (2022) 789.
- [144] J.X. Zhang, J.P. Youngblood, Cellulose nanofibril (CNF)-coated PFAS-free, grease-resistant all-bio-based molded pulp containers for food packaging, *ACS Appl. Polym. Mater.* 5 (2023) 5696–5706.
- [145] L.Y. Ma, S. Liu, J.H. Shi, R.A. Wu, P. Lu, Recyclable oil resistant paper with enhanced water resistance based on alkyl ketene dimer modified sodium alginate, *Nord. Pulp Pap. Res. J.* 38 (2023) 533–543.
- [146] K. Chi, J.M. He, W.S. Lin, S.M.Q. Bokhari, J.M. Catchmark, Electrostatically complexed natural polysaccharides as aqueous barrier coatings for sustainable and recyclable fiber-based packaging, *ACS Appl. Mater. Interfaces* 15 (2023) 12248–12260.
- [147] A.R. Patel, K. Dewettinck, Edible oil structuring: an overview and recent updates, *Food Funct.* 7 (2016) 20–29.
- [148] T. Tran, D. Rousseau, Influence of shear on fat crystallization, *Food Res. Int.* 81 (2016) 157–162.
- [149] Y. Gao, Z. Meng, Crystallization of lipids and lipid emulsions treated by power ultrasound: a review, *Crit. Rev. Food Sci. Nutr.* 64 (2024) 1882–1893.
- [150] S.U. Pickering, Emulsions, *J. Chem. Soc. Trans.* 91 (1907) 2001–2021.
- [151] C. Linke, S. Drusch, Pickering emulsions in foods - opportunities and limitations, *Crit. Rev. Food Sci. Nutr.* 58 (2018) 1971–1985.
- [152] A. Pawlik, D. Kurukji, I. Norton, F. Spyropoulos, Food-grade Pickering emulsions stabilised with solid lipid particles, *Food Funct.* 7 (2016) 2712–2721.
- [153] A. Shi, X. Feng, Q. Wang, B. Adhikari, Pickering and high internal phase Pickering emulsions stabilized by protein-based particles: a review of synthesis, application and prospective, *Food Hydrocoll.* 109 (2020) 106117.
- [154] B. Haney, D. Chen, L.-H. Cai, D. Weitz, S. Ramakrishnan, Millimeter-size pickering emulsions stabilized with Janus microparticles, *Langmuir* 35 (2019) 4693–4701.
- [155] B.P. Binks, B. Vishal, Particle-stabilized oil foams, *Adv. Colloid Interf. Sci.* 291 (2021) 102404.
- [156] L. Ribourg-Birault, A. Meynier, S. Vergé, E. Sallan, A. Kermarrec, X. Falourd, C. Berton-Carabin, A.-L. Fameau, Oleofoams: the impact of formulating air-in-oil systems from a lipid oxidation perspective, *Curr. Res. Food Sci.* 8 (2024) 100690.
- [157] J. Kozeny, Über kapillare Leitung des Wassers im Boden, *Akad. Wissenschaftern Wien* 132 (1927) 271–306.
- [158] J. Kozeny, Über kapillare Leitung des Wassers im Boden (Aufstieg, Versickerung und Anwendung auf die Bewässerung), *Sitzungsber. Akad. Wiss. Wien* 136 (1927) 271–309.
- [159] P.C. Carman, Fluid flow through granular beds 15, Institution of Chemical Engineers London, 2024.
- [160] P.C. Carman, Fluid flow through granular beds, *Chem. Eng. Res. Des.* 75 (1937) S32–S48.
- [161] J.I. Crossley, J.M. Aguilera, Modeling the effect of microstructure on food extraction, *J. Food Process Eng.* 24 (2001) 161–177.
- [162] E. Koos, Capillary suspensions: particle networks formed through the capillary force, *Curr. Opin. Colloid Interface Sci.* 19 (2014) 575–584.
- [163] J. Rodríguez, M.J. Martín, M.A. Ruiz, B. Clares, Current encapsulation strategies for bioactive oils: from alimentary to pharmaceutical perspectives, *Food Res. Int.* 83 (2016) 41–59.
- [164] A. Trajkovska Petkoska, D. Daniloski, N.M. D' Cunha, N. Naumovski, A.T. Broach, Edible packaging: sustainable solutions and novel trends in food packaging, *Food Res. Int.* 140 (2021) 109981.
- [165] S. Basak, M.S. Dangate, S. Samy, Oil- and water-resistant paper coatings: a review, *Prog. Org. Coat.* 186 (2024) 107938.

Corrigendum for Chapter: Literature Review

- A is the lipid migration cross-sectional area (m^2) and is hence $2D$.
- In the literature review chapter, it says the mass flux J is proportional to $m(x - l)l$ and $m(x + l)l$. However, the proportionality constant was not stated in Eqn. 1. Instead, the correct version should be:

$$J = K[m(x - l)l - m(x + l)l] = -2Kml^2$$

where K is a proportionality constant with units ($\text{m}^3 \text{s}^{-1}$)

-

$$J = -2Kl^2 \frac{dm}{dx} = -D \frac{dm}{dx}$$

The diffusivity D absorbs $2Kl^2$ in a proportionality constant.

- Fig. 2 is a representation of a zoomed-in view into a porous bed in which lipid is rising due to capillary action. The zoomed-in view is to be regarded as a small section of a larger powder bulk. On average, the flow is therefore rising homogenously, even if in the zoomed-in section the flow seemed converging.

Chapter 3

Methodology

A Method for Raman Chemical Imaging from Point Probes: Hyperspectral Characterisation of Food Powder Structures

Luc Dewulf¹, Michael K. Hausmann², Annabel Bozon³, Gerhard Niederreiter², Agba D. Salman¹

¹ School of Chemical, Materials and Biological Engineering, University of Sheffield, Sheffield, S1 3JD, United Kingdom

² Nestlé Research, Route du Jorat 57, 1000 Lausanne 26, Switzerland

³ Nestlé Product Technology Centre, Lange Straße 21, 78221 Singen, Germany

LDewulf1@Sheffield.ac.uk, ORCID: <https://orcid.org/0000-0001-9376-447X>

Raman Chemical Imaging, Hyperspectral Imaging, Laser Spectroscopy, Food Powder, Food Microstructure, Oil Migration, Distribution Map, Global Intensity Map

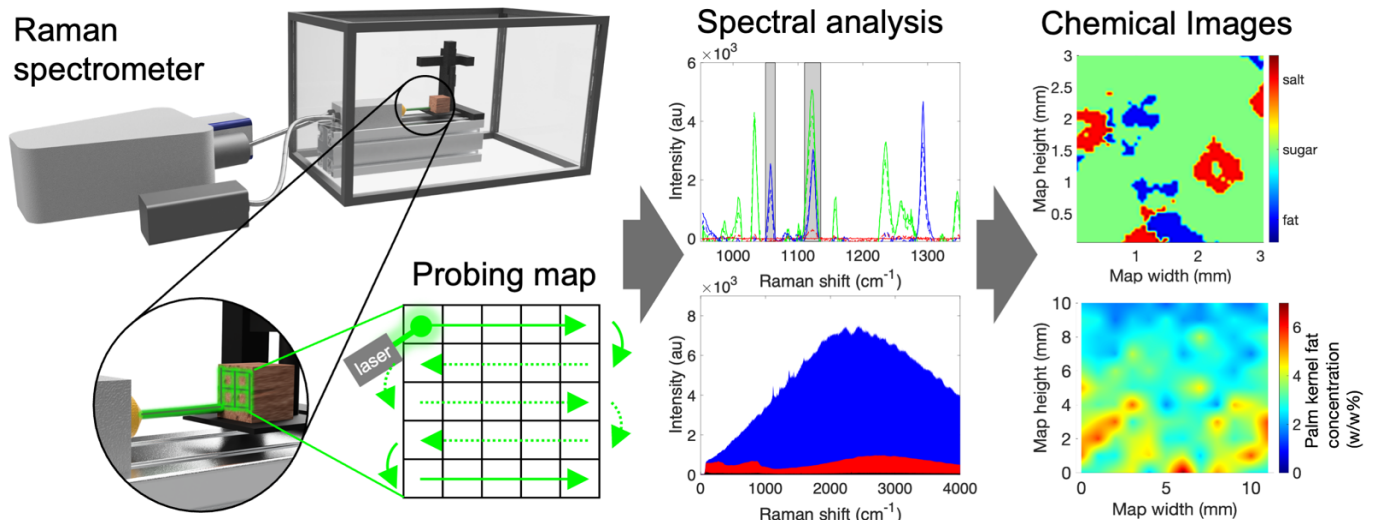
L. Dewulf *et al.*, *Food vs packaging: Dynamics of oil migration from particle systems into fibrous material*, *Powder Technology*. 439 (2024) 119721. <https://doi.org/10.1016/j.powtec.2024.119721>

Abstract

A technique to generate images from Raman spectra collected from fibre bundle point probes is presented. Raman spectroscopy from single-beam laser systems is the most common Raman technique, and by scanning sample surfaces in point-by-point array patterns, 2D images can be generated revealing spatial information of sample surface composition. A coherent methodology for hyperspectral Raman chemical imaging is presented for particulate food structures, beginning with hardware setup for mapping and automated spectra acquisition. For the first time, an open-source Matlab code is described for signal processing, background and baseline corrections, and image reconstruction. The workflow is exemplified in two case studies reflecting the two major imaging scenarios:

- Distribution map: A method is presented for high-resolution microscopic spatial mapping of multicomponent food powders and species identification assisted by the first of two program scripts. Raman chemical images were reconstructed depicting each food species with a pre-allocated colour, thereby visualizing the ingredient distribution.
- Global intensity map: A method is presented for macroscopic spatial mapping of a single species in a multicomponent food mix, relating spectral intensity with physical concentration using the second script. Raman chemical images were reconstructed representing concentration with a colour gradient, showing species migration during food shelf life.

1 Graphical abstract



3 Specifications table

Subject area	Food Science
More specific subject area	Raman spectroscopic chemical imaging
Name of your method	Hyperspectral Raman chemical imaging for distribution maps and global intensity or concentration maps of powder-based food structures
Name and reference of original method	L. Dewulf <i>et al.</i> , <i>Food vs packaging: Dynamics of oil migration from particle systems into fibrous material</i> , <i>Powder Technology</i> . 439 (2024) 119721. https://doi.org/10.1016/j.powtec.2024.119721 This paper describes a Raman chemical imaging method to monitor oil distribution within a food compact and measure oil migration from foods into fibre-based packaging during an accelerated shelf-life test [1]
Resource availability	Laser source (e.g. diode laser LCX, Oxxius S.A., Lannion, France) Spectrometer and CCD sensor (e.g. iHR320 and Synapse, Horiba, Longjumeau, France) Micrometer stage (e.g. SM 3.25, Märzhäuser, Wetzlar, Germany) Micrometer stage controller (e.g. Tango Desktop, Märzhäuser, Wetzlar, Germany) Power Automate (https://www.microsoft.com/power-platform/products/power-automate) Matlab (https://matlab.com)

Background

Many globally produced consumer foods are in particulate form such as powders, granules or compacts. Frequent examples include coffee, dairy powders, seasoning compacts or chocolate. Understanding and measuring ingredient distribution of the food during manufacturing, shelf-life and consumption is key to ensure intended product performance, storage stability and food safety. Optical techniques have proven useful due to generally rapid acquisition times at relatively low cost [2]. However, visible light-based methods can be challenging due to color similarity of many ingredients, and infrared techniques generally suffer from interference with water [3].

In Raman laser spectroscopy a monochromatic light, as from a laser, is targeted at a sample and the inelastic backscattering (stokes scattering) is quantified by measuring the number of photons emitted at a shifted wavelength, expressed in units of intensity. Functional groups in polarizable organic molecules give rise to vibrational modes at specific wavelengths (or Raman) shifts, termed fingerprint regions. With sufficient spatial resolution of the probing laser beam, differentiation of individual food particle components is possible. Purely noncovalent structures such as inorganic salts or metals do not display any Raman scattering and can therefore also be differentiated in mixtures with covalently bonded species.

Of major interest is the ability to generate 2D photos of food systems from Raman spectra, resulting in spatial Raman chemical images or maps in a process termed hyperspectral imaging. In shelf-life tests for instance, this can be augmented to a temporal map by measuring at selected time steps. Commercial 2D wide-field Raman cameras or 1D line probes are often expensive and software for conversion of spectra to images are frequently proprietary, limiting its implementation. Instead, most commonly available Raman systems are zero-dimension (0D) fibre bundle or point probes, meaning a single laser beam is used, necessitating to mechanically displace the probe or sample over the desired probing area. Information extracted from the spectrum at each probed point (or pixel) can then be translated into the corresponding pixel in the reconstructed image at the exact same spatial location. Coupled with an open-source software implementation to reconstruct spectra into maps, a low-cost Raman chemical imaging system can be realised.

A Raman chemical imaging system is presented consisting of a hard- and software component. The setup was an original equipment manufacturer (OEM)-type Raman spectrometer with self-built additions for spatial mapping. Two Matlab-based codes were written for Raman spectra post-processing and chemical image reconstruction. Imaging is enhanced by colour, with generally two main scenarios of colour-coding being of interest. Depending on the purpose, it is suggested to make the distinction between so-called distribution maps and global intensity maps [4]. (i) In distribution maps, the spatial distribution of ingredients, e.g. in a powder mixture is desired. For example to assess mixing homogeneity, each species is encoded in a different color, thereby providing a visual representation of spatial ingredient distribution. It follows that adequate spatial resolution of the image can only be guaranteed if the laser beam probing diameter is less than the particle size. Resolution of the point probe can be calculated from the Rayleigh criterion in which the probing spot follows the point spread function. To avoid convolution, probing points should lie at distances d (m) exceeding

$$d = \frac{0.61\lambda}{NA} \quad 1$$

where λ is the laser wavelength (m) and NA the numerical aperture (unitless) of the focusing lens employed [5]. It should also be noted here that surface roughness, e.g. due to the sample consisting of different particle sizes, contributes to Raman scattering and influences the signal intensity, a phenomenon described by Kubelka and Munk [6] and Schrader and Bergmann [7]. In addition, as colour represents species, representing microscopic concentration of the species at the probing pixel is challenging. (ii) Instead, in global intensity (or concentration) maps, it is often desired to quantitatively monitor the concentration variation of a single species across the area of interest, for which

1 probing diameters larger than the particle size are more suitable as surface roughness is averaged. As less resolution
2 is required, larger samples can be analyzed faster and the species concentration directly represented with a color
3 gradient. It follows that confusion would arise if colour represented different species as well as concentration
4 simultaneously, hence why the distinction between distribution maps and global intensity maps is maintained in this
5 work.

8 **Method details**

10 *Raman spectrometer setup*

12 The Raman spectrometer setup (Fig. 1) consisted of a 532 nm green continuous wave diode laser (LCX, Oxixus
13 S.A., Lannion, France) connected to a fibre bundle point probe (Superhead, Horiba, Longjumeau, France) with
14 exchangeable objective lenses (Epiplan, Zeiss, Jena, Germany) and an integrated video camera for focus. Acquired
15 Raman signal was analysed in a spectrometer (iHR320) with CCD camera (Synapse Plus), controlled via the LabSpec6
16 software (all Horiba, Longjumeau, France). As the probe is a single point probe, a stepper motor driven micrometer
17 stage to displace the food powder sample was integrated (SM 3.25, Märzhäuser, Wetzlar, Germany). The maximum
18 displacement in xyz was 25 mm with a step resolution of 100 nm. The stage was controlled via the Märzhäuser
19 software (Tango Desktop, Märzhäuser, Wetzlar, Germany) that is capable of reading an xyz coordinate list in order to
20 displace the sample over a grid of pre-defined area. In high-precision applications as here, backlash control is crucial.
21 Backlash is the lost motion due to clearance or gaps, in this case due to the lead screw in the micrometer stage.
22 Backlash compensation techniques exist such as using magnetic or optical rulers, zero positioning at a fixed position
23 (e.g. with a laser sensitive photodiode), or unidirectional scanning instead of more efficient serpentine scanning used
24 here. In the present case, backlash control was built-in via the micrometer stage stepper motor controller (Tango
25 desktop, Märzhäuser, Wetzlar, Germany). In previous work using the same setup [1], the same features were observed
26 on repeated scans at the same location, giving confidence in the accuracy of the scanning position in this hardware
27 setup.

28 Depending on acquisition parameters, recording a spectrum usually requires a few seconds. Over a scanning
29 grid of several 100 points, the time requirement rapidly exceeds several hours of experimental time. To automate the
30 repeated signal acquisition and stage movements, Microsoft Power Automate (Microsoft, Redmont, WA, USA) was
31 deployed as a desktop automation tool accessing execution buttons on the LabSpec6 and Märzhäuser software in a
32 pre-defined workflow. The probe and sampling stage were housed in a lightproof box made from black anodized metal
33 panels to prevent signal interference from the environmental light.

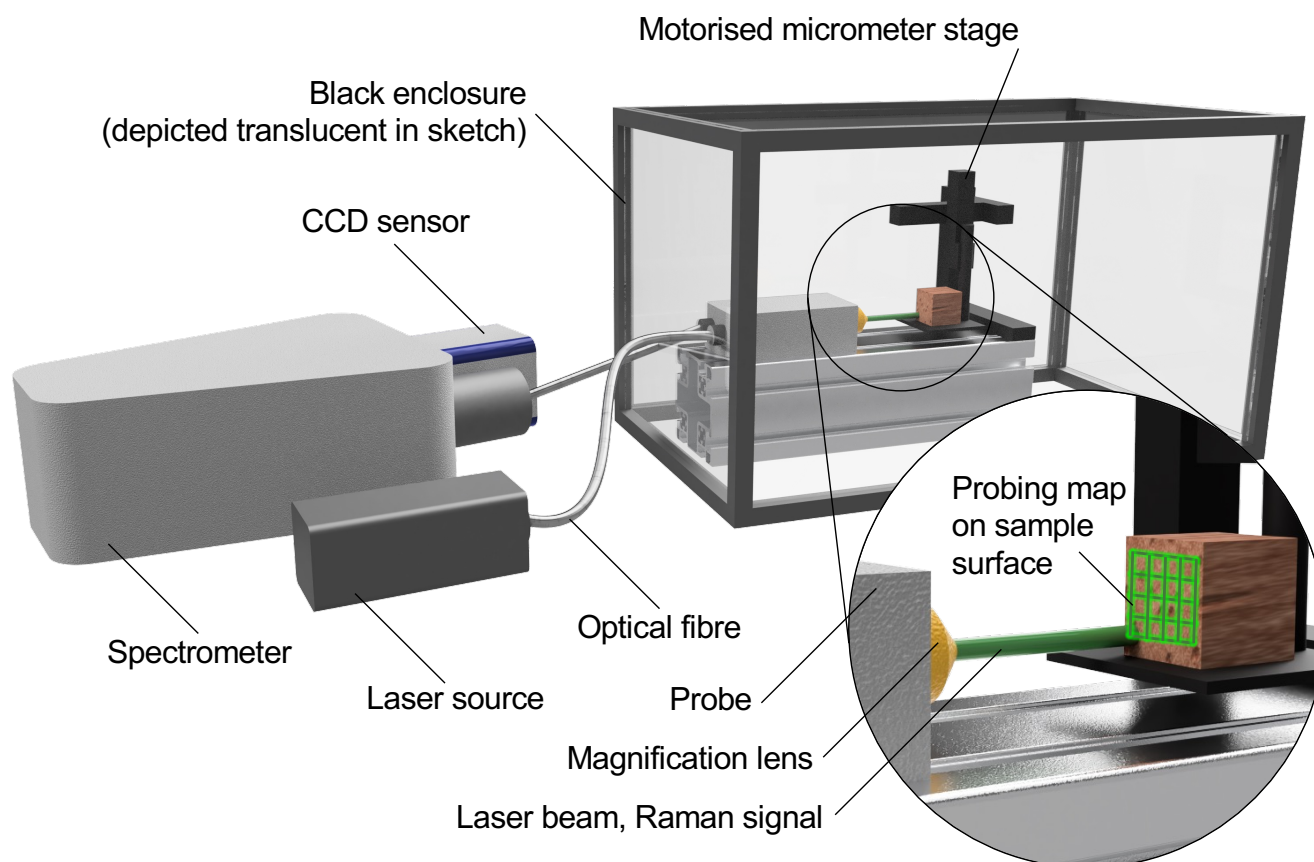


Fig. 1. Raman spectrometer setup for chemical imaging consisting of a laser source, a probe head with magnification lens, motorized micrometer stage with sample holder, spectrometer and CCD sensor.

Program for distribution map Raman chemical imaging

The aim in distribution maps is to identify the species in a mixture at any sampling point or pixel, assign it a color, and reconstruct the scanning map into a colored image displaying the spatial distribution of the different species. A three-component food powder mix consisting of salt, sugar and palm fat is used as an example and was scanned in a map array. At each probing pixel, acquired Raman spectra were stored separately in a tab-delimited .txt file with Raman shift (cm^{-1}) in the first and corresponding Raman intensity values (arbitrary units) in the second column respectively.

First the files are located in the PC using the `folderPath` command, before listing their names with `dir(fullfile(folderPath, '*.txt'))`; `natsortfiles` applies a natural ordering of the file names in sequence of increasing number. This is important in order to analyse the files in the probing order and for correct pixel placement in the reconstructed image. The background scan is loaded and the intensity values selected as the second column in the .txt file with `(:, 2)`. As the sample probing and background were acquired with the same settings, the Raman shift in the background file is used for all samples with `shift=bckgr(:, 1);`. The final image is composed of coloured pixels in the same grid arrangement as the probing pattern, which is preallocated with `map=zeros(height, width)`, where height are the number of pixels in the vertical and width in the horizontal direction.

`fileIndex=1` starts the calculation loops by assigning the first `map` entry the number 1. Thus, the image limits will be from 1 to 61 horizontally, and from 1 to 60 vertically. The choice of one more horizontal pixel has been

made deliberately to ease distinction for the reader between map height and width. During Raman scanning, the most efficient probing pattern is achieved by moving the probe or sample in a meandering S-shaped pattern. In this case, the probing sequence started on the top-left corner, moved across to the right, then down a row, across to the left and so on. By default, Matlab populates arrays from left to right and top to bottom. Hence, the meandering pattern needed to be coded by accounting for odd and even rows. This was achieved by specifying that for odd rows, evaluated by `mod(row,2)==1`, the column indices `colIndices` run left to right (`colIndices = 1:61`), whereas when the rows are otherwise even, `colIndices` run right to left (`colIndices = 61:-1:1`). To stop the entire loop when all files have been analysed, the loop is asked to break once the `fileIndex` outgrows the number of files counted by `length(files)`.

Once the meandering filling pattern for the `map` array is defined, calculations for background removal and baseline corrections are applied. In a new `for` loop, for each `colIndices` the `filePath` is constructed with `filePath=fullfile(folderPath,files(fileIndex).name)` and the data in the file loaded with `raw = data(:,2)`. The raw Raman intensity data is extracted from the second column with `raw=data(:,2)`. To remove signal interference from background radiation, the background intensity extracted earlier in the script is subtracted from the raw Raman signal at the specific scanning point, obtaining the background corrected `bckgr_corr` intensity. As the spectra showed fluorescence, a common approach is to apply a baseline correction by fitting a polynomial [4]. In this case a 4th order fit obtained with `bslin` removed the majority of fluorescence and displayed distinct peaks, yielding the baseline-corrected spectrum `bslin_corr`.

A clean Raman spectrum allows discrimination of species as long as their peaks are not convoluted or overlapping. In this case, a prominent peak for palm fat is in the Raman shift region from 1050 to 1065 cm^{-1} , for which the indices of these shift values are evaluated by `indices=shift>=lower&shift<=upper`, where the lower and upper values are the shift boundaries. The set of baseline-corrected intensity values in this range is then found by `bslin_corrInRange=bslin_corr(indices)`. The palm fat peak in this region is characteristic of the C-C stretch in fatty acids, which neither of the other two components have [8]. As such, if the maximum `max()` of the peak is larger than the noise (estimated at 100 intensity counts), the spectrum in question is palm fat and the pixel can be coloured accordingly. This condition is encoded with an `if` command, assigning a dummy variable of 0 for palm fat in `map`. If this condition was unmet, the peak within the region 1110 to 1135 cm^{-1} is evaluated, characteristic of the C-OH deformation in sucrose and gauche conformation of C-C in fatty acids [9, 10]. This scenario demonstrates a case of overlapping peaks, yet by logic any species not fulfilling the first condition but the second one must be sugar, hence assigning an entry of 1 to `map` to designate sugar. A cutoff value of > 1000 was used to avoid noise. If neither conditions 1 or 2 at peaks were met, the spectrum was considered to be salt due to its absence of Raman scattering, and assigned a variable of 2 in `map`.

The logical species discrimination based on peaks allows the `map` array to be populated for plotting. While plotting the discrete values of 0, 1, and 2 is possible, it was chosen to smooth the `map` for a less abrupt transition between individual species, employing 'cubic' interpolation in x and y, resulting in new coordinates `FineX`, `FineY`, and `FineZ`. The finer coordinate grid was plotted as a surface with `surf`, and the `colormap(jet)` used to encode for the `FineZ` axis. To indicate pure components instead of the dummy variables 0, 1, 2, the colorbar was annotated with palm fat, sugar and salt respectively with the `colorbarHandle`. A square pixel arrangement in the resulting plot is ensured by setting `axis equal`. While `surf` results in 3D plots, it is customary to display Raman chemical images in 2D, for which the view was set to `view(0,90)`. An implementation of the code is shown in the method validation section.

%% Load and prepare files

```

44 folderPath = 'distributionmap_spectra/'; % define folder containing spectra
45 files = dir(fullfile(folderPath, '*.txt')); % get list of all .txt files
46 files = natsortfiles(files); % sort file names in natural order
47 bckgr = load('background_950-1350.txt'); % background spectrum
48 shift = bckgr(:,1); % Raman shift data
49 bckgrI = bckgr(:,2); % background intensity data
50 map = zeros(60, 61); % allocate matrix of map size (60 rows, 61 columns)

```

```

1  %% Calculation loop
2  fileIndex = 1; % initialize index to track current file
3  for row = 1:60
4      if mod(row, 2) == 1 % odd rows: left to right
5          colIndices = 1:61;
6      else % even rows: right to left
7          colIndices = 61:-1:1;
8      end
9      for col = colIndices
10         if fileIndex > length(files) % check if there are more files to process
11             break; % stop if there are no more files
12         end
13         filePath = fullfile(folderPath, files(fileIndex).name); % file path
14         data = load(filePath); % loads spectrum data
15         raw = data(:, 2); % extract the 2nd column
16         bckgr_corr = raw - bckgrI; % background correction
17         bslin = polyfit(shift, bckgr_corr, 4); % fit baseline
18         y = polyval(bslin, shift); % evaluate baseline y's
19         bslin_corr = bckgr_corr - y; % baseline correction
20         indices = shift >= 1050 & shift <= 1065; % 1st range for conditions
21         bslin_corrInRange = bslin_corr(indices); % get values in this range
22         maxValue = max(bslin_corrInRange); % calc. max peak in given range
23         if maxValue > 100 % logic: if maxValue is > 100
24             map(row, col) = 0; % then assign 0 (is palm fat)
25         else
26             indices = shift >= 1110 & shift <= 1135; % 2nd range for conditions
27             bslin_corrInRange = bslin_corr(indices); % get values in this range
28             maxValue = max(bslin_corrInRange); % calc. max peak in given range
29             if maxValue > 1000 % logic: if maxValue is > 1000
30                 map(row, col) = 1; % then assign 1 (is sugar)
31             else
32                 map(row, col) = 2; % then assign 2 (is salt)
33             end
34         end
35         fileIndex = fileIndex + 1;
36     end
37 end
38 %% Smoothing + plotting
39 [x, y] = meshgrid((1:size(map, 2)) * 0.05, (1:size(map, 1)) * 0.05); % meshgrid
40 (mm)
41 scale_factor = 3; % smoothing factor
42 fine_x = linspace(0.05, size(map, 2) * 0.05, size(map, 2) * scale_factor); %
43 fine x
44 fine_y = linspace(0.05, size(map, 1) * 0.05, size(map, 1) * scale_factor); %
45 fine y
46 [FineX, FineY] = meshgrid(fine_x, fine_y); % fine scale on meshgrid
47 FineZ = interp2(x, y, map, FineX, FineY, 'cubic'); % interpolation cubic method
48 figure; % create surface plot
49 h = surf(FineX, FineY, FineZ);
50 colormap(jet); shading interp; view(0, 90); axis equal;
51 colorbarHandle = colorbar;
52 colorbarHandle.Ticks = [0, 1, 2];
53 colorbarHandle.TickLabels = {'palm fat', 'sugar', 'salt'};
54 xlabel('Sample width (mm)'); ylabel('Sample height (mm)');

```

```
xlim([0.05, size(map, 2) * 0.05]); ylim([0.05, size(map, 1) * 0.05]);
```

Program for global intensity Raman chemical imaging

The aim of global intensity maps is to depict the spatial density or concentration distribution of a single species with a colour gradient. Similarly here, the fingerprint region of the species of interest needs to be identified from the acquired spectra at each probing point. The maximum intensity value or area under the intensity curve (integral intensity) can then be correlated to physical species quantity via a calibration equation and the concentration thus represented on the reconstructed coloured map. This time, a two-component food compact consisting of salt and palm kernel T is used as an example and was scanned in a map array.

File loading and preparation followed the same sequence as the distribution map code above. A `sum` array is allocated to store the integral intensity of the species in the calculation loop. As previously, the acquired raw spectra are background corrected with `data=data-bckgr`. As in the present case the sample consisted of only salt and palm kernel fat, the integral intensity under the entire fat curve is used by subtracting an average salt signal `data=data-salt_avg`. The area under the remaining palm kernel fat signal is numerically calculated with the `trapz` trapezoidal method according to [11]

$$I = \int_a^b i(\omega) d\omega \approx \frac{1}{2} \sum_{n=1}^N (\omega_{n+1} - \omega_n) [i(\omega_n) + i(\omega_{n+1})] \quad 2$$

where I is the integral intensity (au), i is the intensity (au) at each Raman shift ω (cm^{-1}), and $a = \omega_1 < \omega_2 < \dots < \omega_N < \omega_{N+1} = b$, and $(\omega_{n+1} - \omega_n)$ is the spacing between each consecutive Raman shift interval. This step is carried out for each probing point of the map and the results stored in the `sum` array. To relate Raman intensity to physical concentration c of palm kernel fat on the probing surface, a least squares regression calibration curve was constructed with equation

$$I = 9.1062 \times 10^6 c \quad 3$$

which is implemented via `conc = sums/9.1062E+6`.

Now the physical concentration profile needs to be overlaid onto the sampling map, which followed the same S-shaped meandering probing pattern as in the distribution map above. To do this, the `coordinates` array is populated with `x` and `y` coordinates of the probing pattern, achieved by filling rows in the meandering pattern. `coordinates` and `sums` are then concatenated in the `map` array. To achieve a smoother surface of the final global concentration image, the mapping grid is divided into a finer `meshgrid` and a natural interpolation method applied. The finer data was then plotted as a surface with the `colormap('jet')` representing the `z` values, or palm kernel fat concentration. Equal distance between tick marks and hence square pixel size is ensured with `axis equal`. An implementation of the code is shown in the method validation section.

%% Load and prepare files

```
folderPath = 'globalintensitymap_spectra/'; % define folder containing files
files = dir(fullfile(folderPath, '*.txt')); % get list of all .txt files
files = natsortfiles(files); % sort file names in natural order
bckgr = load('background_0-4000.txt'); % background spectrum
bckgr = bckgr(:,2); % background intensity data
salt_avg = load('salt_average_0-4000.txt'); % average salt spectrum
salt_avg = salt_avg(:,2); % average salt spectrum intensity data
number_of_files = numel(files); % get number of files
```

```

1 sums = []; % allocate array to store sums
2 %% Calculation loop
3 for i = 1:number_of_files % loop through each file
4     data = load(fullfile(files(i).folder, files(i).name)); % load as matrix
5     data = data-bckgr; % background correction
6     data = data-salt_avg; % salt signal subtraction
7     area = trapz(data(:, 1), data(:, 2)); % calc. area under curve using trapz
8     sums = [sums; area]; % append result to sums array
9 end
10 conc = sums/9.1062E+6; % calibration curve
11 rows = 11; % number of vertical probe points 11
12 cols = 12; % number of horizontal probe points 12
13 x = zeros(rows * cols, 1); % initialize array for x
14 y = zeros(rows * cols, 1); % initialize array for y
15 index = 1;
16 for j = 1:rows
17     if mod(j, 2) == 1 % odd row: left to right
18         for k = 1:cols
19             x(index) = k-1;
20             y(index) = j-1;
21             index = index + 1;
22         end
23     else
24         for k = cols:-1:1 % even row: right to left
25             x(index) = k-1;
26             y(index) = j-1;
27             index = index + 1;
28         end
29     end
30 end
31 %% Smoothing + plotting
32 coordinates = [x, y]; % combine x and y into a single array
33 map = [coordinates conc]; % combine map with coordinates in single array
34 x = map(:, 1); % extract plotting data from map array
35 y = map(:, 2);
36 z = map(:, 3);
37 [X, Y] = meshgrid(unique(x), unique(y)); % create a meshgrid for x and y
38 fine_x = linspace(min(x), max(x), 500); fine_y = linspace(min(y), max(y), 500);
39 % fine
40 [FineX, FineY] = meshgrid(fine_x, fine_y); % Interpolate the 'z' data onto
41 finer grid
42 FineZnatural = griddata(x, y, z, FineX, FineY, 'natural'); % 'natural'
43 interpolation
44 figure;
45 h = surf(FineX, FineY, FineZnatural); % surface plot
46 colormap('jet'); shading interp; view(0,90);
47 lims = clim; clim manual; clim([0 7]); xlim([0 11]); ylim([0 10]);
48 axis equal; grid off;
49 xlabel('Map width (mm)'); ylabel('Map height (mm)'); yticks(0:2:12);
50
51
52
53

```

1 Method validation

2
3 Both case studies in the previous section are exemplified with acquired experimental data.

4 *Distribution map Raman chemical imaging*

5
6
7 The aim in distribution maps is to identify the component in a mixture at any sampling point, assign it a color, and reconstruct the scanning map into a colored image displaying the spatial distribution of the different species. Fig. 8
9 2 shows the sequential methodology applied to a typical three-component food powder mix consisting of 25 w/w% salt (Josal, Südwestdeutsche Salzwerke, Heilbronn, Germany), 70 w/w% sugar (Cuisine Noblesse, Offenburg, Germany) and 5 w/w% palm fat (Ertilor PK 40 SG, Fuji Oil, Osaka, Japan), each species having been sieved to 425-600 μm (Retsch, Haan, Germany). The powder mix was gently pressed into a Raman inactive aluminium sample holder onto the micrometer stage. As the aim was to locate species bearing diameters of 500 μm , a resolution of 1/10th of this size, 50
10 μm , was chosen for sufficient spatial detail, setting the micrometer stage step size of 50 μm in the coordinate list. The
11 laser beam was focused with a 20x lens with numerical aperture 0.4 (Epiplan, Zeiss, Jena, Germany), resulting in a
12 probing point resolution of $d = 0.81 \mu\text{m}$ according to the Rayleigh criterion (equation 1). As d is less than 50 μm , there
13 is no risk of overlapping probing points. The resulting array of 61 \times 60 points resulted in a 3.05 \times 3 mm² map (Fig. 2a).
14 The choice of one more horizontal pixel has been made deliberately to ease the distinction between map height and
15 width for the reader. For efficient mapping, a meandering S-shaped pattern was constructed starting on the top-left
16 corner, moving across to the right, then down a row, across to the left and so on.

17
18 During Raman scanning on the sample surface (Fig. 2b), laser power was set to 100 mW, exposure time to 1
19 second with single accumulation, achieving sufficient signal-to-noise ratio while minimizing risk of sample degradation
20 at higher power and longer exposure. A full Raman shift range scan, background and baseline corrected, from 0-4000
21 cm^{-1} on the pure components salt, sugar and palm fat yielded a shorter bandwidth of interest from only 950-1350
22 cm^{-1} (Fig. 2 c). Raman scanning of the powder mix sample was thus performed on the shorter bandwidth allowing time
23 reduction to approximately 10 s for signal acquisition and stage movement to the consecutive probing pixel. As the
24 time requirement amounted to 61 \times 60 \times 10 s = 10.2 h, Microsoft power automate was used to iteratively access
25 scanning and displacement buttons on the LabSpec6 and TangoDesktop control software. Acquired spectra were
26 automatically saved in tab-delimited .txt files and exported for processing with the Matlab distribution-map.m code
27 described above. An exemplary background scan and three other typical sample scans from the powder mix identified
28 as salt, sugar and palm fat, are shown in Fig. 2d.

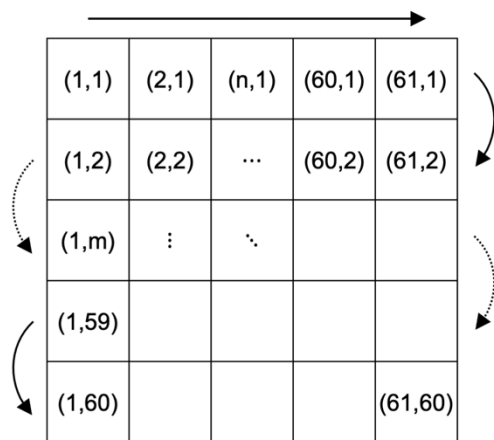
29
30 The Matlab script applies a background correction by subtracting the background spectrum from the sample
31 spectrum at each probing point, shifting the spectra somewhat lower on the intensity scale. Another reason for
32 spectrum correction is fluorescence. Both Stokes Raman scattering and fluorescence results in emission induced by
33 incident radiation. While Raman scattering is the excitation of a molecule to a virtual state and relaxation to an energy
34 level higher than the ground state, fluorescence is the excitation of a molecule to a higher energy level than for Raman,
35 and relaxation to the ground state. This larger magnitude relaxation results in a higher intensity photon emission than
36 a Raman photon, hence fluorescence is often matching or even masking Raman spectra and is henceforth undesired.
37 The extent of fluorescence emission is dependent on the incident light energy. As energy and wavelength are inversely
38 related to each other, low wavelength lasers such as green 532 nm generally result in large extents of fluorescence
39 emission. Long wavelength, lower energy lasers such as red 785 nm lasers generally exhibit less fluorescence, as the
40 excitation is lower, albeit also generating weaker Raman emissions. It is often desirable to mathematically subtract
41 fluorescence from spectra by baseline correction.

42
43 A multitude of baseline correction methods from simple polynomial fitting to sophisticated iterative methods
44 have been suggested [4], with a 4th order polynomial regression successfully removing fluorescence in the present
45 case. The three exemplary background corrected and baseline corrected sample spectra (dotted lines) are plotted
46 together with the pure species spectra (continuous lines) for comparison, showing that the exemplary sample spectra
47 from the powder mix are either salt, sugar or palm fat (Fig. 2e).

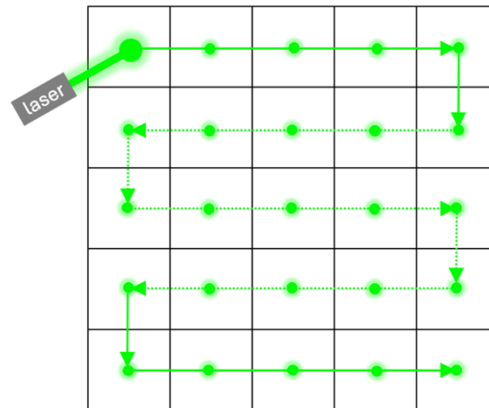
48
49 Discrimination of the species being probed in a given pixel in the map could now be performed by logical
50 conditions, given the peaks for the two organic components occurred at different locations, and that salt showed

1 unpronounced peaks. As a first condition, if a peak occurred within the band $1050\text{-}1065\text{ cm}^{-1}$ the species was palm
2 fat, as this vibrational mode is attributed to the C-C stretching in fatty acids, which neither occurs in sugar nor salt [8].
3 If this first condition was unmet, a different peak was selected, such as in the band $1110\text{-}1135\text{ cm}^{-1}$, characteristic of
4 the C-OH deformation in sucrose and gauche conformation of C-C in lity acids [9, 10]. Despite the overlapping fat and
5 sugar spectra, the discrimination is now only between sugar with a large peak, and salt with a shallow peak attributed
6 to noise, palm fat or sugar traces on the salt particle. A cutoff value of 1000 intensity counts was chosen to distinguish
7 between the two. The selected species at each probing point was stored in an array in the Matlab script, which was
8 used to reconstruct a 2D distribution map (Fig. 2f) of the three species, assigning the colours red to salt, green to sugar,
9 and blue to palm fat. Over the scanned area of 9.15 mm^2 , the distribution map allows visualization of the species
10 location, showing discrete clusters of palm fat and sugar particles in a continuous matrix of sugar as the major
11 component in the formulation, approximately in line with the formulation composition.

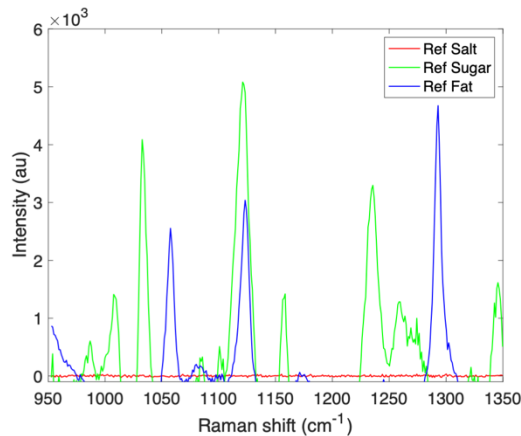
a) Coordinate list



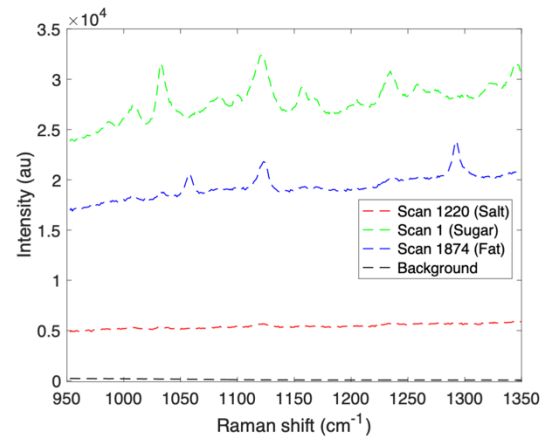
b) Probing map on sample



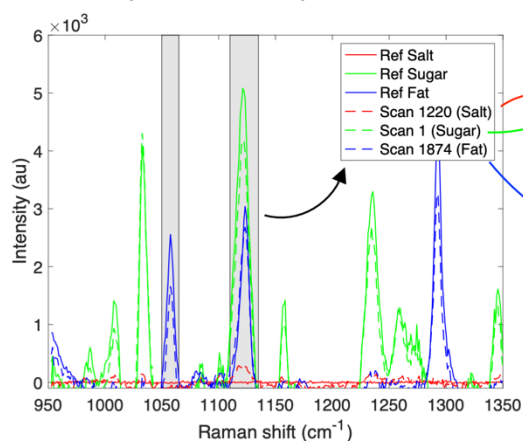
c) Pure species reference spectra



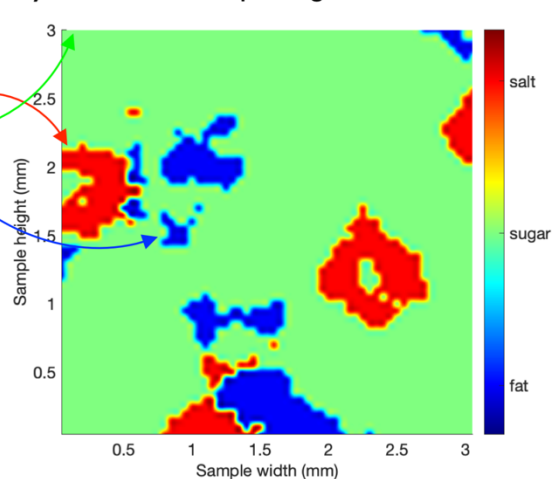
d) Exemplary acquired sample spectra



e) Peak comparison and species identification



f) Distribution map image reconstruction



1
2 **Fig. 2.** Methodology for generation of distribution maps Raman chemical images from point probes: a) Coordinate
3 pixel list of the mapping array, b) Raman spectra acquisition at each pixel on predefined map array, c) background
4 corrected and 4th order polynomial baseline corrected pure species reference spectra, d) raw acquired exemplary
5 background and sample spectra, e) background corrected and baseline corrected sample spectra plotted with
6 reference spectra for species identification, f) probing pixels were coloured with specie-specific colour, resulting in the
7 distribution map.

1 Global intensity Raman chemical imaging

2
3 The aim of global intensity maps is to measure the spatial density or concentration distribution of a single
4 species and reconstruct the scanning map into a coloured image where the colour represents physical concentration.
5 Fig. 3 shows the sequential methodology applied to a typical two-component food powder mix consisting of 95 w/w%
6 salt (Josal, Südwestdeutsche Salzwerke, Heilbronn, Germany) and 5 w/w% palm kernel fat (Isega, Aschaffenburg,
7 Germany). The salt was sieved to 425-600 μm (Retsch, Haan, Germany), mixed with palm kernel fat, and pressed into
8 a 4 g cubic compact in a universal testing machine (3367, Instron, Norwood, MA, US) before being placed on a sheet
9 of wicking paper (3MM CHR, Whatman, Marlborough, MA) for one week shelf life testing at 30°C/40%RH to mimic a
10 typical food body undergoing oil migration into wrapper packaging material. The aim was to visualize the special palm
11 kernel fat distribution after one week over the side-surface of the sample body.

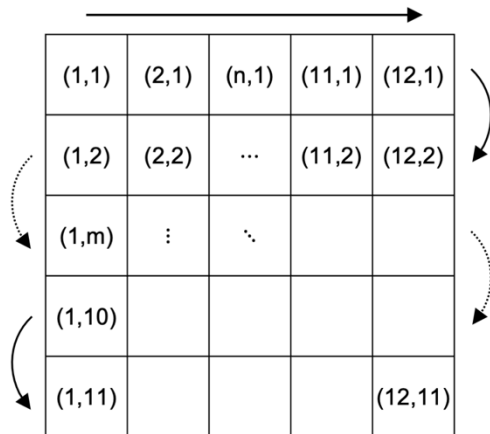
12 As global concentration was required, resolution is less dependent on microscopic particle size of the powder
13 substrate, but rather on the spatial resolution desired over the macroscopic sample area. A 2x magnification lens with
14 numerical aperture 0.19 was used resulting in a minimum required displacement greater than resolution $d = 1.7 \mu\text{m}$
15 according to the Rayleigh criterion equation 1. 12 x 11 steps in increments of 1 mm were chosen in the coordinate list,
16 sampling an area of 11 x 10 mm^2 on the food sample (Fig 3a).

17 During Raman scanning on the sample surface (Fig. 3 b), laser power was set to 100 mW, exposure time to 1
18 second with single accumulation, achieving sufficient signal-to-noise ratio while minimizing risk of sample degradation
19 at higher power and longer exposure. As in global intensity or concentration maps only the single species palm kernel
20 fat was measured, which showed a larger Raman activity than salt, no specific peak selection at certain bands was
21 required as in distribution mapping. In addition, the relationship between intensity and physical palm kernel fat was
22 not established on maximum peak height, which is susceptible to sensor spikes and outliers, but on integral intensity,
23 measured as the area under the intensity curve. The integral intensity of the full spectrum at each probe point was
24 hence evaluated at a broad bandwidth between 0-4000 cm^{-1} , shown in Fig 3c with the background signal, the average
25 background-corrected salt, and an exemplary palm kernel fat signal. To obtain the fat signal only, the Matlab script
26 subtracted the background and an average salt signal from the signal at each probe point, as well as performing
27 baseline correction with a 6th order polynomial.

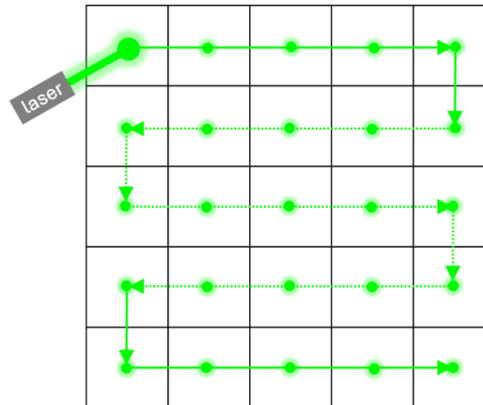
28 To correlate global Raman integral intensity to physical palm kernel fat concentration on the food surface, a
29 5-point linear calibration curve was constructed by preparing and scanning 5 samples at 0, 1.25, 2.5, 3.75 and 5 w/w%
30 palm kernel fat over the same map area, depicted as intensity plots in Fig. 3d. Constructing calibration curves from a
31 sample area with many probe points instead of a single measurement is especially important in particulate samples,
32 where sample heterogeneity can be significant, and thus can be averaged by spatially distributing the measurements.
33 To avoid bias from outliers, it is suggested to evaluate median as opposed to mean integral intensity at each pixel [4],
34 which was correlated to calibration sample palm kernel fat concentration by linear regression with R^2 value of 0.98
35 and gradient $9.1062 \times 10^6 \text{ au/w/w\%}$ (Fig. 3e). The large errors bars represent in-sample standard deviation and
36 reflect the heterogenous nature of liquid media distribution in particle systems, as in the present case of palm kernel
37 fat with salt.

38 The calibration curve encoded in the Matlab script converted integral intensity into concentration between
39 the minimum and maximum concentration detected in the map. A conventional linear colour map with 0 w/w% palm
40 kernel fat set as blue, and 7 w/w% set as red was used to reconstruct the map into a continuous colour gradient (Fig.
41 3f). As can be seen from the visual representation of the food body surface after one week shelf life testing, palm
42 kernel fat concentration varied from top to bottom, with concentrations in the top third between 1-2 w/w%, increasing
43 to 4-6 w/w% in the bottom third, with local hotspots of up to 7 w/w% palm kernel fat.

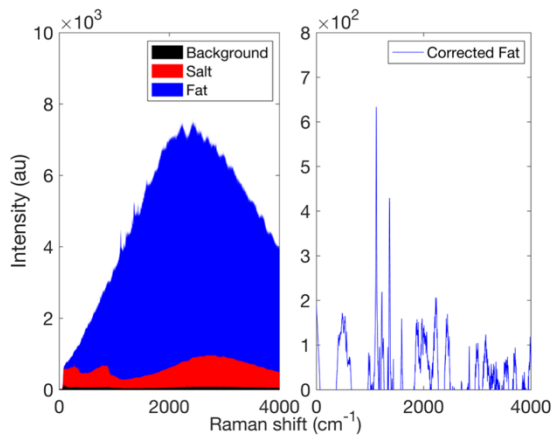
a) Coordinate list



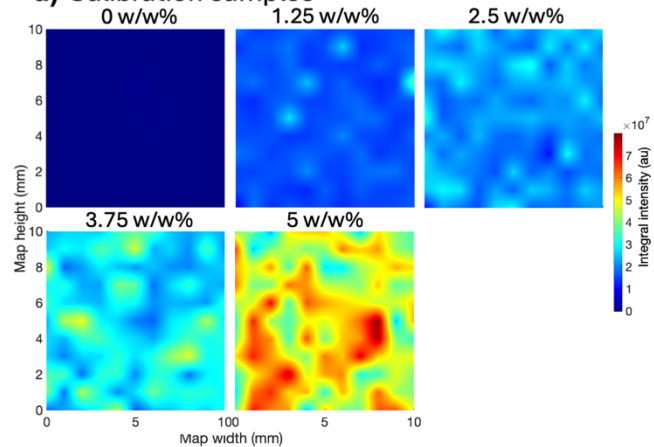
b) Probing map on sample



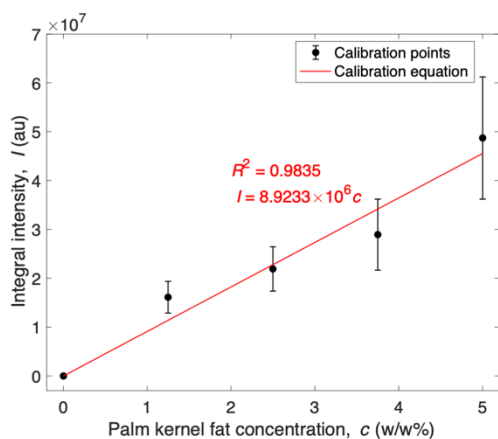
c) Integral intensity of acquired spectra



d) Calibration samples



e) Calibration curve



f) Global concentration image reconstruction

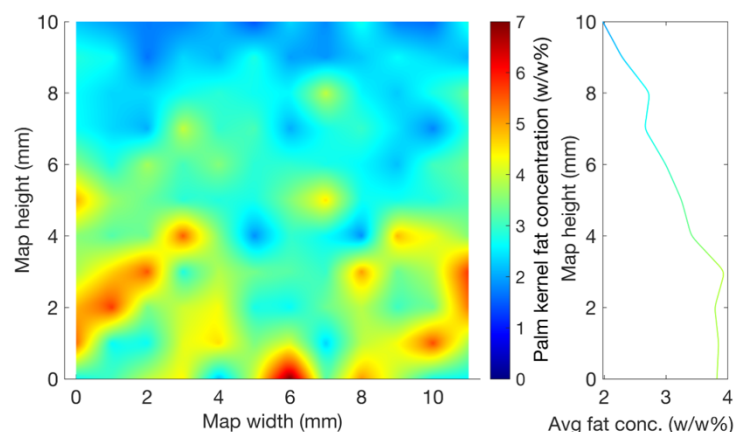


Fig. 3. Methodology for generation of global intensity maps Raman chemical images from point probes: a) Coordinate pixel list of the mapping array, b) Raman spectra acquisition at each pixel on predefined map array, c) integral intensity of acquired palm kernel fat spectra evaluated as the area under the curve, corrected for background and salt and the fluorescence via 6th-order polynomial baseline correction, d) chemical images of the calibration samples acquired under the same conditions, e) least squares regression calibration curve correlating palm kernel fat concentration with integral Raman intensity, f) palm kernel fat concentration at each pixel is represented with linear colour gradient between 0 w/w% (blue) and 7 w/w% (red).

1 Limitations

2 The nature of Raman vibrational spectroscopy limits this technique to Raman active species, or to some extent to
3 differentiate between Raman inactive and active species. A limit on the maximum achievable resolution is the
4 maximum magnification of the lens on the probe head, usually commercially available up to 150 \times , and the smallest
5 step displacement of the motorized stage, in the present case 100 nm. Discretization of species is simplest for non-
6 overlapping or convoluted spectra, and under the condition that fluorescence can be corrected by baselining. Finally,
7 a 785 nm or 830 nm laser would have been more appropriate than the 532 nm laser used in this work, as longer
8 wavelength lasers generally strike a better balance between minimizing fluorescence due to less incident energy, yet
9 producing strong Raman signals.

11 Abbreviations

12 OD – zero dimensional (point)
13 1D – one dimensional (line)
14 2D – two dimensional (area)
15 3D – three dimensional (volume)
16 au – arbitrary unit
17 CCD – charge-coupled device
18 OEM – original equipment manufacturer
19 RH – Relative humidity (%)
20 w/w% – weight per weight %

22 Symbols

23 d – laser resolution (m)
24 λ – laser wavelength (m)
25 NA – numerical aperture of objective (-)
26 I – signal intensity (au)
27 c – fat concentration (w/w%)

29 CRediT author statement

30 **Luc Dewulf:** Conceptualization, Methodology, Software, Validation, Formal analysis, Investigation, Data Curation,
31 Writing - Original Draft, Writing - Review & Editing, Visualization. **Michael K. Hausmann:** Writing - Review &
32 Editing, Supervision. **Annabel Bozon:** Writing - Review & Editing, Supervision. **Gerhard Niederreiter:** Supervision,
33 Funding acquisition. **Agba D. Salman:** Writing - Review & Editing, Supervision, Funding acquisition.

35 Acknowledgments

36 The author thanks EPSRC (grant 2602203) and Nestlé for funding this research. The iForge makerspace and Open
37 Access Mechanical Workshop were gratefully used workshop facilities for building the hardware setup. The School
38 workshop technicians Andy Patrick, Oz McFarlane, Usman Younis, Adrian Lumby, Mario Dorna, Richard Stockley and
39 Vinnie Walsh are sincerely thanked for troubleshooting during setup of the Raman system.

41 Declaration of interests

42 The authors declare that they have no known competing financial interests or personal relationships that could
43 have appeared to influence the work reported in this paper.

44 The authors declare the following financial interests/personal relationships which may be considered as potential
45 competing interests:

48 Supplementary material *and/or* additional information

1 As this thesis was written in publication format, the supplementary data would be made available at the publication
2 step. As this article is not published yet, but for the convenience of the reader, the supplementary material was
3 uploaded on the University of Sheffield google drive at this link. The utilisation of the supplementary material was
4 described in the chapter and is described in README files.

5 https://drive.google.com/drive/folders/1YiOYJwegscpEJ-S950IJSqYjKssjmXMN?usp=share_link

7 References

- 8 [1] L. Dewulf, M.K. Hausmann, A. Bozon, G. Niederreiter, S. Palzer, A.D. Salman, Food vs packaging: dynamics of oil
9 migration from particle systems into fibrous material, *Powder Technology*, 439 (2024) 119721.
10 [2] L. Dewulf, M.K. Hausmann, A. Bozon, G. Niederreiter, S. Palzer, A.D. Salman, Particle-based food systems subject
11 to lipid migration – A review of measurement, modelling, and mitigation approaches, *Powder Technology*, 445 (2024)
12 120097.
13 [3] A.K. Shukla, *Spectroscopic Tools for Food Analysis*, IOP Publishing, Bristol, 2019.
14 [4] H.W.S. Reiner Salzer, *Infrared and Raman Spectroscopic Imaging*, Wiley-VCH, Heidelberg, 2014.
15 [5] A.-S. Jääskeläinen, L. Galvis Rojas, C.G. Bertinetto, Localization of Cereal Grain Components by Vibrational
16 Microscopy and Chemometric Analysis, in: N. Sozer (Ed.) *Imaging Technologies and Data Processing for Food*
17 *Engineers*, Springer International Publishing, Cham, 2016, pp. 41-68.
18 [6] P. Kubelka, F. Munk, Ein Beitrag Zur Optik Der Farbanstriche, *Zeitung für Technische Physik*, 12 (1931) 593-601.
19 [7] B. Schrader, G. Bergmann, Die Intensität des Ramanspektrums polykristalliner Substanzen, *Fresenius' Zeitschrift*
20 *für analytische Chemie*, 225 (1967) 230-247.
21 [8] R.M. El-Abassy, P.J. Eravuchira, P. Donfack, B. von der Kammer, A. Materny, Fast determination of milk fat content
22 using Raman spectroscopy, *Vibrational Spectroscopy*, 56 (2011) 3-8.
23 [9] R. Goodacre, B.S. Radovic, E. Anklam, Progress toward the Rapid Nondestructive Assessment of the Floral Origin of
24 European Honey Using Dispersive Raman Spectroscopy, *Applied Spectroscopy*, 56 (2002) 521-527.
25 [10] S. Gallier, K.C. Gordon, R. Jiménez-Flores, D.W. Everett, Composition of bovine milk fat globules by confocal Raman
26 microscopy, *International Dairy Journal*, 21 (2011) 402-412.
27 [11] The MathWorks Inc., *Trapz: trapezoidal numerical integration*, Matlab Documentation, Natick, MA, USA, 2024.

Chapter 4

Mitigation Strategy



Food vs packaging: Dynamics of oil migration from particle systems into fibrous material

Luc Dewulf^{a,*}, Michael K. Hausmann^b, Annabel Bozon^c, Gerhard Niederreiter^b, Stefan Palzer^b, Agba D. Salman^a

^a Department of Chemical and Biological Engineering, University of Sheffield, Mappin Street, Sheffield S1 3JD, United Kingdom

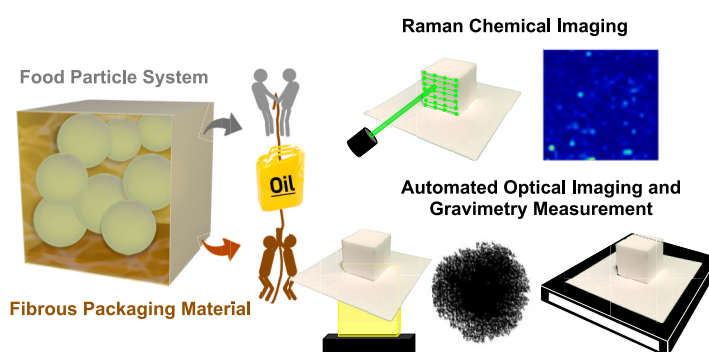
^b Nestlé Research, 1000 Lausanne, Switzerland

^c Nestlé Product Technology Centre, Lange Straße 21, 78221 Singen, Germany

HIGHLIGHTS

- Particle size reduction from 500 to 50 μm made stronger capillarity in particle system.
- Undesired oil-release into paper packaging was essentially stopped to 0%.
- Raman chemical imaging (RCI) was successfully used first-time for oil quantification.
- Optical oil stain quantification on paper was automated for fast result acquisition.
- Larger particle system leaked 50% of oil into packaging, smaller particle system 0%.

GRAPHICAL ABSTRACT



ARTICLE INFO

Keywords:

Particle and fibre packaging systems
Quantitative Raman laser chemical imaging
Oil migration
Oil release
De-oiling

ABSTRACT

Paper packaging for compacted or tableted foods is seen as a key sustainable packaging of the future. Yet its fibrous structure is susceptible to absorb oils, fats, greases and other small molecules from the contacting food. Underlying phenomena associated with oil release from compacted food on fibre-based packaging, such as viscous liquid flow, capillarity, and gravity from compacted particle systems into fibre networks are not fully understood yet. As such, oil stain mitigation on packaging remains a challenge. Using model food tablets of 95% 500 and 50 μm particle size with 5% sunflower oil as the liquid phase, this work employed for the first-time quantitative Raman spectroscopic chemical imaging (RCI) coupled with automated image quantification for comparison of oil flow dynamics between food compacts and contacting paper packaging. The extent of de-oiling from the compact and imbibed into paper showed similar exponential decay with time for both porous systems. For the first time, oil migration dynamics on the food compact surface was 2D visualised via Raman spectroscopy and showed markedly different trends with varying environment climatic conditions and compact microstructure. The larger particle system leaked up to 50% of oil into paper, whereas the 50 μm system retained 100% of its oil, creating an effective internal oil barrier. This novel technique opens the way for further understanding liquid transfer between porous food media and harnessing microstructure engineering to increase food and packaging performance.

* Corresponding author.

E-mail address: ldewulf1@sheffield.ac.uk (L. Dewulf).

<https://doi.org/10.1016/j.powtec.2024.119721>

Received 29 November 2023; Received in revised form 24 March 2024; Accepted 28 March 2024

Available online 29 March 2024

0032-5910/© 2024 The Authors. Published by Elsevier B.V. This is an open access article under the CC BY license (<http://creativecommons.org/licenses/by/4.0/>).

1. Introduction

Pressured by changing consumer behaviour, fast moving packaged goods companies around the world pledge to become more environmentally sustainable by reducing conventional packaging, especially plastic and metal [1]. Due to its comparatively high tensile strength, paper is currently used to reinforce multilayer sandwich packaging, with plastic or metal layers to provide necessary barriers against small molecules migration. However, the absence of moisture or oxygen barrier properties of paper limit its use in the food sector to products that are less susceptible to environmental conditions. Paper packaging enjoys high consumer acceptance due to its biodegradability, potential carbon neutral sourcing, and psychological effects related to haptics and optics [2]. Yet, a significant disadvantage of paper or indeed of any other fibrous food-contact material is its propensity to absorb mobile substances from the food, such as oils, fats, and greases [3]. With increasing employment of paper as a food-contact wrapping material, attempts to understand, model, and control oil and fat migration from food to packaging is timely and relevant.

Food systems in powder, granular, tableted, or compacted form and fibrous packaging materials resemble each other in the sense that both are porous media in contact with each other, and thus fundamental phenomena apply to both systems. A food system (such as a seasoning compact) comprising particulate ingredients and a liquid component (such as oil) in contact with a fibrous packaging material (such as paper) undergoes a transport phenomenon whereby the mobile substance transfers from the food into the paper, which is often referred to as oil release [4], oil migration [5], or de-oiling, where the three are used synonymously. Regarding oil release, the commonality is thus that the particle-based food system and fibre network packaging are both stationary porous media with oil migrating from one porous phase to the adjacent.

Literature makes proof of considerable work having been conducted on liquid transport into porous material. Washburn pioneered the explanation of liquid transport into porous beds via capillary suction formulating the Washburn Eq. [6]. The work was then extended from powder systems to other porous structures, such as fibrous media like fabric or paper, which have been well reviewed [7–9]. Relating to packaged consumer foods, the process of oil imbibition into paper via wetting and capillary suction is therefore fundamentally rather well understood.

On the other hand, considerably less work has been conducted on liquid flow out of porous media or between porous phases. Literature shows that the flow of liquid out of particle systems shows time-dependent behaviour, affected by liquid saturation, capillarity, and gravity, as was demonstrated for the case of glass spheres in a packed bed [10]. In their study, the amount of liquid holdup within the bed was measured during natural gravity drainage. The amount of liquid retained was larger in a capillary dominated regime, and thus the liquid outflow was larger in a gravity-dominated regime.

From the literature on liquid flow processes in porous and fibrous bodies it can be summarised that the extent of liquid phase transfer between bodies depends on gravity, viscous flow, and capillarity effects in both particle and fibre system, schematically summarised in Fig. 1. During imbibition, diffusion is rather considered a slow process occurring after capillary suction [11] and therefore unlikely to play a role in immediate oil imbibition into paper, although in long-term food shelf-life tests disagreement still exists over which processes dominate [5].

Real food compacts are wrapped in packaging from all sides with potential contact between food and paper on all faces. For experimentation however, simplification into a 1D system is appropriate and confines the oil flow direction to the vertical, either up or down akin to a tug competition for oil between food and paper. Attraction due to the earth's gravitational acceleration always acts as a downwards force, in the current setup favouring imbibition into paper. Pressure drop due to viscous laminar flow is theoretically present in both porous materials,

but is more pronounced in food as the smaller pore size in paper can overcome the viscous pressure loss. For a basic pipe flow geometry, this can be modelled with the Hagen-Poiseuille Eq. [12]. In the competition for oil, a larger viscous flow resistance would result in a prolonged retention of oil in the food structure. While viscous effects act as a resistance to oil flow, capillarity is the driving force in porous media, stemming from the pressure drop across the meniscus in the solid-liquid-gas region, calculated for a simple capillary geometry from the Laplace-Young Eq. [13]. Depending on the relative magnitude of the resulting capillary forces, the oil will be drawn into the paper or possibly retained in the food.

In order to better understand this dynamic behaviour of liquid outflow from porous material, it becomes clear that sophisticated experimental methods are required. Recently, advanced imaging, non-invasive and non-destructive techniques for particle system microstructure have been developed [14]. Microscopic techniques have rapid acquisition times, but capture processes on the sample surface, while tomographic methods reach the internal structure but suffer from acquisition times possibly much longer than the timescales of the transport processes within the sample. A potentially powerful analysis method yet underutilised for liquid-particle systems is Raman laser spectroscopy. Raman spectroscopy is a spectroscopic technique in which a monochromatic light, e.g., from a laser, is shone on a sample and the inelastic backscattering (Stokes scattering) is quantified by measuring the number of photons excited or absorbed, expressed as intensity. For a sample to exhibit a Raman effect, the molecule must be polarisable, which is overwhelmingly the case in covalently bonded samples such as in most organics, but not in purely ionic species without shared electrons. As such, Raman spectroscopy is suitable to monitor temporal and spatial behaviour of an organic phase migrating through an inorganic phase.

Raman-based techniques have been used widely across the food science domain for analytical purposes of food safety and authenticity control [15–17]. In these cases, measurements at a single point in location and time of the bulk material is often sufficient. Much less reported in the food sector is quantitative Raman chemical or hyperspectral imaging (RCI) or mapping. Few previous examples exist, such as RCI to map the distribution of nutrients in fruit and vegetables [18] and of different tissues in meat [19] and other frozen foods [20]. For food powder systems, mixing efficiency of corn-flour and icing sugar was evaluated via RCI [21]. Application of RCI techniques in tablets and compacts has only been reported for pharmaceutical tablets, not yet in the food domain. In pharma, main objectives were spatial mapping of active pharmaceutical ingredient distribution [22,23], disintegrant

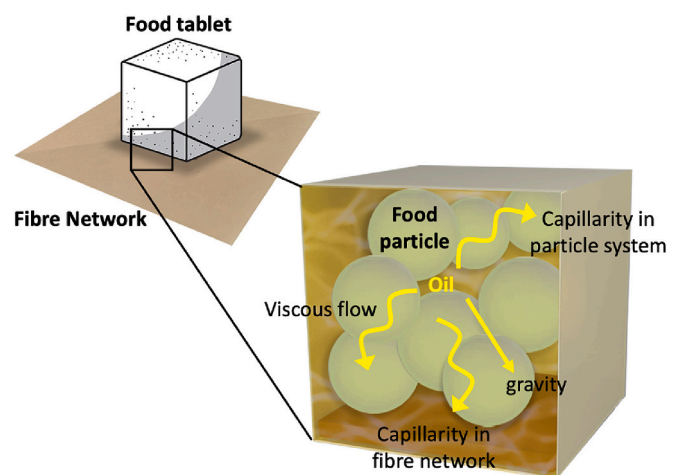


Fig. 1. Schematic of different drive (fibre capillarity, gravity) and resistance (food capillarity, viscosity) processes occurring during oil release from particle food systems to fibre-based packaging.

[24,25], and impurities [26], or the differentiation between polymorphs [27,28]. The common difficulty in Raman scanning of irregular surfaces was addressed in a study on convex tablets [29], and coverage of tablet coating [30]. Yet, as in previous studies, all systems were solid-phase and static, whereby RCI of dynamic liquid-solid systems have been unreported in food and pharma. For such systems, few examples exist such as in two-component liquid mixing in aerospace flows [31], or the coupling of RCI with seed particles for particle image velocimetry [32–34]. However, the application of RCI for profiling fluid transport in particle-based compacted food systems remains unreported.

Similar to particle-bed systems, imbibition of liquid into fibrous material such as paper has been shown to be a dynamic time-dependent system. While due to the small interstitial pore size between fibres the flow regimes are more influenced by capillarity than gravity, the finite medium thickness (i.e. paper thickness) and sheet size, as well as fibre swelling results in an unsteady system (i.e. non-constant with time) [35]. Previous work aiming to establish the dynamics of oil imbibition into paper, on a fundamental level [36,37] or specifically for food packaging [38], used photographic oil stain measurements, that are still often evaluated manually. In addition, oleogels were used and as such reports of the interaction between particulate systems in contact with fibrous material remain little reported.

Conclusively, while work on the individual processes and the resulting dynamic behaviour for liquid transport into porous bodies has been reported previously, the complexity of mass transfer between two porous bodies, specifically between particulate food systems and fibrous packaging is less well described in literature. This work will contribute towards a better understanding of the dynamic behaviour of liquid migration between particulate food powder systems and fibrous packaging, ultimately aiming to control this unwanted phenomenon in the consumer foods industry. Raman laser spectroscopy is applied for the first time to evaluate dynamic liquid flow distribution in particle systems, and self-written automated imaging software is used for evaluation oil flow dynamics in fibre networks.

2. Materials and methods

To model a typical food system prone to de-oiling, a model food compact was created using 95 w/w% table salt and 5 w/w% sunflower oil manually mixed in 100 g portions a beaker by adding first the salt and then oil. Table salt was obtained from Südwestdeutsche Salzwerke AG and sieved to a fraction of 500–600 μm for sample A and B, and 50–60

μm for sample C using sieves (AS 200 Basic, Retsch, Haan, Germany). High oleic sunflower oil was obtained from Olam, Singapore, and viscosity measured rheometrically as 73 mPa.s at 20 °C and 59 mPa.s at 30 °C at a shear rate of 0.1 s^{-1} in the bob and cup geometry (Kinexus Pro, Malvern, UK).

After mixing, for each food compact 4 g of salt+oil mixture were compacted in a $14 \times 14 \text{ mm}$ square die to a height of 13.5 mm using a universal testing machine (3367, Instron, Norwood, MA), resulting in a compact density of 1.5 g/cm^3 . Salt+oil compacts were subjected to oil release measurements within 30 min of compacting by placing on a paper substrate at 20 °C (sample A) and 30 °C (sample B and C) environment temperature. To model fibrous packaging material, blotting paper (3MM CHR, Whatman, Marlborough, MA) was used, with true density 1.55 g/cm^3 , and cut to squares of $8 \times 8 \text{ cm}$. The procedure is summarised in Fig. 2.

2.1. Quantitative Raman chemical imaging

Raman measurements of the compact surface were carried out once per day over 4 days by scanning a grid of $14 \times 13.5 \text{ mm}$ at 0.5 mm increments, resulting in 812 individual spectra. The compact was moved to each position by an xyz micrometer stage (SM 3.25, Märzhäuser, Wetzlar, Germany). To avoid focus errors, the compact was kept in the experimental setup over the 4 days, resulting in a single compact subjected to Raman imaging per sample A, B, and C. The laser source was a green 532 nm diode continuous wave laser (LCX, Oxxius S.A., Lannion, France) at the minimum possible setting of 94 mW power to avoid heating the sample. The beam diameter was measured as approximately 700 μm by measurement with the integrated photographic camera. The surface temperature of the compact when exposed to laser light was measured as 30 °C with a handheld infrared laser. Raman signal was acquired with a spectrometer (iHR320) with 1800 groves/mm, 500 nm blaze grating, and CCD camera (Synapse Plus, Horiba, Longjumeau, France). Signal acquisition time was 5 s and accumulated over 3 repeated measurements. The integral peak intensity was then calculated at each time and location point in order to trace the oil flow dynamics according to

$$I = \int_{\omega_0}^{\omega_n} i_{\omega} = \sum_{\omega_0}^{\omega_n} i_{\omega} \quad (1)$$

where I is the integral intensity (a.u.), ω_0 and ω_n are the lower and upper

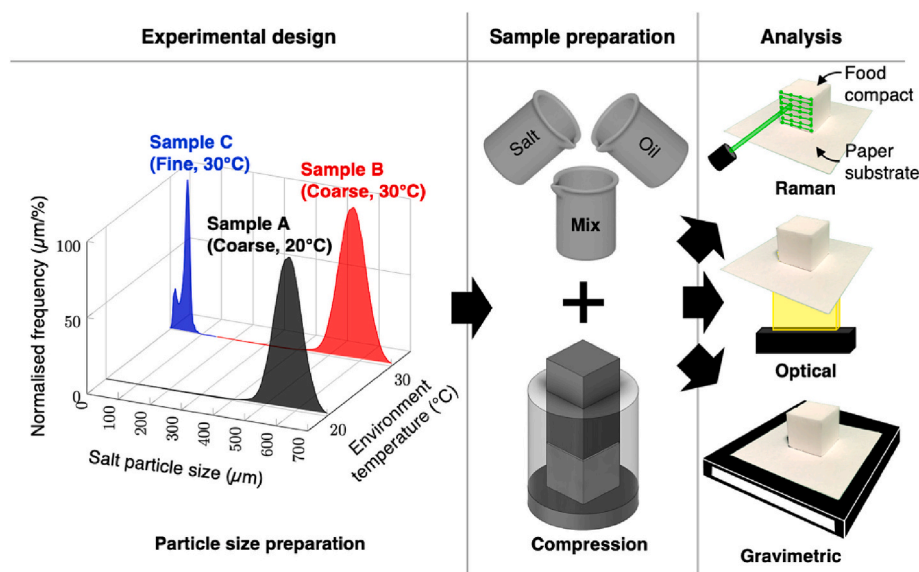


Fig. 2. Summary of experimental design, sample preparation and analysis of oil release from food compacts into paper.

spectral limits respectively (cm^{-1}), and i_ω is the intensity (a.u.) at each Raman shift ω . The measured peak intensity was then converted to oil concentration based on a calibration curve constructed by performing Raman imaging on three compacts each of a set of 15 compacts with 0, 2.5, 5, 7.5, and 10 w/w% oil and the balance salt. Oil concentration was then mapped on the initial measurement grid to construct 2D images of the local surface oil distribution of the compact with a resolution of 812 pixels on a 0.5×0.5 mm raster. In addition, the surface oil concentration averaged over the entire sample image was evaluated by

$$\bar{c} = \frac{\int_{p_0}^{p_n} p_p c_p}{\int_{p_0}^{p_n} p_p} = \frac{\sum_{p_0}^{p_n} p_p c_p}{\sum_{p_0}^{p_n} p_p} \quad (2)$$

where \bar{c} is the average surface oil concentration (w/w%), p_0 and p_n are the first and last pixel in the image respectively, and c_p is the oil concentration (w/w%) evaluated at each pixel p_p .

2.2. Optical oil stain quantification

Optical measurements of the oil stain on paper were carried out every 12 h over 4 days from the underside of the paper in triplicate measurements. The compacts were removed only during the rapid optical scanning and then placed back on exactly the same positions on the paper substrate with the help of reference points printed on the top side of the sample paper. Due to refractive index matching of oil and paper fibres, light transmission of oil-imbibed paper is greatly enhanced in contrast to oil-free paper with more scattering, and thus resulting in different grey values [36]. By calibrating the ratio of pixel to actual distance on paper, the number of darker pixels was converted to oil stain area in cm^2 , filtered for noise in samples with obvious oil stains, and unfiltered for sample with no obvious oil stains.

2.3. Gravimetric measurement

Gravimetric measurements of oil imbibed into paper were similarly carried out every 12 h over 4 days in triplicates on an analytical balance (Precisa 125 A, Mettler Toledo, Nänikon, Switzerland). For each measurement, the food compact was removed from the paper substrate and the paper weighted, tared to its initial weight without oil at the beginning of the experiment.

3. Results and discussion

3.1. Raman calibration

In a first step, Raman spectra of pure salt and sunflower oil were acquired over the range 0 to 3500 cm^{-1} and the peaks annotated with values generally accepted in literature (Fig. 3). As high oleic sunflower oil is a mixture of mostly oleic- and linoleic acid-derived triacylglycerides, there is no unique spectrum but instead different peaks associated with molecular vibrations occurring in the functional groups of the different oil components (Table 1) [39,40]. As expected, the spectrum of pure salt is free of peaks and close to the baseline, allowing a clear discrimination between salt and oil. Moreover, the experimental peaks are congruent with reported literature peak values, giving confidence in the acquisition method [39,40]. To avoid lengthy measurements over the entire spectrum, spectra were only collected between 2800 and 3050 cm^{-1} , as this region has three prominent peaks of the sunflower oil fingerprint, as shown in the inset of Fig. 3.

For the quantification of the surface oil concentration on the compact in terms of concentration and not solely Raman intensity, a calibration curve was constructed for each salt+oil compacts made from coarse salt

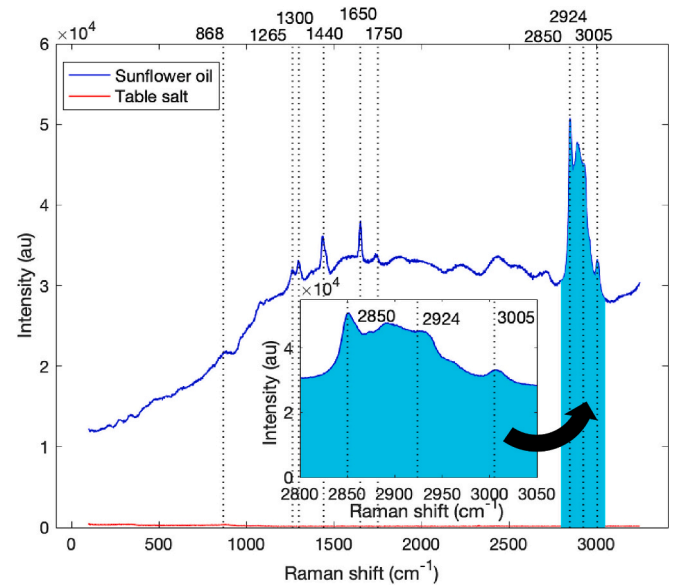


Fig. 3. Acquired full range Raman spectrum of pure salt (blue line) and sunflower oil (red line) with annotated literature peaks [39,40]. Inset shows the selected range from 2800 to 3050 cm^{-1} chosen for further quantitative Raman chemical imaging. (For interpretation of the references to colour in this figure legend, the reader is referred to the web version of this article.)

Table 1

Generally accepted major Raman peaks in edible oils, adapted from [39,40].

Raman shift (cm^{-1})	Vibration mode	Functional group
868	C-C stretching	$-(\text{CH}_2)_n-$
968	C=C bending	trans RHC=CHR
1008	CH_3 bending	HC- CH_3
1150	C-C stretching	$-(\text{CH}_2)_n-$
1265	=C-H bending (scissoring)	cis RHC=CHR
1300	C-H bending (twisting)	$-\text{CH}_2$
1440	C-H bending (scissoring)	$-\text{CH}_2$
1525	C=C stretching	RHC=CHR
1650	C=C stretching	cis RHC=CHR
1750	C=O stretching	RC=OOR
2850	C-H symmetric stretching	$-\text{CH}_2$
2897	C-H symmetric stretching	$-\text{CH}_3$
2924	C-H asymmetric stretching	$-\text{CH}_2$
3005	=C-H symmetric stretching	cis RHC=CHR

for samples A and B, and salt+oil compacts made from fine salt for sample C. Fig. 4 shows the calibration spectra of the coarse samples. As expected, the 0 w/w% oil sample is parallel to the baseline, while increasing oil concentrations in the calibration compacts resulted in increasing spectral intensities, with almost equal distance between spectra for each 2.5 w/w% oil concentration increase. Fig. 5 shows the resulting calibration curve of integral intensity calculated with Eq. (1) against compact oil concentration. While the large error bars result from the large variations in spectra for each sample, it is still possible to evaluate a linear trend by least squares regression given as $I = 2.142 \times 10^5 c + 4.255 \times 10^5$ with $R^2 = 0.97$.

Fig. 6 similarly shows the calibration spectra for compacts from fine salt particles. The intensities are generally about 5 times as large and converge for the 7.5 and 10 w/w% samples. This could be due to the fact that dispersing oil homogeneously in fine powder is less efficient compared to coarse powder, some clumps and agglomerates were observed in the fine compacts. Fig. 7 shows the calibration curve for the fine samples given as $I = 2.2446 \times 10^6 c + 2.513 \times 10^6$, with $R^2 = 0.87$ reflecting the larger variations in the fine sample calibration.

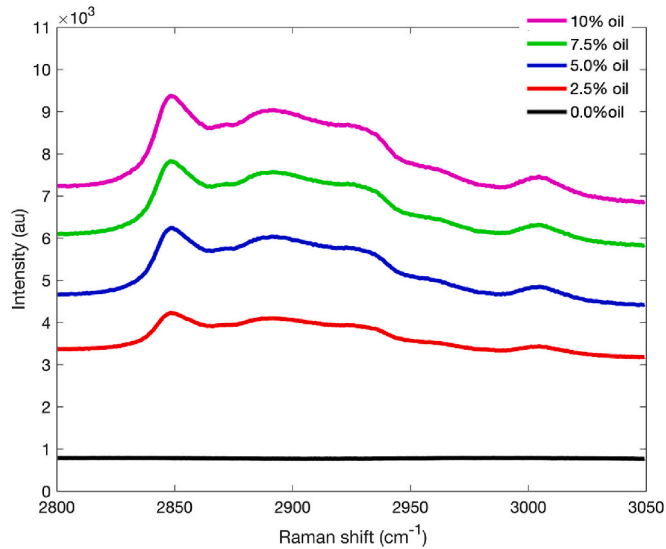


Fig. 4. Acquired Raman calibration spectra for salt+oil compacts made from coarse salt.

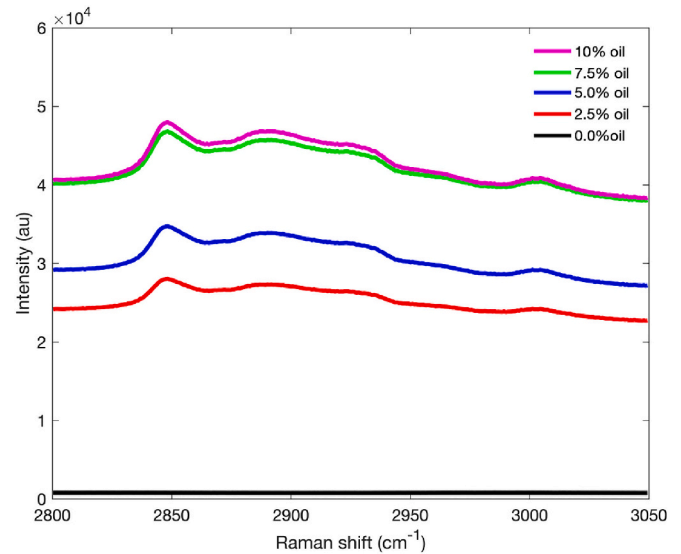


Fig. 6. Acquired Raman calibration spectra for salt+oil compacts made from fine salt.

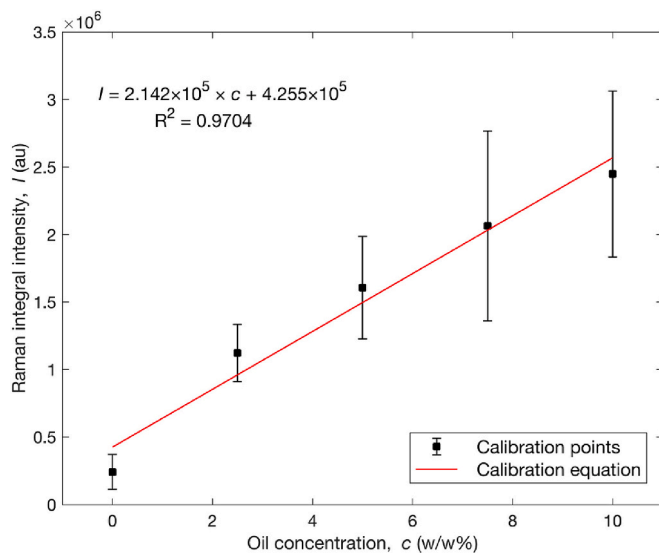


Fig. 5. Calibration curve for salt+oil compacts made from coarse salt.

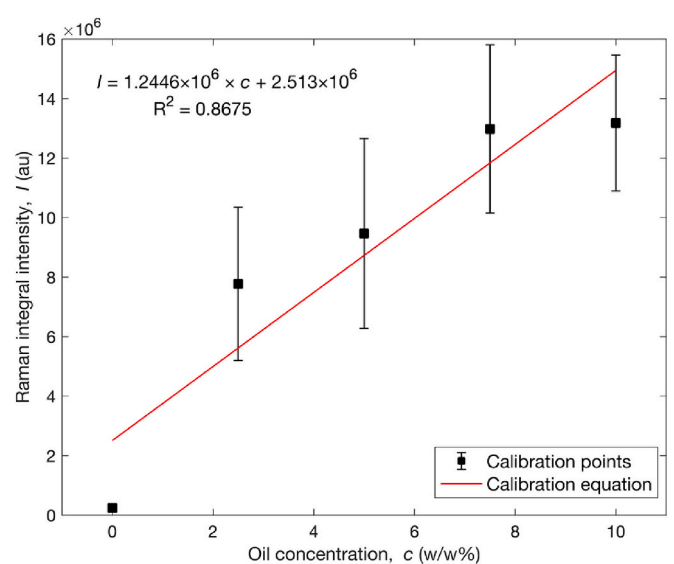


Fig. 7. Calibration curve for salt+oil compacts made from fine salt.

3.2. Quantitative Raman chemical imaging

After calibration, salt+oil compacts were prepared according to the procedure in Fig. 2 and placed on paper substrate for analysis. The Raman spectra of the compact surface, converted to surface oil concentration and reconstructed in 2D quantitative Raman chemical images are shown in Fig. 8, where the x and y axes represent width and height of the compacts respectively, and the z axis is represented as a colour scale from 0 to 100 w/w% oil concentration. Generally, all three samples exhibit an overwhelmingly blue colour, indicating a concentration around 0 to 10 w/w% oil, as expected due to the 95 w/w% salt and 5 w/w% initial oil concentration. Sample A and B contain distinct spots of high oil concentration up to 100 w/w% oil (red colour), which could be attributed to the larger particle size and thus larger liquid bridges formed, which contain a high oil concentration, in addition to variability induced by manual mixing. The fact that the high concentration clusters are in the same locations over the 4 days confirms that they are not artifacts. Conversely, the surface colour of sample C appears more homogenous, likely due to the smaller particle size and smaller oil bridges.

While some areas show 1–2 mm diameter agglomerates with higher oil concentration, the overall concentration is more evenly distributed than in the coarse samples with individual pixel-sized hotspots. The increasing homogenous distribution of liquid between coarse and fine particle systems was previously described for liquid imbibition into tablets and powder beds [41,42], but is likely also applicable to the reverse process of liquid release in this study. Comparing the samples over time, changes in particle size (sample B vs C) have a much more drastic effect than temperature at a fixed particle size (sample A vs B). This is manifested by the fact that the oil concentration changes little in the 4 days of sample C, suggesting more oil is retained. On the other hand, sample B shows stark changes from areas of up to 40 w/w% down to 0. Colour comparison between sample A and B shows that for the same particle size but different temperature, the concentration drop is only marginally slower in sample A compared with sample B.

In addition to the novel Raman chemical imaging for picturing previously unknown surface oil dynamics, average and normalised average ($t_0 = 100$ w/w%) surface oil concentration against time, calculated from Eq. (2), was plotted in Fig. 9. Comparison of the three samples shows

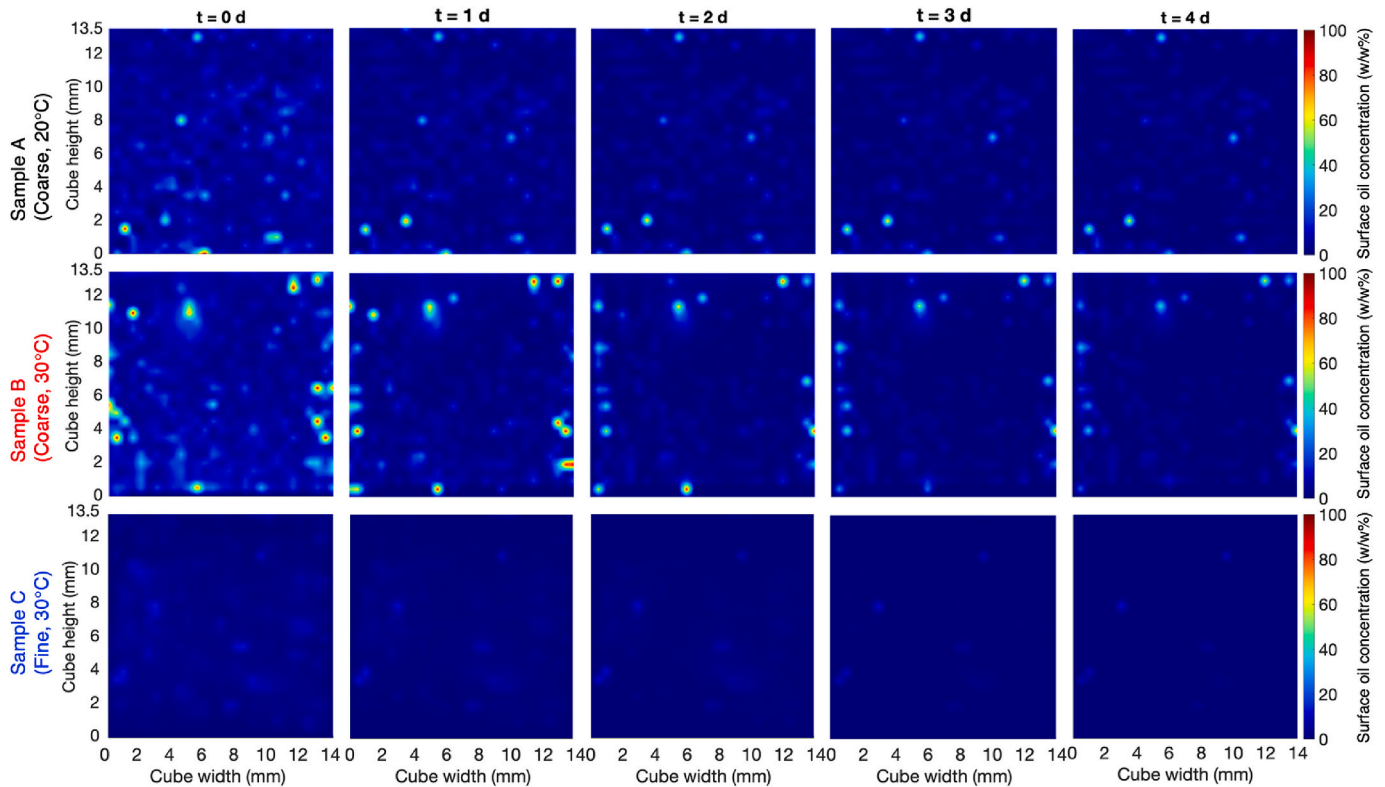


Fig. 8. Quantitative Raman chemical images of sample A, B, and C showing the dynamic behaviour of surface oil concentration on the faces of salt+oil compacts in contact with paper substrate.

that all three food compacts have reducing surface oil concentrations, with samples A and B having the most drastic change from 6.5 and 9.5 w/w% initially to 2 w/w% after 4 days for both samples. As expected, sample B has a minimally faster oil release of in total $(9.5-2) \times 100 / 9.5 = 80\%$, compared to 70% for sample A, owing to the higher temperature and resulting lower oil viscosity of 59 mPa.s for sample B compared to 73 mPa.s for A. Sample C loses oil slowest from 3 to 0 w/w%. Although the nominal initial oil concentration was 5 w/w% in all samples, the variations in initial concentrations could be due to the time lag between compaction and sample measurement, due to the Raman analysis duration of 5 h until all 812 data points were sampled, or due to the

phenomenon that liquid is forced to the sides of a tablet during compaction, which has previously only been reported for extrusion [43]. The latter argument is supported by hotspots in Fig. 8 being mostly located at the edges of compact samples A and B. The large spread in data for samples A and B indicated by the large error bars reflects the local variation from 0 to 100 w/w% in both samples in Fig. 8, whereas sample C has less concentration variation in Fig. 8 (0–30 w/w%) and thus less data spread in Fig. 9. Given the measured laser beam diameter of approximately 700 μm , the probing beam is similar in size to the particles in the coarse compact, and hence in extreme cases either an oil pocket or salt crystal was probed, resulting in stark differences in surface oil concentrations. In the fine compact, the ratio of laser beam diameter to particle size is larger and the additional smaller oil bridges mean more averaged local salt+oil mixtures are probed, and the event of sampling pure oil pockets or pure salt particles occurs seldom.

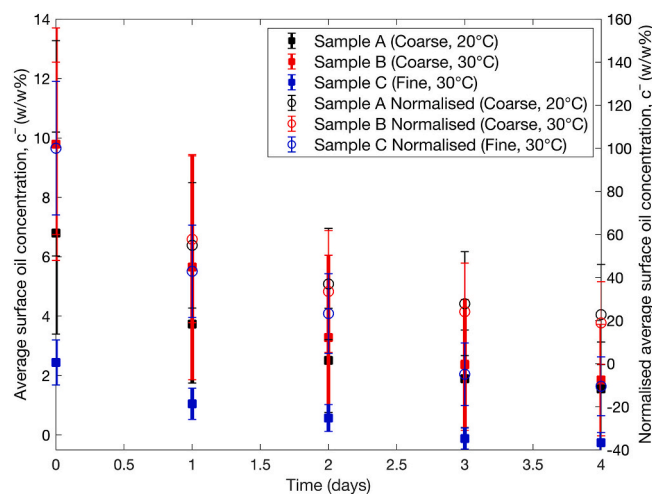


Fig. 9. Average and normalised average ($t_0 = 100$ w/w%) surface oil concentration obtained from Raman chemical images using Eq. (2) for each sample over 4 days.

3.3. Optical quantification

Techniques to measure oil transport in paper and other fibrous materials are much more established [36,37] and were used to validate the Raman chemical imaging measurements. Optical images of the underside of paper in contact with food compacts were taken and quantified via automated image analysis (Fig. 10). The increasing oil stain on paper for the coarse salt and oil compact (sample A, B) in contrast to the clear paper for the fine compact (sample C) confirm the trend seen previously in Raman chemical imaging. Similarly, the comparison of the same particle size at different temperatures seen in Raman chemical imaging is reflected by the larger oil stain at 30 °C compared to 20 °C. Fig. 11 shows the variation of quantified oil stain area over time in graphical representation, depicting the same trend seen previously. The same tendency of oil stain increase at early contact times and plateauing at later times has been previously seen for in the domain of mechanical Engineering with lubrication grease blobs on blotting paper [36,37].

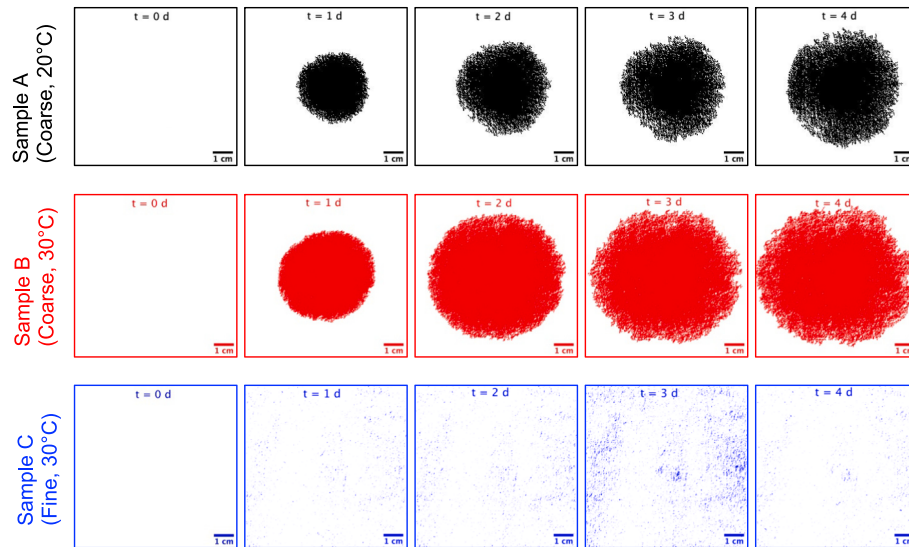


Fig. 10. Images of expanding oil stain measured via optical imaging and automated image quantification. The noise was filtered out for samples A and B with obvious oil stains but was not applied to sample C without obvious oil stains.

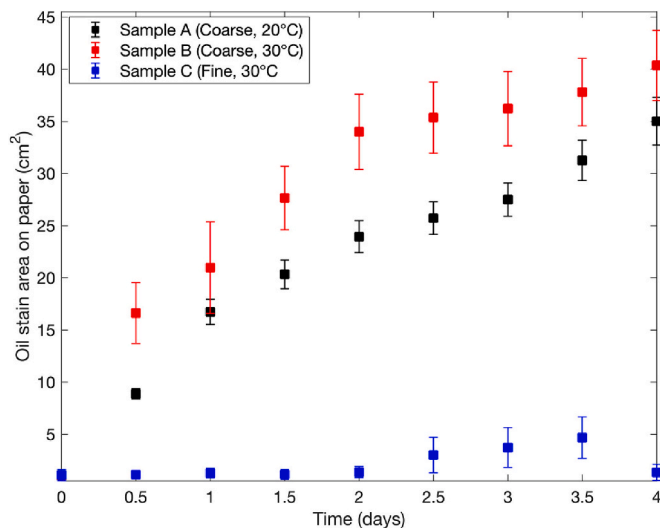


Fig. 11. Area of expanding oil stain over time measured via optical imaging and automated image quantification.

3.4. Gravimetric analysis

Fig. 12 shows the mass of oil transferred from the food compacts into paper measured as the mass gain of the paper sample. Assuming a fixed paper grammage with isotropic porosity and constant thickness, the mass gain should follow the trend of automated oil stain imaging, in accordance with previous reports [36,37]. Indeed, sample A and B show increasing mass gain with time, showing a faster oil release at 30 °C compared to 20 °C and reaching similar final values of 0.1 g after 4 days, both observations being in accordance with the Raman chemical images in Fig. 8. and optical imaging in Fig. 10. Mass gain for Sample C is negligible following the trend of only minor changes from the spectroscopic and optical imaging. Given that each compact contained 5 w/w% = 0.2 g oil, the liquid hold-up of the coarse samples is only about half of the initial oil quantity (0.1 g), compared to almost the full 0.2 g oil for the fine samples.

The observed trend of increasing oil release at higher temperatures can be explained with the decreasing oil viscosity and thus easier flowability of oil from the food into paper at elevated temperatures. The

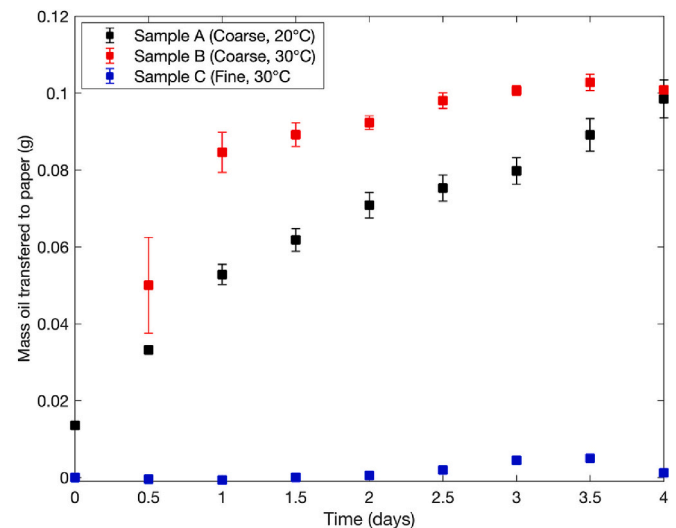


Fig. 12. Mass of oil transferred to paper over time measured gravimetrically.

observed trend of reduced oil release in food compacts of fine particles compared to large ones can be explained by the smaller inter-particle spacing in fine compacts, resulting in smaller radii of curvature and thus larger capillary forces according to the fundamental Young-Laplace Eq. [13]. The larger suction forces in small particle systems results in a higher retention of liquid in the system, which was confirmed in multiple works in the Chemical Engineering domain on water flow through separation columns packed with glass beads. For instance, liquid retention in a monodisperse 3 mm glass sphere bed was 3.1 w/w% of the initial fully saturated water content before drainage [10]. In another work employing 500 μm glass spheres, matching the particle size of sample A and B in this work, water retention was 5 w/w% [44]. The discrepancy to the 10 w/w% retention in the present work is therefore not only due to the reduced particle size, but also other parameters such as contact angle and viscosity. Another packed bed work employing an aqueous xanthan solution of 100 mPa.s viscosity, similar to the 75 mPa.s of sunflower oil used herein, achieved a maximum 4 w/w% liquid retention, albeit for 10 cm glass spheres [45]. Besides the thermodynamic effect of particle-size induced capillarity, the dynamic effect of increased fluid-wall friction plays a role [46]. As shown by reduced

dynamism in the Raman images for smaller particle sizes, the narrower inter-particle channel reduces the available hydraulic diameter and thus increases the viscous pressure drop according to the fundamental Hagen-Poiseuille equation, thereby slowing the flow [12]. In packed bed process flow applications, this phenomenon has been previously described with the Carman-Kozeny equation [47,48].

4. Conclusion

For the first time, it was achieved to concurrently measure oil release from a food compact into a fibrous packaging substrate by imaging the oil dynamics in both the food sample via quantitative Raman chemical imaging, and the paper substrate via gravimetry and optical imaging and automated quantification. Oil release from the food compact into paper was slightly reduced when the temperature was decreased from 30 to 20 °C, attributing this effect to the reduced oil viscosity. Oil release was almost completely stopped when the particle size was reduced from 500 to 600 to 50–60 µm, attributing this effect to the larger capillary suction and narrower channel diameter in the finer compact. The advantage of Raman spectroscopy was the ability of monitoring the oil release process locally and continuously or ‘on-line’, while paper-based techniques were discontinuous and only showed overall results. The analytical techniques developed in this work have been demonstrated by the findings to be highly useful in quantifying oil release from food into packaging. The results further show that an edible internal oil barrier can be created by reducing the particle size of the solid food fraction. This enables consumer food research to understand and develop more sustainable paper-based packaging compatible with oil containing foods. The next step of this research is suggested to be predictive modelling of the oil flow based on the physical properties of the porous and liquid systems.

CRedit authorship contribution statement

Luc Dewulf: Writing – review & editing, Writing – original draft, Visualization, Validation, Supervision, Software, Resources, Project administration, Methodology, Investigation, Funding acquisition, Formal analysis, Data curation, Conceptualization. **Michael K. Hausmann:** Supervision, Resources, Project administration. **Annabel Bozon:** Supervision, Resources, Project administration. **Gerhard Niederreiter:** Supervision, Funding acquisition. **Stefan Palzer:** Funding acquisition. **Agba D. Salman:** Writing – review & editing, Supervision, Funding acquisition.

Declaration of competing interest

The authors declare the following financial interests/personal relationships which may be considered as potential competing interests:

Luc Dewulf reports financial support was provided by Engineering and Physical Sciences Research Council. Luc Dewulf reports financial support was provided by Nestle Research & Development. If there are other authors, they declare that they have no known competing financial interests or personal relationships that could have appeared to influence the work reported in this paper.

Data availability

Data will be made available on request.

Acknowledgements

The author thanks EPSRC (grant 2602203) and Nestlé for funding this research, Professor Arnulf Materny and Dr. Patrice Donfack from Constructor University Bremen, Germany, for Raman training, the workshop staff and Dr. Riyadh Al-Asady for technical support, Adrien Six for graphic design, and the iForge makerspace at the University of Sheffield for workshop facility.

References

- [1] B.L. Tardy, J.J. Richardson, L.G. Greca, J. Guo, J. Bras, O.J. Rojas, Advancing bio-based materials for sustainable solutions to food packaging, *Nat. Sustain.* 6 (2023) 360–367.
- [2] S. Otto, M. Strenger, A. Maier-Nöth, M. Schmid, Food packaging and sustainability – consumer perception vs. correlated scientific facts: a review, *J. Clean. Prod.* 298 (2021) 126733.
- [3] M.J. Kirwan, *Handbook of Paper and Paperboard Packaging Technology*, Wiley, Hoboken, NJ, 2012.
- [4] L. Manzocco, S. Calligaris, M. Camerin, L. Pizzale, M.C. Nicoli, Prediction of firmness and physical stability of low-fat chocolate spreads, *J. Food Eng.* 126 (2014) 120–125.
- [5] J.M. Aguilera, M. Michel, G. Mayor, Fat migration in chocolate: diffusion or capillary flow in a particulate solid? A hypothesis paper, *J. Food Sci.* 69 (2006) 167–174.
- [6] E.W. Washburn, The dynamics of capillary flow, *Phys. Rev.* 17 (1921) 273–283.
- [7] M. Dubé, M. Rost, M. Alava, Conserved dynamics and interface roughening in spontaneous imbibition: a critical overview, *Europ. Phys. J. B Condens. Matter Complex Syst.* 15 (2000) 691–699.
- [8] Q. Meng, H. Liu, J. Wang, A critical review on fundamental mechanisms of spontaneous imbibition and the impact of boundary condition, fluid viscosity and wettability, *Adv. Geo-Energy Res.* 1 (2017) 1–17.
- [9] M. Alava, M. Dubé, M. Rost, Imbibition in disordered media, *Adv. Phys.* 53 (2004) 83–175.
- [10] W. Van Der Merwe, C. Maree, W. Nicol, Nature of residual liquid holdup in packed beds of spherical particles, *Ind. Eng. Chem. Res.* 43 (2004) 8363–8368.
- [11] M. Mirzajanzadeh, V.S. Deshpande, N.A. Fleck, Water rise in a cellulose foam: By capillary or diffusional flow? *J. Mech. Phys. Solids* 124 (2019) 206–219.
- [12] S.P. Suter, R. Skalak, The history of Poiseuille’s law, *Annu. Rev. Fluid Mech.* 25 (1993) 1–20.
- [13] C.F. Gauss, *Principia Generalia Theoriae Figurae Fluidorum in Statu Aequilibræ*, in: C.F. Gauss (Ed.), *Werke: Fünfter Band*, Springer Berlin Heidelberg, Berlin, Heidelberg, 1877, pp. 29–77.
- [14] L. Metilli, M. Francis, M. Povey, A. Lazidis, S. Marty-Terrade, J. Ray, E. Simone, Latest advances in imaging techniques for characterizing soft, multiphase food materials, *Adv. Colloid Interf. Sci.* 279 (2020) 102154.
- [15] L. Wu, X. Tang, T. Wu, W. Zeng, X. Zhu, B. Hu, S. Zhang, A review on current progress of Raman-based techniques in food safety: from normal Raman spectroscopy to SESORS, *Food Res. Int.* 169 (2023) 112944.
- [16] M. Petersen, Z. Yu, X. Lu, Application of Raman spectroscopic methods in food safety: a review, *Biosensors* 11 (2021) 187.
- [17] Y. Xu, P. Zhong, A. Jiang, X. Shen, X. Li, Z. Xu, Y. Shen, Y. Sun, H. Lei, Raman spectroscopy coupled with chemometrics for food authentication: a review, *TrAC Trends Anal. Chem.* 131 (2020) 116017.
- [18] K. Wang, Z. Li, J. Li, H. Lin, Raman spectroscopic techniques for nondestructive analysis of agri-foods: a state-of-the-art review, *Trends Food Sci. Technol.* 118 (2021) 490–504.
- [19] C. Qu, Y. Li, S. Du, Y. Geng, M. Su, H. Liu, Raman spectroscopy for rapid fingerprint analysis of meat quality and security: principles, progress and prospects, *Food Res. Int.* 161 (2022) 111805.
- [20] E.M. Achata, C. Esquerre, A.A. Gowen, C.P. O’Donnell, Feasibility of near infrared and Raman hyperspectral imaging combined with multivariate analysis to assess binary mixtures of food powders, *Powder Technol.* 336 (2018) 555–566.
- [21] S. Gupta, T. Omar, F.J. Muzzio, SEM/EDX and Raman chemical imaging of pharmaceutical tablets: a comparison of tablet surface preparation and analysis methods, *Int. J. Pharm.* 611 (2022) 121331.
- [22] T. Firkala, A. Farkas, B. Vajna, I. Farkas, G. Marosi, Investigation of drug distribution in tablets using surface enhanced Raman chemical imaging, *J. Pharm. Biomed. Anal.* 76 (2013) 145–151.
- [23] A. Kondo, T. Koide, T. Fukami, Evaluation of the effect of Disintegrant distribution on the dissolution behavior of pharmaceutical tablets using Raman chemical imaging, *Chem. Pharm. Bull.* 71 (2023) 454–458.
- [24] D.L. Galata, B. Zsiros, L.A. Mészáros, B. Nagy, E. Szabó, A. Farkas, Z.K. Nagy, Raman mapping-based non-destructive dissolution prediction of sustained-release tablets, *J. Pharm. Biomed. Anal.* 212 (2022) 114661.
- [25] C. De Bleye, P.Y. Sacré, E. Dumont, L. Netchacovitch, P.F. Chavez, G. Piel, P. Lebrun, P. Hubert, E. Ziemons, Development of a quantitative approach using surface-enhanced Raman chemical imaging: first step for the determination of an impurity in a pharmaceutical model, *J. Pharm. Biomed. Anal.* 90 (2014) 111–118.
- [26] J. Cailletaud, C. De Bleye, E. Dumont, P.-Y. Sacré, Y. Gut, N. Leblanc, P. Letellier, Y.-M. Ginot, P. Hubert, E. Ziemons, Detection of low dose of piroxicam polymorph in pharmaceutical tablets by surface-enhanced Raman chemical imaging (SER-CI) and multivariate analysis, *Int. J. Pharm.* 574 (2020) 118913.
- [27] R. Slipets, O. Ilchenko, C. Mazzoni, F. Tentor, L.H. Nielsen, A. Boisen, Volumetric Raman chemical imaging of drug delivery systems, *J. Raman Spectrosc.* 51 (2020) 1153–1159.
- [28] S. Sašić, T. Prusnick, Raman chemical imaging of intact non-flat tablets in regular and high-confocal mode, *Anal. Methods* 12 (2020) 471–482.
- [29] J. Cailletaud, C.D. Bleye, E. Dumont, P.-Y. Sacré, Y. Gut, L. Bultel, Y.-M. Ginot, P. Hubert, E. Ziemons, Towards a spray-coating method for the detection of low-dose compounds in pharmaceutical tablets using surface-enhanced Raman chemical imaging (SER-CI), *Talanta* 188 (2018) 584–592.
- [30] M. Yamashita, H. Sasaki, K. Moriyama, Vapor phase alkyne coating of pharmaceutical excipients: discrimination enhancement of Raman chemical imaging for tablets, *J. Pharm. Sci.* 104 (2015) 4093–4098.

- [31] N.J. Lawson, The application of laser measurement techniques to aerospace flows, *Proc. Inst. Mechan. Eng. Part G: J. Aerospace Eng.* 218 (2004) 33–57.
- [32] A. Malarski, J. Egermann, J. Zehnder, A. Leipertz, Simultaneous application of single-shot Ramanography and particle image velocimetry, *Opt. Lett.* 31 (2006) 1005–1007.
- [33] A. Braeuer, S.R. Engel, S. Dowy, S. Luther, J. Goldlücke, A. Leipertz, Raman mixture composition and flow velocity imaging with high repetition rates, *Opt. Express* 18 (2010) 24579–24587.
- [34] M. Wellhausen, G. Rinke, H. Wackerbarth, Combined measurement of concentration distribution and velocity field of two components in a micromixing process, *Microfluid. Nanofluid.* 12 (2012) 917–926.
- [35] J.B. Rosenholm, Liquid spreading on solid surfaces and penetration into porous matrices: coated and uncoated papers, *Adv. Colloid Interf. Sci.* 220 (2015) 8–53.
- [36] F. Valoppi, P. Lassila, A. Salmi, E. Haeggström, Automated image analysis method for oil-release test of lipid-based materials, *MethodsX* 8 (2021) 101447.
- [37] Q. Zhang, F. Mugele, P.M. Lugt, D. Van Den Ende, Characterizing the fluid–matrix affinity in an organogel from the growth dynamics of oil stains on blotting paper, *Soft Matter* 16 (2020) 4200–4209.
- [38] J. Lange, C. Pelletier, Y. Wyser, Novel method for testing the grease resistance of pet food packaging, *Packag. Technol. Sci.* 15 (2002) 65–74.
- [39] R.M. El-Abassy, P. Donfack, A. Materny, Visible Raman spectroscopy for the discrimination of olive oils from different vegetable oils and the detection of adulteration, *J. Raman Spectrosc.* 40 (2009) 1284–1289.
- [40] R.M. El-Abassy, P. Donfack, A. Materny, Assessment of conventional and microwave heating induced degradation of carotenoids in olive oil by VIS Raman spectroscopy and classical methods, *Food Res. Int.* 43 (2010) 694–700.
- [41] H.R. Charles-Williams, R. Wengeler, K. Flore, H. Feise, M.J. Hounslow, A. D. Salman, Granule nucleation and growth: competing drop spreading and infiltration processes, *Powder Technol.* 206 (2011) 63–71.
- [42] A.L. Mundozah, J.J. Cartwright, C.C. Tridon, M.J. Hounslow, A.D. Salman, Hydrophobic/hydrophilic static powder beds: competing horizontal spreading and vertical imbibition mechanisms of a single droplet, *Powder Technol.* 330 (2018) 275–283.
- [43] S. Mascia, M.J. Patel, S.L. Rough, P.J. Martin, D.I. Wilson, Liquid phase migration in the extrusion and squeezing of microcrystalline cellulose pastes, *Eur. J. Pharm. Sci.* 29 (2006) 22–34.
- [44] A.E. Sáez, M.M. Yépez, C. Cabrera, E.M. Soria, Static liquid holdup in packed beds of spherical particles, *AIChE J.* 37 (1991) 1733–1736.
- [45] S. Schwidder, K. Schnitzlein, Predicting the static liquid holdup for cylindrical packings of spheres in terms of the local structure of the packed bed, *Chem. Eng. Sci.* 65 (2010) 6181–6189.
- [46] M. Soustelle, *Thermodynamics of Surfaces and Capillary Systems*, Wiley, 2016.
- [47] J. Kozeny, Über kapillare Leitung des Wassers im Boden (Aufstieg, Versickerung und Anwendung auf die Bewässerung), *Sitzungsber. Akad. Wiss. Wien* 136 (1927) 271–309.
- [48] P.C. Carman, Fluid flow through granular beds, *Chem. Eng. Res. Des.* 75 (1937) S32–S48.

Corrigendum for Chapter: Mitigation Strategy

- Prior to characterisation, the uniformity of the salt mix was assessed by eye. As the Raman characterisation was carried out over a macroscopic area of the compact, nonuniformity of a few particles are average out. No obvious nonuniformity over an area larger than the scanning interval of 0.5 mm was observed. As stated in the methodology section, the characterisation of the compacts carried out were: quantitative Raman chemical imaging, optical oil stain quantification, and gravimetric measurements.
- First order kinetics fitting was performed to obtain the characteristic time for Fig. 11 and 12. The first order kinetics model used was

$$y = y_{\infty}(1 - e^{-kt})$$

where y is the ordinate oil stain area on paper (Fig. 11) or mass of oil transferred to paper (Fig. 12), y_{∞} is the final y -value, k is the rate constant, and t is the time on the abscissa. The characteristic time, representing the time to reach about 63.2% of the final value, is $\tau = \frac{1}{k}$.

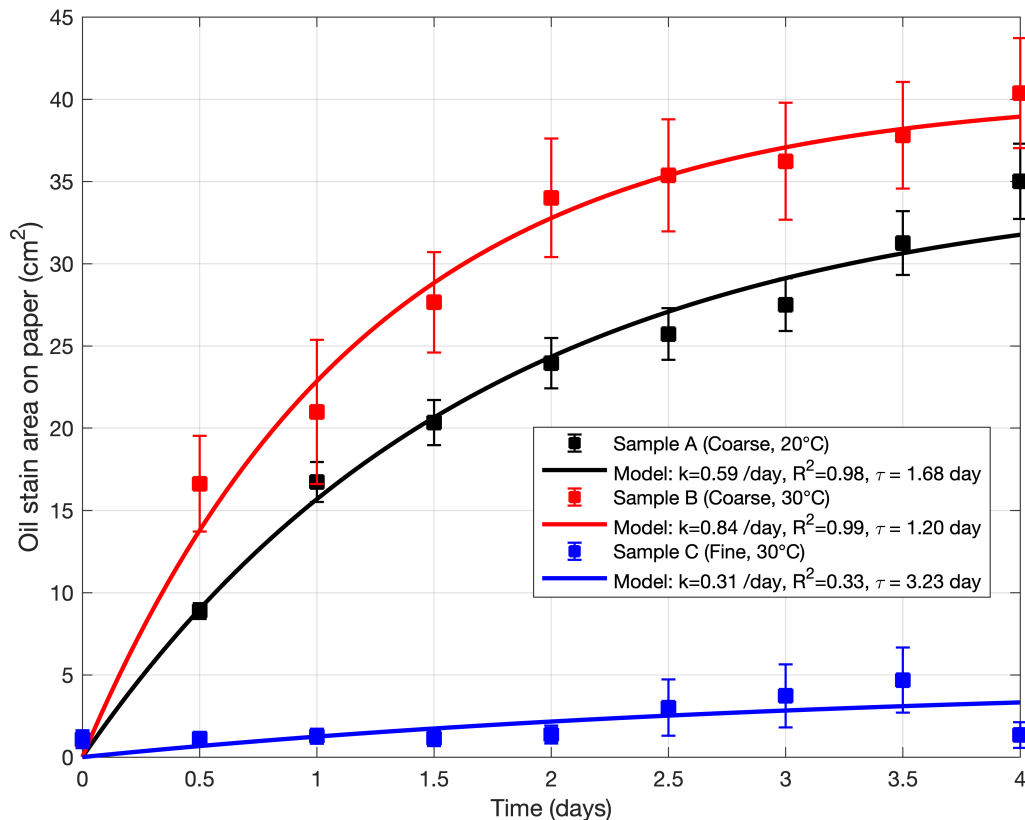


Fig. 11 with first-order kinetic modelling. Area of expanding oil stain over time measured via optical imaging and automated image quantification.

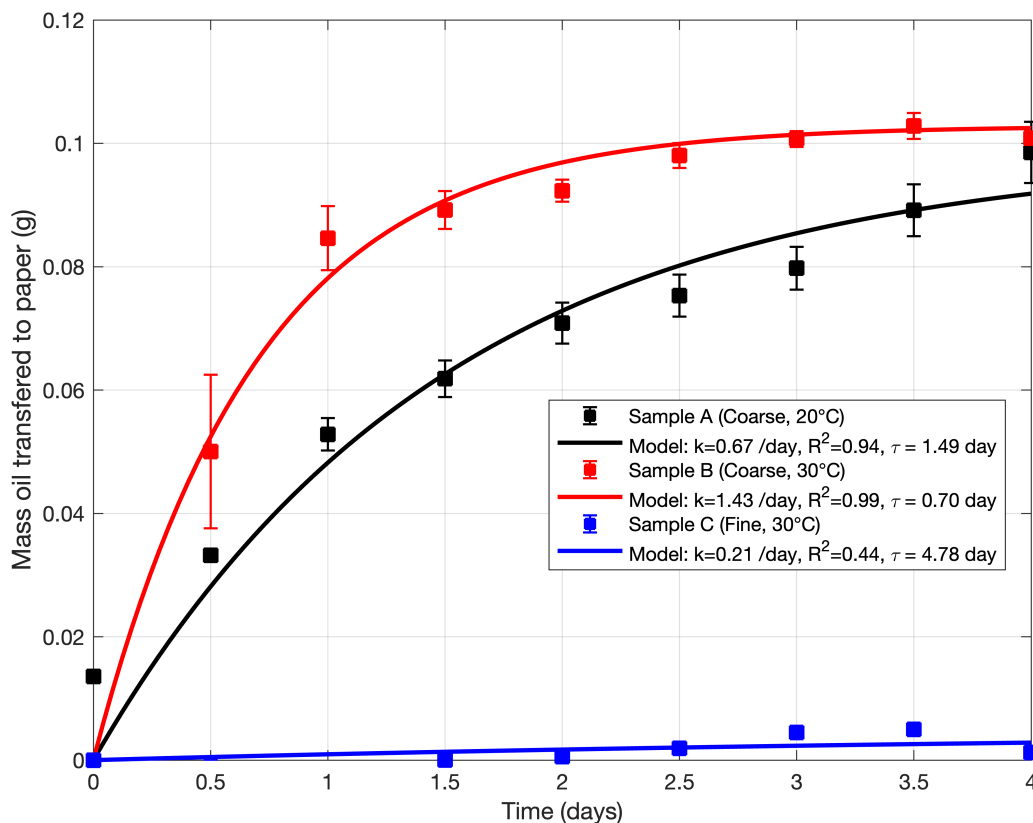


Fig. 12 with first-order kinetic modelling. Mass of oil transferred to paper over time measured gravimetrically.

- 100 mW laser power was only used in this work. All other chapters used 50 mW or less. 100 mW was the lowest powder setting of the laser source. After a fault due to a power outage at university the laser had to be reconfigured to half the previous power, and there 50 mW was the minimum now. Besides the limitations set by the equipment, prior work on Raman for lipids cited in the chapter above used similar power ranges e.g. [39, 40].

Chapter 5

Modelling



Fat migration from a particulate food system into fibrous material via capillary flow – first-principle modelling and experimental validation

Luc Dewulf^{a,b,*}, Jordan M. MacInnes^a, Michael K. Hausmann^b, Annabel Bozon^c, Gerhard Niederreiter^b, Stefan Palzer^d, Agba D. Salman^a

^a School of Chemical, Materials, and Biological Engineering, University of Sheffield, Sir Robert Hadfield Building, Mappin Street, Sheffield S1 3JD, United Kingdom

^b Nestlé Research, 57 Route du Jorat, 1000 Lausanne 26, Switzerland

^c Nestlé Product Technology Centre Food, Lange Straße 21, Singen 78221, Germany

^d Nestlé Ltd., Avenue Nestlé 55, Vevey 1800, Switzerland

ARTICLE INFO

Keywords:

Fat migration
Lipid migration
Capillary
Mechanistic modelling
Food microstructure
Paper fibre packaging

ABSTRACT

Fat migration from compacted particulate foods into fibrous paper-based wrappers causes undesired fat stains on packaging and is a major concern for food manufacturers that are increasingly moving towards more sustainable paper-based packaging. While fibre-based materials are prone to absorb fats by capillary sorption, mechanisms of fat migration from the food matrix are dependent on the underlying food microstructure and full understanding is still lacking. Here, we developed a first-principle capillary flow model predicting liquid fat flow from model seasoning compacts (95 w/w% salt, 5 w/w% palm kernel fat) into contacting blotting paper. Compacts with systematic variations in salt particle size from $5 \leq d_{50} \leq 500 \mu\text{m}$ were produced in ternary design of experiments assessing the pore microstructure effect on capillarity and permeability. Measurements from x-ray microtomography and fat wicking kinetics were used to evaluate microstructural information for model parameters. Model validation was then performed in a physical set up characterising the fat migration behaviour on the compact side via Raman chemical imaging and on the paper side via optical stain imaging. Experiment and model were in better agreement (R^2 up to 0.96) for compacts from coarse particles than for compacts with small porosity features. Yet, the model directed development towards using smaller particle sizes achieving almost 0 % fat migration into paper packaging for optimal samples.

1. Introduction

The majority of consumer foods are dry solids in particulate form such as beverage powders, seasoning compacts, or moulded chocolate. Many such products contain lipids such as fats or oils for enhanced texture, mouthfeel and flavour. As most multiphase food systems, also particulate foods are inherently thermodynamically unstable and tend towards physical equilibrium by phase separation. Physical stability of food is thus attempted by kinetic stabilisation via food microstructure or ingredient formulation to extend the equilibration time, giving rise to metastability (Aguilera, 2011). In lipid containing foods, phase separation of fat or oil from the food matrix is termed lipid migration or leakage, and manifests itself in quality defects on the food surface as in fat bloom in chocolate or grease stains on paper-based packaging.

As we comprehensively summarised in our recent review (Dewulf

et al., 2024a), the main research focus of lipid migration in particulate food systems has been on continuous food matrices, especially chocolate, with modelling approaches restricted to Fickian diffusion and empirical models. Diffusion is the migration of components driven by a concentration difference between a phase poor and rich in lipids, where the stationary medium is continuous. This modelling approach is especially attractive when limited information about the food microstructure and only few spatial and temporal sampling points are available for determination of the migrant concentration. Ziegler et al. were the first to implement simplified diffusion models for chocolate (Ziegler et al., 1996a, 1996b; Ziegler and Schwingshandl, 1998), until more elaborate and complex models for confectionary followed (Cikrikci and Oztop, 2018; Harshe et al., 2023).

Much less attention has been put to lipid migration in triphasic food systems consisting of gas-liquid-solids. Porous media are inherently more difficult to model due to the requirement for knowledge of the

* Corresponding author at: School of Chemical, Materials, and Biological Engineering, University of Sheffield, Sir Robert Hadfield Building, Mappin Street, Sheffield S1 3JD, United Kingdom.

<https://doi.org/10.1016/j.cherd.2026.02.012>

Received 2 October 2025; Received in revised form 29 January 2026; Accepted 6 February 2026

Available online 7 February 2026

0263-8762/© 2026 Institution of Chemical Engineers. Published by Elsevier Ltd. All rights are reserved, including those for text and data mining, AI training, and similar technologies.

microstructure such as pore size and more extensive information of the migrant physical properties such as surface tension and viscosity. With modern characterisation techniques available, implementation of more challenging but realistic models on capillary flow as opposed to diffusion has been advocated (Shah and Takhar, 2023).

Models in which oil migration in food is modelled as liquid flow in capillaries are still limited to liquid imbibition into the porous medium, e.g. during deep frying (Verma et al., 2025) or for the case of sunflower oil imbibing into cocoa powder (Carbonell et al., 2004). Oil migration driven by capillary action in the direction out of the macroscopic food body was first described by us for the case of model seasoning cubes in contact with a fibrous packaging substrate, resulting in oil staining on the paper (Dewulf et al., 2024b). It was suggested that oil migration between the two porous bodies, seasoning compact and paper, is driven by the relative magnitudes of capillary suction. Unwanted oil stain extent was reduced from several tens of cm^2 to virtually zero by modulating the capillarity of the seasoning compact in favour of oil retention in the compact which was achieved by reducing the particle size.

Outside of the food domain, liquid mass transfer driven by capillarity amongst other forces between two porous bodies is relevant in other processes including leaf filtration where the filter cake is one, and the filter leaf the other porous body (Sutherland, 2008); in the felt wicking process in paper manufacturing (Biermann, 1996), and in enhanced oil recovery (Siyal et al., 2023). An especially synonymous system is the process of wick debinding in ceramics and powder sintering, in which a liquid binder is transferred from the green powder body into a receiving powder bed (Lin and Hourng, 2005). Bao and Evans constructed a model for the volume transferred with time using the capillary pressure difference between the two porous bodies and Darcy permeability parameters, however assuming an infinite supply of binder (Bao and Evans, 1991). Somasundaram et al. accounted for a decreasing binder concentration, but employed a purely 1D model without a swelling phase (Somasundaram et al., 2008), different from the thin paper used herein and radially expanding liquid.

The aim of this work is to advance understanding of capillary induced fat migration from seasoning compacts into paper packaging by assessing flow behaviour in the compact and paper to provide a predictive first-principle physical model. The remainder of this article first establishes the model before describing auxiliary experimental methods to measure model parameters, terminating with model validation from a mimicking physical experimental setup.

2. Materials and methods

2.1. Experimental design

To investigate and model the effect of microstructural changes on fat migration behaviour in seasoning compacts, model formulations were prepared from 95 w/w% salt (Südwestdeutsche Salzwerke AG, Heilbronn, Germany) and 5 w/w% red-stained palm kernel fat (Isega, Aschaffenburg, Germany). Palm kernel fat was fractionated at 30 °C by centrifugation to obtain the liquid fraction. Sample preparation carried out at 20 °C prevented migration occurring before testing at 30 °C. 7 different formulations with varying size fractions in the particle size range $5 \leq d_{50} \leq 500 \mu\text{m}$ and different mass fractions were prepared according to the ternary design (Fig. 1). d_{50} is the volume-based median particle size of a distribution, meaning that for each of the three distinct size classes $d_{50} = 5$, $d_{50} = 250$, and $d_{50} = 500 \mu\text{m}$, 50 % of the particle volume (or mass) lie above and below the median, as shown in Fig. 2 for the initial (dashed line) and formulated (solid line) particle size classes. Coarse and medium size fractions were obtained by sieving (Retsch, Haan, Germany), and the fine fraction was obtained by jet milling (Tecnologia Meccanica, Treviolo, Italy). While particle shape influences particle packing and channel morphology, resulting parameters such as permeability or pore size distribution were evaluated in the final

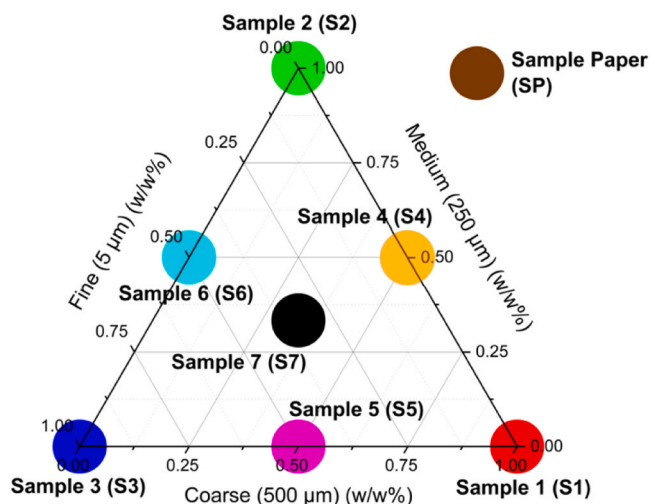


Fig. 1. Ternary design for the 7 seasoning compact formulations and paper sample with varying particle size and mass fractions (colour coding is consistent with graphs throughout this work).

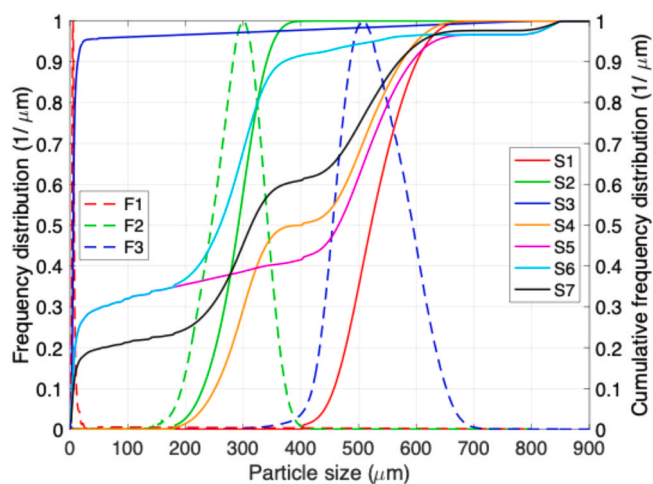


Fig. 2. Normalised differential (dashed lines) and cumulative (solid lines) particle size distribution of the initial three particle size fractions and resulting samples 1–7 by physical mixing.

compact, not individually as a function of particle shape. 4 g of salt mix of each sample were compacted to a fixed height of 13.5 mm in a square 14×14 mm die (Instron, Norwood, MA, US) resulting in different compaction loads for each formulation, and were placed on blotting paper (Whatman 3MM, Maidstone, UK) to mimic packaging paper for 1 week undergoing fat migration testing. Commercially available seasoning compacts are usually in rectangular tablet or cube shape, and the cubic shape was used in this work for relevance to an applied product. Blotting paper tests in which the lipid matrix is in contact with a wicking paper are common and standardised practice from pet food to lubrication research (Lange et al., 2002; Zhang et al., 2020; ISO, 2008). While the interface between lipidous matrix and paper may have an impact on channelling and preferential flow paths, consistency of the paper, of the sample mass (solid samples) or contact force (paste or liquid samples), and of the contact area enable minimisation of the error.

2.2. Fat migration model

Commercially available seasoning compacts are usually in rectangular tablet or cube shape and packaged in folded wrappers from all 6

sides. To reduce model complexity, our setup described previously was used (Dewulf et al., 2024b) placing the compact salt + fat compact with one side onto a sheet of packaging substrate resting on a glass slide, reducing the setup to 1D flow downwards in the compact, and 1D radial axisymmetric flow in the paper; a setup termed quasi 2D (Fig. 3). For mathematical simplification to avoid direction changes from vertical to horizontal in the paper, the model assumes the compact to sit inside the paper material. This is resulting in a small deviation from the physical model at early time scales, yet experiments not shown suggested that vertical breakthrough of fat through thin paper is much faster than radial horizontal flow, justifying this simplification. Even for the slowest migrating sample 3, the vertical breakthrough was estimated as a 1D slab from data below to be about 1 day, a small error in relation to the small fat stain magnitude. Further, the compact-paper interface is assumed to be circumferential, for which the cubic compact with side lengths S and cross-sectional area A_c is converted to an interfacial radius r_i via $A_c = S^2 = \pi r_i^2$.

The real fat flow pattern through the porous medium during fat migration is likely channelled due to pore connectivity. Instead, a simple drainage setup is assumed with initially isotropic fat distribution in the compact and a fat-free paper. Atmospheric pressure p_0 surrounds the setup. The fat front in the compact is assumed to be level at all times, with the compact-side pressure just inside it denoted p_c . Fat migration measurements showed that at such small capillary sizes, gravity is negligible, and thus the compact-side pressure just inside the compact-paper interface remains p_c as well. The possibility to neglect gravity was further confirmed with the Bond number from $Bo = R^2 \Delta \rho g / \sigma$, where R is the particle radius, $\Delta \rho$ is the pressure difference between air and fat, g is the gravitational constant, and σ is the fat surface tension. Because $Bo = 0.02 < 1$ for the coarsest particle radius of 250 μm , gravitational effects were neglected (Willett et al., 2007).

The paper-side pressure at the interface is p_i and the paper-side pressure at the fat front in the fibrous medium is termed p_p . By continuity of pressure, the pressure differentials must balance with the atmosphere according to

$$p_0 + (p_c - p_0) + (p_i - p_c) + (p_p - p_i) + (p_0 - p_p) = p_0 \quad (1)$$

As proposed in our previous work (Dewulf et al., 2024b) the thermodynamic driving force is the difference in capillary pressure or suction between the paper and compact, which hence needs to be quantified. Capillary pressure is defined as the pressure difference across the liquid-gas meniscus surrounded by a solid wall, which applies in this scenario where salt particles create interstitial capillaries or pores partly saturated with fat. The smaller the pore size, the larger the capillary suction. Summing over the entire cross-sectional area and assuming a concave meniscus (higher gas pressure), the compact-side capillary pressure $p_{cap,c}$ is thus

$$p_c - p_0 = p_{liq} - p_{gas} = - p_{cap,c} \quad (2)$$

Analogously, the paper-side capillary pressure $p_{cap,p}$ is the difference across the fat-air meniscus in paper, similarly assuming a concave meniscus

$$p_0 - p_p = p_{gas} - p_{liq} = p_{cap,p} \quad (3)$$

While thermodynamic feasibility depends on the direction of net capillary pressure, fat migration kinetics towards equilibrium depends on the resistance to fat flow, which is similarly affected by the pore size. The smaller the pores, the larger the wall friction that the fat is exposed to. Capillarity and Kinetics thus operate in juxtaposition where capillary suction and thus thermodynamic driving force increases with smaller pores, yet the kinetic resistance also increases with reduced channel size.

Resistance or its reciprocal, the permeability K is frequently used to describe the resistance to flow passage according to Darcy (1856). For fat migration in the compact, the pressure differential dp over the superficial flow distance dl is proportional to the fat viscosity μ and the superficial velocity $v(l)$ divided by a proportionality constant K_c , the permeability of fat in the compact (for Newtonian fluids).

$$\frac{dp}{dl} = \frac{\mu}{K_c} v(l) \quad (4)$$

Integrating between the interface and the compact-side fat front at length l_c yields the pressure loss due to resistance for fat flowing with velocity v_c . v_c is independent of the fat length l in the compact.

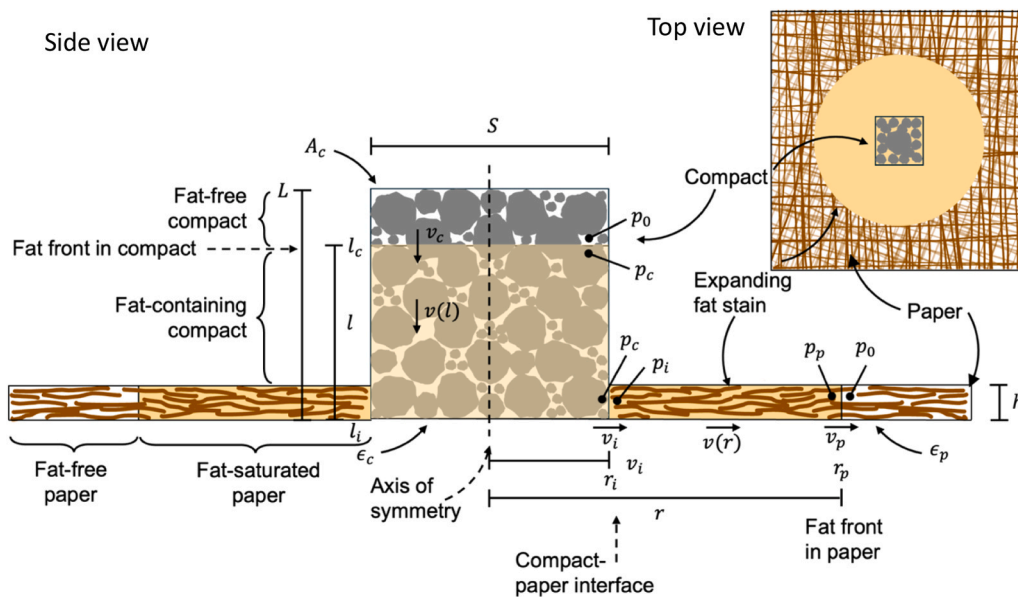


Fig. 3. Setup of quasi-2D axisymmetric capillary flow model for fat migration from model seasoning compact into fibrous paper substrate. A_c - compact cross-sectional area, ϵ_c - compact voidage, ϵ_p - paper voidage, h - paper height, l - length, l_c - fat length in compact, l_i - fat length in compact at interface, L - compact length, p_0 - atmospheric pressure, p_c - fat pressure in compact, p_i - fat pressure at interface, p_p - fat pressure in paper, r - paper fat stain radius, r_i - fat stain radius at interface, r_p - fat stain radius at fat front, S - compact side length, $v(l)$ - superficial fat velocity in compact, $v(r)$ - superficial fat velocity in paper, v_c - superficial fat front velocity in compact, v_i - superficial fat velocity at interface, v_p - superficial fat front velocity in paper.

$$p_i - p_c = \frac{\mu}{K_c} v_c l_c \quad (5)$$

Analogously the pressure loss between the paper-side fat front and the compact-paper interface is calculated from the permeability in paper K_p for fat flowing at superficial velocity $v(r)$.

$$\frac{dp}{dr} = \frac{\mu}{K_p} v(r) \quad (6)$$

Due to 2D radial expansion, fat velocity in paper $v(r)$ varies with the fat stain radius r , but can be written in terms of constants parameters at the paper-side fat front as $v(r)r = v_p r_p$, resulting in an expression for the paper-side pressure loss

$$p_p - p_i = \frac{\mu}{K_p} v_p r_p \ln\left(\frac{r_p}{r_i}\right) \quad (7)$$

As the pressure balance (Eq. 1) now depends on two interdependent lengths, l_c and r_p , mass conservation can be used to represent one length in terms of the other, where the true fat mass flow rate $v_c \epsilon_c \rho$ entering the interfacial area must be the same as the mass flow rate at the fat front in the paper. ϵ_c and ϵ_p are the compact and paper voidages respectively.

$$v_c \epsilon_c \rho \pi r_i^2 h = v_p \epsilon_p \rho 2\pi r_p h \quad (8)$$

where h is the paper thickness. Also, by conservation of mass, the initial total mass of fat in the cube at time $t = 0$ is equal to the sum of fat in the cube and paper at any time $t \geq 0$

$$L \epsilon_c r_i^2 = l_c \epsilon_c r_i^2 + h \epsilon_p r_p^2 \quad (9)$$

Substituting into Eq. 7 therefore yields an expression for the paper-side pressure drop in terms of compact-side fat length l_c .

$$p_p - p_i = \frac{\mu}{K_p} \frac{v_c \epsilon_c r_i^2}{2h \epsilon_p} \ln\left(\sqrt{\frac{\epsilon_c}{h \epsilon_p}} (L - l_c)\right) \quad (10)$$

Similarly, for the case in which the pressure balance (Eq. 1) needs to be written in terms of fat stain radius in the paper, using the same substitution (Eq. 5), the compact-side pressure loss can be written in terms of r_p .

$$p_i - p_c = \frac{\mu}{K_c} v_p \frac{2\epsilon_p r_p h}{\epsilon_c r_i^2} \left(\frac{L \epsilon_c r_i^2 - h \epsilon_p r_p^2}{\epsilon_c r_i^2}\right) \quad (11)$$

In the continuity of pressure relation (Eq. 8) the individual terms can now be populated to express fat migration in the cube and paper. Solving the pressure relation with substitutions made, yields the relationship for the compact-side fat superficial velocity v_c as a differential equation in terms of l_c . It is again visible that velocity is the ratio between thermodynamic driving force, being the net capillary pressure in compact and paper, divided by the sum of kinetic resistances in both porous media.

$$v_c = \frac{dl_c}{dt} = \frac{p_{cap,c} - p_{cap,p}}{\frac{\mu}{K_c} l_c + \frac{\mu}{K_p} \frac{\epsilon_c r_i^2}{2h \epsilon_p} \ln\left(\sqrt{\frac{\epsilon_c}{h \epsilon_p}} (L - l_c)\right)} \quad (12)$$

While the model assumes a simple level drainage flow out of the compact, the true flow pattern may be different. Yet, a concentration c at each time point, averaged over the entire compact length can be found from the initial fat concentration of 5 w/w% as $c = 5(l_c/L)$.

Expressing the paper-side fat superficial velocity v_p as a differential equation in terms of r_p yields a similar relationship

$$v_p = \frac{dr_p}{dt} = \frac{p_{cap,c} - p_{cap,p}}{\frac{\mu}{K_c} \frac{2\epsilon_p r_p h}{\epsilon_c r_i^2} \left(\frac{L \epsilon_c r_i^2 - h \epsilon_p r_p^2}{\epsilon_c r_i^2}\right) + \frac{\mu}{K_p} r_p \ln\left(\frac{r_p}{r_i}\right)} \quad (13)$$

While the relationship is in terms of the radius r_p , the corresponding fat stain area A_p in the paper is then found from $A_p = \pi r_p^2$.

2.3. Capillary sorption

Physical sorption tests have previously been used to evaluate microstructural parameters such as capillary pressure and permeability of fibrous structures as in resin moulding (Pucci et al., 2015), or in beverage powder beds for reconstitution (Kammerhofer et al., 2019, 2018). Liquid imbibition into a powder bed however flows in the opposite direction to oil migration or leakage out of a powder structure, which is much less reported in literature. It is known that particle structures with rough surfaces or chemical heterogeneity cause velocity variations of the contact line of the wetting liquid. This results in a contact angle hysteresis during between advancing and receding contact angles, a phenomenon reported when the particles are moving (Willett et al., 2003). The capillary sorption setup here is for liquid fat imbibition into a stationary medium, and the evaluated parameters from the sorption tests are therefore also used for leaking fat flow in the migration model.

For imbibition into fat-free compact, for each sample, 1 g of salt was compacted to the same density of 1.5 g/cm³ as for the cubic samples in a hollow aluminium cylinder of cross-sectional area 78.5 mm² (Fig. 4). In a tensiometer (Krüss, Hamburg, Germany), the sample holder was lowered at a rate of 5 mm/min onto a free surface of liquid fat at an environmental temperature of 30 °C until contact was made, and the mass², m^2 , of imbibed fat recorded against time t until full pore saturation. Spontaneous fat imbibition due to capillary suction in paper was measured the same way on a 10 mm wide strip of paper. Experiments were repeated with (Merck, Darmstadt, Germany) and tared for the empty sample holder.

To link the fundamental microstructural properties with parameters obtained mathematically, the simplified Washburn equation is derived. When considering the liquid fat in a single capillary tube of radius r_{cap} (Fig. 4a), the advancing contact angle between the meniscus and capillary walls is θ , and the pressure difference across the meniscus can be calculated from the Young-Laplace equation (Young, 1805; Laplace, 1805)

$$p_{gas} - p_{liq} = p_{cap} = \frac{2\sigma \cos\theta}{r_{cap}} \quad (14)$$

The frictional pressure loss Δp for fat with viscosity μ to flow a certain distance l through the capillary, safely assuming a laminar flow regime, is taken from the Hagen-Poiseuille equation (Hagen, 1839; Poiseuille, 1839)

$$\frac{dl}{dt} = \frac{r_{cap}^2 \Delta p}{8\mu l} \quad (15)$$

Washburn was the first to combine Eqs. 14 and 15 by substituting p_{cap} for Δp to obtain an expression for flow velocity dl/dt for capillary rise from a free surface (Washburn, 1921)

$$\frac{dl}{dt} = \frac{2\sigma \cos\theta r_{cap}}{4\mu l} \quad (16)$$

In the above experimental sorption setup, the porous media are considered bundles of capillary tubes with varying radii, and hence the apparent advancing contact angle θ_a is used (Fig. 4b, c). Replacing the length with the mass equivalent, the simplified Washburn equation yields

$$\frac{m^2}{t} = \frac{c^2 A^2 r_{cap} \rho^2 \sigma \cos\theta_a}{4 \mu} = C \frac{\rho^2 \sigma \cos\theta_a}{\mu} \quad (17)$$

where m is the fat mass, A is the cross-sectional area of the sample holder, ρ is the fat density, and C is called the geometric porous medium factor, which groups variables that are purely dependent on the porous medium microstructure, but independent of the migration substance. The form of Eq. 17 is convenient as it results in an initially straight line when plotting m^2 against t unless microstructural changes such as

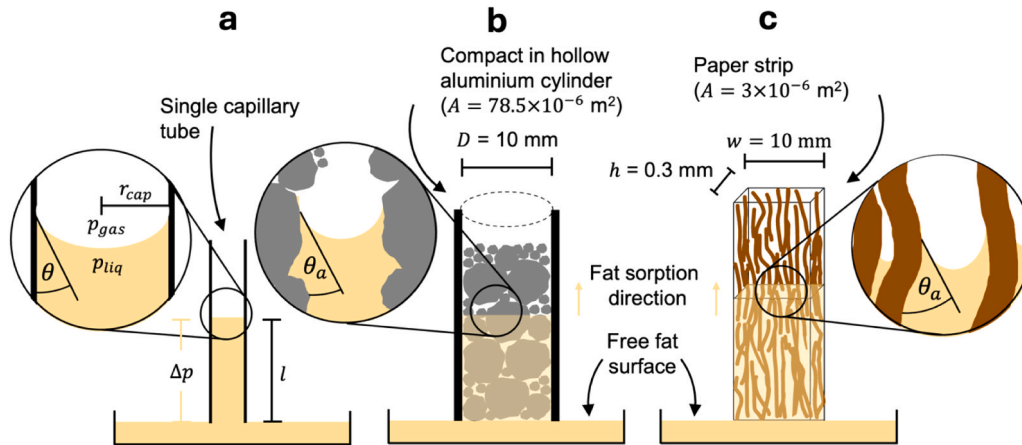


Fig. 4. Sorption test setup for imbibition from free surface into a) single capillary tube, b) salt compact and c) paper sample.

swelling occur. By performing a sorption experiment with a liquid of virtually 0 contact angle, such as hexane, the geometric porous medium factor can be determined from the sorption line gradient.

Eq. 4 earlier defined the permeability according to Darcy in terms of flow path length l . Writing the mass equivalent and replacing Δp with p_{cap} yields Darcy's equation resembling the Washburn sorption profile from which Kp_{cap} be found.

$$\frac{m^2}{t} = \frac{\rho^2 c^2 A^2}{\mu} K p_{cap} \quad (18)$$

2.4. Microtomography

As the factors in Kp_{cap} cannot be deconvoluted from each other, it is practical to complement sorption measurements with other techniques, such as x-ray microtomography. X-ray scans were acquired for each sample at 70 kVp, 114 μA , 8 W with 0.5 mm Al filter and exposure time 1000 ms per acquisition (ScancoMedical, Brüttisellen, Switzerland). The field of view was 7 mm diameter with a stack height of 500 μm at 1.5 μm voxel size. To obtain the pore size distribution, thresholded and binarized tomographic images were analysed with the Münch algorithm in Fiji/ImagJ (Münch and Holzer, 2008), which essentially fills pores with the largest possible spheres and populates a pore size distribution. Pore size class intervals were set from 1.5 μm to 1000 μm in 10 μm intervals, and the median pore size evaluated from the cumulative pore size graph. Capillary pressure was then calculated from the Young-Laplace Eq. 14, using parameters evaluated from the sorption tests.

2.5. Fat migration tests

Model validation was performed by a physical setup of the model in Fig. 3 by placing sample food compacts onto paper substrate at 30 °C for 1 week and evaluating the surface fat concentration and fat stain area at time 0, 0.5, 1.5, 2.5, 4.5, and 6.5 days.

2.5.1. Raman chemical imaging

To measure fat concentration c on the compact surface, the method of Raman chemical imaging was employed described previously (Dewulf et al., 2024b) (Fig. 5a). As palm kernel fat and salt have similar refractive indices, differentiation by visible light imaging is unsuitable. Techniques targeting the lipid phase such as staining with fluorescent Nile red are possible solutions (Greenspan et al., 1985). Instead, to avoid changing the fat properties, Raman chemical imaging was used as a new technique in food fat migration studies. Due to the use of a single point Raman laser probe, it was possible to control incident laser beam intensity better than using white light, leading to more consistent measurements. Compared to bulk techniques such as gravimetry, imaging

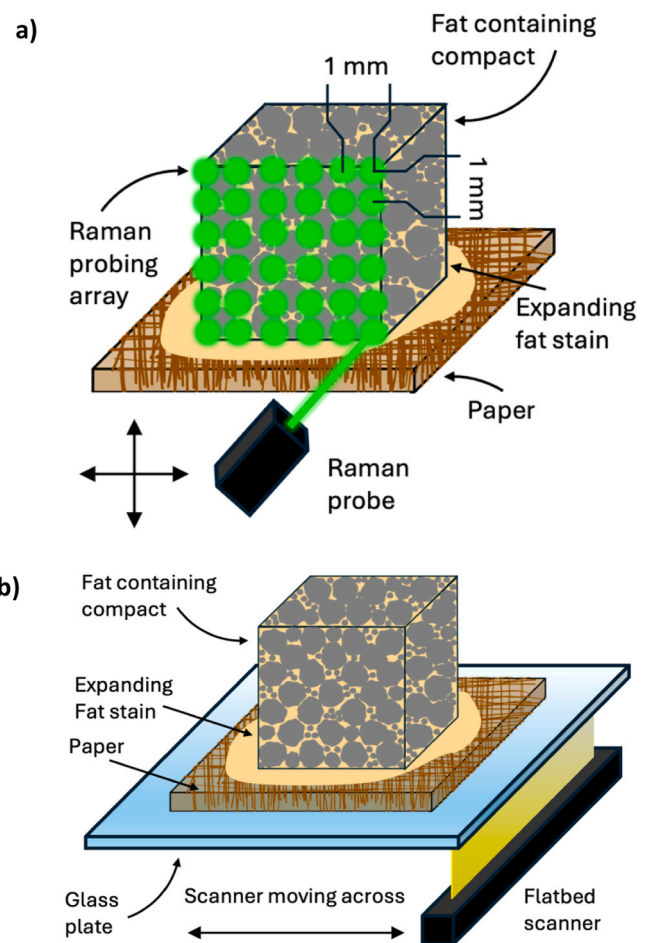


Fig. 5. Raman chemical imaging setup for model validation: a) Raman chemical imaging of compact surface, b) optical scanning of fat stain on paper.

techniques provide additional spatial granularity.

Briefly, a Raman laser point source (532 nm, continuous wave diode, 94 mW, Oxixius, Lanion, France) was used with a focal point resolution of 1.7 μm estimated from the Rayleigh criterion $R = 0.61\lambda/NA$ where R is the resolution, λ the laser wavelength, and NA is the numerical aperture of the $2 \times$ lens of 0.19. The compact sample surface was scanned in a 10–12 mm grid at 1 mm increments, by moving the sample on a motorized stage (Märzhäuser, Wetzlar, Germany), resulting in 132 individual spectra of the sample surface acquired between Raman shifts of

0 and 3000 cm^{-1} . Spectra were acquired for $3 \times 5 \text{ s}$ for each probing point in a spectrometer (iHR320) with 1800 groves/mm, 500 nm blaze grating and CCD camera (Synapse, Horiba, Longjumeau, France).

2.5.2. Optical stain imaging

To measure the extend of fat stain area A_p in the paper, the method of optical stain imaging and quantification was employed described previously (Dewulf et al., 2024b) (Fig. 5b). A flatbed scanner (LiDE300, Canon) was used at 1200 dpi resolution to scan the underside of the paper substrate. The area of fat stain was automatically quantified via a Fiji/ImagJ macro by discrimination between the red fat stain and white paper. Paper samples were only placed on the scanner bed for the short minute-long duration of imaging. In addition, perimeter of the fat stains was calculated and the roundness calculated by $O = 4\pi A_p/P^2$ where O is the fat stain roundness and P is the fat stain perimeter.

3. Results and discussion

3.1. Capillary sorption

Sorption tests were performed to evaluate microstructural parameters required for the capillary model Eqs. 12 and 13. Fig. 6a shows the sorption profiles of mass^2 against time for palm kernel fat at 30°C for all 7 salt compact samples and the paper sample. All samples reached full saturation after at most 2500 s, beyond which a plateau indicates no more fat uptake. Different final plateau masses indicate varying void fractions ϵ due to different salt particle sizes in each formulation. The gradient of the initial straight section was obtained as m^2/t and is tabulated in Table 2. Samples 1, 2, and 4 with coarse and medium salt particles imbibe fat equally within a few seconds of contact with the free surface, indicating rapid flow of fat between pores. For samples formulated with a fine salt fraction, the fat uptake rate to saturation is significantly reduced. Sample 5 consisting of a 50/50 w/w% coarse/fine fraction reaches saturation only after 1000 s, and with a medium/fine ratio (sample 6) equilibrium time extends to 1500 s. The 1/3 coarse/medium/fine mix (sample 7) lies between the former, while with purely fine salt as in sample 3, the gradient is the shallowest and reaches equilibrium after only 2000 s. Initial uptake of fat by the fat-free unsaturated virgin paper sample SP is fast initially, and a plateau is only reached at longer time scales beyond $\sim 2500 \text{ s}$ (42 min). The steady increase in fat uptake is attributed to the fibres swelling and inducing a capillary suction by newly created free volume (Pucci et al., 2016; Vo et al., 2020). Approaches to extract microstructural information from swelling samples differ in literature: one approach is to account for fast uptake at early timescales into the unsaturated pores, and accounting for a saturated uptake at longer timescales, more representative of the slow migration process occurring in the present setup (Pucci et al., 2016; Vo et al., 2020). As measurement timescales in the fat staining tests were in 12-hour increments, the effect of swelling at several minute time scales was expected negligible, also reported in the inkjet printing literature (Wong et al., 2023).

Sorption experiments and acquisition of the capillary rise gradient m^2/t were also repeated for hexane (Fig. 6b) in order to calculate the geometric porous medium factor C from Eq. 17, assuming $\theta_a = 0$ for hexane (Table 1). As C depends on microstructure only and not on liquid properties, a clear trend is visible of decreasing C with smaller microstructural features from 5.3 mm^5 for the coarse salt sample to $7.5 \times 10^{-2} \text{ mm}^5$ for fine sample, reducing to $2.9 \times 10^{-3} \text{ mm}^5$ for paper. The apparent advancing contact angle of palm kernel fat on the other hand is predominantly dependent on the fat properties and thus varies between 73° and 82° across all samples. The void fraction of each compact was calculated from the final mass of fat imbibed. The overall trend across samples is that ϵ increases with decreasing particle size fractions from approximately 0.3 for sample 1–0.5 for samples 3. Saturated paper contained about 60 v/v% voidage (Table 2). Using the

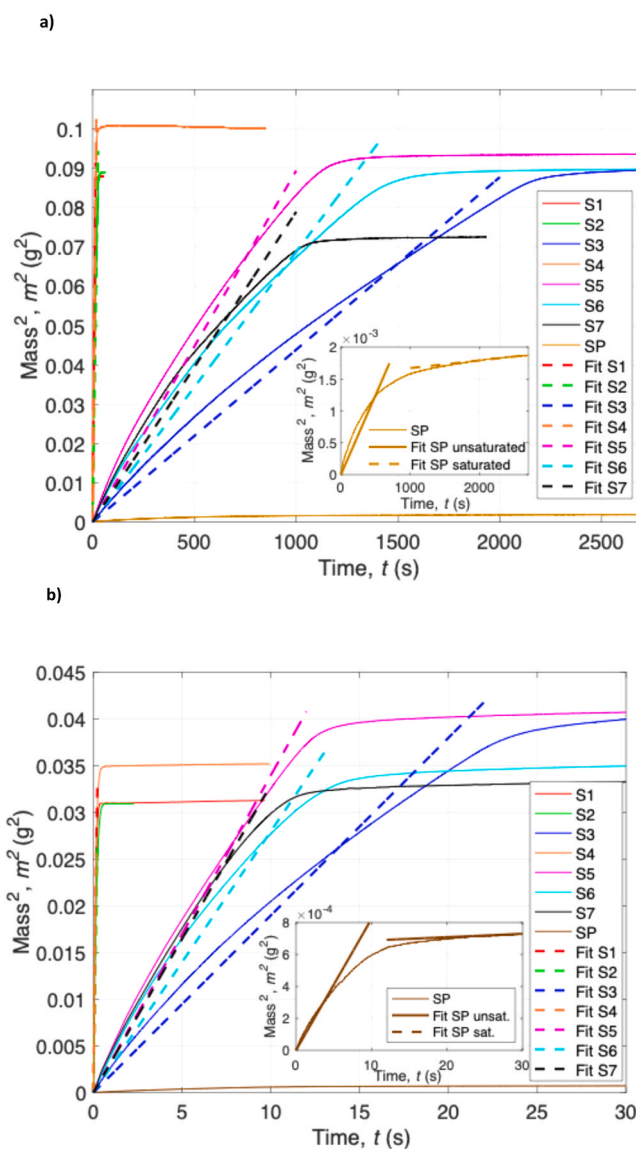


Fig. 6. Sorption profiles for a) hexane, and b) molten palm kernel fat imbibition into salt compact and paper samples. Single line is average of triplicate repeats.

Table 1

Hexane and palm kernel fat properties measured at shelf-life test conditions of 30°C .

	Density (kg/ m^3)	Surface tension (N/ m)	Viscosity (mPa. s)
Hexane	658	0.018	0.3
Palm kernel fat	900	0.03	6

evaluated physical and microstructural properties, the convoluted capillary pressure-permeability Kp_{cap} was found from Eq. 18.

3.2. Microtomography

Fig. 7 shows 3D views of the reconstructed microtomographic images for the salt + fat compacts, and paper samples, where the fat-free unsaturated paper sample was analysed after rapid fat uptake from sorption test, and the saturated sample after a week from actual validation experiments. Salt, porosity, and paper fibre phases were digitally colour

Table 2
Microstructural parameters obtained from microtomography and sorption tests.

	Sample 1	Sample 2	Sample 3	Sample 4	Sample 5	Sample 6	Sample 7	Paper unsaturated	Paper saturated
$(m^2/t)_{\text{hexane}}$ (g ² /s)	1.38×10^{-1}	1.06×10^{-1}	1.95×10^{-3}	1.96×10^{-1}	2.85×10^{-3}	2.53×10^{-3}	3.00×10^{-3}	7.65×10^{-5}	2.11×10^{-6}
$(m^2/t)_{\text{fat}}$ (g ² /s)	4.05×10^{-3}	4.80×10^{-3}	4.06×10^{-5}	6.55×10^{-3}	6.89×10^{-5}	6.22×10^{-5}	7.35×10^{-5}	2.11×10^{-6}	1.13×10^{-7}
C (mm ²)	5.30	4.06	7.46×10^{-2}	7.48	1.09×10^{-1}	8.99×10^{-2}	1.15×10^{-1}	2.89×10^{-3}	8.06×10^{-5}
θ_a (°)	79.4	73.3	82.3	77.5	80.1	79.8	80.9	79.8	69.7
r_{50} (μm)	93.1	49.1	3.5	54.2	7.3	6.5	7.2	11.6	3.1
P_{cap} (Pa)	118	350	1350	240	810	1050	1320	1350	13500
ϵ (-)	0.33	0.37	0.48	0.28	0.43	0.48	0.34	0.60	0.50
K (m ²)	3.7×10^{-10}	1.2×10^{-10}	1.6×10^{-13}	4.1×10^{-10}	5.6×10^{-13}	3.2×10^{-13}	5.8×10^{-13}	4.8×10^{-12}	2.33×10^{-14}

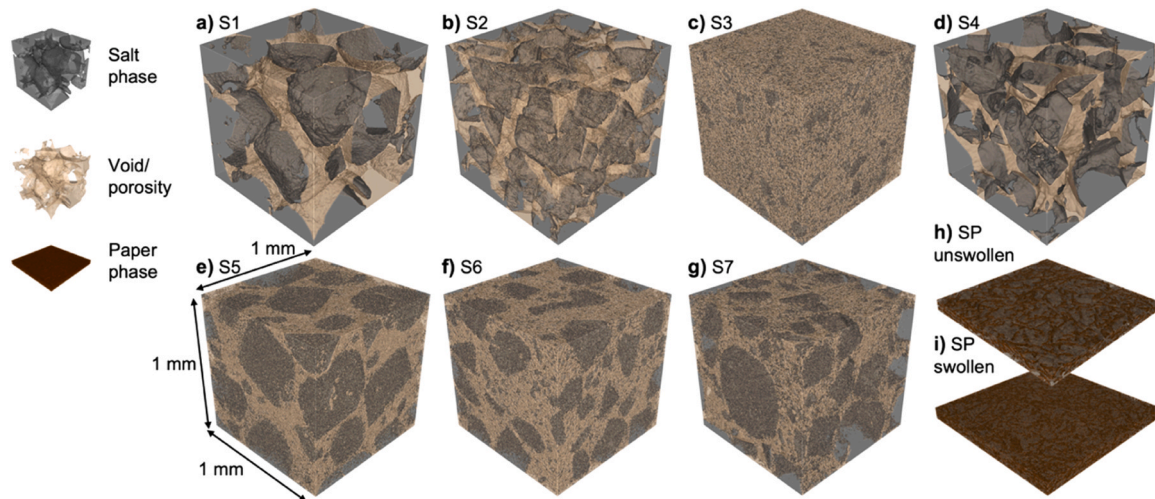


Fig. 7. Reconstructed x-ray microtomography images of a) -g) compact (S1-S7), unswollen (h) and swollen (i) paper samples depicting the salt, porous, and paper fibres phases. While the entire samples were scanned, only cutout sections of 1 mm are shown for clarity. Salt and fat compacts illustrate the different microstructures resulting from varying the salt particle size and fraction. Qualitatively, salt particles are rounded with some angularity. X-ray tomography imaging was used to evaluate pore size distribution.

coded and rendered translucent at 50 % opacity for better differentiation compared to the original black/white image.

For the salt + fat compacts, visual inspection can give qualitative indication of the microstructure and pore size. For S1 consisting of a coarse salt fraction, large solid particles (grey) are visible that resulted in large interstitial channel size (beige). This trend is maintained for sample 2 consisting of a purely medium salt fraction. In S3 pore size is much narrower owing to the smaller salt particles, yet due to increasing surface energy, finer particles disperse less and tend to stick to each other more due to larger van der Waals forces, which explains the larger agglomerates in samples containing a fine 5 μm salt fraction. Expectedly in S4, the 50/50 coarse/medium salt fractions result in somewhat narrower porosity than S1 due to more efficient packing as smaller particles can fill the gaps between larger ones. S5 being a mix of coarse and fine salt fractions has distinct visible coarse particles but a pore structure similar to S3, suggesting that the fine particles are dispersed between the larger ones. Comparing the opacity of the void phase in S1 with S5, the latter void phase is less transparent as in the 3D representation grey pixels from dispersed salt interrupt the continuous void phase in smaller space intervals, rendering it opaque, a trend also observed in S6. The ternary salt fraction mix S7 shows a packing regime with features of S1–3 with clear large, medium, and finely dispersed small salt particles. Comparison of the unswollen and swollen paper samples shows that pore sizes seem larger in the fat-free unswollen sample, explaining the rapid fat uptake as frictional resistance in larger channels is low, as quantified in Fig. 6b. As the paper swells and saturates, pores visibly narrow and create higher resistance to interstitial fat flow, decreasing the uptake rate at longer sorption times.

Fig. 8 shows the normal and normalized cumulative capillary pore radius distribution of the porous phase evaluated from the 3D microtomography images. Cumulative pore size distributions allow for better comparison when normalized, as shown on the secondary ordinate. The area under the curve of the normal pore size distribution represents the total pore volume. Due to the logarithmic abscissa, curves are shallower towards the large end of pore radii of $r_{\text{cap}} > 20\mu\text{m}$, which is the case for S1, 2, and 4 consisting of wide interstitial channels. Samples 3, 5–7, and paper on the other hand have distinctively more pores in the small radius range $r_{\text{cap}} < 20\mu\text{m}$.

Pore size decreases with increasing fines fraction causing the S-shaped cumulative curves to move leftward following the same trend as discussed qualitatively from the 3D tomograms. Median pore r_{50} values were evaluated at 0.5 cumulative normalized pore volume and are tabulated in Table 2. Based on median radii, capillary pressures were calculated for each sample from the Young-Laplace Eq. 14 and also populated in the table, with the assumption that the median pore radius is a valid representation when the particulate sample is simplified into a bundle of capillary tubes. S1 with the largest proportion of coarse salt particles contains the largest median radius of $r_{50} = 93\mu\text{m}$ and therefore the smallest capillary pressure of 117 Pa. In line with previous trends, S2 and S4 produce the next smaller pore radii of 49 and 54 μm resulting in 350 and 239 Pa capillary pressure. Interestingly S4 with an expectedly more efficient particle packing due to a bimodal particle size distribution has a larger median pore radius than monomodally distributed S2, which could be attributed to particle shape effects playing a role in packing beyond mere particle size. Following the same trend as in the fat sorption tests, S5 is next slowest owing to a coarse/fine particle mix,

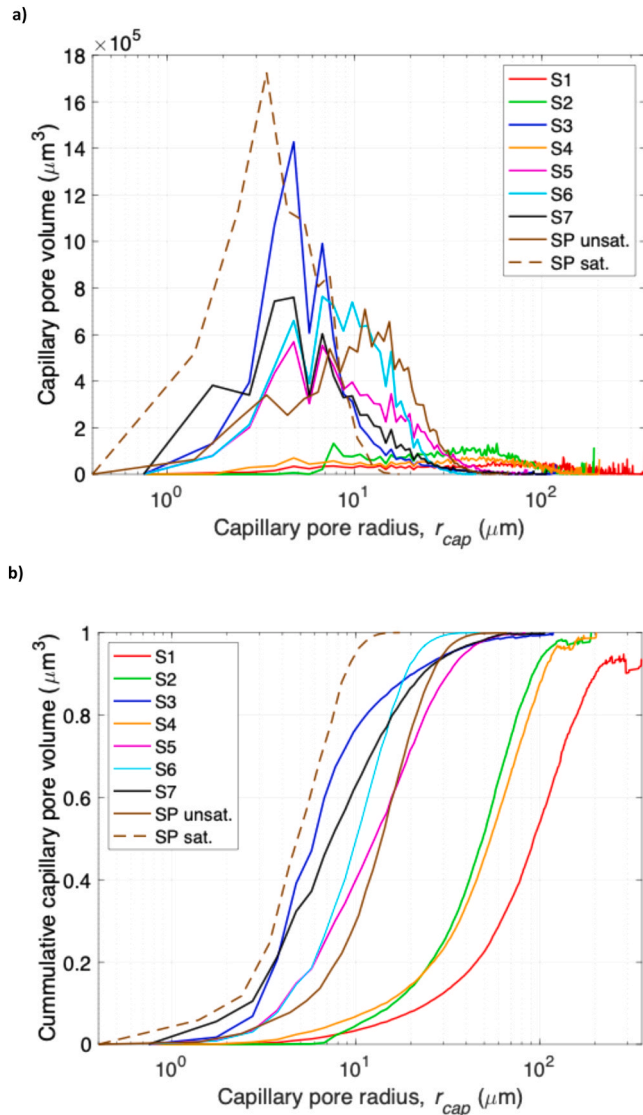


Fig. 8. (a) Normal and (b) cumulative capillary pore radius distribution of porous phase in compact, unsaturated and saturated paper samples measured by 3D microtomography.

yielding an $r_{50} = 7.3\mu\text{m}$ and $p_{cap} = 810\text{ Pa}$. Replacing the coarse with a medium salt fraction in S6 resulted in the next smallest pore radius of $6.5\mu\text{m}$ with p_{cap} of 1047 Pa . The ternary coarse/medium/fine mix S7 is expected to show an efficient packing regime and thus results in $r_{50} = 7.2\mu\text{m}$, giving rise to a capillary pressure of 1320 Pa . S3 from purely fine salt yields the smallest interstitial pores at $3.5\mu\text{m}$ radius which are close to the d_{50} particle size of $5\mu\text{m}$. The resultant capillary pressure is hence largest in S3 with 1348 Pa . Fat-free unsaturated virgin paper was evaluated to have an r_{50} of $11.6\mu\text{m}$, similar to compact S5, resulting in a p_{cap} of 1348 Pa , while the swollen saturated paper was found to have a smaller r_{50} of $3.1\mu\text{m}$ resulting in a much larger p_{cap} of 13.5 kPa . The theoretically opposite trend of sorption flow rate and capillary pressure is thus reflected experimentally.

3.3. Raman chemical imaging

Raman chemical imaging of the compact surface was performed to physically validate the fat concentration c on the compact-side of the mathematical capillary model. Raman spectroscopy is especially applicable in biphasic systems such as salt and fat, where crystalline salt is Raman inactive, yet covalently bonded atoms in palm kernel fat produce

a Raman signal, which can be differentiated from each other as contrasted in Fig. 9a. As palm kernel fat is generally a mixture of mostly lauric, myristic, and oleic acids, there is no single spectrum but instead multiple peaks with molecular vibrations associated with the different functional groups (Fig. 9b). Annotations on the spectrum indicate literary accepted Raman shifts and their origins in palm kernel fat (De Géa Neves and Poppi, 2018; Souza et al., 2019), giving confidence in the acquisition method. The raw spectrum is corrected by subtracting the background, salt and 2nd order polynomial baseline correction for fluorescence, and the remaining integral intensity is evaluated (Fig. 9c). The surface palm kernel fat concentration at each probing point of each sample at each time point is evaluated via the calibration curve (Fig. 9d).

Fig. 10 shows the calibration curves for each compact formulation. As an optical technique, Raman spectroscopy is extremely sensitive to rough surface morphology as explained in the Munke-Kubelka theory (Kubelka, 1931; Miranda et al., 2014; Schrader and Bergmann, 1967). In the present case, as the laser beam resolution ($1.7\mu\text{m}$) is much smaller than even the smallest particle size of $5\mu\text{m}$, light diffraction heavily depends on the compact formulation from different salt particle size fractions. To control for different extents of diffuse reflection as a result of the various microstructures prepared from differing salt particle sizes, a separate calibration curve was constructed for each sample at 0, 1.67, 3.33, 5 and 6.67 w/w% palm kernel fat, with linear trendlines. For five calibration points it is customary to employ a linear as opposed to a non-linear or polynomial calibration curve due to the risk of overfitting. In order to obtain the Raman fat spectrum without background or salt signal interference, the background and salt signal were subtracted, as is customary in literature (El-Abassy et al., 2009). This was performed by acquiring a Raman signal of air and of a fat-free salt compact, and subtracting both intensities at each shift from each acquired Raman sample signal.

General trends observed earlier can also be seen in the calibration curve. S1, 2, and 4 have the shallowest gradients meaning Raman intensity increases slower with increasing fat concentration. The two reasons for this are that with larger particles and pores, the likelihood of the beam probing not a particle but an interstitial pool of pure fat is larger. Also, larger particles cause more diffuse scattering, reflecting less Raman signal into the probe in the same beam path as the incident signal. With increasing fines fraction the compact surface becomes smoother as smaller particles fill the void between larger ones. Consequently, S3 and 5–7 have distinctively higher calibration gradients as more pore sizes tend towards beam resolution as well as an increase in specular signal reflection. Error bars here show standard deviation of Raman intensity over the compact surface and thus rather represent the inhomogeneous nature of surface morphology.

Raman acquisition at each of the 132 probing points of each of the 7 samples at each time point 0–6.5 days were thus converted to a fat concentration. By interpolation between probing points, the full original field of view was reconstructed into a chemical image with fat concentration on the compact surface color-coded between 0 (blue) and initial 5 w/w% (red). For all samples, S1–7 at day 0, the fat concentration is generally isotropically distributed around 5 w/w%. Image artifacts throughout the time series of S2 and S6 exist due to minor misalignment of the initial sample position resulting in some background being captured.

Markedly different trends and thus fat migration patterns occurred for the different compact samples. For S1 with coarse particles the concentration profile decreased from 0 to 6.5 days, where the fat concentration at 0.5 days starts to decrease from the bottom at the contact with paper. The bottom fat drainage continues until at about 2.5 days half the compact has leaked out fat, resulting in the bottom half to have a remaining fat concentration of about 2 w/w% while the top half remains at 3–5 w/w%. At 6.5 days, almost all fat has leaked and the overall surface concentration is 0.5 w/w% fat. S2 follows a similar pattern of bottom leakage with slower gradient than for S1. This is expected as S2 has a higher capillary pressure (350 Pa) and lower permeability

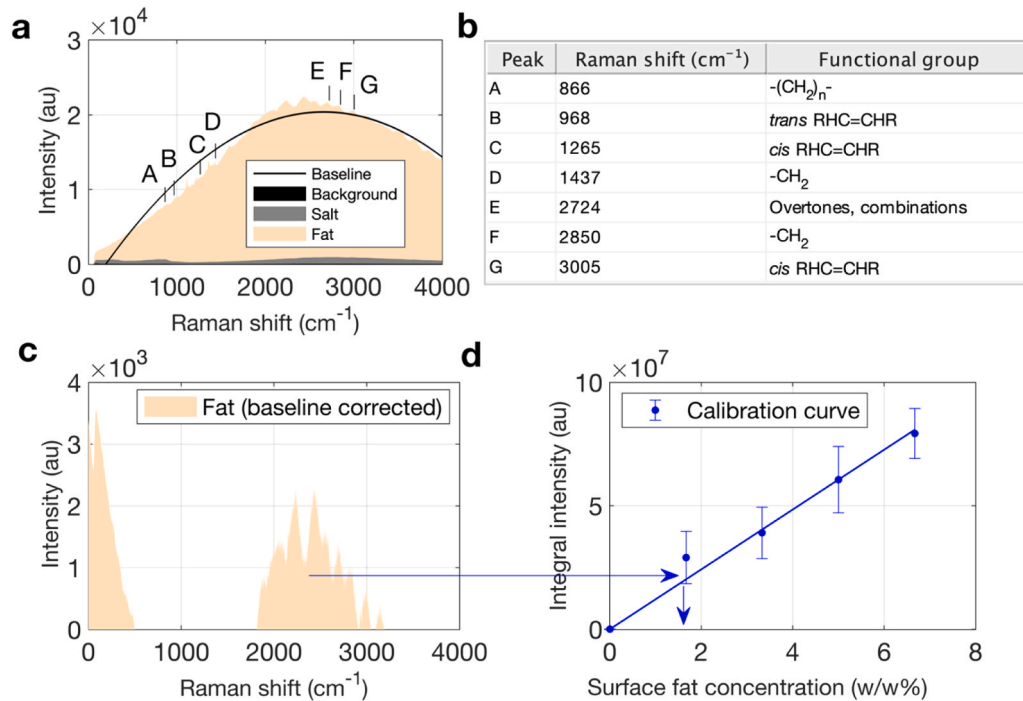


Fig. 9. Method of Raman spectra treatment and conversion to surface palm kernel fat concentration with an exemplary acquired spectrum: a) Raw Raman background, salt, and palm kernel fat spectra with 2nd order polynomial baseline correction, b) Functional groups of palm kernel fat constituents with annotated peaks accepted in literature (De Géa Neves and Poppi, 2018; Souza et al., 2019), c) Palm kernel fat spectrum corrected for background, salt, and baseline, d) Conversion to palm kernel fat concentration on the compact surface via the calibration curve for each formulation.

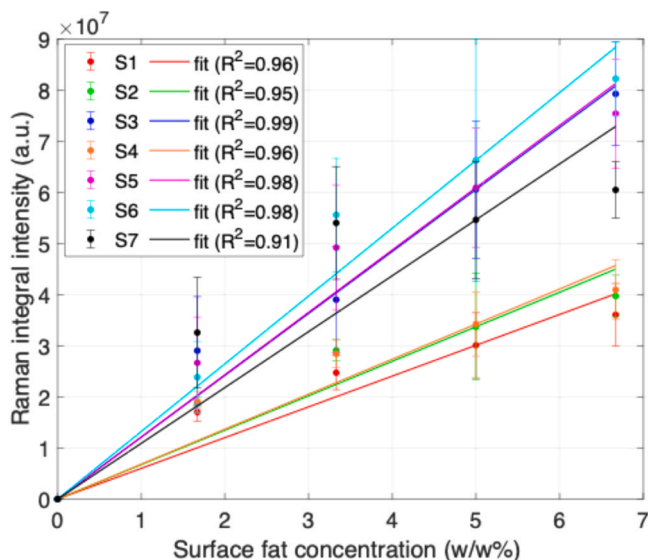


Fig. 10. Calibration curves of Raman intensity with surface fat composition for each sample. Error bars represent ± 1 standard deviation from the mean of the entire acquired image of triplicate samples.

($1.2 \times 10^{-10} \text{ m}^2$), thus acting by retaining more fat in the compact in competition with paper. The gradient of S4 is even slower and the sample does not leak out all fat at the end of the 6.5 day period with a remaining surface fat concentration of 2 w/w%. For S3, Raman chemical images show an unexpected fast disappearance of surface fat without any clear anisotropic or gradient to essentially 0 w/w% at 2.5 days. Following the trend of S1, 2, 4 a higher p_{cap} and lower K should have resulted in slower fat migration. The observed opposite phenomenon could be explained by the increased p_{cap} drawing fat from the surface

into the inside core of the compact, instead of fat migration down into the paper. As Raman is a surface technique the exact location of the fat deeper inside the core cannot be measured. The unexpected fat migration pattern was also observed for S5, 6 and 7 that contained a fine salt fraction. Both compacts lost their surface fat concentration to virtually 0 w/w% after 1.5 days, while for S7 fat migration to 0 w/w% lasted 6.5 days, albeit also with a homogenous and not stratified pattern.

3.4. Paper stain imaging

Paper stain imaging of the paper substrate was performed to physically validate the extent of fat stain area A_p on the paper-side of the mathematical capillary model. While fat stain area was quantified by automated image analysis, it also allows direct qualitative analysis of the quality defects on paper packaging that cause consumer rejection of the food product. Fig. 12a Shows the paper stains for S1–7 at each time 0–6.5 days, analogous to Fig. 11, allowing direct comparison between fat migration in Raman chemical images on the compact surface and the resultant migration behaviour in paper.

S1 shows the largest radial fat stain growth from initially 0 cm² at 0 days to 65 cm² after 6.5 days. This trend is in line with the migration pattern in the Raman chemical images in S1 where surface fat migration is rapid and the fat drainage profile towards the bottom suggests migration into the paper sheet below. Fat stains on paper of S2 and 4 develop slower with final stained areas of 55 and 56 cm², similarly in line with the slower migration pattern on the compact surface. S3 consisting of the smallest salt size fraction develops barely any visible fat stains on paper after 6.5 days (cm²). This observation is in contrast with the Raman chemical images for S3 that indicate a rapid migration of surface fat. As the surface fat clearly does not migrate into the contacting paper as in S1 and 2, it is likely that migration from the compact surface into the vicinity of the compact core occurs, driven by high capillary suction. The same phenomenon of little fat migration in paper but rapid migration in the contacting compact was observed for S5 and 6 containing 50/50 w/w% fine and coarse/medium salt fractions

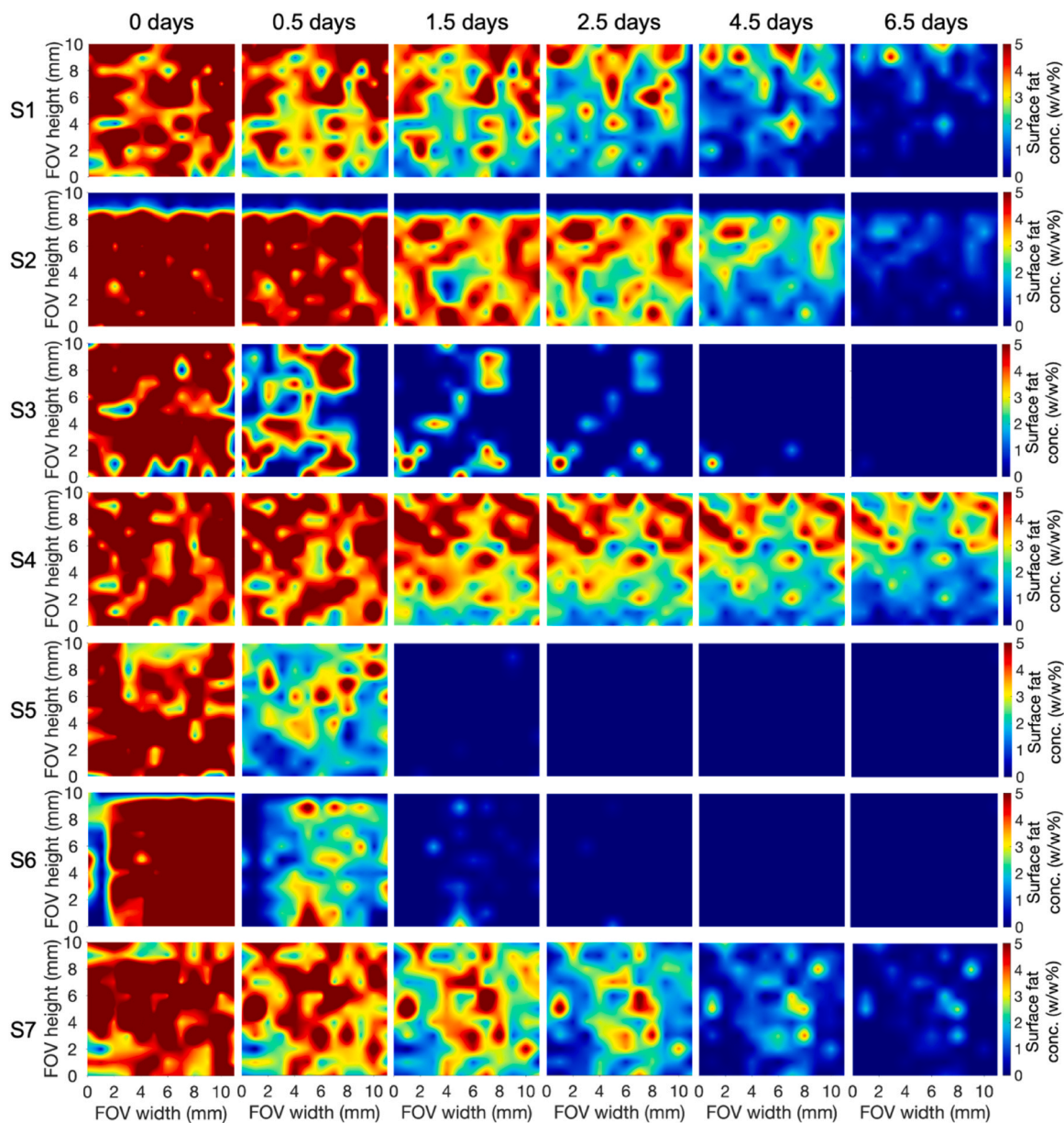


Fig. 11. Surface Raman chemical images of compact samples during fat migration tests over 6.5 days. Underside of compacts rested on paper throughout the migration test duration. FOV - field of view.

respectively. S7 shows some fat stain growth up to 3.9 cm^2 at 6.5 days, while Raman chemical images show a concentration decrease to 0.5 w/w%. By conservation of mass the fat stain should be much larger if all the fat migrated into the paper, suggesting that even with 1/3 of the fine salt fraction some fat is retained within the compact.

Fig. 12b shows the perimeter of the fat stains on paper, which was used to calculate the roundness tabulated in Table 3. Together with the Fig. 12b a qualitative assessment of the fat stain images is thus possible. Fat stains of compacts of coarse salt fractions are generally rounded. The anisotropy of the macroscopic stain is stemming from migration preferably in the machine direction of the paper along the fibre direction, and slightly less in the cross direction (Wong et al., 2023). Fat stains produced by compacts from fine salt are irregular in shape, while also being smaller than the compact footprint. As such, the model assumption of radially axisymmetrically expanding fat stains on paper is more applicable to larger stains than smaller ones. Roundness assess the irregularity of the circle edge, and is unity for a perfect circle, while highly irregular edges have values tending towards 0. Exemplarily for S1,

roundness decreased between near perfect 0.98 at 0.5 days to 0.51 at 6.5 days, indicating a roughening of the stain edge suggesting some fingering of the fat front. On average however, stains are qualitatively circular and suitable for an approximation as a circle. Samples producing only minor fat stains such as S3 and S5-S7 have roundness closer to 0, very likely as a combined effect of fingering and the naturally irregular stain shape.

3.5. Model validation

Fig. 13a shows the surface fat concentration over time on the compact, measured via Raman chemical imaging, together with the corresponding compact-side fat migration model Eq. 12. Similarly, Fig. 13b shows the fat stain area on paper over time, measured via optical stain imaging, together with the corresponding paper-side migration model Eq. 13. Overall, both models validate the experimental trends of decreasing surface fat concentration on the compact surface and increasing fat stain area on paper over 6.5 days.

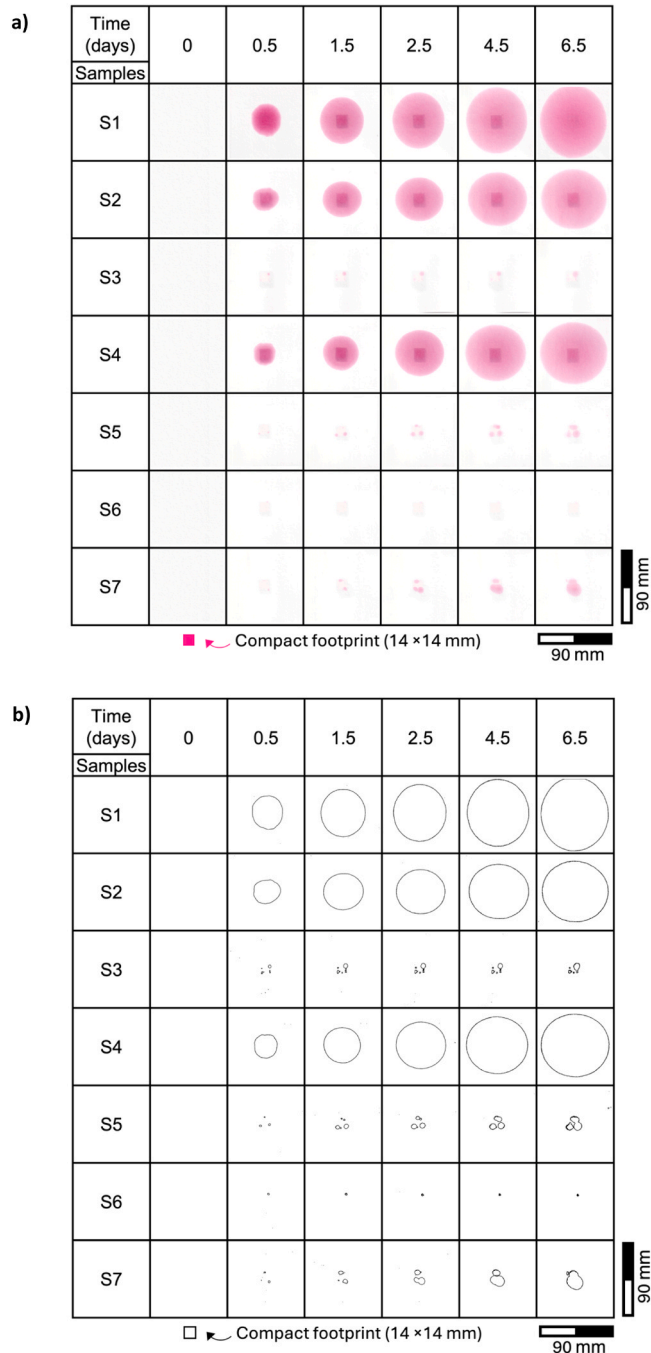


Fig. 12. Fat stain development on paper during fat migration tests over 6.5 days. a) Raw images, b) analysed circumference for roundness calculation. Compacts rested centrally on paper throughout the migration test duration.

For S1, experimental and model values for both surface fat concentration and fat stain area are almost congruent with R^2 values of 0.92 and 0.96 respectively. A similarly good fit exists between experimental and model values in S2 for both fat concentration ($R^2 = 0.95$) and stain area ($R^2 = 0.94$). For the 50/50 coarse/medium salt formulation S4, the model slightly overpredicts fat migration in the compact, while a more realistic prediction is made for fat stain area with ($R^2 = 0.82$). The generally acceptable model predictions for compact formulations with only coarse and medium salt fractions suggest that the physical modelling assumptions are acceptable. For all three samples, the low capillary pressure on the compact-side (117.7–350.1) and higher p_{cap} of swollen paper of 13.5 kPa results in the driving force tending towards

Table 3 Roundness of fat stains on paper, measured from the area and circumference by image analysis.

Time (days)	0	0.5	1.5	2.5	4.5	6.5
Sample 1	-	0.98 ± 0.08	0.95 ± 0.05	0.64 ± 0.03	0.37 ± 0.01	0.51 ± 0.01
Sample 2	-	0.85 ± 0.05	0.94 ± 0.04	0.63 ± 0.03	0.40 ± 0.02	0.27 ± 0.01
Sample 3	-	0.04 ± 0.03	0.03 ± 0.02	0.03 ± 0.01	0.03 ± 0.02	0.02 ± 0.01
Sample 4	-	0.65 ± 0.04	0.78 ± 0.03	0.86 ± 0.03	0.42 ± 0.01	0.36 ± 0.01
Sample 5	-	0.24 ± 0.09	0.10 ± 0.05	0.07 ± 0.03	0.06 ± 0.02	0.04 ± 0.01
Sample 6	-	0.44 ± 0.39	0.19 ± 0.20	0.30 ± 0.39	0.67 ± 0.74	0.83 ± 0.96
Sample 7	-	0.37 ± 0.27	0.24 ± 0.09	0.19 ± 0.07	0.15 ± 0.05	0.13 ± 0.02

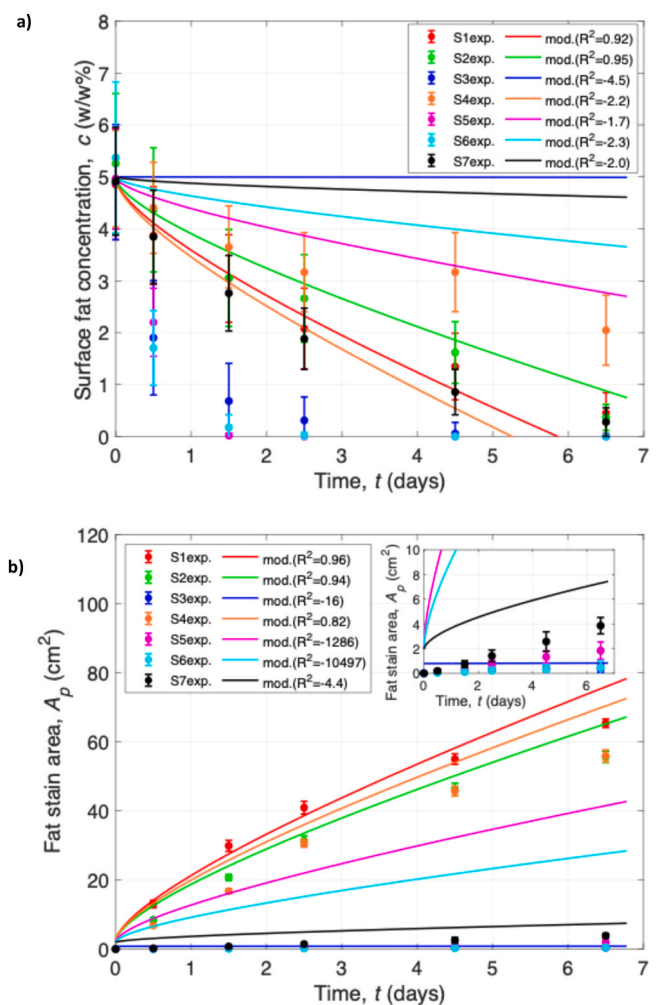


Fig. 13. Experimental (exp.) data and model (mod.) prediction of a) surface fat concentration and b) fat stain area on paper. Error bars represent ± 1 standard deviation from the mean of triplicate samples.

the paper, thus making fat migration out of the compact into paper thermodynamically feasible. As permeability of the compacts is comparatively high (1.2×10^{-10} to 4.6×10^{-10} m²), little kinetic resistance to fat leakage exists and thus fat outflow is observable and large fat stains form. Further, on the compact side, the model simplifies fat to be distributed isotropically across width and depth (but not length) of the

compact with globally uniform superficial velocity. As Raman imaging only characterises the compact surface, model and experimental agreement suggests that the core and surface fat compositions are equal and fat migration occurs from both regions simultaneously. In addition, as the model is based on mass balance principles (Eqs. 8, 9), the assumption that all migrated fat from the compact is imbibed by the paper is generally valid for the coarse and medium salt particle size range.

For S3, 5–7, containing a fine salt fraction, experimental and model values are starkly different to each other, as are fat migration patterns in the compact and paper. S3, 5 and 6 with 100 % and 50 % fine salt fraction show a rapid surface fat decrease (Fig. 13a), which is slightly less steep for S7 with a 33 % fine salt fraction. The model however predicts very shallow fat migration gradients or virtually no fat release from the S3 compact. Conversely for fat stain area on paper, model values agree better in experimental results: for S3 and 7, the model predicts low fat stain areas, with overestimates of fat stain area for S5 and 6. Negative or correlation coefficients larger than unity essentially signify that the model performs worse and prediction than a simple average, highlighting the model's unsuitability for fine particle samples.

The discrepancy between model and experimental values for samples containing a fine salt fraction can be explained with the drastically modified microstructure upon introduction of 5 μm salt particles. The model assumes that fat migration from the compact into paper is thermodynamically feasible if $p_{cap,p} > p_{cap,c}$, which is the case for all samples as the capillary pressure in unsaturated paper is always larger than for the compact. In addition to the thermodynamic driving force, kinetic resistance influences the fat migration rate. Due to the model obeying conservation of mass, the model predictions on the paper-side in Fig. 13b are equivalent. The large capillary suction induced by the fine salt likely draws surface fat away from the surface closer to the compact core, thus showing a fast concentration drop in S3, 5, and 6, in a process akin to paper with a similar capillary pressure absorbing liquids towards its core. In addition, for samples with fine salt, only small fat stains on paper are produced, suggesting that the low permeability induced by fine salt additionally reduces the quantity of fat reaching the paper. The observation that smaller particles and thus smaller interstitial channels reduce fat migration has similarly been concluded from other work. Static liquid holdup in packed beds of spherical spheres has been reported higher for smaller particles owing to the larger specific area in contact with liquid and increased capillary pressure (Van Der Merwe et al., 2004; Schwidder and Schnitzlein, 2010; Sáez et al., 1991). Throughflow of liquid through packed beds has been well-predicted for particle sizes of defined spheres by the relation of Carman and Kozeny, essentially a more specific Darcy equation, and similarly predicts a increasing pressure drop and thus flowrate decrease of the mobile phase for decreasing particle size and interparticle void size (Carman, 1937; Kozeny, 1927).

As the model for the compact-side is only one dimensional vertically, but does not account for horizontal fat distribution, it fails to capture fat migration in the compact width or depth. Rapid tomographic techniques such as MRI could be used to visualise the surface core fat distribution, as well as 2D or 3D modelling approaches that capture the horizontal fat flow, as opposed to the 1D approach limiting this work.

4. Conclusion

The aim of this work was to model liquid fat migration of a seasoning compact comprising salt and palm kernel fat into an underlying paper sheet to investigate and predict the effect of salt particle size on fat flow dynamics. A 1D first-principle model was constructed with capillary pressure as the thermodynamic driving force and permeability as the kinetic resistance evaluated by microtomography and sorption studies, and validated with a physical setup. Fat migration was experimentally measured on the compact surface via Raman chemical imaging to compare with model predictions of flow behaviour in the compact,

while fat migration on the paper was measured via optical stain imaging for comparison with fat stain growth predicted by the model. Experiments and model agreed well for coarse compact samples with R^2 up to 0.96, and agreed less for fine salt fractions, in which migration behaviour was suggested to not solely be one-dimensionally towards the paper but also horizontally into the compact core. Across all variations of different mass fractions of different particle sizes, samples with small particle sizes retained more fat and resulted in less undesirable fat stains on packaging due to a high capillary suction of the compact relative to paper, and high kinetic resistance due to small flow channels in small interstitial pores.

Nomenclature

Latin

- A – Cross-sectional area (m^2)
- C – Geometric porous medium factor (m^5)
- D – Diameter of sorption test cylinder (m)
- h – paper height or thickness (m)
- K – Darcy permeability (m^2)
- L – Cube length (m)
- l – Length (m)
- m – Fat mass (kg)
- O – Fat stain roundness (-)
- p – Pressure (Pa)
- P – Fat stain perimeter (m)
- r – Fat stain radius (m), capillary pore radius (m)
- R – Particle radius (m)
- S – Cube side length (m)
- t – Time (s)
- v – Fat flow velocity (m/s)
- w – width of paper strip in sorption test (m)

Greek

- Δp – Pressure difference (Pa)
- $\Delta \rho$ – Density difference (kg/m^3)
- ϵ – Voidage (-)
- θ – Contact angle ($^\circ$)
- μ – Viscosity (Pa.s)
- π – Constant (3.1415)
- ρ – Density (kg/m^3)
- σ – Surface tension (N/m)

Subscripts

- o – atmosphere-side
- 50 – 50th percentile, median
- a – apparent
- c – cube-side
- cap – capillary
- fat – fat
- gas – gas-side
- hexane – hexane
- i – cube-paper interface in the model
- liq – liquid-side
- p – paper-side in the model

CRedit authorship contribution statement

Gerhard Niederreiter: Supervision, Funding acquisition. **Annabel Bozon:** Supervision, Resources, Project administration. **Salman Agba D:** Writing – review & editing, Supervision, Funding acquisition. **Stefan Palzer:** Writing – review & editing, Funding acquisition. **Luc Dewulf:** Writing – review & editing, Writing – original draft, Visualization, Methodology, Investigation, Formal analysis, Data curation, Conceptualization. **Hausmann Michael K:** Supervision, Resources, Project administration. **MacInnes Jordan M:** Methodology.

Declaration of Competing Interest

The authors declare that they have no known competing financial interests or personal relationships that could have appeared to influence the work reported in this paper.

Acknowledgements

The author thanks EPSRC (grant 2602203) and Nestlé for funding this research, as well as the iForge makerspace and the Open Access Mechanical Workshop at the university for the accessible workshop facilities used to self-build the experimental setup. Shengda Hou is sincerely thanked for fruitful discussions on Raman spectroscopy.

Data availability

Data will be made available on request.

References

- Aguilera, J.M., 2011. Food Microstructures for Health, Well-being, and Pleasure. In: Aguilera, J.M., Simpson, R., Welti-Chanes, J., Bermudez-Aguirre, D., Barbosa-Canovas, G. (Eds.), *Food Engineering Interfaces*. Springer New York, New York, NY, pp. 577–588.
- Bao, Y., Evans, J.R.G., 1991. Kinetics of capillary extraction of organic vehicle from ceramic bodies. Part I: flow in porous media. *J. Eur. Ceram. Soc.* 8, 81–93.
- Biermann, C.J., 1996. *Handbook of Pulping and Papermaking*. Academic Press, San Diego.
- Carbonell, S., Hey, M.J., Mitchell, J.R., Roberts, C.J., Hipkiss, J., Vercauteren, J., 2004. Capillary flow and rheology measurements on chocolate crumb/sunflower oil mixtures. *J. Food Sci.* 69, E465–E470.
- Carman, P.C., 1937. Fluid flow through granular beds. *Chem. Eng. Res. Des.* 75, S32–S48.
- Cikrikci, S., Oztop, M.H., 2018. Oil migration in hazelnut paste/chocolate systems using magnetic resonance imaging. *J. Food Meas. Charact.* 12, 1460–1472.
- H. Darcy, *Les fontaines publiques de la ville de Dijon: exposition et application des principes à suivre et des formules à employer dans les questions de distribution d'eau*, Librairie des corps impériaux des ports et chaussées et des mines, Paris, 1856.
- De Géa Neves, M., Poppi, R.J., 2018. Monitoring of adulteration and purity in coconut oil using raman spectroscopy and multivariate curve resolution. *Food Anal. Methods* 11, 1897–1905.
- Dewulf, L., Hausmann, M.K., Bozon, A., Niederreiter, G., Palzer, S., Salman, A.D., 2024a. Particle-based food systems subject to lipid migration – A review of measurement, modelling, and mitigation approaches. *Powder Technol.* 445, 120097.
- Dewulf, L., Hausmann, M.K., Bozon, A., Niederreiter, G., Palzer, S., Salman, A.D., 2024b. Food vs packaging: dynamics of oil migration from particle systems into fibrous material. *Powder Technol.* 439, 119721.
- El-Abassy, R.M., Donfack, P., Materny, A., 2009. Visible Raman spectroscopy for the discrimination of olive oils from different vegetable oils and the detection of adulteration. *J. Raman Spectrosc.* 40, 1284–1289.
- Greenspan, P., Mayer, E.P., Fowler, S.D., 1985. Nile red: a selective fluorescent stain for intracellular lipid droplets. *J. Cell Biol.* 100, 965–973.
- Hagen, G., 1839. Ueber die Bewegung des Wassers in engen cylindrischen Röhren. *Ann. der Phys.* 122, 423–442.
- Harshe, Y.M., Deyber, H., Schafer, O., Sandoz, L., Breton, O., 2023. Impact of composition and aeration on the migration of TAGs in sandwich type confectionery products. *Food Res. Int.* 169, 112848.
- ISO, 2008. Paper and board — Determination of grease resistance, Part 1: Permeability test. ISO, Geneva.
- Kammerhofer, J., Fries, L., Dupas, J., Forny, L., Heinrich, S., Palzer, S., 2019. Dynamic wetting of multicomponent particle systems. *Powder Technol.* 357, 74–82.
- Kammerhofer, J., Fries, L., Dymala, T., Dupas, J., Forny, L., Heinrich, S., Palzer, S., 2018. Penetration rates into heterogeneous model systems and soluble food material. *Powder Technol.* 339, 765–774.
- Kozeny, J., 1927. Über kapillare Leitung des Wassers im Boden (Aufstieg, Versickerung und Anwendung auf die Bewässerung). *Sitz. Akad. Wiss. Wien.* 136, 271–309.
- Kubelka, P., 1931. Ein Beitrag zur Optik der Farbanstriche. *Z. Tech. Phys.* 12, 593–601.
- Lange, J., Pelletier, C., Wyser, Y., 2002. Novel method for testing the grease-resistance of pet food packaging. *Packag. Technol. Sci.* 15, 65–74.
- Laplace, P.-S., 1805. *Traité de mécanique céleste*. Courcier, Paris.
- Lin, T.-L., Hourng, L.-W., 2005. Investigation of wick debinding in metal injection molding: numerical simulations by the random walk approach and experiments. *Adv. Powder Technol.* 16, 495–515.
- Miranda, A.M., Castilho-Almeida, E.W., Martins Ferreira, E.H., Moreira, G.F., Achete, C. A., Armond, R.A.S.Z., Dos Santos, H.F., Jorio, A., 2014. Line shape analysis of the Raman spectra from pure and mixed biofuels esters compounds. *Fuel* 115, 118–125.
- Münch, B., Holzer, L., 2008. Contradicting geometrical concepts in pore size analysis attained with electron microscopy and mercury intrusion. *J. Am. Ceram. Soc.* 91, 4059–4067.
- Poiseuille, J.L.M., 1839. *Recherches sur les causes du mouvement du sang dans les veines*. Imprimerie Royale, Paris.
- Pucci, M.F., Liotier, P.-J., Drapier, S., 2015. Capillary wicking in a fibrous reinforcement – Orthotropic issues to determine the capillary pressure components. *Compos. Part A Appl. Sci. Manufacturing* 77, 133–141.
- Pucci, M.F., Liotier, P.-J., Drapier, S., 2016. Capillary wicking in flax fabrics – Effects of swelling in water. *Colloids Surf. A Physicochem. Eng. Asp.* 498, 176–184.
- Sáez, A.E., Yépez, M.M., Cabrera, C., Soria, E.M., 1991. Static liquid holdup in packed beds of spherical particles. *AIChE J.* 37, 1733–1736.
- Schrader, B., Bergmann, G., 1967. Die Intensität des Ramanspektrums polykristalliner Substanzen. *Fresenius' Z. F. üR. Anal. Chem.* 225, 230–247.
- Schwidder, S., Schnitzlein, K., 2010. Predicting the static liquid holdup for cylindrical packings of spheres in terms of the local structure of the packed bed. *Chem. Eng. Sci.* 65, 6181–6189.
- Shah, Y., Takhar, P.S., 2023. Capillary pressure in unsaturated food systems: its importance and accounting for it in mathematical models. *Food Eng. Rev.* 15, 393–419.
- Siyal, A., Rahimov, K., AlAmeri, W., Al-Shalabi, E.W., Ahmed, S., 2023. A comprehensive review on the capillary desaturation curves for sandstone and carbonate reservoirs. *SPE Reserv. Eval. Eng.* 26, 651–675.
- Somasundram, I.M., Cendrowicz, A., Wilson, D.I., Johns, M.L., 2008. Phenomenological study and modelling of wick debinding. *Chem. Eng. Sci.* 63, 3802–3809.
- Souza, G.K., Diório, A., Johann, G., Gomes, M.C.S., Pomini, A.M., Arroyo, P.A., Pereira, N.C., 2019. Assessment of the physicochemical properties and oxidative stability of kernel fruit oil from the acrocomia totai palm tree. *J. Am. Oil Chem. Soc.* 96, 51–61.
- Sutherland, K., 2008. *Filters and Filtration Handbook*. Elsevier, Oxford.
- Van Der Merwe, W., Maree, C., Nicol, W., 2004. s. In: *Nature of Residual Liquid Holdup in Packed Beds of Spherical Particle*, 43. *Industrial & Engineering Chemistry Research*, pp. 8363–8368.
- Verma, U., Riley, I.M., Lukić, B., Broche, L., Verboven, P., Delcour, J.A., Nicolaï, B.M., 2025. High-speed computed tomography to visualise the 3D microstructural dynamics of oil uptake in deep-fried foods. *Nat. Commun.* 16, 2600.
- Vo, H.N., Pucci, M.F., Corn, S., Le Moigne, N., Garat, W., Drapier, S., Liotier, P.J., 2020. Capillary wicking in bio-based reinforcements undergoing swelling – Dual scale consideration of porous medium. *Compos. Part A Appl. Sci. Manufacturing* 134, 105893.
- Washburn, E.W., 1921. The dynamics of capillary flow. *Phys. Rev.* 17, 273–283.
- Willett, C.D., Adams, M.J., Johnson, S.A., Seville, J.P.K., 2003. Effects of wetting hysteresis on pendular liquid bridges between rigid spheres. *Powder Technol.* 130, 63–69.
- Willett, C.D., Johnson, S.A., Adams, M.J., Seville, J.P.K., 2007. Chapter 28 Pendular capillary bridges. In: Salman, A.D., Hounslow, M.J., Seville, J.P.K. (Eds.), *Handbook of Powder Technology*. Elsevier Science B.V, pp. 1317–1351.
- Wong, C.L., Wang, S., Karimnejad, S., Wijburg, M.G., Mansouri, H., Darhuber, A.A., 2023. Transient deformation and swelling of paper by aqueous co-solvent solutions. *Soft Matter* 19, 1202–1211.
- Young, T., 1805. III. An essay on the cohesion of fluids. *Philos. Trans. R. Soc. Lond.* 95, 65–87.
- Zhang, Q., Mugele, F., Lugt, P.M., Van Den Ende, D., 2020. Characterizing the fluid–matrix affinity in an organogel from the growth dynamics of oil stains on blotting paper. *Soft Matter* 16, 4200–4209.
- Ziegleder, G., Moser, C., Geier-Greguska, J., 1996b. Kinetik der Fettmigration Teil II: Einfluß von Lagertemperatur, Diffusionskoeffizient, Festfettgehalt. *Lipid / Fett* 98, 253–256.
- Ziegleder, G., Moser, C., Geier-Greguska, J., 1996a. Kinetik der Fettmigration in Schokoladenprodukten Teil I: Grundlagen und Analytik. *Lipid / Fett* 98, 196–199.
- Ziegleder, G., Schwingshandl, I., 1998. Kinetics of fat migration within chocolate products. Part III: fat bloom. *Lipid/Fett* 100, 411–415.

Corrigendum for Chapter: Modelling

Tabulated salt particle size fractions and median (d_{50}) particle size of each sample.

Sample	Fine fraction ($d_{50} = 5 \mu\text{m}$)	Medium fraction ($d_{50} = 250 \mu\text{m}$)	Coarse fraction ($d_{50} = 500 \mu\text{m}$)	Sample d_{50} mm
S1	1	0	0	5
S2	0	1	0	250
S3	0	0	1	500
S4	0.5	0.5	0	63.75
S5	0.5	0	0.5	126.25
S6	0	0.5	0.5	187.5
S7	0.33	0.33	0.33	83.05

Chapter 6

Application

Surface and core effects in oil migration from particulate seasoning tablets into paper packaging via Raman and Magnetic Resonance Imaging

Luc Dewulf^{1,2}, Steven Reynolds³, Michael K. Hausmann², Annabel Bozon⁴, Gerhard Niederreiter², Stefan Palzer⁵, Agba D. Salman¹

¹ School of Chemical, Materials, and Biological Engineering, University of Sheffield, Sir Robert Hadfield Building, Mappin Street, S1 3JD, Sheffield, United Kingdom

² Nestlé Research, Route du Jorat 57, 1000 Lausanne 26, Switzerland

³ School of Medicine and Population Health, University of Sheffield, Royal Hallamshire Hospital, Glossop Road, S10 2JF, Sheffield, United Kingdom

⁴ Nestlé Product Technology Centre Food, Lange Straße 21, 78221 Singen, Germany

⁵ Nestlé Ltd., Avenue Nestlé 55, Vevey 1800, Switzerland

Abstract

Oil migration from oil-containing food tablets into fibre-based packaging causes undesired oil stains on the packaging, necessitating effective preventive strategies. Seasoning tablets are popular culinary condiments wrapped in individual wrappers, increasingly made from paper. The oil migration behaviour into packaging is dependent on the food formulation and microstructure, but oil migration characterisation to guide mitigation and control strategies have been limited. In this study, model seasoning tablets from salt (55 w/w%), sunflower oil (10 w/w%), and the balance sugar, starch, maltodextrins and MSG, with systematically varying salt particle size from 5 to 500 μm were prepared in a ternary design of experiments. Oil migration behaviour over a shelf-life study of 8 weeks was evaluated on the tablet surface via Raman Chemical Imaging, in the tablet core via Magnetic Resonance imaging, and on the paper via optical stain imaging. The migration process was modelled as 1D Fickian diffusion in a semi-infinite body and matched experimental data. Image quantification showed that surface oil concentration is lower by 1-2 w/w% than core oil concentration, likely due to reduced entrapment of oil in interstitial pores at the external tablet surface. Oil migration is reduced with a higher fraction of fine salt than coarse salt particles, resulting in different porous microstructures characterised by x-ray microtomography. Thus, for the first time extensive oil migration characterisation and modelling was applied to seasoning tablets suggesting particle size reduction as an effective mitigation strategy.

1. Introduction

Many consumer foods are dry solid macrostructures made from smaller particles with lipids. An example of such bulk structures is chocolate containing a cocoa powder, sugar and milk particles in a continuous cocoa butter phase. Filled chocolate products contain additional oils in ganache or fondant fillings enrobed by a chocolate layer. Other lipid macroscopic particle structures are seasoning or bouillon tablets consisting of typical ingredients in the 100 μm

particle size range such as salt, sugar, and carbohydrates mixed with 5 to 30 w/w% oil or fat [1]. Compared to solid dry ingredients that undergo physical phase changes at higher temperature, oil and fats have melting points around the typical ambient storage, transport and consumption temperature of foods of 20-35 °C. As with many liquid-solid food systems, lipid-containing foods suffer from physical instability induced by temperature or humidity. This phase separation between lipids and solids is termed oil or fat migration [2]. In macroscopic food structures, lipid migration results in quality defects on the food surface such as fat bloom on chocolate induced by the solubilisation and recrystallisation of fat on the outer surface. For seasoning tablets, lipid leakage from the food result in stains on the packaging especially with increasingly used sustainable fibre-based paper wrappers. As consumers perceive surface quality defects on food or packaging as inferior products, an increasing interest exists to measure and predict lipid migration on the food surface but also in the core structure. A recent review comprehensively summarises measurement, modelling and mitigation strategies for particle-based food structures [2].

Surface techniques to quantify lipid migration are generally experimentally easier than tomographic techniques to measure core fat content. To evaluate fat migration in chocolate for example, whiteness or gloss, as an indirect result of diffuse light reflection from fat crystals has been used [3]. Techniques such as scanning electron microscopy are rather qualitative as the scanning area is often too small to capture the entire macroscopic sample [4]. Surface methods that directly quantify chemical fat composition are based on spectroscopic techniques such as near infrared (NIR) for chocolate [5] or Raman spectroscopy for model seasoning tablets [6].

In Raman spectroscopy, the sample surface is illuminated by a laser at a specific wavelength. Raman active, that is, polarisable molecules, are excited by the incident light and relax emitting photons at a shifted wavelength to the incident beam. The emitted signal is diffracted in a spectrometer and analysed by a charge-coupled device, yielding spectra where peak intensity is related to molecule concentration. As the relationship between a substance's concentration and Raman intensity is however not linear, quantitative Raman spectroscopy, especially for 2D imaging (Raman chemical imaging), is still underreported.

Lipid migration effects on the food surface are inevitably linked to the core structure of the food, which is experimentally more difficult to measure as it is opaque to optical radiation. X-ray tomography has been used to visualise chocolate microstructure [7], the field of view (FOV) is however often smaller than the entire food product, and differentiation between different ingredients is challenging due to often similar density and resulting grey values in images. Instead, magnetic resonance imaging has proven an effective technique to visualise solely the lipid fraction in multiphasic foods [8].

In ^1H (proton) magnetic resonance imaging the sample is exposed to repeated radio frequency (RF) emission by a magnetic coil, which induces a nuclear spin of the hydrogen nuclei, measured by receiving RF antennas as the echo. By varying the repetition (TR) and echo (TE) time sequences, and measuring the signal intensity when magnetization recovers (T_1) or relaxes (T_2) the resonance of the ^1H nuclei can be measured. As such, components from molecules with high hydrogen content such as lipids can be differentiated from material with low hydrogen density such as salt, sugar, or carbohydrates. When measuring T_2 relaxation

times, signal intensity not only depends on relative concentration of ^1H , but also on molecular mobility of the hydrogen-containing molecules, and therefore formulations with small microstructural pores or particles yield lower intensities than large features with little spatial constraints. Current reviews [6, 9] show that for lipid migration analysis, MRI has almost exclusively been used in chocolate research with a variation of experimental setups and sequences.

Beyond mere imaging, previous studies modelled lipid migration kinetics, predominantly using Fickian diffusion models, which are easily applicable for multi-ingredient foods with an unknown or complex microstructure, as only information of migrant concentration with time is required, and little spatial information. The first simple diffusion models for lipid migration were developed by Ziegler *et al.* who measured concentration initially and at one location with time [10, 11]. As MRI renders concentration gradients inside the food structure, diffusion models became more refined, eased by higher computing power to solve more complex models analytically [12, 13].

As previous work focuses on chocolate and lipid migration to the food surface, there is a lack of understanding of lipid migration in other food systems, especially culinary products with markedly different microstructure to chocolate. Further, understanding of lipid stain formation on packaging is required, especially with the increasing drive towards fibre-based packaging. This work aims to advance understanding of oil migration from seasoning tablets into paper packaging and employs Raman chemical imaging coupled with MRI to visualise and model for the first time surface and core effects on oil migration.

2. Materials and Methods

2.1 Experimental design

Salt was obtained from Südwestdeutsche Salzwerte AG (Heilbronn, Germany), and processed into three size fractions: coarse ($d_{50} = 500 \mu\text{m}$) and medium ($d_{50} = 250 \mu\text{m}$) size fractions were obtained from sieving (Retsch, Haan, Germany), and the fine fraction ($d_{50} = 5 \mu\text{m}$) was obtained by jet milling (Tecnologia Meccanica, Treviolo, Italy). Sugar ($d_{50} = 649 \mu\text{m}$) was obtained from Cuisine Noblesse (Offenburg, Germany), maltodextrin IT6 (DE6) ($d_{50} = 316 \mu\text{m}$) and maltodextrin IT47 (DE47) ($d_{50} = 198 \mu\text{m}$) were obtained from Rouquette (Lestrem, France), corn starch ($d_{50} = 30 \mu\text{m}$) was obtained from Cargill (Düsseldorf, Germany), monosodium glutamate (MSG) ($d_{50} = 78 \mu\text{m}$) was obtained from Kwan Yik (Guangdong, China). d_{50} is the volume-based median particle size of a distribution, meaning that 50% of the particle volume (or mass) lie above and below the median. Apart from salt all dry ingredients were without further modification. High oleic sunflower oil was obtained from Nestrade (Vevey, Switzerland), mixed with 1% fat brown B (Santa Cruz Biotechnology, Dallas, TX, US) and paper-filtered (Whatman 595, Maidstone, UK) to obtain a brown sunflower oil for better stain contrasts on fibre packaging.

To evaluate the impact of salt particle size, 7 formulations with varying salt size fraction and amount were prepared according to the ternary design in Fig. 1 and Table 1. 500 g seasoning powders were prepared for each formulation 1-7 by high shear mixing (EL1, Eirich, Hardheim, Germany) using a pin-type agitator. Ingredient addition and mixing sequences were aligned to prior studies [14, 15]. First, crystalline components (salt, sugar, MSG) dry mixed at 1000 rpm for 30 seconds, followed by sunflower oil addition over 30 s, and further mixing for a minute, before addition of the amorphous components and final mixing for 2 minutes. Samples were kept at 20 °C and 40% relative humidity (RH) in sealed bags for 48 h for moisture to equilibrate before tableting. 4 g of seasoning powder of each formulation were compacted to a fixed height of 13.5 mm in a square 14×14 mm die (Instron, Norwood, MA, US), and were placed on blotting paper (Whatman 3MM, Maidstone, UK) to mimic packaging paper for 8 weeks undergoing oil migration testing at 25 °C and 50% RH shelf-life test conditions. Oil concentration measurements on the tablet surface, core and on packaging paper were taken at time 0, 1, 4, and 8 weeks as explained below.

Table 1. Formulation recipe for the 7 seasoning tablet formulations. Quantities are given as w/w%.

w/w%	F1	F2	F3	F4	F5	F6	F7
Salt (coarse)	55	0	0	27.5	27.5	0	18.3
Salt (medium)	0	55	0	27.5	0	27.5	18.3
Salt (fine)	0	0	55	0	27.5	27.5	18.3
HOSO*	10	10	10	10	10	10	10
Sugar	10	10	10	10	10	10	10
Maltodextrin IT6 (DE6)	10	10	10	10	10	10	10
Maltodextrin IT 47 (DE47)	5	5	5	5	5	5	5
MSG [†]	5	5	5	5	5	5	5
Corn starch	5	5	5	5	5	5	5

* HOSO = high oleic sunflower oil, [†] MSG = monosodium glutamate

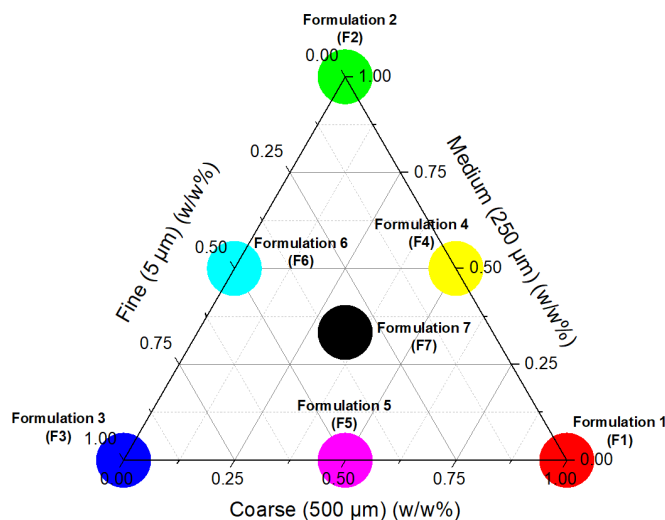


Fig. 1. Ternary design for the 7 seasoning tablet formulations with varying salt particle size and mass fractions (colour coding consistent with graphs throughout this work).

2.2 Microtomography

To obtain 3D representations of the seasoning tablet's internal microstructure, x-ray microtomography scans were acquired for each formulation at 70 kVp, 114 μ A, 8W with 0.5 mm Al filter and exposure time 1000 ms per acquisition (ScancoMedical, Brüttisellen, Switzerland). The field of view was 7 mm diameter with a stack height of 500 μ m at 0.8 μ m voxel size. The region of interest was cropped to 2000 \times 2000 μ m, and the three main phases recoloured digitally according to their contrast and threshold, and the voidage calculated from the void pixel count by image analysis (3D slicer software) [16].

2.3 Raman chemical imaging

To measure oil concentration changes on the compact surface, the method of Raman chemical imaging was used described previously [6]. In brief, a Raman point laser (532 nm, continuous wave diode, 94 mW, Oxxius, Lanion, France) was used with a focal point resolution of 1.7 μ m estimated from the Raleigh criterion $R = 0.61\lambda/NA$ where R is the resolution, λ is the laser wavelength, and NA is the numerical aperture of the 2 \times lens of 0.19. The tablet surface was scanned in a 20 \times 20 mm grid at 1 mm increments, by moving the sample on a motorized x-y stage (Märzhäuser, Wetzlar, Germany), resulting in 441 individual spectra of the tablet surface acquired between Raman shifts of 0 and 3000 cm^{-1} . Spectra were acquired for 10 seconds and accumulated 3 times for each probing point in a spectrometer (iHR320) with 1800 groves/mm, 500 nm blaze grating and CCD camera (Synapse, Horiba, Longjumeau, France). Spectral signals were processed for baseline corrections and 1st derivative, before evaluation of the tablet surface oil concentration via calibration curves.

The reason for spectrum correction is mostly fluorescence. Both stokes Raman scattering and fluorescence results in emission induced by incident radiation. While Raman scattering is the excitation of a molecule to a virtual state and relaxation to an energy level higher than the ground state, fluorescence is the excitation of a molecule to a higher energy level than for Raman, and relaxation to the ground state. This larger magnitude relaxation

results in a higher intensity photon emission than a Raman photon, hence fluorescence is often matching or even masking Raman spectra and is henceforth undesired. The extent of fluorescence emission is dependent on the incident light energy. As energy and wavelength are inversely related to each other, low wavelength lasers such as green 532 nm generally result in large extents of fluorescence emission. Long wavelength, lower energy lasers such as red 785 nm lasers generally exhibit less fluorescence, as the excitation is lower, albeit also generating weaker Raman emissions.

2.4 Magnetic resonance imaging

Magnetic resonance imaging was used to measure oil concentration changes in the core of the seasoning tablets. Samples were scanned in a 9.4 T vertical bore MRI scanner (Advance III, Bruker, Ettlingen, Germany) with 25 mm diameter radio frequency volume coil. Each cube was carefully placed in a glass vial with the same orientation for each time point (0-8 weeks). Glass beads covered the cube to hold it in place during image acquisition. Images were acquired with a RARE spin-echo sequence (RARE factor 2) with a TR/TE ratio of 8/1000 ms. The whole cube volume was imaged with a FOV of 20x20 mm and 100 μm isotropic in-plane resolution, and with 17 slices of 1 mm in the coronal direction. Images were acquired and processed using Paravision 5.1 (Bruker). Image analysis was performed in Matlab (Mathworks, Natick, MA, US).

2.5 Optical paper stain scanning

To measure oil stain area on the paper packaging, the method of optical stain quantification was used described previously [6]. A flatbed scanner (LiDE300, Canon) was employed at 1200 dpi resolution to scan the underside of the paper. The area of fat stain was automatically quantified via a self-written ImageJ/Fiji macro by discriminating between the brown sunflower oil stain and the white blotting paper based on black/white thresholding.

2.4 Diffusion modelling

To model oil migration from the seasoning tablets into the packaging paper substrate, a 1D oil flow vertically down without oil gradient in the width or depth of the tablet is assumed, based on Fick's 2nd law [17]

$$\frac{\partial^2 c}{\partial x^2} = \frac{1}{D} \frac{\partial c}{\partial t} \quad 1$$

where c is the oil concentration, x the location along the vertical migration axis, t is the time after placing the tablet on paper and start of the migration test, and D is the diffusivity of oil in the seasoning tablet matrix. The problem now resembles a semi-infinite slab (tablet) in contact with an infinite sink (paper packaging), where the contact between the two occurs at $x = 0$. Solving the partial differential equation yields the expression [18]

$$\frac{c(x, t) - c(0, t)}{c(x, 0) - c(0, t)} = \text{erf}\left(\frac{x}{2\sqrt{Dt}}\right) \quad 2$$

where $c(x, t)$ is the oil concentration at time x and t , $c(0, t)$ is the oil concentration at the tablet-paper interface at any time t , $c(x, 0)$ is the initial oil concentration, and erf is the error

function. When at a given time point the average concentration of the entire tablet, that is, over x is evaluated, the diffusion model is an integral

$$\bar{c}(t) = c(\bar{x}, t) = c(0, t) + (c(x, 0) - c(0, t)) \frac{1}{L} \int_0^L \operatorname{erf}\left(\frac{x}{2\sqrt{Dt}}\right) dx \quad 3$$

where L is the overall height of the tablet surface, i.e. x extends between $0 < x < L$. The models Eq. 2 and 3 were solved with Matlab.

3 Results and discussion

3.1 Microtomography

Fig. 2 shows reconstructed and recolored 3D x-ray tomographic images of sections of the seasoning tablets. In raw tomographic images (not shown), salt crystals with a high lattice density result in a strong image contrast and can easily be discerned from the remaining components oil, sugar, starch, maltodextrins, and MSG, which are less dense and result in more grey contrast. The density of air gas is lower than of solid or liquid matter so that void pixels appear black. Images were recoloured according to their phases, and because only the size fraction of salt was changed while all other components remained constant, it is still possible to group the components into their three most relevant phases.

Formulation 1 (Fig. 2a) composed of coarse salt fractions has clearly visible large salt particles dispersed in a continuous matrix of amorphous, sugar, and oil particles, with visible air pockets occupying 13.4 v/v%. F2 (Fig. 2b) composed of the same excipients but with a medium sized salt fraction has visibly smaller particles, with a similar void fraction of 15.8 v/v%. F4 (Fig 2d), in which the salt is a half/half mixture of coarse and medium particles, has expectedly similar morphology with similar voidage of 17.4 v/v%. The microstructure changes drastically with smaller salt particles in F3 (Fig 2c) in which the salt fraction consists of fine salt only. Particles appear much more dispersed, with some salt agglomerates due to larger surface energy in smaller particles causing coherence. As finer particles tend to pack less efficiently due to interparticle friction and Van der Waals forces, while the bulk density is dictated by tablet compression, the void fraction is starkly reduced to 5.9 v/v%. F5 (Fig. 2e), composed of coarse and fine salt, shows distinct large salt particles with interspersed fine salt. F6 (Fig. 2f) from medium and fine salt shows a similar morphology as F5 with similar void fraction. F7 (Fig. 2g), being a ternary mix of coarse, medium, and fine salt fractions shows a mix of all three morphologies. The slightly higher void fraction of 9.3 v/v% suggests a more efficient packing, which is expected for multimodal particle size distributions, thus leaving more open space unoccupied by particles.

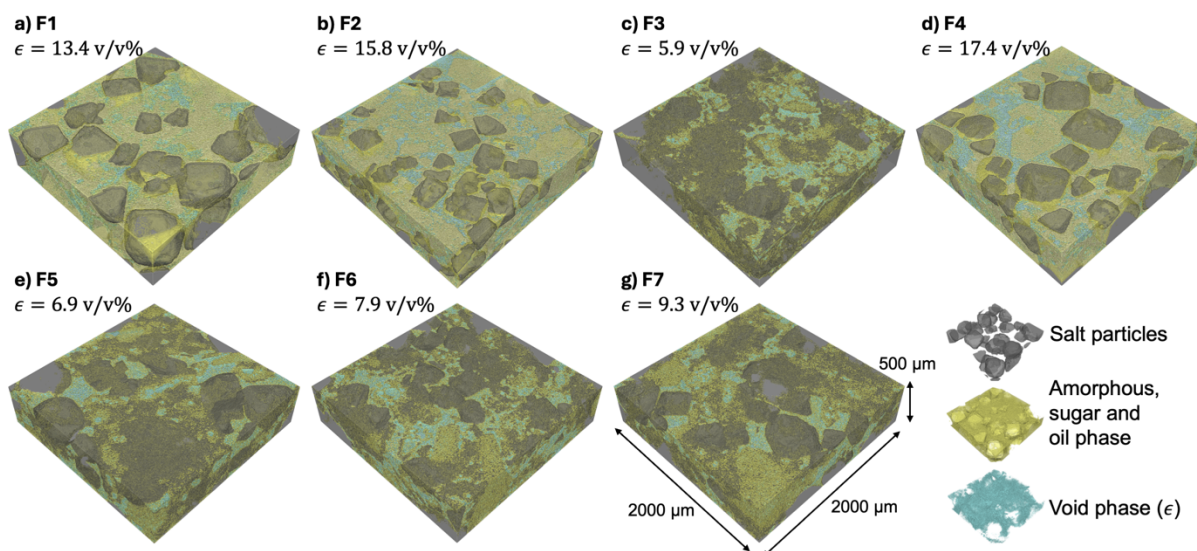


Fig. 2 Reconstructed x-ray microtomographic images of sections of the seasoning tablet formulations.

3.2 Raman chemical imaging

Raman chemical imaging was used to image oil concentration on the tablet surface for each formulation and each time point. Prior studies for Raman chemical imaging for lipid migration of seasoning tablets were performed only on biphasic salt-lipid systems, which are relatively simple as crystalline salt is Raman inactive but covalently bonded atoms in lipids are Raman active [6]. The seven-component formulation in the present work is thus a complex case, however the aim was to only trace the oil fraction necessitating to separate the oil signal from the remaining components signals. Figure 3 Shows the raw materials spectra for each formulation component. The annotated high oleic sunflower oil spectrum of interest is comparable to literature and with characteristics peaks tabulated in Table 2 based on the molecular vibration origin [19-21]. Generally the HOSO spectrum is approximately an order of magnitude larger than the remaining ingredients profiles, however exhibiting large fluorescence. For this reason, acquired spectra of seasoning tablet samples were baseline adjusted by a second order polynomial and signal intensity was enhanced by obtaining the moving average of the first derivative according to standard procedures in Raman signal processing [22]. Raman intensity of sunflower oil was taken as the resultant peak height.

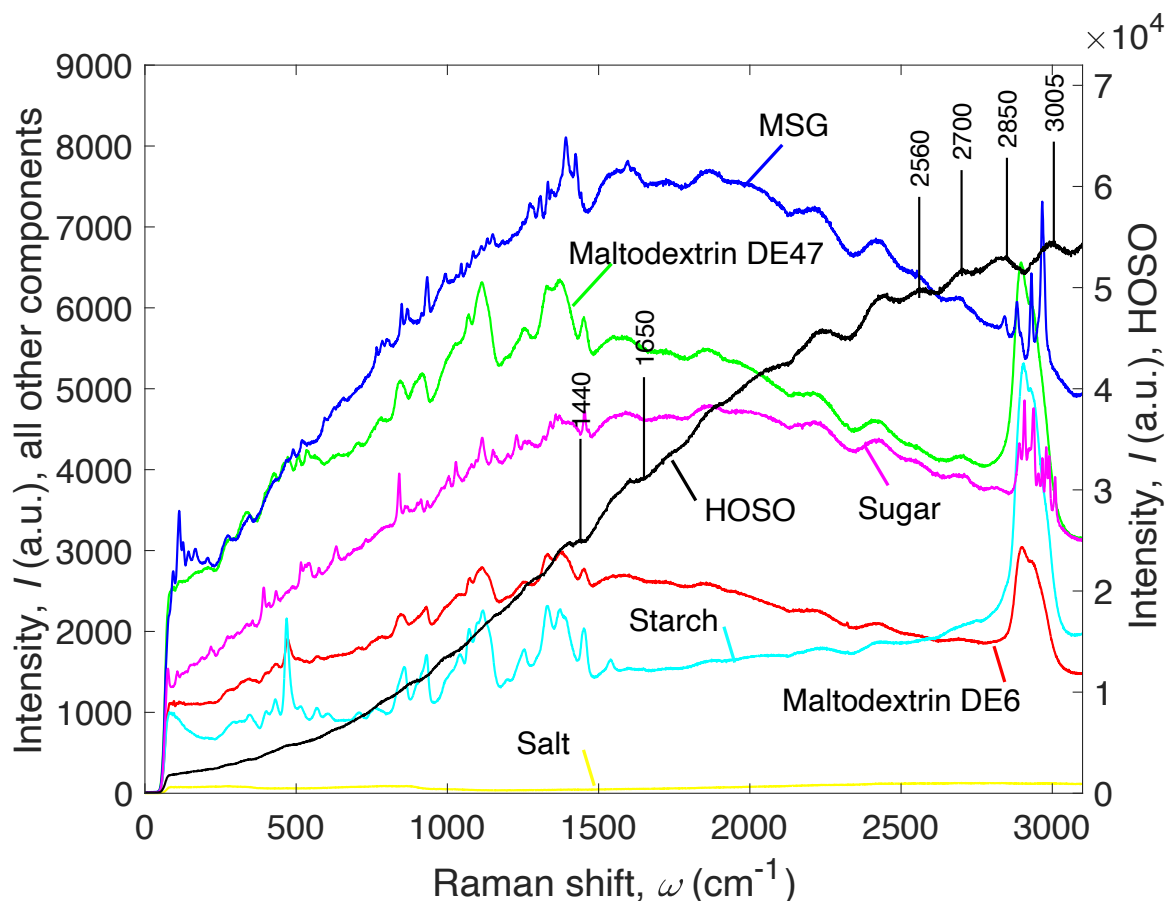


Fig. 3. Raman spectra of raw materials comprised in the formulations, annotated for sunflower oil. HOSO = high oleic sunflower oil, MSG = monosodium glutamate.

Table 2. Generally accepted Raman peaks in high oleic sunflower oil, adapted from [19-21].

Raman shift (cm^{-1})	Functional group	Vibration mode
1440	-CH ₂	C-H bending (scissoring)
1650	cis RHC=CHR	C=C stretching
2500 - 2700	Overtones and combinations	
2850	-CH ₂	C-H symmetric stretching
3005	cis RHC=CHR	=C-H symmetric stretching

To convert Raman peak intensity to concentration on the compact surface, a calibration curve was constructed (Fig. 4). Raman spectroscopy is extremely sensitive to surface roughness and has been the subject of numerous studies and theories [23, 24]. In the present work, as the laser beam resolution ($1.7 \mu\text{m}$) is about the same size as some amorphous fines such as starch, but

smaller than the smallest particle size of salt of 5 μm , the diffraction patterns of reflected Raman signal heavily depend on the compact formulation from different salt particle size fractions.

For this reason, a separate calibration curve was constructed for each sample at 0, 3.33, 5, 6.67, 10, 13.33, and 16.67 w/w% sunflower oil concentration prepared in the same way as formulations 1-7, and fitted with 4th order trendlines. Concentrations above the initial sunflower oil concentration of 10 w/w% was chosen to be able to quantify potential oil accumulation or locally higher concentration regions. The nonzero Raman signals at 0 w/w% sunflower oil concentration signify that the tablet excipients other to oil also contribute to a small extent to the Raman intensity. Error bars show the standard deviation of Raman intensity over the entire tablet surface and thus rather represent the inhomogeneous surface morphology. General trends can be observed in the calibration curves: for all formulations, the intensity gradients are steepest at low concentration between zero and 8 w/w% sunflower oil. For formations prepared from coarse particles the intensity quickly reaches a plateau with increasing sunflower oil concentration. On the other hand, formulations F3, F5 and F7 with fine fractions have monotonically growing ingredients with increasing oil concentration. The reason for this is likely that in coarse salt tablets the likelihood of probing a large pure salt crystal without oil is higher than in formulations with fine salt as can be seen from the x-ray images (Fig. 2). In addition, formulations with large voidages hold more oil in the tablet core whereas formulations with small void fractions contain more surface oil as it is pushed to the surface during tableting, manifesting in higher intensities. In addition, coarser particles and larger pores cause more diffuse reflection, diffracting less Raman signal into the probe in the same beampath as the incident light. With an increasing fines fraction the tablet surface becomes smoother. Consequently, F3 and F5-7 have distinctively higher calibration gradients as more surface features tend towards beam resolution resulting in increased specular signal reflection.

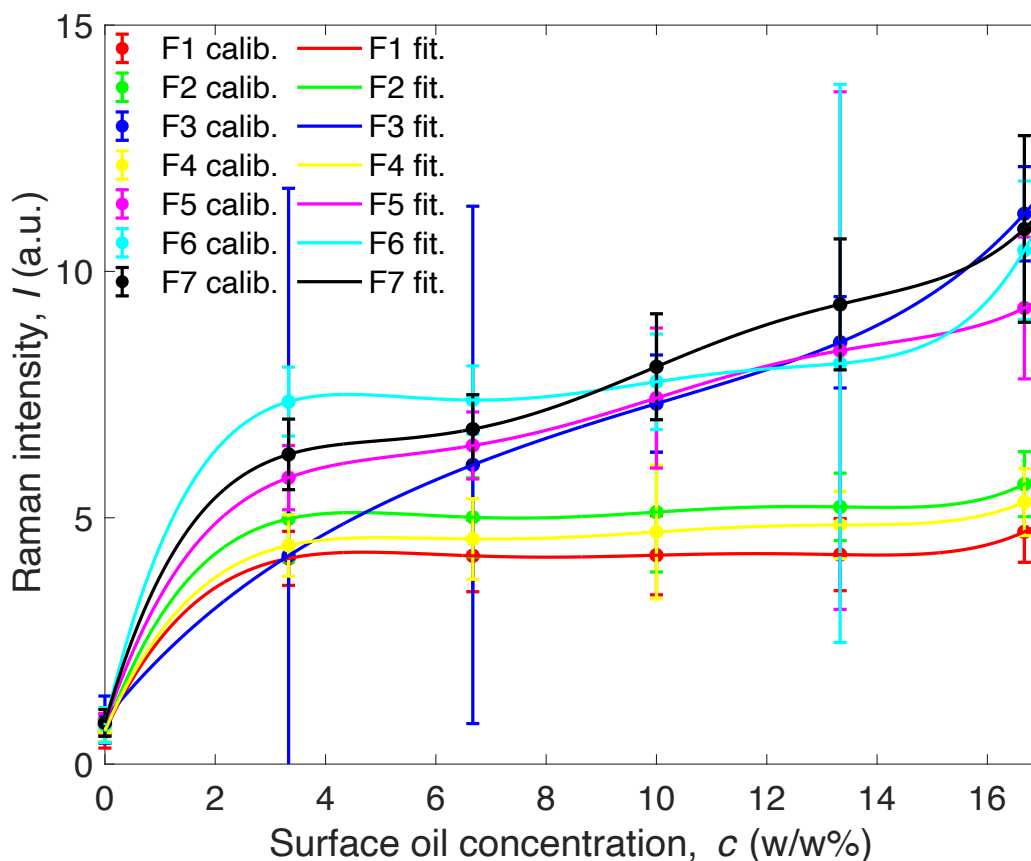


Fig. 4. Experimental calibration points with 4th order polynomial calibration fits for each formulation. Error bars are standard deviation over the entire tablet surface. Error bars of the calibration curves represent ± 1 standard deviation from the mean, where the mean was evaluated over the entire tablet surface. The error bars therefore rather represent the inhomogeneity of the table surface.

Raman acquisitions at each of the 441 probing points of each of the 7 formulations at each time point 0-8 weeks were converted to surface oil concentration (Fig. 5). First, a second order polynomial was fitted to each spectrum to correct for fluorescence (Fig. 5a). The baseline corrected spectrum was obtained by subtracting the fitted baseline from the raw spectrum (Fig. 5b). To enhance signal peaks, it is customary to obtain the first derivative of the baseline-corrected spectrum (Fig. 5c). The peak between 2630-2700 cm^{-1} , recurrent in all sample spectra, was selected and the maximum peak intensity determined (Fig. 5d). This maximum peak was converted to the corresponding tablet surface oil concentration via the calibration curve (Fi. 5e), and repeated for all spectra for all formulations at each time point. By interpolation between probing points, the full original field of view was reconstructed into a chemical image with oil concentration on the tablet surface color-coded between 0 (blue) and initial 10 w/w% (red) (Fig 6). For all samples, F1-7 at time 0, the oil concentration is generally isotropically distributed around 10 w/w%. As the oil migration test proceeds, markedly different oil migration patterns occur for different formulations.

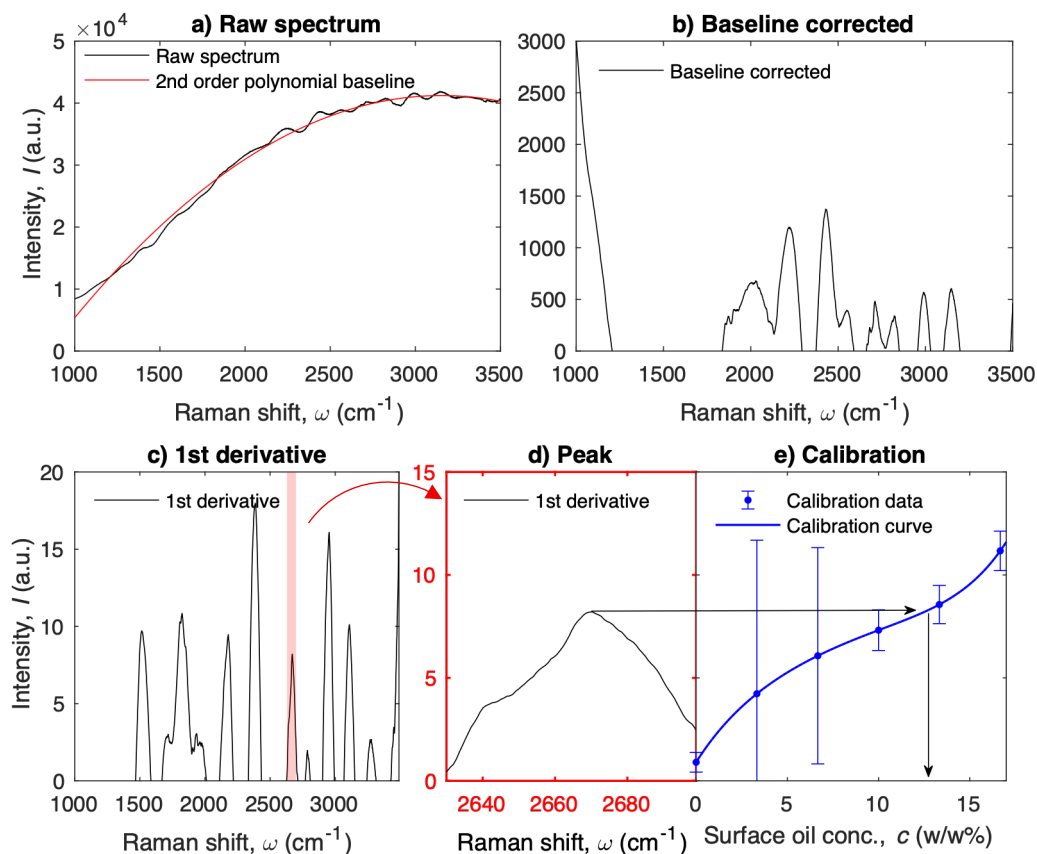


Fig. 5. Procedure for obtaining tablet surface oil concentration from Raman spectra, exemplified for a spectrum of F3. a) 2nd order polynomial is fitted to raw spectrum for baseline correction, b) baseline corrected sample obtained by subtracted the fitted baseline from the raw spectrum, c) spectrum of the first derivative, d) zoom into the peak area between 2630 and 2700 cm^{-1} used throughout all samples, highlighted in red, e) peak intensity converted to surface oil concentration by calibration curve for each formulation. Error bars of the calibration curves represent ± 1 standard deviation from the mean, where the mean was evaluated over the entire tablet surface. The error bars therefore rather represent the inhomogeneity of the table surface.

Formulation 1 with a coarse salt fraction exhibits a patchy oil concentration pattern on the tablet surface at time 0, due to the large oil-free salt particles and larger oil-rich pools in the interstitial spaces, compared to the small Raman probing beam. While oil-rich areas have oil concentrations exceeding 10 w/w%, the low concentration of depleted patches results in an overall initial oil concentration of 10 w/w%. While being a rectangular tablet surface, the edges seem oil-free, suggesting oil migration to have started immediately with poor oil retention capabilities. After 1 week, the overall oil concentration has markedly reduced with a lower oil concentration closer to the bottom against the contacting paper of 2-3 w/w%, while the tablet top is still oil rich at about the initial oil concentration. Oil migration continues until in week 4 global surface oil concentration is 2-3 w/w% with localised hotspots of up to 10 w/w%, likely due to interstitial oil entrapment, which can also be seen at 8 weeks. A similar pattern is visible for F2 comprised of a medium salt fraction with rapid oil leakage into paper within a week,

resulting in a constant global oil composition of 1-3 w/w% until week 8. The slightly larger void fraction in F2 (15.8 v/v%) over F1 (13.4 v/v%) suggests that while being able to hold more liquid oil, oil flow due to larger pores is fast with little resistance to oil migration. F4 composed of coarse and medium salt fractions shows a similar behaviour to F1 and 2, with rapid oil migration occurring within a week of contacting the paper packaging.

Markedly different migration trends occur for formulations with fine salt. F3 composed of a purely fine salt fraction shows a relatively homogenous surface pattern with defined edges, suggesting oil retention throughout the matrix without edge effects. In fact, the initial concentration is maintained constant throughout 8 weeks at a global surface average of 10 w/w%. This suggests that a microstructure comprised of low voidage with small pores performs better at retaining oil than structures of large voidage with large pores. F5 and 6 composed of coarse and fine, and medium and fine salt fractions expectedly show behaviours of purely coarse and purely fine samples. As the surface topography in F5 is not fully smooth, a patchy structure is visible with an overall oil concentration decreasing from initially 10 w/w% to 9 w/w% after 8 weeks, as an average between oil rich and poor regions on the tablet surface. In F6, the surface oil concentration reduces to globally about 8 w/w% at t8 with similar patchy areas. Thus, a mixture of fine and coarse/medium particles retains oil less well, owing to slightly higher voidage, but likely also larger pores than purely fine particles. F7, in which the salt fraction is a mix of all 3 size fractions, results in a homogenous surface topology due to efficient particle packing of the multimodal size distribution. Overall concentration reduces to 8.5 w/w% after 8 days, also suggesting that the microstructure retains oil well.

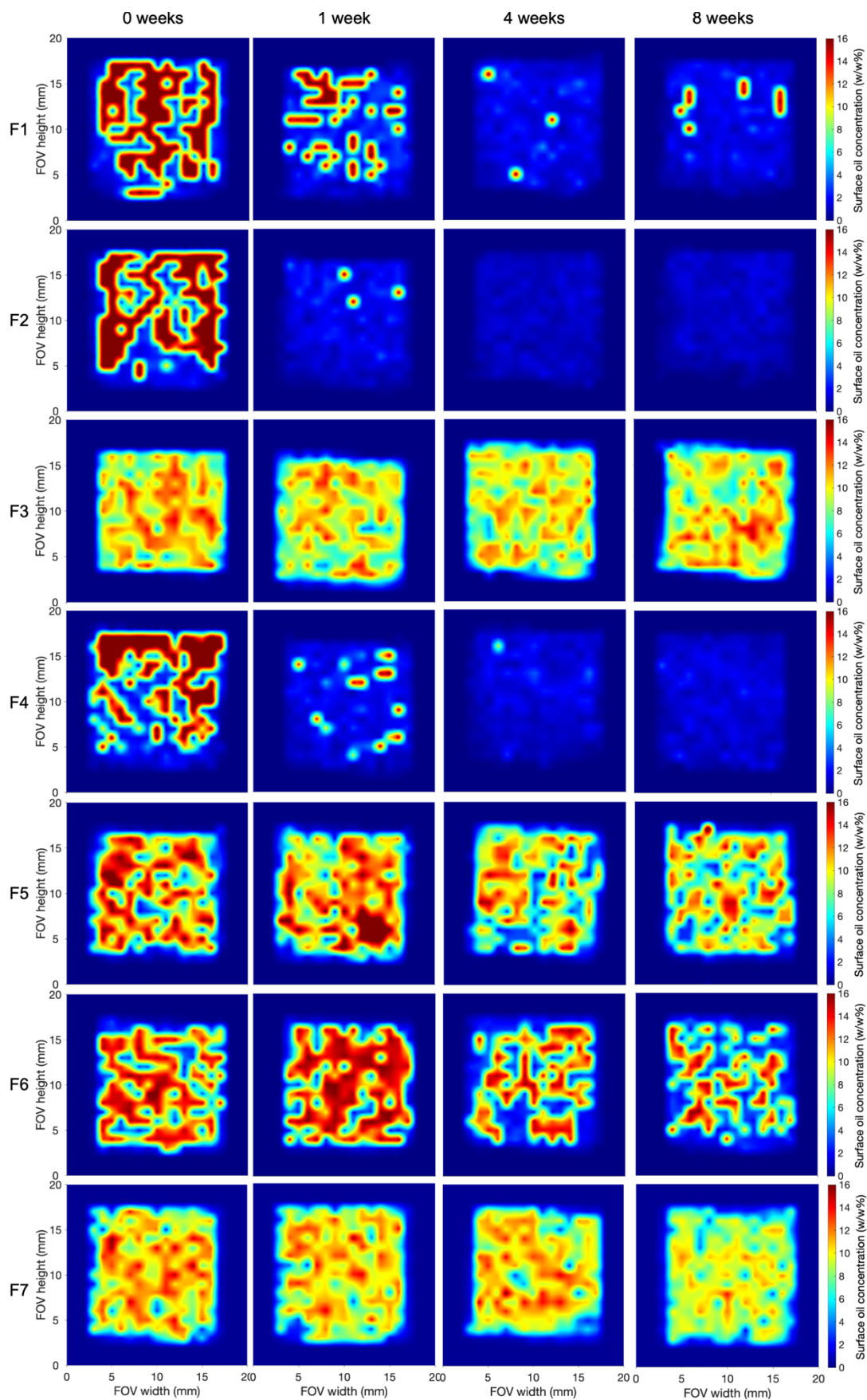


Fig. 6. Raman chemical images depicting oil for each time point for each sample.

3.3 Magnetic resonance imaging

As prior studies of lipid migration in seasoning tablets solely focused on the tablet surface, magnetic resonance imaging was used to visualise oil concentration in the core of the seasoning tablets. The intensity was obtained from the T2 relaxation times and thus is affected by the relative proton density and molecular mobility of the sunflower oil. While proton density (and thus oil concentration) at times zero was equal across all samples and varied with oil migration behaviour, molecular mobility was dependent on the tablet microstructure. The tablets from coarse salt fractions with large interstitial pores and low molecular inhibition showed higher intensity than formulations with fine salt fractions restricting the oil in the interparticle pores. As such, intensity for each formulation had to be normalised to the same mean intensity at $t = 0$ via a calibration function (Fig. 7). The calibration equation was constructed relating arbitrary intensity to oil concentration using seven samples equally spaced between zero and 20 w/w% oil prepared in the same way as formulations F1-7. In comparison to Raman imaging, the calibration equation was linear with $R^2 = 0.99$, so that intensity normalisation for all samples allowed a single master calibration curve to be used. For image analysis, the grayscale of each magnetic resonance images was linearly scaled between 0 (black) and 256 (white) proportional to the core oil concentration.

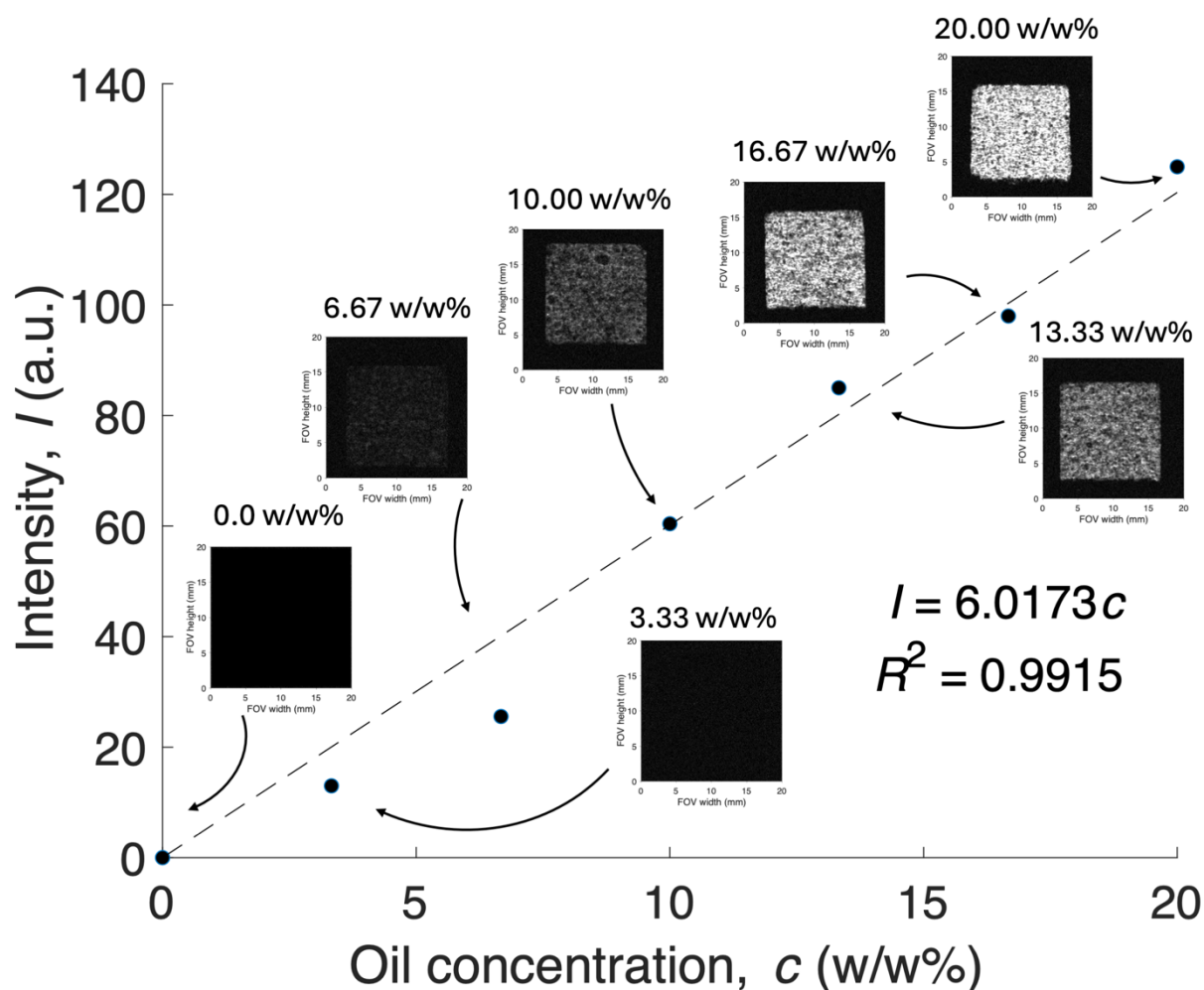


Fig. 7. Calibration curve relating mean whole image MRI intensity against oil concentration with images of central slices of the calibration samples.

While in Raman imaging the concentration scale varied between 0 and 16 w/w%, it varied between 0 and 40 w/w% in MRI images, owing to the smaller voxel resolution of $100\ \mu\text{m}^2 \times 1\ \text{mm}$, compared to the pixel resolution of $1\ \text{mm}^2$ in Raman imaging. Therefore, the pixel signal in MRI images acquired the oil intensity over a smaller area than in RCI, resulting in a more granular map and possibly locally higher intensity and thus oil concentration.

Fig 7 shows the resultant MRI images. The MRI images of F1 (coarse salt fraction) at time 0 shows a marble-like oil distribution across the core of the seasoning tablet. Some bright patches of several mm diameters suggest clusters of high oil concentration, present in the larger interstitial void spaces between large salt particles. After 1 week, overall brightness decreases from initially 10 w/w% to a global oil concentration of 4.5 w/w%, while some oil-rich clusters remain. Oil migration reached an equilibrium at this stage as global oil content plateaus after 4 and 8 weeks, with some oil remaining trapped locally. F2 (medium salt fraction) exhibits a finer grain structure due to smaller pore sizes. The oil concentration reduces similarly rapidly as in F1 to reach 3.5 w/w% after 8 days, with the notable difference that the oil is more evenly distributed and only one hotspot is visible compared to F1 with multiple clusters of oil. This is expected in porous media with smaller pores causing the oil to be more evenly distributed. The resemblance of F1 and F2 with F4 from x-ray tomography and RCI is also valid for MRI, showing a similar speckled oil distribution with similarly rapidly decreasing global oil concentration over 8 weeks, owing to higher voidage and larger pores.

F3 (fine salt fraction) exhibits a considerably finer grain structure due to a finer microstructure forcing the oil to be more evenly distributed. Some darker patches of low oil concentration are likely areas of fine poorly mixed particle agglomeration, characteristic of fine dry particle mixing as fine particles have higher surface energy [25]. Throughout the shelf-life test, overall concentration decreases only marginally by 0.5 w/w%. F5 from coarse and fine salt fractions shows an intermediate grain structure decreasing from initially 10 w/w% to about 8 w/w% in global oil concentration after 8 weeks. Interestingly, a vertical concentration gradient can be discerned with a lower oil concentration in the tablet on the side contacting the paper, growing in concentration towards the tablet top, suggesting that the oil is first drawn from the tablet underside, akin to a diffusion process. F6 from medium and fines salt fractions shows some distinct oil-poor areas surrounded by more homogenous oil distribution. The oil-free patches are much larger than pure salt particles and therefore likely agglomerated fine salt or amorphous material. Global oil concentration decreased from 10 w/w% to 9 w/w%. F7 from all salt size fractions shows a mixture of all behaviours with some oil-free patches and oil-rich patches, while the concentration decreases to 8 w/w%.

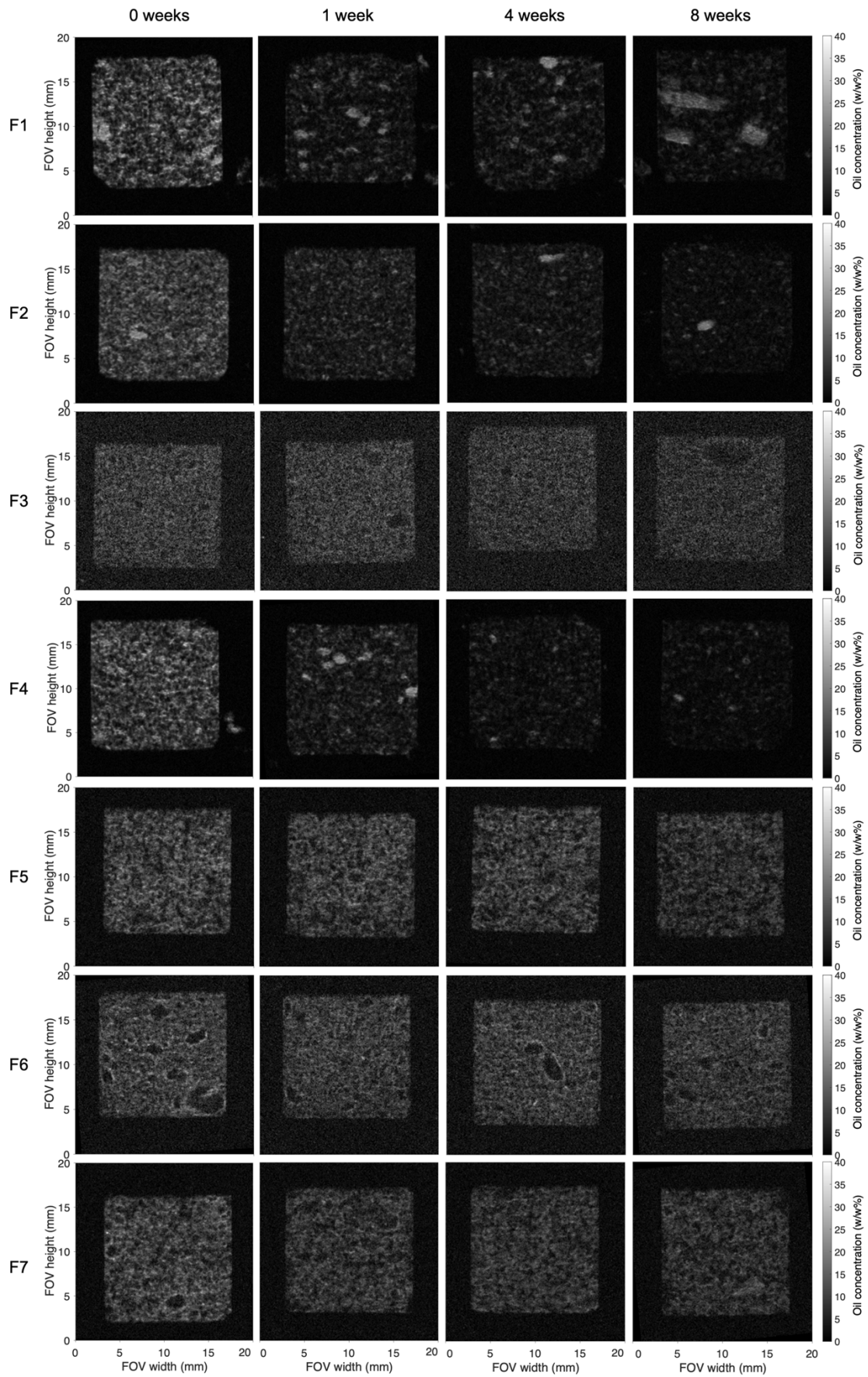


Fig. 7. Central slice in coronal orientation of the final normalised magnetic resonance images for each sample at each time point with grayscale coherent across all samples.

3.4 Optical stain imaging

Optical paper stain of the resultant oil stains during the shelf-life test underneath the tablets showed direct links with migration patterns by Raman chemical imaging and magnetic resonance imaging (Fig. 9). Oil stains on paper for the tablets from coarse particles in F1, F2, and F4 grew from initially 0 to 70 cm². This observation is correlating the rapid oil migration patterns via RCI and MRI suggesting that the oil from the seasoning tablets migrates into the paper. Similarly, for F5 to F7 with fine salt fractions, oil stains are relatively smaller at each time point due to reduced or migration on the tablet surface and core. From the oil stain images on paper is also suggests that the oil stain growth rate directly depends on the oil leakage behaviour in the tablet surface and core.

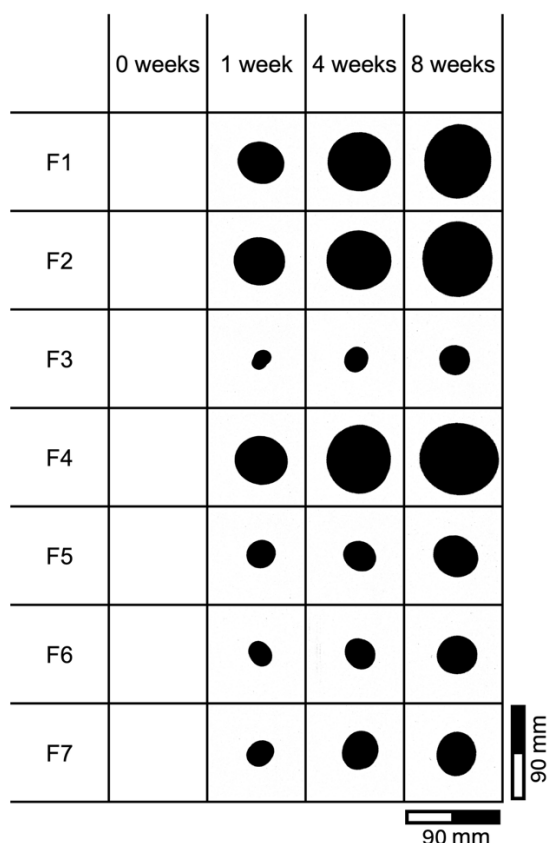


Fig. 9. Thresholded optical stain images of oil in paper for each sample at each time point.

As the samples analysed with each technique are not identical, localised effects such as hotspots or clusters cannot be compared, yet overall similar trends on the surface and core of the tablets can be identified. Rapid oil migration out of the seasoning tablets as in F1, F2, and F4 characterised by rapid colour changes to blue is congruent with the rapid brightness loss in MRI. Formulations with slow oil leakage measured on the tablet surface such as F3, F5-7 also showed slow concentration reduction in the grey value of MRI images. Moreover, MRI does not show significant concentration discrepancies across field of view width of the tablet. This suggest that the one 1D vertical migration assumption without horizontal flow in the width or depth of the tablet is acceptable.

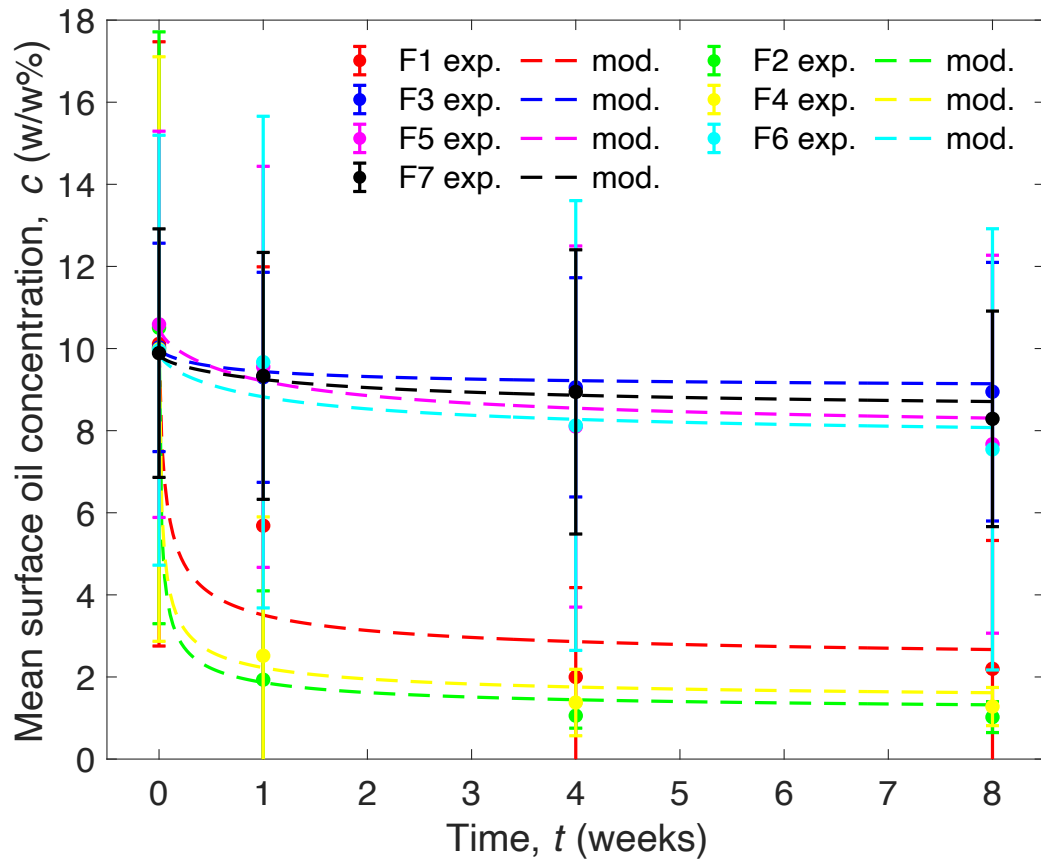
The observations of the 7-component mix with 55 w/w% salt, 10 w/w% oil and the balance sugar and amorphous components in this study differ from a previous study with 95 w/w% salt and 5 w/w% palm kernel fat. While in the present work migration testing was done over 8 weeks and in the prior study 7 days, the ternary design (Fig. 1) between the two studies was identical, thus the difference lies in the tablet composition. For formulation with coarse or medium salt fractions, RCI in the previous study yielded a clear oil migration gradient on the tablet surface, with low oil concentration near the bottom and high concentration at the top, leaking over time in a drainage pattern. In this present study on the other hand, coarse particle formulations yielded fairly isotropic oil leaking pattern on the tablet surfaces, without top-to-bottom gradients. The difference between the two studies could be due to the shorter measurement intervals in the previous study capturing a more precise time resolution compared to the longer time intervals and reduced time resolution for this study. For formulations with fine salt particle fractions, the previous study indicated rapid and homogenous fat decrease to near 0 w/w% surface fat within a few days, however with minimal fat stain development on paper substrate, suggesting fat migration into the core of the tablet. In the present study, surface oil migration is much more gradual and decreases at about the same rate as core oil content to generate visible oil stains. Comparing their x-ray images, in the previous study it was suggested that the fine particle structure absorbs fat further towards the table core via capillary suction, yet preventing migration into paper due to low permeability of fat flow as the channel size is reduced. In the present study, it can be seen from the XCT images that the additional sugar and amorphous phase significantly fills the pore space between salt particles, thus reducing the porosity. As such, oil content on the tablet surface is not drawn horizontally into the cube core but migrated vertically in a 1D fashion at the same rate as the core oil fraction.

3.5 Diffusion modelling

As surface and core migration patterns in the seasoning tablet are similar, the diffusion model was simplified to 1D vertically from the tablet top into the underlying paper packaging. Diffusivity D was evaluated from Eq. 3 using the average oil concentration $\bar{c}(t)$ over the tablet surface or tablet core at each time point t . Assuming a semi-infinite sink with nonzero tablet-paper interfacial concentration, $c(0, t)$ was taken to be constant at each time point at the equilibrium concentration at $t = 8$ weeks, $c(\bar{x}, t)$ was taken as the average $\bar{c}(t)$ at $t = 0$. Fig 10 shows the experimental and model fit of the average oil concentration against time for (a) surface oil via RCI and b) core oil via MRI. Error bars show the standard deviation of Raman intensity over the entire tablet surface and thus rather represent the inhomogeneous surface and core morphologies. Comparing experimental data between surface and core measurements, tablets from coarse and medium salt fraction, the surface oil concentration is approximately 2 w/w% lower for all time points $t > 0$ than the core oil concentration. This was attributed to the surface oil exposure to the environment and hence less entrapment than the core oil. In addition, capillary suction into the tablet core, observed more pronouncedly in a similar study, is likely to cause surface oil reduction. For tablets from fine salt fractions, the concentration difference between surface and core is about 1 w/w%, owing to closer entrapment and reduced permeability of oil and thus higher stability of oil on the tablet surface.

The diffusivities evaluated globally above were also used to predict the local oil migration profiles across the height of the tablet. Profiles from experimental data were evaluated in the FOV height and width for both surface and core by averaging concentration at each acquired pixel in the rows and columns respectively (Fig. 11). The profiles confirm prior observations from Fig. 6 and 8 such as rapid concentration decrease for coarse and medium salt formulations and slower concentration decrease for fine salt formulations. While coarse formulation bared a top-to-bottom concentration gradient, especially for surface oil, fine formulations only showed a shallow gradient, suggesting again that surface oil in larger porosity formulations is highly mobile and migrates fast compared to core oil in fine formulations being highly stabilised in the finer microstructure. Width profiles show larger variability for RCI samples due to lower acquisition resolution compared to MRI samples, and are generally more variable for coarse formulations due to occasional oil clusters that are absent in more evenly distributed fine formulations. Obvious stratifications in the width profiles can not be detected, reinforcing the earlier assumption of predominantly 1D migration. The diffusion profiles based on equation 2 overall match the experimental profiles while differing locally, especially for coarse formulations. For samples at $t = 0$, the model assumes a constant profile at the global initial concentration with a concentration decrease close to the interfacial concentration at $x = 0$. Especially coarse formulations leaked immediately before acquisition completion and thus show a gradient instead of a constant profile. For further time points the model assumes profiles of decreasing gradients with time. While the experimental profiles demonstrate some gradient behaviour, the experimental gradients are shallower than the model. At further time points 4 and 8 weeks the model gradient flattens and is more congruent with the experimental profiles. Comparing to the capillary flow model suggested previously, both capillary and diffusion models are able to explain some lipid migration behaviour.

a)



b)

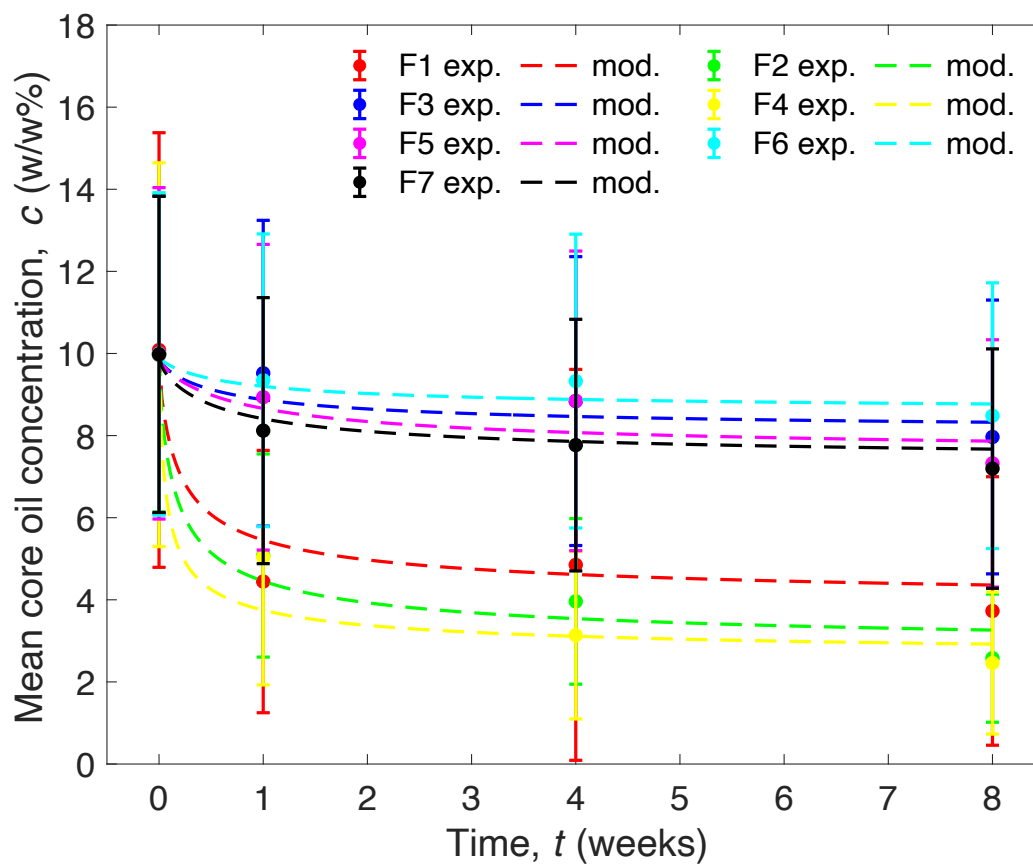


Fig. 10. Experimental data and model curve for oil migration in the seasoning tablet a) on the tablet surface measured via Raman chemical imaging, and b) in the tablet core measured via magnetic resonance imaging. Error bars are standard deviation over the entire tablet surface or core.

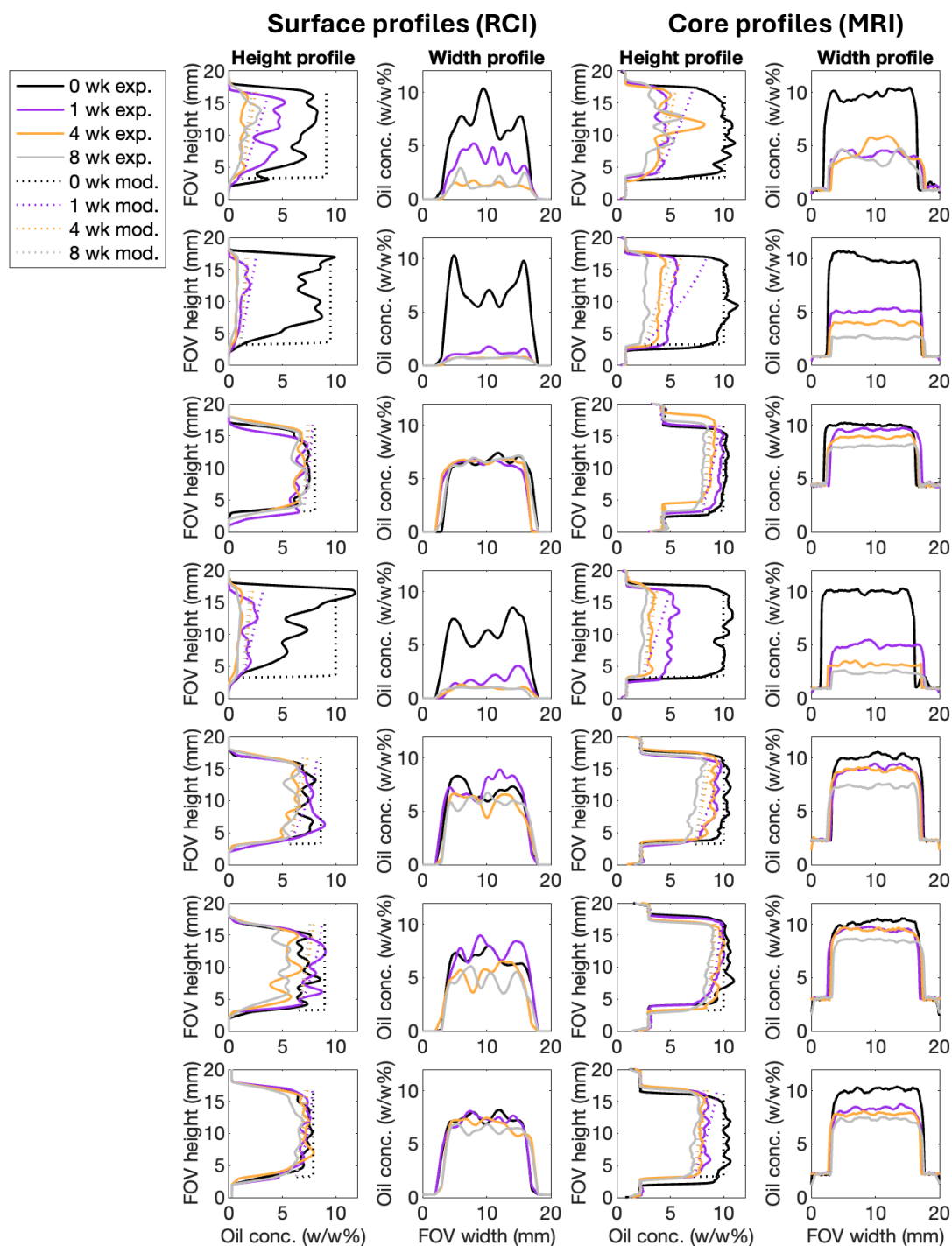


Fig. 11. Height and width profiles of oil concentration in seasoning tablet surface and core

1. Conclusion

The aim of this work was to characterise oil migration in seasoning tablets into an underlying paper sheet to investigate the effect of salt particle size on flow dynamics on the tablet surface and in the tablet core. Tablet formulations were prepared from salt (55 w/w%), oil (10 w/w%), and the balance sugar, starch maltodextrins and monosodium glutamate, with salt fraction

particle sizes from 5 to 500 μm . Characterisation was performed with Raman chemical imaging (surface) and magnetic resonance imaging (core), and modelled as 1D Fickian diffusion. Imaging methods confirmed prior observations for simple salt-lipid systems that oil retention is higher in formulations with smaller pores, as a result of smaller salt fractions inducing higher capillary suction and higher frictional resistance in flow channels. Analogously, oil stains on packaging resulting from coarse salt tablets are larger as capillary pressure is reduced and permeability in large interstitial pores increases. Oil concentration on the surface was lower by 2% than in the tablet core, likely due to oil being less stable in interstitial pores at the surface than in the core surrounded by neighbouring particles.

CRedit authorship contribution statement

Luc Dewulf: Writing – review & editing, Writing – original draft, Visualization, Validation, Supervision, Software, Resources, Project administration, Methodology, Investigation, Formal analysis, Data curation, Conceptualization. **Steven Reynolds:** Investigation, Data curation, Writing – review & editing. **Michael K. Hausmann:** Supervision, Resources, Project administration. **Annabel Bozon:** Supervision, Resources, Project administration. **Gerhard Niederreiter:** Supervision, Funding acquisition. **Stefan Palzer:** Funding acquisition, Writing – review & editing. **Agba D. Salman:** Writing – review & editing, Supervision, Funding acquisition.

Declaration of competing interest

The authors declare the following financial interests/personal relationships which may be considered as potential competing interests: Luc Dewulf reports financial support was provided by Engineering and Physical Sciences Research Council. Luc Dewulf reports financial support was provided by Nestlé Research & Development. If there are other authors, they declare that they have no known competing financial interests or personal relationships that could have appeared to influence the work reported in this paper.

Data availability

Data will be made available on request.

Acknowledgements

The author thanks EPSRC (grant 2602203) and Nestlé for funding this research, as well as the iForge makerspace and the Open Access Mechanical Workshop at the University of Sheffield for the accessible workshop facilities used to self-build the experimental setup. Special thanks go to Dr Richard Hodgkinson for encouragement and liaison for MRI.

References

- [1] S. Gupta, P. Bongers, Bouillon cube process design by applying product driven process synthesis, *Chemical Engineering and Processing: Process Intensification*, 50 (2011) 9-15.
- [2] L. Dewulf, M.K. Hausmann, A. Bozon, G. Niederreiter, S. Palzer, A.D. Salman, Particle-based food systems subject to lipid migration – A review of measurement, modelling, and mitigation approaches, *Powder Technology*, 445 (2024) 120097.
- [3] J. Bricknell, R.W. Hartel, Relation of fat bloom in chocolate to polymorphic transition of cocoa butter, *Journal of the American Oil Chemists' Society*, 75 (1998) 1609-1615.
- [4] H. Hondoh, K. Yamasaki, M. Ikutake, S. Ueno, Visualization of oil migration in chocolate using scanning electron microscopy–energy dispersive X-ray spectroscopy, *Food Structure*, 8 (2016) 8-15.
- [5] C. Cevoli, A. Evangelisti, P. Gradari, A. Fabbri, Storage of wafer cookies: Assessment by destructive techniques, and non-destructive spectral detection methods, *Journal Of Food Engineering*, 336 (2023).
- [6] L. Dewulf, M.K. Hausmann, A. Bozon, G. Niederreiter, S. Palzer, A.D. Salman, Food vs packaging: dynamics of oil migration from particle systems into fibrous material, *Powder Technology*, 439 (2024) 119721.
- [7] S.K. Reinke, F. Wilde, S. Kozhar, F. Beckmann, J. Vieira, S. Heinrich, S. Palzer, Synchrotron X-Ray microtomography reveals interior microstructure of multicomponent food materials such as chocolate, *Journal of Food Engineering*, 174 (2016) 37-46.
- [8] M.J. McCarthy, K.L. McCarthy, Quantifying transport phenomena in food processing with nuclear magnetic resonance imaging, *Journal of the Science of Food and Agriculture*, 65 (1994) 257-270.
- [9] S. Cikrikci, M.H. Oztop, Mathematical modeling and use of magnetic resonance imaging (MRI) for oil migration in chocolate confectionery systems, *Food Engineering Reviews*, 9 (2017) 50-70.
- [10] G. Ziegleder, C. Moser, J. GeierGreguska, Kinetics of fat migration within chocolate products .2. Influence of storage temperature, diffusion coefficient, solid fat content, *Fett-Lipid*, 98 (1996) 253-256.
- [11] G. Ziegleder, I. Schwingshandl, Kinetics of fat migration within chocolate products. Part III: fat bloom, *Fett-Lipid*, 100 (1998) 411-415.
- [12] S. Cikrikci, M.H. Oztop, Oil migration in hazelnut paste/chocolate systems using magnetic resonance imaging, *Journal of Food Measurement and Characterization*, 12 (2018) 1460-1472.
- [13] Y.M. Harshe, H. Deyber, O. Schafer, L. Sandoz, O. Breton, Impact of composition and aeration on the migration of TAGs in sandwich type confectionery products, *Food Research International*, 169 (2023) 112848.
- [14] L.F. Julien Mahieux, Ulrich Bobe, Volker Kehlenbeck, Annabel Bozon, Jose Krauch, Process for preparing a bouillon tablet, in: WIPO (Ed.), 2019.
- [15] A.B. Ulrich Bobe, Volker Kehlenbeck, Jimmy Perdana, Process for making a bouillon tablet or bouillon cube, in: WIPO (Ed.), 2019.
- [16] A. Fedorov, R. Beichel, J. Kalpathy-Cramer, J. Finet, J.-C. Fillion-Robin, S. Pujol, C. Bauer, D. Jennings, F. Fennessy, M. Sonka, J. Buatti, S. Aylward, J.V. Miller, S. Pieper, R. Kikinis, 3D Slicer as an image computing platform for the Quantitative Imaging Network, *Magnetic Resonance Imaging*, 30 (2012) 1323-1341.
- [17] A. Fick, Über dffusion, *Annalen der Physik*, 170 (1855) 59-86.
- [18] J. Crank, *The Mathematics of Diffusion*, Clarendon Press, Oxford, 1975.
- [19] D. Lin-Vien, N.B. Colthup, W.G. Fateley, J.G. Grasselli, *The Handbook of Infrared and Raman Characteristic Frequencies of Organic Molecules*, Academic Press, San Diego, 1991.

- [20] R.M. El-Abassy, P. Donfack, A. Materny, Assessment of conventional and microwave heating induced degradation of carotenoids in olive oil by VIS Raman spectroscopy and classical methods, *Food Research International*, 43 (2010) 694-700.
- [21] R.M. El-Abassy, P. Donfack, A. Materny, Visible Raman spectroscopy for the discrimination of olive oils from different vegetable oils and the detection of adulteration, *Journal of Raman Spectroscopy*, 40 (2009) 1284-1289.
- [22] *Imaging Technologies and Data Processing for Food Engineers*, Springer, Berlin, 2016.
- [23] P. Kubelka, F. Munk, Ein Beitrag Zur Optik Der Farbanstriche, *Zeitung für Technische Physik*, 12 (1931) 593-601.
- [24] B. Schrader, G. Bergmann, Die Intensität des Ramanspektrums polykristalliner Substanzen, *Fresenius' Zeitschrift für analytische Chemie*, 225 (1967) 230-247.
- [25] J.N. Israelachvili, *Intermolecular and surface forces*, Academic Press, New York, 2011.

Chapter 7

Summarising discussion

In this work, for the first time, lipid migration from seasoning tablets into paper packaging was investigated. A systematic approach was undertaken starting with a literature review, followed by a methodology chapter, an experimental chapter exploring the migration mitigation strategy, a modelling chapter, and concluding with an application chapter. The thesis was written in *publication style* with each chapter consisting of a published paper or submitted manuscript, in which each article already contains a thorough discussion. As such, this discussion serves to briefly link each chapter and conclude the comprehensive storyline of the thesis.

The literature review revisited the fundamental mass transfer mechanisms of lipid migration in particulate systems being capillary flow and diffusion, and the interplay between thermodynamic driving force and kinetics giving rise to metastability. Characterisation techniques from literature were described and their advantages and disadvantages discussed for different purposes. Raman chemical imaging was identified as a potential yet never used technique for lipid migration studies. The literature review also discussed physical lipid stabilisation techniques for particulate systems. Pore microstructuration was identified as a novel strategy never used for seasoning tablets before. Modelling approaches described in literature were reviewed and it was concluded that capillary flow models are more realistic than diffusion models yet require abundant microstructural data and are thus underutilised. Overall the extensive literature review was used to guide the succeeding work of this thesis.

The methodology chapter described in detail the major characterisation technique Raman chemical imaging that was developed for the first time for lipid migration analysis. Specifically the two major Raman imaging techniques are discussed: distribution imaging and global intensity imaging. A detailed description of the self-built hardware for signal acquisition and self-coded software for signal processing is provided for 2D image generation from spectra. Explanations of resolution of laser point probes and how to handle multiple Raman active species are described as a groundwork for the subsequent chapters.

The literature review and methodology chapters are followed by three original research chapters. In the first of these, the novel strategy to mitigate lipid migration in food tablets via microstructuration was successfully tested. Additionally, the two major characterisation techniques for lipid migration measurement in the table (Raman chemical imaging) and in the packaging paper (automated stain quantification) are used complementarily. This chapter thus proved the concept that changing the tablet microstructure to yield smaller interstitial pores by

reducing particle size enables to retain more lipid in the tablet, resulting in visibly less lipid stains on the paper. With a particle size of $d_{50} = 50 \mu\text{m}$ there were no visible lipid stains on the paper packaging, essentially fulfilling the desired outcome to entirely suppress lipid migration from food into packaging.

While the prior chapter was a successful initial application of the novel mitigation strategy and characterisation techniques used in this thesis, the underlying mass transfer mechanisms were unexplored and thus a mathematical description was needed. The second original research chapter was therefore a modelling chapter. The literature review identified models based on capillary flow as gaps in literature and hence a detailed quasi 2D first-principle model that captures both lipid migration in the tablet and in the contacting paper packaging was established. The model was built from the Young-Laplace equation for capillary suction and the Darcy equation for permeability and was validated with a series of physical experiments replicating the theoretical model. Different particle sizes and thus capillary pressures and permeability values were explored by systematically varying salt particle size from $d_{50} = 5 \mu\text{m}$ to $d_{50} = 500 \mu\text{m}$ in a ternary mixture design of experiments.

Model and experiments compared well for coarse salt particles as the predicted lipid concentration in the tablet was congruent with the measured values, and predicted lipid area in paper packaging was similar with measured data. Thus the proposed capillary flow transport phenomenon was applicable and valid. The model predictions failed to predict lipid concentration on the tablet surface for formulations with very fine particle sizes and thus very narrow pores. While the model predicted slow concentration changes, the lipid concentration dropped very fast to almost 0 w/w% on the tablet surface as measured via Raman chemical imaging. As the lipid on the tablet structure is not trapped in interstitial pores, it was suggested that the high capillary suction draws this unstabilised surface lipid towards the tablet core, or at least into the inside vicinity of the tablet surface, rendering it free of lipid. The assumption that globally lipid is more stabilised and migrates less towards a contacting paper packaging in fine tablet microstructures was still valid. Lipid stains on paper packaging decreased with a decrease in salt particle size. In fact, lipid stains on packaging were almost non-existent for tablets made from 100% of the particle fraction consisting of $d_{50} = 5 \mu\text{m}$ particles. As such, the 1D model assumption was partly valid for this simplified lipid-salt system.

The prior chapters identified the gap in literature, explained self-developed characterisation techniques, demonstrated a successful lipid migration mitigation strategy and detailed an elaborate capillary flow model capable of explaining most of the observed mass transfer behaviour. As in the modelling chapter it was proposed that for fine tablet structures lipid migrates into the tablet core, it was desired to investigate not only the tablet surface with Raman chemical imaging, but also the internal tablet structure via nuclear magnetic resonance (NMR) tomography. Additionally, the model system so far was a lipid-salt tablet only. For a more complex and realistic food system, a 7-component seasoning tablet mix was desired. Modelling via a capillary approach is difficult for complex formulations, therefore diffusion modelling was appropriate for the more complex seasoning structure.

The third original research chapter was thus an applied chapter due to its use of a real seasoning formulation comprising 7 components. It also enabled visualisation of the tablet cross section and thus lipid distribution in the core, which was not possible previously with surface Raman characterisation. The diffusion modelling approach omits simplifications described so

far in lipid migration literature and instead uses a numerical solution to Fick's second law. Similarly to the two previous chapters, the salt particle size was changed according to the same systematic design of experiment.

Comparisons of 7-component samples within the study showed the same expected behaviour on the tablet surface as on the resulting packaging paper. Fast concentration reduction of surface lipid was observed for coarse salt particles, congruent with large resulting lipid stains on packaging. Conversely, surface concentration changed slowly for samples from fine salt fractions and resulted in small lipid stains on paper, meaning more lipid is retained in the tablet. NMR tomography confirmed results for this 7-component study that surface and core lipid concentration change at the same rate with only maximum 2 w/w% difference. These observations support the assumption of a 1D lipid flow vertically out of the tablet and into the paper. It also reinforces the modelled hypothesis from the prior chapter that a fine tablet microstructure results in high capillary suction retaining more lipids in the tablet structure, ensuing less lipid stains on paper packaging.

Comparison of the 7-component samples with the prior 2-component lipid-salt modelling samples showed stark differences. In both types of formulations the general lipid migration mitigation strategy to reduce lipid staining on paper packaging by particle size reduction was valid. In the 7-component samples however, lipid in the tablet core and on the tablet surface migrated at approximately the same rate. In the 2-component samples, lipid concentration on the tablet surface in fine salt formulations decreased much faster than for coarse formulations of the same modelling study, and also decreased much faster than for fine formulations of the 7-component study. In the 2-component modelling study it was suggested that surface lipid migrates rapidly into the tablet core away from the surface. This migration into the core was not observed for the 7-component study. It thus can be said that observations from a lipid-salt binary system are not directly comparable with a seasoning tablet system containing multiple components. In addition, the 7-component formulation behaved much more as a 1D system, whereas the inconsistent deviation from experiments for fine microstructure in the 2-component samples suggest some 2D horizontal behaviour. The 1D assumption used for diffusion modelling in the 7-component study likely valid as little deviation between core and surface lipid concentration was observed. Additionally, in both systems, the underlying design of experiment framework was the same and showed that a particle size reduction, effecting narrower pore channels (confirmed with 3D x-ray tomography images), is able to significantly reduce lipid staining on paper packaging.

Despite a holistic attempt at advancing knowledge on lipid migration from compacted food particle matrices, more learnings could be obtained from future work. For example, the particulate food formulations in this work did not undergo phase change. It would be interesting to investigate physical phase changes, for example deliquescence of crystalline materials or glass transition of amorphous ingredients in the compacts, and their effect on lipid mobility and hence migration. Further, to obtain higher resolution Raman chemical images, a higher spatial pixel density could be acquired with longer experiment running time. Modelling could be improved by expanding the 1D vertical flow approach taken in this work to include 2 or 3D horizontal lipid migration within the compacts. Finally, different paper packaging substrates could be investigated with various different fibre networks and grease permeability parameters.

Chapter 8

Conclusion

This thesis in publication-style aimed to advance knowledge in the field of lipid migration from particle-based compacted consumer foods into paper-based packaging. Specifically, it aimed at understanding the current state of the art described in literature, developing a appropriate lipid migration mitigation strategy, build powerful analytical techniques, and model mathematically the mass transport phenomenon to understand the fundamental mechanisms. The target food structure was a lipid-containing seasoning tablet in contact with paper packaging. This work was successful in all aims. Specifically:

- A published literature review summarised prior published literature on the fundamental mass transfer mechanisms proposed in literature, previously reported characterisation techniques for lipid migration assessment, modelling approaches described in the open literature, and mitigation strategies for particle-containing food systems. Most importantly, the literature review enabled to identify gaps in the prior art and select and direct the future research of this thesis.
- A method paper manuscript described in detail the analytical technique of Raman chemical imaging from point probes, a technique identified from the literature review as powerful for surface characterisation yet unreported for lipid migration studies. The self-developed laser hardware and signal processing software are described for this novel application to generate 2D images of lipid concentration on the food tablet.
- A published original research paper described the new strategy to mitigate lipid migration in seasoning tablets, a microstructure restructuring approach identified as novel during the literature review. Building on the theory of capillary suction described by the Young-Laplace equation, lipid-salt tablets with narrow interstitial pores were prepared by reducing salt particle size. The first implementation of Raman chemical imaging and automated stain quantification of paper packaging showed that reducing the particle size from $d_{50} = 500 \mu\text{m}$ to $d_{50} = 50 \mu\text{m}$ almost fully prevented lipid stains on contacting paper packaging. This was a successful proof of the characterisation techniques and the lipid immobilisation technique
- A second original research article describes a mathematical model constructed to explain the transport phenomena occurring in the model system of the previous chapter from first principles. The model is based on capillary flow, a modelling approach identified

as underutilised due to the requirement of microstructural data, which was acquired here via lipid sorption profiles and x-ray microtomography. The model is built by accounting for thermodynamics (capillary pressure) and kinetics (permeability) of both tablet and paper packaging and was able to predict the lipid migration behaviour validated in an experiment by Raman chemical imaging and automated stain quantification.

- A third submitted original research manuscript expanded on the previously used 2-component lipid-salt tablets and utilised an applied 7-component mix, varying the salt size fraction in a systematic design of experiments. In addition to surface characterisation via Raman chemical imaging and automated stain quantification on paper, nuclear magnetic resonance tomography was used to characterise lipid migration in the tablet core. As multi-ingredient formulations are complex to characterise microstructurally, a numerically solved diffusion model was established linking the effect of formulation changes to lipid diffusivity.

Conclusively, this thesis has achieved experimentally and mathematically to advance knowledge and understanding of lipid migration from model and applied seasoning tablets formulations into paper packaging, and developed advanced characterisation techniques, novel modelling approaches, and successful mitigation strategies to an academically challenging and industrially highly relevant subject.

Appendix A

Additional data of application chapter

Based on the ternary Design of Experiments in [chapter 6](#)

Formulation

Top view

Side view

F1



F2



F3



F4



F5

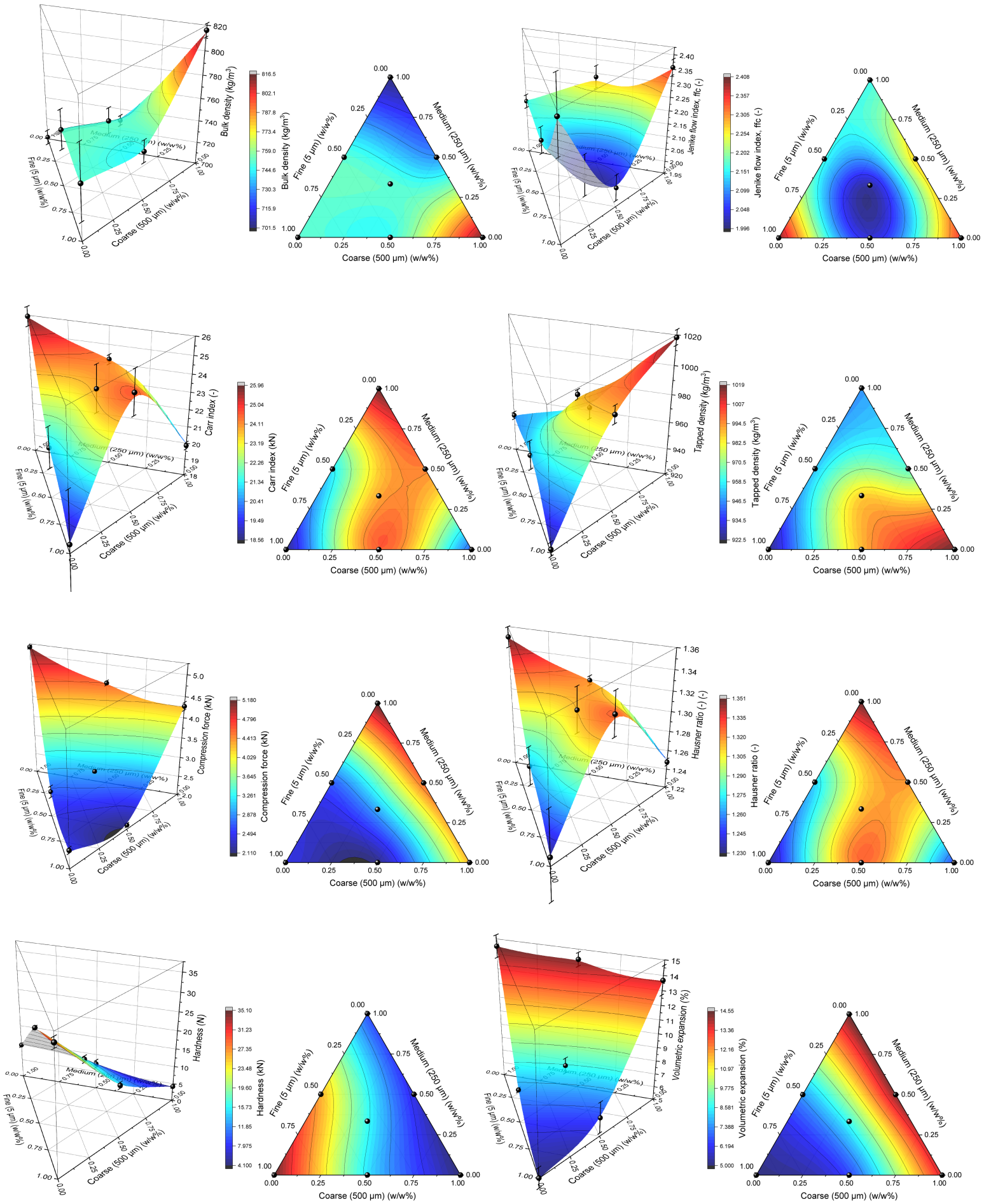


F6



F7





Appendix B

List and links of publications

Chapter 2 Literature Review: *Particle-based food systems subject to lipid migration – A review of measurement, modelling, and mitigation approaches*

<https://doi.org/10.1016/j.powtec.2024.120097>



Chapter 3 Methodology: *A Method for Raman Chemical Imaging from Point Probes: Hyperspectral Characterisation of Food Powder Structures*

<https://dx.doi.org/10.2139/ssrn.5163406>



Chapter 4 Mitigation Strategy: *Food vs packaging: Dynamics of oil migration from particle systems into fibrous material*

<https://doi.org/10.1016/j.powtec.2024.119721>



Chapter 5 Modelling: *Fat migration from a particulate food system into fibrous material via capillary flow – first-principle modelling and experimental validation*

<https://doi.org/10.1016/j.cherd.2026.02.012>



Chapter 6 Application: *Surface and core effects in oil migration from particulate seasoning tablets into paper packaging via Raman and Magnetic Resonance Imaging*

https://drive.google.com/drive/folders/1xz1JeM_ChJgGhnxxSjMCMGimbmX1ldR?usp=share_link



Patent: A filed but yet unpublished patent (application number: EP24190622) emerged from PhD work of the author, and for which the author is first inventor. While not directly linked to lipid migration in seasoning tablets, the aim was still to control oil content in consumer foods, specifically noodles. The entire experimental work and writing of this patent was undertaken during the author's PhD at the University of Sheffield.



https://drive.google.com/drive/folders/1wf0o616gvSNp6C0swUr6Zyw2TiMa10p_?usp=share_link

Conference: 10th International Granulation Workshop, Sheffield, UK



https://drive.google.com/drive/folders/1R0qjmZM62AgqNrAIduWB0ira7p_F4MbQ?usp=share_link

Conference: Partec, Nürnberg, Germany



https://drive.google.com/drive/folders/1qmPRR3fUzQ3V1HzUBWw1FKGo3l112orWf?usp=share_link

Conference: American Institute of Chemical Engineers Annual Meeting, San Diego, CA, US



https://drive.google.com/drive/folders/10b85TaqD6HIL29P1704zteTIspDgsj8Y?usp=share_link

Conference: Institution of Chemical Engineers ChemEngDay, London, UK



https://drive.google.com/drive/folders/10b85TaqD6HIL29P1704zteTIspDgsj8Y?usp=share_link

Conference: 27th International Congress of Chemical and Process Engineering, Prague, Czech Republic



https://drive.google.com/drive/folders/1wkckbST0yudWMgxmVvyoN6JkLKY_LHwT?usp=share_link

Conference: 11th International Conference on Conveying and Handling of Particulate Solids, Edinburgh, UK



https://drive.google.com/drive/folders/1106SperES_HCYiIFNxp99ti36ziy1rW?usp=share_link

Conference: Nestlé PhD Day, Lausanne, Switzerland



https://drive.google.com/drive/folders/14bKbpwy_P1i2dlVx5b6LyAkM14AgGfET?usp=share_link

Conference: European Federation of Chemical Engineering, European PhD Workshop on Food Engineering and Technology, Athens, Greece



https://drive.google.com/drive/folders/1zAH75LV7nS1qnveEeNzE_jJoSNaWZqc8?usp=share_link

Appendix C

Evidencing Development Summary

It is a University of Sheffield requirement for each PhD student to submit an *Evidencing Development Summary* along with their thesis as stated here: <https://www.sheffield.ac.uk/rpi/pgr/ddp/evidencing-development>

Evidencing Development Summary

Process for submitting this form

Completion of this Evidencing Development Summary (EDS) is required to meet the DDP Regulatory requirement and obtain a doctoral award.

You should complete it around two to three months before the end of your normal registration period (or four to six months if you are a part time student).

Once completed, this form should be approved and signed by your supervisor. Please note this cannot be a typed signature. You should then submit it to Research, Partnerships & Innovation (RPI) via ddpsummary@sheffield.ac.uk, who will take it forward for Faculty approval.

If you are a student in the **Faculty of Health** who has completed your EDS in PebblePad, you need only obtain your supervisor's signature on the first page of this form and can disregard the rest. However you must still forward this signed form on to RPI for Faculty approval. From academic year 24/25 onwards the Faculty of Health will no longer use PebblePad. Therefore students commencing their programme on or after this date are required to fill in all sections of this form.

Guidance for completing this form

Use the following table to write a 100-200 word reflection on your development of each of the eight core competencies. You should refer to your TNA document to draw out examples, and you may wish to give your answer in the style of a job application using examples. See below for advice on using [STAR](#) examples:

In cover letters, application forms and interviews, using the [STAR approach](#) (Situation, Task, Action, Result) can help give a clear structure for your examples:

- Situation you were in
- Task you had to do
- Actions you took, explained clearly and specifically
- Result – positive outcome and/or what you learned

Name:	Luc Dewulf
Registration Number:	210116834
Department:	School of Chemical, Biological and Materials Engineering

Personal skills (time management, resilience, problem-solving, critical thinking)

While speaking French and German as mother tongue, I wished to improve my language skills and took up Spanish by taking the Spanish Level 1 Module comprising 3 contact hours per week with continuous assessment and a formal written and oral examination. By engaging with the course and meeting with Spanish speakers outside of the course I achieved the module and can now speak and write some basic Spanish, which is useful given its wide reach as an international language. This required me to be resilient while managing my other PhD commitment such as the PhD research.

Communication, networking and collaboration

Being driven by providing outstanding research required me to go beyond our laboratory capabilities and seek external research infrastructure and input and did this for each of my 3 chapters. For Raman spectroscopy I visited Prof. Arnulf Materny in Bremen, learning in his specialised Raman lab the fundamentals of what would become the main characterisation technique in my thesis; for fluid-mechanical modelling I sought assistance from Dr. Jordan MacInnes, with whom I have kept in touch since him being my foundation year tutor; and lastly for magnetic resonance imaging I leveraged my network to access the preclinical MRI scanner at Hallamshire Hospital at a reduced cost. Thus, I strongly built on my previous communication, networking and collaboration skills and deepened them to strengthen the scientific excellence in my PhD work.

Professional skills (academic defence, academic writing, project/resource management)

The novel experimental techniques that I developed during my PhD, especially for Raman Chemical Imaging, required me to do extensive hardware modifications to build my own sampling setup. Instead of offloading this work to the department technicians, I decided to proactively seek access to the workshop and machine my own parts, and as such gain professional skills. As part of this route I attended a 2-week machining course provided by the AMRC to which I was invited through my network of the technical staff at the university. Accomplishing this course (see certificates below) enabled me to freely access and use any machine in the workshop which resulted in accelerated hardware construction to my specific needs which would not have been possible by outsourcing to the department technicians. In fact, my workshop skillset became unique in the research group so that other PhD students from our group asked me to design and manufacture items for them.



Certificate of Attendance

The University of Sheffield AMRC Training Centre is pleased to present this course certificate for the successful completion of

Introduction to Manual Milling Techniques

Awarded to
Luc Dewulf

Date: 8th - 11th July 2024
Duration: 4 days
Venue: AMRC Training Centre, Rotherham



Sponsored by the
Regional Growth Fund



Certificate of Attendance

The University of Sheffield AMRC Training Centre is pleased to present this course certificate for the successful completion of

Introduction to Manual Turning Techniques

Awarded to
Luc Dewulf

Date: 15th - 18th July 2024
Duration: 4 days
Venue: AMRC Training Centre, Rotherham



Sponsored by the
Regional Growth Fund

Leadership, i.e. autonomy and influence

Besides the mechanical workshop mentioned above, I needed access to more modern and rapid manufacturing techniques such as laser cutter and 3D printers. To be able to use these tools, I became active in the iForge Makerspace, a student-led workshop at the university. Beyond mere design and making I became active in the leadership team that runs the iForge. Running the iForge Operations Team, I learned to lead a team of up to 10 iForge reps, running daily operations tasks in the iForge such as health and safety supervision, restocking the space, all the way to motivating the team to come for a weekend cleanup to to get engaged in outreach activities such as the “Science Alive fair” for primary school children or the “If I were an Engineer” challenge for secondary school children. In a further step of leadership development I was a recruiter for the iForge, recruiting students to run the makerspace according to strict expectations and assets that we aim to have in recruits. This then required to select candidates and finally recruits to match the desired skillsets and that we sought. Beyond iForge work, I have also been a passionate GTA each of the 4 years of my PhD, tutoring and lecturing two modules (Science of formulated products, and Continuous pharmaceutical manufacturing and process optimization).



Ownership and understanding of the scope for career development options

In a sign of ownership I published multiple research papers during my PhD. One of them was based on work I did for another PhD student during my masters thesis, unrelated to my current PhD, thus requiring me to work in parallel. Another paper was a literature review by invitation, going beyond basic requirements for a PhD student, and thus shows my awareness and ownership of my career development in an R&D setting. In fact, due to my outstanding academic performance and deliverables in my PhD, I was offered a position in the worlds larger food R&D organisation as an Associate R&D Scientist.

Understanding the importance of Impact & translation (public engagement, enterprise & IP)


In a great sign of impact I developed a patent in our lab that is now in the process of filing with the company co-sponsoring my PhD. This required the technical skillset underlying the technical innovation, for which the previously mentioned acquired skills were of essential support. Beyond mere technicalities, I pitched the idea to key company stakeholders and convinced them of the value added for their company in filing the IP. Following their go-ahead I interacted constructively with external patent lawyers on the draft patent publication and subsequent defence against the search report of the European Patent Office. Successfully passing the EPO the patent is now in the process of being filed at the World Intellectual Property Office for global protection. This showed my innovative capacities as well as the impact and entrepreneurship in developing an idea in parallel to my PhD research.


Responsible Research and Innovation (ethics and data management)

As PhD students we are required to complete Professional Behaviour and Ethical Conduct module, teaching me professional and ethical research conduction and publishing. This taught me how to acknowledge intellectual and professional contributions to my PhD work correctly so that every contributing member is rightfully credited for their work. Further, the requirement to develop a data management plan taught me secure and accessible data storage and archiving.

Qualitative skills and/or quantitative and digital skills, depending on discipline




The novel experimental techniques that I developed during my PhD, especially for Raman Chemical Imaging, not only required me to do extensive hardware creation, but also required me to write my own MATLAB code for spectral analysis and image generation. As such, I taught myself extensive numeracy and programming skills, such that other PhD students from the group asked me to write code for them and analyze their data. Hence, I ended up writing code to analyse roller compactor particle size, and compare between angle of repose and the normal distribution, and analysis of x-ray tomographic images to translate gray value into tablet density. Thus, I self-initiated and self-taught myself quantitative skills for computational data analysis.

Supervisor Signature:	Date:
 <i>Signatures blacked-out for data protection</i>	25/06/2025

Faculty Officer:	Date:
 <i>Signatures blacked-out for data protection</i>	07.07.2025

*Please note, students do not need to obtain the signature of the Faculty Officer - this will be actioned by RPI.

Luc Dewulf

Nationality: German, French
Date of birth: 21st February 1997, Essen, GER
 [ORCID](https://orcid.org/0000-0001-9376-447X) https://orcid.org/0000-0001-9376-447X
 [LinkedIn](http://www.linkedin.com/in/lucdewulf1) http://www.linkedin.com/in/lucdewulf1
 [ResearchGate](https://www.researchgate.net/profile/Luc-Dewulf-2) https://www.researchgate.net/profile/Luc-Dewulf-2

Education

- 2021 – 2025** PhD, Chemical Engineering, University of Sheffield, Sheffield, UK, with the Nestlé Institute of Packaging Sciences. Topic: On Lipid Migration from Particle-based Compacted Consumer Foods into Paper Packaging
- 2020 – 2021** MSc (Research) Physics, Soft Matter and Functional Interfaces Programme University of Edinburgh, Edinburgh, UK, with Crover Ltd., Edinburgh, UK. Topic: Granular rheology and locomotion in bulk cereal grains for drones immersible in grain storage silos.
- 2016 – 2020** First Class MEng (Hons) Chemical Engineering with Chemistry, University of Sheffield, Sheffield, UK.
First of class in first year, best Design Project (Bachelor thesis) in 3rd year, and best Research Project (Masters thesis) in 4th year. Topic: Green synthesis of porous nanosilica particles for drug-delivery use.
- 2015 – 2016** Interdisciplinary Science and Engineering Foundation Year, University of Sheffield, Sheffield, UK, First of class with final grade 88 %.
- 2013 – 2015** International Baccalaureate Diploma, Plymouth College, Plymouth, UK, final grade of 37 out of 45 points, 82 %.

Achievements and Awards

EPSRC Doctoral Training Partnership (DTP) Scholarship (2021-2025)

Fully funded stipend for the entire duration of the PhD at the University of Sheffield

EPSRC Studentship (2020-2021)

Fully funded MSc by Research stipend within the Soft Matter and Functional Interfaces (SOFI) Programme between Durham University, University of Leeds, and University of Edinburgh

Best MEng Research Project Report (2020)

Awarded for the highest ranking 4th year research project report

Kenneth Littlewood Memorial Award (2019)

Awarded for the highest ranking 3rd year design project report, when judged both on the overall mark awarded, which must be at least first class, and on the excellence of its presentation

Sheffield Undergraduate Research Fellowship Prize (2018)

Awarded as the best student researcher in the highly competitive summer research placement scheme

Chemical and Biological Engineering First Year Student Prize (2017)

Awarded for the best examination performance by a student in the first year of study

Ede and Ravenscroft Prize (2017)

Awarded for the best overall performance by a student in the first year of undergraduate study

Newson Gale Scholarship (2017 – 2020)

Awarded for four years to recognise academic excellence

Interdisciplinary Programmes Foundation Year in Science and Engineering Prize (2016)

Awarded for outstanding performance across all modules in the Science and Engineering Foundation Year